Defect-engineered (Ti,Al)N thin films

Dissertation

zur Erlangung des Grades

des Doktors der Ingenieurwissenschaften

der Naturwissenschaftlich-Technischen Fakultät

der Universität des Saarlandes

von

Isabella Citlalli Schramm Benítez

Saarbrücken

2017

Dedicado a mi Familia

Abstract

This thesis investigates the effect of point defects (nitrogen vacancies and interstitials) and multilayering ((Ti,Al)N/TiN) on the phase transformations in cathodic arc-evaporated *cubic* (Ti,Al)N thin films at elevated temperatures. Special attention is paid to the evolution of the beneficial spinodal decomposition into *c*-TiN and *c*-AlN, the detrimental formation of *wurtzite* AlN and the potential application as hard coating in cutting tools.

c-$(Ti_{1-x}Al_x)N_y$ thin films with varying Al fractions and N content (y = 0.93 to 0.75) show a delay in the spinodal decomposition when increasing the amount of N vacancies. This results in a 300 °C upshift in the age hardening and a delay in the *w*-AlN formation, while additions of self-interstitials enhance phase separation. High temperature interaction between hard metal substrates and thin films is more pronounced when increasing N deficiency through diffusion of substrate elements into the film. Low N content films (y = 0.58 to 0.40) showed formation of additional phases such as Ti_4AlN_3, Ti_2AlN, Al_5Ti_2 and Al_3Ti during annealing and a transformation from Ti_2AlN to Ti_4AlN_3 via intercalation. The multilayer structure of TiN/TiAlN results in surface-directed spinodal decomposition that affects the decomposition behavior. Careful use of these effects appears as a promising method to improve cutting tool performance.

Zusammenfassung

Diese Arbeit untersucht den Effekt von Punktdefekten (Stickstoffleerstellen und Zwischengitteratome) und Multilagen ((Ti,Al)N/TiN) auf die Phasenumwandlung in lichtbogenverdampften *kubischen* (Ti,Al)N-Dünnschichten bei erhöhten Temperaturen. Besonderes Augenmerk liegt auf der Entwicklung der vorteilhaften spinodalen Entmischung in c-TiN und c-AlN und der nachteiligen Bildung von *Wurtzit*-AlN, sowie der möglichen Anwendung als Hartstoffbeschichtung von Schneidwerkzeugen.

c-$(Ti_{1-x}Al_x)N_y$ mit unterschiedlichem Al-Anteil und N-Gehalten von y = 0,93 bis 0,75 zeigt mit zunehmenden Stickstoffleerstellen eine Verzögerung der spinodalen Entmischung. Dadurch verschiebt sich die Ausscheidungshärtung um 300 °C zu höheren Temperaturen und die *w*-AlN-Bildung wird verzögert, während der Einbau von Eigenzwischengitteratomen die Entmischung beschleunigt. Die Hochtemperaturwechselwirkung zwischen Hartmetallsubstrat und Dünnschicht durch Diffusion von Substratelementen in die Schicht nimmt mit steigendem Stickstoffdefizit zu. Stickstoffarme Schichten (y = 0,58 bis 0,40) zeigen während der Wärmebehandlung zusätzliche Phasen wie Ti_4AlN_3, Ti_2AlN, Al_5Ti_2 und Al_3Ti und eine Umwandlung von Ti_2AlN in Ti_4AlN_3 durch Interkalation. Die Multischichtstruktur von TiN/TiAlN führt zu einer oberflächengerichteten spinodalen Entmischung, die das Entmischungsverhalten beeinflusst. Ein gezielter Einsatz dieser Effekte erscheint als ein vielversprechender Weg, um die Leistungsfähigkeit von Schneidwerkzeugen zu verbessern.

Sammanfattning

I denna avhandling behandlas inverkan av punktdefekter (kvävevakanser och interstitialer) och multilagring ((Ti,Al)N/TiN) på högtemperaturfasomvandlingar i tunna arcförångade skikt av kubiska (Ti,Al)N. Störst vikt har lagts på utvecklingen av det fördelaktiga spinodala sönderfallet till c-TiN och c-AlN, den ofördelaktiga omvandlingen till w-AlN och potentialen som hårda skikt i verktygstillämpningar.

Tunna c-$(Ti_{1-x}Al_x)N_y$ skikt med olika Al-andel och en N-halt mellan ($y = 0.93$ och 0.75) uppvisar ökad undertryckning av det spinodala sönderfallet med ökat kvävevakanshalt. Detta resulterar i bildandet av w-AlN skiftas upp i temperatur vilket gör att åldershärdningen höjs med 300 °C. Däremot medför närvaron av självinterstitialer ett snabbare sönderfall. Växelverkan mellan hårdmetallsubstraten och de tunna skikten vid hög temperatur ökar med minskad kvävehalt i skiten genom diffusion av atomer från substratet in i filmen. Filmer med låg kvävehalt ($y = 0.58$ till 0.40) bildar även andra faser så som Ti_4AlN_3, Ti_2AlN, Al_5Ti_2 och Al_3Ti under värmebehandling och fasomvandlingen från Ti_2AlN till Ti_4AlN_3 sker via en mekanism kallad intercalation. Multilagring av TiN/TiAlN resulterar i ett ytriktad spinodalt sönderfall vilket påverkar det totala sönderfallsförloppet. Nyttjande av dessa resultat syns som lovande vägar till förbättrade verktygsegenskaper.

Long summary

Taken together, this work contributes mainly to the understanding of the effect of point defects on the phase transformations in *cubic* (Ti,Al)N alloys. Furthermore, it increases the understanding of the predicted mechanism behind the early decomposition onset of (Ti,Al)N/TiN multilayers by surface-directed spinodal decomposition. The specific contributions to the field are presented in greater detail below.

Impact of nitrogen vacancies on the high temperature behavior and mechanical properties of $(Ti_{1-x}Al_x)N_y$ alloys

This is the first study of the thermal response and structural evolution in nitrogen deficient cubic solid solution $(Ti_{1-x}Al_x)N_y$ (y < 1) thin films for different Al metal ratios (x = 0.26, 0.48 and 0.60) and a N deficiency from y = 0.92 to 0.75. The results show a substantial improvement of the thermal stability by reducing the nitrogen content for alloys with a Al metal fractions of x = 0.48 and 0.60. Alloys with x = 0.28 presented nucleation and growth of Al-Ti clusters inside the grains and *w*-AlN formation at grain boundaries. The decomposition paths shown in this study are consistent (with minor deviations) with predictions performed by Alling et al. on *c*-(Ti,Al)N_y (y < 1) via static ab initio calculations [1].

Based on the results, a typical cutting tool substrate (cemented carbide WC/Co based) was used in order to investigate the film-substrate interaction in the presence of N vacancies. A medium Al metal fraction in the *c*-$(Ti_{1-x}Al_x)N_y$ was selected (x = 0.48), and the thermal stability in terms of *w*-AlN formation was studied for a larger N-to-metal range $0.92 \geq y \geq 0.46$. The results show a clear age hardening effect (due to spinodal decomposition) upshifted by at least 300 °C when reducing the N fraction in coatings with a $y \geq 0.75$. This upshift is consistent with the enhanced thermal stability in terms of suppressing *w*-AlN formation. High N deficiency (y = 0.46) in the coating

leads to a change of phase evolution and a strong interaction with WC and Co at elevated temperatures.

The effect of point defects (interstitials and anti-sites) generated during film growth in combination with N vacancies was investigated in terms of phase stability and hardness. Based on previous results, a fixed Al metal and N-to-metal fraction in the c-$(Ti_{1-x}Al_x)N_y$ was selected (x = 0.46 and y = 0.87). The defect density was varied by applying a negative substrate bias from -30 to -80 V. The results show an improvement in the as-deposited hardness for the highly biased films (-80 V). At elevated temperatures, the hardness behavior shows age hardening shifted to higher hardness values and to lower temperatures by increasing the negative bias. Highly bias films present an increased driving force for phase separation at elevated temperatures.

Solid state formation of Ti_4AlN_3 in cathodic arc evaporated $(Ti_{1-x}Al_x)N_y$ alloys

The decomposition pathway in highly nitrogen-deficient solid solution *cubic* $(Ti_{1-x}Al_x)N_y$ ($0.58 \geq y \geq 0.40$) alloys was investigated for a wide range of Al metal fractions x = 0.28 to 0.63. This is the first study showing the formation of Ti_4AlN_3 (MAX phase) in thin films via solid state reaction in nitrogen deficient c-$(Ti_{1-x}Al_x)N_y$ alloys. A transformation mechanism from Ti_2AlN to Ti_4AlN_3 via intercalation is suggested and it is confirmed by the presence of an intermediate $Ti_6Al_2N_4$ phase. $Ti_6Al_2N_4$ has an intergrown structure whose unit cell consists of Ti_2AlN and Ti_4AlN_3 half unit cells. It is the first study showing the existence of the intergrown structure $Ti_6Al_2N_4$.

Surface directed spinodal decomposition at TiAlN/TiN interfaces

This work investigates the mechanism behind the early onset of spinodal decomposition in arc evaporated $(Ti_{1-x}Al_x)N/TiN$ multilayers, and the positive effect of artificial interfaces on the hardness. Two compositions (x = 0.50 and 0.67) were investigated in a combined study of experiments and phase-field simulations. The results show that the

decomposition is initiated at the multilayer interfaces, consistent with surface-directed spinodal decomposition (SDSD). Regardless of the composition, the same decomposition onset temperature is observed since the internal interfaces are responsible for the SDSD.

Lange Zusammenfassung

Zusammenfassend betrachtet ist die vorliegende Arbeit ein Beitrag zum Verständnis der Auswirkung von Punktdefekten auf die Phasenumwandlungen in *kubischen* (Ti,Al)N Legierungen. Darüber hinaus verbessert sie das Verständnis des vorhergesagten Mechanismus hinter dem vorgezogenen Beginn der Entmischung in (Ti,Al)N/TiN Multischichten durch oberflächengerichtete spinodale Entmischung. Die spezifischen Beiträge zum Stand der Forschung sind im Folgenden detailliert dargelegt.

Effekt von Stickstoffleerstellen auf das Hochtemperaturverhalten und die mechanischen Eigenschaften von $(Ti_{1-x}Al_x)N_y$-Legierungen

Dies ist die erste Untersuchung der Wärmetönungen und der Strukturentwicklung in Dünnschichten der kubischen Mischkristalllegierung $(Ti_{1-x}Al_x)N_y$ (y < 1) mit Stickstoffdefizit bei verschiedenen Aluminiumanteilen (x = 0,26, 0,48 und 0,60) und Stickstoffgehalten von y = 0,92 bis 0,75. Die Ergebnisse zeigen eine grundlegenden Verbesserung der thermischen Stabilität durch Reduzierung des Stickstoffgehalts in Legierungen mit Aluminiumanteilen von x = 0,48 bis 0,60. Legierungen mit x = 0,28 zeigen Keimbildung und Wachstum von Al-Ti-Clustern innerhalb der Kristallite und die Bildung von *w*-AlN an den Korngrenzen. Die ermittelten Reaktionspfade der Entmischung sind konsistent (mit geringen Abweichungen) mit Vorhersagen von Alling *et al.* für c-(Ti,Al)N$_y$ (y < 1) basierend auf statischen ab initio-Berechnungen [1].

Basierend auf diesen Ergebnissen wurde der Effekt von Stickstoffleerstellen auf die Schicht-Substrat-Wechselwirkung anhand eines typischen Schneidwerkzeugsubstrats (WC/Co-basiert) untersucht. Dazu wurde c-$(Ti_{1-x}Al_x)N_y$ mit einem mittleren Aluminiumanteil (x = 0,48) ausgewählt und die thermische Stabilität im Sinne der *w*-AlN-Bildung über einen weiten Bereich von Stickstoffgehalten zwischen $0,92 \geq y \geq 0,46$ bestimmt. Die Ergebnisse zeigen eine deutliche Verschiebung der Ausscheidungshärtung (durch spinodale Entmischung) zu bis zu 300 °C höheren

Temperaturen durch Reduktion des Stickstoffgehalts auf $y \geq 0,75$. Diese Verschiebung ist konsistent mit der erhöhten thermischen Stabilität im Sinne unterdrückter w-AlN-Bildung. Ein hoher Stickstoffmangel ($y = 0,46$) in der Schicht führt zu einer veränderten Phasenentwicklung und starker Wechselwirkung mit WC und Co bei erhöhten Temperaturen.

Der Effekt von wachstumsinduzierten Punktdefekten (Zwischengitteratome und Anti-Site-Defekte) in Kombination mit Stickstoffleerstellen auf Härte und Phasenstabilität wurde bestimmt. Basierend auf den vorangegangen Ergebnissen wurde c-$(Ti_{1-x}Al_x)N_y$ mit festem Aluminiumanteil und Stickstoff-Metall-Verhältnis ($x = 0,46$ und $y = 0,87$) ausgewählt. Die Defektdichte wurde durch eine negative Bias-Spannung am Substrat von -30 bis -80 V variiert. Die Ergebnisse zeigen eine verbesserte Härte im abgeschiedenen Zustand bei hoher Bias-Spannung (-80 V). Bei erhöhten Temperaturen führt eine Erhöhung der Bias-Spannung zu einem Härteverlauf mit Ausscheidungshärtung mit steigender Härte bei geringeren Temperaturen. Schichten mit hoher Bias-Spannung zeigen erhöhte treibende Kraft für Entmischung bei erhöhten Temperaturen.

Bildung von Ti_4AlN_3 durch Festkörperreaktionen in lichtbogenverdampften $(Ti_{1-x}Al_x)N_y$-Legierungen

Der Reaktionspfad der Entmischung in *kubischen* $(Ti_{1-x}Al_x)N_y$ ($0,58 \geq y \geq 0,40$) Mischkristalllegierungen mit hohem Stickstoffdefizit wurde für eine große Spanne von Aluminiumanteilen, $x = 0,28$ bis $0,63$, untersucht. Dies ist die erste Studie, die die Bildung von Ti_4AlN_3 (MAX-Phase) in Dünnschichten durch eine Festkörperreaktion in c-$(Ti_{1-x}Al_x)N_y$-Legierungen mit Stickstoffdefizit zeigt. Ein Umwandlungsmechanismus von Ti_2AlN in Ti_4AlN_3 durch Interkalation wurde vorgeschlagen und durch die Anwesenheit einer Übergangsphase $Ti_6Al_2N_4$ belegt. $Ti_6Al_2N_4$ hat eine verwachsene Struktur, deren Einheitszelle aus jeweils halben Einheitszellen von Ti_2AlN und Ti_4AlN_3 besteht. Es ist die erste Untersuchung, die die Existenz dieser verwachsenen Struktur $Ti_6Al_2N_4$ belegt.

Oberflächengerichtete spinodale Entmischung an TiAlN/TiN-Grenzflächen

Diese Studie untersucht den Mechanismus zwischen dem vorgezogenen Einsetzen der spinodalen Entmischung in lichtbogenverdampften $(Ti_{1-x}Al_x)N$/TiN Multischichten und dem positiven Effekt künstlicher Grenzflächen auf die Härte. Zwei verschiedene Zusammensetzungen (x = 0,50 und 0,67) wurden mit einem kombinierten Ansatz von Experimenten und Phasenfeldsimulationen untersucht. Die Ergebnisse zeigen, dass die Entmischung an den Grenzflächen der Multischichten beginnt, was in Übereinstimmung mit dem Modell der oberflächengerichteten spinodalen Entmischung steht. Unabhängig von der Zusammensetzung beginnt die Entmischung bei einer festen Temperatur, weil die inneren Grenzflächen die Entmischung bestimmen.

Utökad sammanfattning

Sammantaget så bidrar detta arbete I huvudsak till förståelsen av inverkan av punktdefekter på fasomvandlingar i kubisk (Ti,Al)N legeringar. Dessutom ökar det förståelsen för de predikterade mekanismerna bakom den tidiga starten av sönderfallet hos (Ti,Al)N/TiN multilager via ytriktat spinodalt sönderfall. Mer detaljerad beskrivning av bidragen till fältet ges nedan:

Inverkan av kvävevakanser på högtemperaturbeteende och mekaniska egenskaper hos $(Ti_{1-x}Al_x)N_y$ legeringar

Detta är den första studien av den termiska responsen och stukturutvecklingen i kvävefattiga kubiska fasta lösningar av $(Ti_{1-x}Al_x)N_y$ (y < 1) tunna filmer med olika Al-metall halt (x = 0.26, 0.48, och 0.60) och kvävehalt varierande från y = 0.92 till 0.75. Resultaten visar en substantiell förbättring av den termiska stabiliteten när kvävehalten sänks för legeringar med en Al-halt på x = 0.48 och 0.60. Legeringar med x = 0.28 uppvisar kärnbildning och tillväxt av Al-Ti kluster inne i korn och w-AlN i korngränserna. Sönderfallet sker, med små avvikelser, enligt den väg som Alling *et al.* predikterade för c-(Ti,Al) N_y (y < 1) med hjälp av *ab initio* beräkningar [62].

Baserat på dessa resultat, ett typiskt skärverktygssubstrat (WC/Co baserad hårdmetall) användes för att undersöka film-substratväxelverkan då kvävevakanser var närvarande. En $(Ti_{1-x}Al_x)N_y$ legering med en Al-halt på x = 0.48 valdes och den termiska stabiliteten på avseende på bildandet av w-AlN studerades för ett större omfång av kvävehalter, 0.92 > y > 0.46. Resultaten visar åldershärning (p.g.a. spinodalt sönderfall) och som sker vid minst 300 °C högre temperatur när kvävehalten sänks till y > 0.75. Detta skift till högre temperaturer är en konsekvens av den ökade termiska stabiliteten när det kommer till att undertrycka bildandet av w-AlN. Höga kvävevakanshalter (y = 0.46) i beläggningen ger en annan fasutveckling och en stark växelverkan med WC och Co vid höga temperaturer.

Inverkan av punktdefekter (interstitialer och "anti-sites") genererade under filmtillväxt i kombination med kvävevakanser studerades med avseende på termisk stabilitet och hårdhet. En legering med $x = 0.46$ och $y = 0.87$ valdes baserat på tidigare studier. Defektdensiteten ändrades genom att variera den negativa substrat biasen från -30 till - 80 V. Resultaten visar en förbättrad hårdhet för beläggningen växt med högst bias (- 80 V). Vid förhöjd temperatur skiftar en ökad negativ bias ålderhärdningen till lägre temperaturer och högre hårdheter. Filmer växta med hög bias uppvisar en ökad drivkraft för fasseparation vid förhöjd temperatur.

Fastfasbildande av Ti_4AlN_3 i arc-belagda $(Ti_{1-x}Al_x)N_y$ legeringar

Sönderfallet i kraftigt kvävefattiga fasta lösningar av $(Ti_{1-x}Al_x)N_y$ $(0.58 > y > 0.40)$ legeringar med ett brett omfång av Al-halter från $x = 0.28$ till 0.63 studerades. Detta är den första studien som visar bildandet av Ti_4AlN_3 (MAX-phase) i tunna filmer via fastfasreaktioner i kvävefattiga $(Ti_{1-x}Al_x)N_y$ legeringar. En omvandlingsmekanism från Ti_2AlN till Ti_4AlN_3 via "intercalation" föreslås och underbyggs med upptäckten av ett mellansteg, bildandet av $Ti_6Al_2N_4$. Strukturen hos $Ti_6Al_2N_4$ är sammanvävd at halvceller från Ti_2AlN och Ti_4AlN_3. Detta är också första gången som existensen och strukturen av $Ti_6Al_2N_4$ visas.

Ytriktat spinodalt sönderfall vid TiAlN/TiN-gränsytor

Detta arbete undersöker mekanismerna bakom den tidiga starten av spinodalt sönderfall i arc-belagda $(Ti_{1-x}Al_x)N/TiN$ multilager och den positiva effekten av artificiella gränsytor på hårdheten. Två sammansättningar $(x = 0.50$ och $0.67)$ studerades med hjälp av en kombination av experiment och fasfältssimuleringar. Resultaten visar att sönderfallet är initierat vid multilagrets gränsytor vilket är konsistent med ytriktat spinodalt sönderfall (SDSD). Oavsett sammansättning, samma starttemperatur då gränsytorna är orsakar sönderfallet via SDSD.

Preface

The work presented in this thesis is a result of my doctoral studies in the *Erasmus Mundus* joint doctoral program, DocMASE, at two research groups in two Universities between 2012 and 2017. Functional materials group at Saarland University (Saarbrücken, Germany) and Nanostructured materials group at Linköping University (Linköping, Sweden) in strong collaboration with SECO Tools (Fagersta, Sweden). In addition, the work was supported by the German Research Society (DFG), the federal state government of Saarland (Germany), the European Regional Development Fund (project AME-Lab), the Swedish Research Council (VR) and the Swedish Foundation for Strategic Research (SSF).

Isabella Citlalli Schramm Benítez

Saarbrücken, 2017

Included papers and my contributions

I. *Impact of nitrogen vacancies on the high temperature behavior of $(Ti_{1-x}Al_x)N_y$ alloys*
    I.C. Schramm, M.P. Johansson Jõesaar, J. Jensen, F. Mücklich and M. Odén
    ***Acta Materialia* 119 (2016) 218**

    Carried out the major part in the planning and characterization, besides ERDA measurements, and wrote the first draft of the paper.

II. *Solid state formation of Ti_4AlN_3 in cathodic arc evaporated $(Ti_{1-x}Al_x)N_y$ alloys*
    I.C. Schramm, C. Pauly, M.P. Johansson Jõesaar, P. Eklund, J. Schmauch, F. Mücklich, M. Odén
    ***Acta Materialia* 129 (2017) 268**

    Carried out the major part in the planning and characterization, besides TEM experiments where I participated, and wrote the first draft of the paper.

III. *Effect of nitrogen vacancies on phase stability and mechanical properties of arc deposited $(Ti_{0.52}Al_{0.48})N_y$ (y < 1) coatings*
    I.C. Schramm, C. Pauly, M.P. Johansson Jõesaar, S. Suárez, F. Mücklich and M. Odén
    ***Surface and Coatings Technology* 330 (2017) 77**

    Carried out the major part in the planning and characterization, besides TEM and EBSD experiments where I participated, and wrote the first draft of the manuscript.

IV. *Enhanced thermal stability and mechanical properties of nitrogen deficient titanium aluminum nitride $(Ti_{0.54}Al_{0.46}N_y)$ thin films by tuning the applied negative bias voltage*
    K.M. Calamba, I.C. Schramm, M.P. Johansson Jõesaar, J. Ghanbaja, J.F. Pierson, F. Mücklich and M. Odén
    ***Journal of Applied Physics* 122 (2017) 065301**

Took part in the experimental work, carried out the APT experiments and the SEM imaging, and contributed to the writing and discussion of the manuscript.

V.   *Surface directed spinodal decomposition at TiAlN/TiN interfaces*
A. Knutsson, I.C. Schramm, K. Asp Grönhagen, F. Mücklich and M. Odén
***Journal of Applied Physics* 113 (2013) 114305**

Took part in the experimental work, carried out the APT experiments, and contributed to the writing and discussion of the paper.

Related papers but not included in the thesis

VI.   *Nanostructured and coherency strain in multicomponent hard coatings*
        R. Forsén, I.C. Schramm, P.O.Å. Persson, F. Mücklich, M. Odén and
        N. Ghafoor
        ***Applied Physics Letters. Materials* 2 (2014) 116104**

VII.   *Tuning hardness and fracture resistance of ZrN/ZrAlN nanoscale*
        multilayers by stress-induced transformation toughening.
        K. Yalamanchili, I.C. Schramm, E. Jiménez-Piqué, L. Rogström,
        F. Mücklich, M. Odén and N. Ghafoor
        ***Acta Materialia* 89 (2015) 22**

VIII.   *Exploring the high entropy alloy concept in (AlTiVNbCr)N*
        K. Yalamanchili, F. Wang, I.C. Schramm, J. Andersson, M.P. Johansson
        Jõesaar, F. Tasnadi, F. Mücklich, N. Ghafoor and M. Odén
        ***Thin Solid Films* 636 (2017) 346**

IX.   *Thermal and mechanical stability of wurtzite-ZrAlN/cubic-TiN and wurtzite-*
        ZrAlN/cubic-ZrN multilayers
        Y.H. Chen, L. Rogström, J.J. Roa, J.Q. Zhu, I.C. Schramm, L.J.S. Johnson,
        N. Schell, F. Mücklich, M.J. Anglada and M. Odén
        ***Surface and Coatings Technology* 324 (2017) 328**

X.   *A coated cutting tool and a method for coating the cutting tool. Nitrogen*
        deficient TiAlN
        I.C. Schramm, M.P. Johansson Jõesaar and M. Odén
        Patent. *International Publication number:* **WO2016169935**

Acknowledgements

Professor Frank Mücklich, my supervisor at UdS. Thank you for giving me the opportunity of being part of your research group and for letting me work with advance techniques, such as atom probe. I have learned so much during this study.

Professor Magnus Odén, my supervisor at LiU. Thank you for all the guidance and support even if most of the times it was from far away, and for the opportunity of researching in a very interesting field, i.e. nitrides.

Dr. Sven Ulrich. I would like to thank you for the acceptance of the revision of this work and being my opponent at the Swedish committee.

Erasmus mundus joint doctoral program. My special gratitude goes to DocMASE program and the funding from Erasmus Mundus that made possible my PhD studies and such wonderful international research experience. Special thanks to *Flavio Soldera.*

Dr. Mats Johansson. Special thanks to you, without your collaboration this thesis would not have been possible. Thank you for all the interesting discussions and support along this thesis, and of course all the samples.

Christoph Pauly. My dear office mate, sharing office for many years is not a long time if one compares it to our life time. Nevertheless, it was a whole PhD student life time. Thank you so much for all the talks, support, patience, collaboration, discussions and, of course, all the M&M´s you gave me.

Collaborators. Thank you for your great contributions to my manuscripts and letting me be part of your projects, for the time spend doing experiments, and for all the interesting discussions. Axel, Björn, Christoph, Jens, Jörg, Katherine, Klara, Kumar, Lina, Mats, Michael, Naureen, Per, Peter, Rikard, Seba, Sebi and my supervisors.

Proof readers: Bea, Christoph, Faadhil, Lourdes, Magnus, Nico, Robin. Special thanks to you, I am sure my thesis would look much different without your precious help.

Therese Dannetun. Thank you so much for helping me in the administrative part and organization of many (all) of my LiU visits.

Functional materials group, Saarland University. I would like sincerely thank for making my work stay very nice and comfortable. Special thanks to Björn, Christoph and Sebi for all the talks, lunch breaks, fun and time spend together.

Table of contents

Acronyms and symbols

1D	one-dimensional
3D	three-dimensional
APT	atom probe tomography
c-	*cubic* crystal structure
CVD	chemical vapor deposition
Da	Dalton
DSC	differential scanning calorimeter
EBSD	electron backscatter diffraction
EDS	energy-dispersive X-ray spectroscopy
EFTEM	filtered analytical transmission electron microscope
ERDA	elastic recoil detection analysis
F	evaporation field
fcc	face-centered cubic
FDA	frequency distribution analysis
FIB	focused ion beam microscopy
G	Gibbs free energy
HAADF	high angle annular dark field STEM
HRTEM	high-resolution TEM
Isosurface	iso-concentration surface
k_f	field factor
LEAP	local-electrode atom probe
μ	Pearson coefficient
m/q	mass-to-charge ratio
MAX	$M_{n+1}AX_n$
N_v	nitrogen vacancies
Proxigram	proximity histogram

PVD	physical vapor deposition
ROI	region of interest
SAD	selected area diffraction
SDSD	surface directed spinodal decomposition
SEM	scanning electron microscopy
STEM	scanning transmission electron microscopy
SZM	structure zone model
TEM	transmission electron microscopy
t_{flight}	time-of-flight
TG	thermogravimetry
T_m	melting point
TMN	transition metal nitride
ToF-E	time-of-flight energy
w-	*wurtzite* crystal structure
XRD	X-ray diffractometry

1. Introduction to the field

Coated cutting tools constitute the majority of tools used nowadays in material removal with geometrically defined edges [2]. The cutting tool experiences an environment of high localized temperatures (~ 1000 °C) and high stresses (~ 700 MPa) during material removal [3], which makes metal machining a demanding process. It also encounters repeated impact loads (interrupted cuts) and interaction with the work piece chips. The use of a coating that withstands these harsh conditions has led to an improvement in tool lifetime and cutting performance. Ideally, this thin film should be chemically inert, stable at high-temperatures, wear resistant with low friction, oxidation resistant and harder than the substrate [3,4]. There is a wide variety of hard coatings designed to meet the requirements of different applications on the market. Nevertheless, the appearance of new workpiece materials (difficult to cut) and the demand for higher production rates (extreme cutting conditions) lead to a strong, ongoing development in this field [2,3,5,6]. In the scope of this thesis, the investigated films have the potential for their application as hard coatings for metal cutting in turning and milling tools.

TiN was the first commercial physical vapor deposited (PVD) coating used in the cutting tool industry in the late 70´s, and since then, nitrides have governed most of the hard coating industry [2]. Among all available transition metal nitrides (TMNs) on the market, (Ti,Al)N is one of the most extensively investigated and used systems [2–4,7]. It was the addition of Al into TiN which substantially improved its properties at elevated temperatures [8,9]. Solid solution (Ti,Al)N coatings with a cubic (rock-salt) structure, typically deposited by PVD, exhibit high hardness (~ 30 GPa), low thermal conductivity and good wear resistance [3,4]. For medium to high Al content, a protective Al_2O_3 upper layer formed at high temperatures (above 700 °C) is responsible for the good oxidation resistance [10,11]. Furthermore, (Ti,Al)N coatings show high thermal stability and hot hardness [3,4]. It is the evolution of hardness at elevated temperatures (age hardening) that is the key characteristic of these coatings.

The quasi-binary isostructural (rock-salt, B1) TiN-AlN phase diagram presents a miscibility gap [12,13]. If a metastable solid solution *cubic* (Ti,Al)N is obtained inside the miscibility gap, the system will tend to phase separate into coherent *c*-TiN and *c*-AlN via spinodal decomposition instead of the thermodynamically stable phases *c*-TiN and *w*-AlN under the right conditions. The main advantage of spinodal decomposition is the formation of nanometer-sized *c*-TiN and *c*-AlN domains [4,14–16]. The difference in elastic properties and lattice parameter between the different domains leads to coherency strain and a Koehler-type hardening [17–19], resulting in age hardening [17]. However, further annealing leads to coarsening of the domains, the formation of *wurtzite* AlN, and a degradation of mechanical properties, especially hardness [17,20,21]. Understanding and modifying the phase transformation in (Ti,Al)N has become a key factor to improve coating performance in the last three decades [4,22,23]. The use of other alloying elements, artificial layer structures, external pressure and stress are some of the proposed solutions for improving the thermal stability and suppressing the *w*-AlN formation [4,24–28]. Although extensive research has been carried out on this system, there are few studies on the impact of point defects on the phase transformations in (Ti,Al)N thin films which is the main scope of this work.

This thesis investigates the unexplored effect of constitutional defects (nitrogen vacancies) and their combination with deposition-induced self-interstitials on the phase transformation of *cubic* solid solution (Ti,Al)N thin films at elevated temperatures. This was indirectly performed by reducing the nitrogen content of the as-deposited alloy and by applying a negative substrate bias voltage during film deposition in a cathodic arc evaporation system. Herein, point defect engineering is demonstrated to significantly impact the phase decomposition pathway, the evolution of microstructure and the hardness at elevated temperatures.

In addition, a deeper understanding of the effect of artificial interfaces in a multilayer configuration (Ti,Al)N/TiN on the phase transformation on (Ti,Al)N was developed. Multilayering has been demonstrated to modify the phase transformation in a positive

way [25]. Here, the internal interfaces are shown to shift the onset for decomposition to lower temperatures due to the appearance of surface-directed spinodal decomposition (SDSD).

The thesis is divided into two main parts. The first part is a background of the research that was carried out. Fundamental concepts are introduced, the employed characterization techniques are presented and the experimental setup is described. It concludes with an overview of the contribution made to the field by this work with a summary of the appended papers (manuscripts). The second part contains the result of the research in the form of scientific papers/manuscripts, which are briefly described below:

In **Paper I**, the effect of nitrogen vacancies on the thermal stability of *cubic* solid solution $(Ti_{1-x}Al_x)N_y$ free-standing coatings is presented for different Al metal ratios (x = 0.26, 0.48 and 0.60) and a N deficiency from y = 0.92 to 0.75.

In **Paper II**, highly N deficient $(Ti_{1-x}Al_x)N_y$ ($0.58 \geq y \geq 0.40$) alloys are investigated for a wide range of Al metal fractions (x = 0.28 to 0.63). The transformation path is presented and a transformation mechanism from Ti_2AlN to Ti_4AlN_3 via intercalation is suggested.

In **Paper III (manuscript)**, substrate-coating interaction in the presence of N vacancies is investigated in $(Ti_{0.52}Al_{0.48})N_y$ coatings. Commercial cemented carbides (WC/Co based) were used as substrate and the N deficiency ranged from y = 0.92 to 0.46.

In **Paper IV**, interaction and impact on thermal stability and mechanical properties when combining different types of point defects (N vacancies and interstitials) in $(Ti_{0.54}Al_{0.46})N_{0.87}$ are presented.

In **Paper V**, the effect of artificial interfaces on the thermal stability of (Ti,Al)N is investigated in a multilayer configuration (Ti,Al)N/TiN. Surface-directed spinodal decomposition is shown experimentally and confirmed by phase field simulations.

2. Phase transformation

A phase transformation describes the change in a system from an initial state to a new one. The main driving force for this to occur is the minimization of the system´s Gibbs free energy. Some examples of phase transformations are the transitions from solid, to liquid, to gaseous state by increasing the temperature; the change in crystal structure by applying pressure; the transition from ferromagnetic to paramagnetic states by crossing the Curie temperature, etc. In order to understand why a system *wants* to transform, to which state and how fast will it be, thermodynamics and kinetics are needed.

In this chapter, some thermodynamic concepts regarding the phase stability and the driving force for phase transformations in alloys are discussed, followed by a description of the main mechanism of transformation in this thesis: diffusion. Finally, for this thesis, three relevant diffusional transformations in solids are presented, i.e. nucleation and growth, spinodal decomposition and coarsening, and intercalation for MAX phase transformation.

2.1 Phase stability

A system is usually defined as a mixture of one or more phases; a phase, being a part of the system where the properties and composition are homogenous and physically different from other parts (phases) [29]. Every system is described by its Gibbs free energy:

$$G = H - TS$$

H is the enthalpy, T the temperature and S the entropy. Enthalpy represents the internal energy of the system and the entropy is related to its randomness.
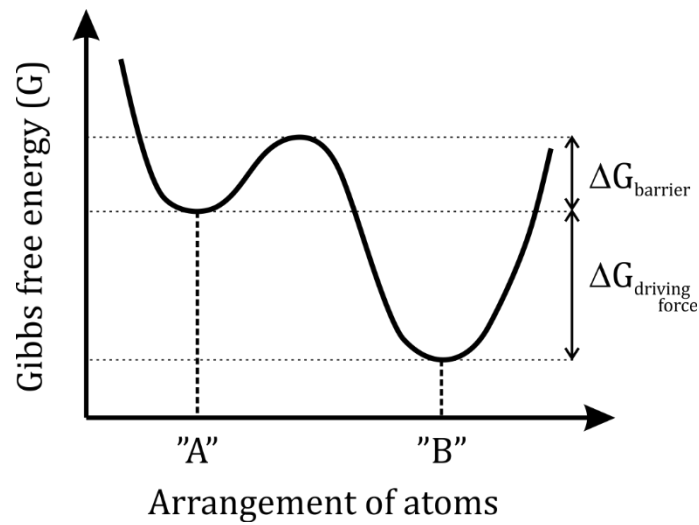
Figure 2.1: A schematic variation of Gibbs free energy with the arrangement of atoms. Configuration "B" has the lowest free energy, were the system is at stable equilibrium. Configuration "A" is a metastable state. Adapted from [29]*.*

There are three main states of a system: *stable, metastable* or *unstable*. The equilibrium *stable* state is defined by the global minimum of the system's free energy, $dG = 0$, while a *metastable* state is any state where the energy is at a local minimum, $dG = 0$. Every other state where $dG \neq 0$ is *unstable*. A simplified example of how the Gibbs free energy changes as a function of arrangement of atoms is shown in Figure 2.1. Two minimums are observed and only one, configuration "A", has the lowest free energy of the system, the equilibrium *stable* state [29]. The system is in thermodynamic equilibrium only when the Gibbs free energy is at its minimum, if this is not the case the system will have a natural tendency (driving force) to achieve the minimum energy. It is then when a phase transformation can take place.

A phase transformation does not necessarily occur straight to the equilibrium *stable* state, but can pass through intermediate metastable states, which may last for short or indefinite periods of time. The duration of any intermediate step will depend on the energy barrier ($\Delta G_{barrier}$) that the system must overcome to change state, e.g. free energy hump between configurations "A" and "B" (Figure 2.1). The higher $\Delta G_{barrier}$ it is, the more difficult it will be for the system to change state. Of course, the duration of these

metastable states also depends on other kinetic factors (which are further described in text below).
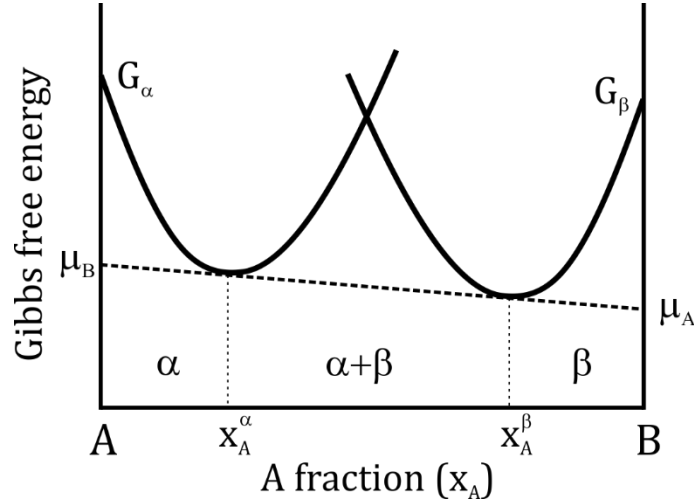

Figure 2.2: Equilibrium of α and β phase shown by the tangent rule construction. Adapted from [29]*.*

To predict the state to which a system wants to transform, it is important to know how the Gibbs free energy changes as a function of the parameter under consideration (e.g. composition, temperature). In alloys, different elements are mixed together and more than one phase can be stable for the same condition. Therefore, the Gibbs free energy becomes composition, temperature and pressure dependent.

A simplified example is where A and B atoms are mixed together but they do not have the same crystal structure in their pure state, one being α phase and the other β. In this case, each phase will have its own Gibbs free energy curve, G_α and G_β. The equilibrium between the two phases will be reached when the chemical potential of each component (A and B) is the same in each phase (α and β):

$$\mu_A^\alpha = \frac{\partial G_\alpha}{\partial X_A} = \frac{\partial G_\beta}{\partial X_A} = \mu_A^\beta$$

This is equivalent to the common tangent rule, where the tangents to each G curve at the equilibrium composition lie on a common line as shown in Figure 2.2. For this

example, the composition range with a high amount of A atoms will present the α phase, compositions rich in B atoms will show the β phase, and a mix of both phases in between. The composition of α and β phases cannot exceed the composition dictated by the common tangent, i.e. there is a miscibility gap.

The complexity increases when more elements (A, B, C, ...) and possible phases (α, β, γ, ...) are involved in a system. Nevertheless, the common tangent rule can always be applied and a similar condition for equilibrium is imposed to the system. The chemical potential of each element must be identical in every phase [29], i.e.

$$\mu_A^\alpha = \mu_A^\beta = \mu_A^\gamma = \cdots$$

$$\mu_B^\alpha = \mu_B^\beta = \mu_B^\gamma = \cdots$$

$$\mu_C^\alpha = \mu_C^\beta = \mu_C^\gamma = \cdots$$

For all examples above, the equilibrium state of an alloy was considered for a fixed temperature and pressure and only composition was varied. Once the temperature is taken into account, an equilibrium phase diagram can be constructed (see examples in Chapter 3).

In this thesis, phase transformations in (Ti,Al)N alloys were investigated by thermal activation at a fixed pressure, in a temperature range where the system is mainly in solid state. Therefore, most attention will be given to phase diagrams where composition and temperature are varied as shown in the following Chapter 3.

2.2 Diffusion

In this thesis, phase transformation occurs via thermal activation, and diffusion is one fundamental mechanism involved. Diffusion is the movement of atoms, and it is induced by a gradient of the chemical potential. In general, there are two types of

diffusion, downhill and uphill. In the first and most common, the atoms move to eliminate concentration gradients. In the second, the movement is towards the high concentration regions. These composition gradients are directly correlated to the chemical potential gradients of the components [29].

Furthermore, the capability of an atom to move in a system is defined as diffusivity. It depends on the type of element, the host phase and its surroundings (e.g. a surface). The differences depend on conditions such as the mechanism of diffusion (substitutional and interstitial), the probability of jumping to a vacant site, the number of vacancies, the chemical potential gradients and the temperature, among others. In an alloy, where differences in element diffusivity can exist, it is more complex to describe how atoms will move (diffuse).

One more important aspect to take in consideration for phase transformation is the presence of defects like grain boundaries, interfaces, dislocations, free surfaces, etc. In the vicinity of these defects, the diffusivity and the equilibrium conditions of a system may change, since they have a more open structure and the movement of atoms along them is much faster than in the lattice. These defects are also called high-diffusivity paths and under certain circumstances, they can be the dominant diffusion path and may control the phase transformation [29].

2.3 Diffusional transformations in solids

In the scope of this thesis, where the phase transformation path of (Ti,Al)N alloys was investigated at elevated temperatures, three diffusional transformations in solids are of relevance and discussed in more detail below.

2.3.1 Nucleation and growth

Nucleation is the self-organization of elements, structural and/or compositional, into a new phase. It occurs via formation of a small nucleus (embryo) inside a region of the system and it is the first step for phase transformation. It can be homogenous or heterogeneous. The first is the ideal case and it takes place randomly inside the system. The second is the most common and it occurs at suitable sites where the energy needed to form an embryo is lower than the homogenous case. Those places can be dislocations, grain boundaries, stacking faults, excess vacancies, inclusions, and free surfaces.

In order to form a stable embryo, there is an energy barrier (ΔG^*) for nucleation to be overcome (Figure 2.3 (a)). This is related to three main contributions: volume generation, interface formation and a strain energy mismatch between the initial phase and the new phase. The first contribution minimizes the free energy of the system and is dominant above a critical embryo radius (r*). The other two add additional energy to the system and are responsible for the nucleation barrier.

Once the nucleus of the new phase is stable, it will grow in order to decrease the Gibbs free energy of the system. This stage is called growth. A schematic view of how the composition varies with time in a nucleation and growth process is shown in Figure 2.3 (b). It starts with the nucleation of a phase with composition X_2, in the matrix with composition X_0, and it ends with two phases (X_1 and X_2), where X_1 is the composition of the depleted matrix.

Sometimes the energy cost for nucleation is too high and intermediate phases are formed before reaching the equilibrium state. These phases may not have the lowest free energy but a low nucleation barrier, making them energetically favorable. This stepwise transformation occurs especially if there are differences in the crystal structure between initial and final state, e.g. formation of Guinier-Preston zones.
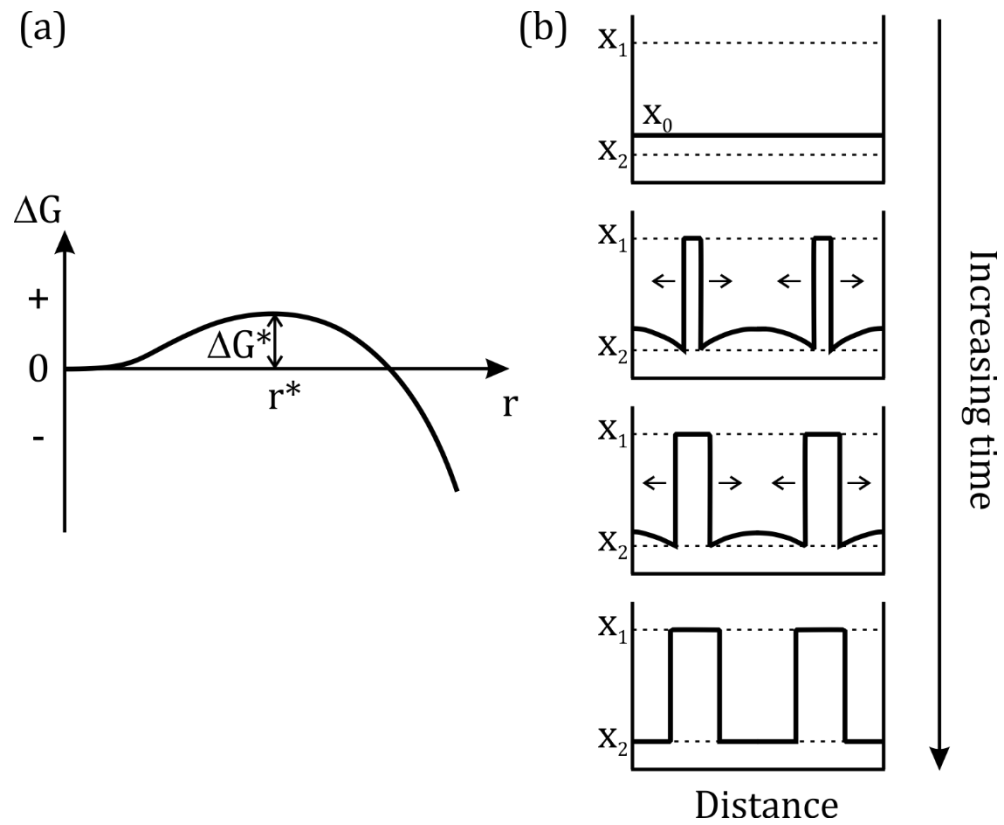
(a)

(b)

ΔG

+

0

-

ΔG^*

r^*

r

X_1

X_0

X_2

X_1

X_2

X_1

X_2

X_1

X_2

Increasing time

Distance

Figure 2.3: (a) Variation of Gibbs free energy with embryo radius r for a homogenous nucleus, where ΔG* is the nucleation activation barrier. (b) Schematic composition profiles at increasing time during nucleation and growth of precipitates with X2 composition. Modified from [29].

2.3.2 Spinodal decomposition and coarsening

Spinodal decomposition is a mechanism where an initial phase separates into two phases without a nucleation barrier (nucleation free). The condition for this to occur, is that the free energy of a given alloy must have a negative curvature, $\partial^2 G / \partial X^2 < 0$, as shown schematically in Figure 2.4 (b) for the composition X_0 at the temperature T_2. Small fluctuations in composition will decrease the free energy of the system, and uphill diffusion will take place until equilibrium composition of both new phases, X_1 and X_2, is reached [30]. The only limitation is the diffusion which can be activated with temperature.
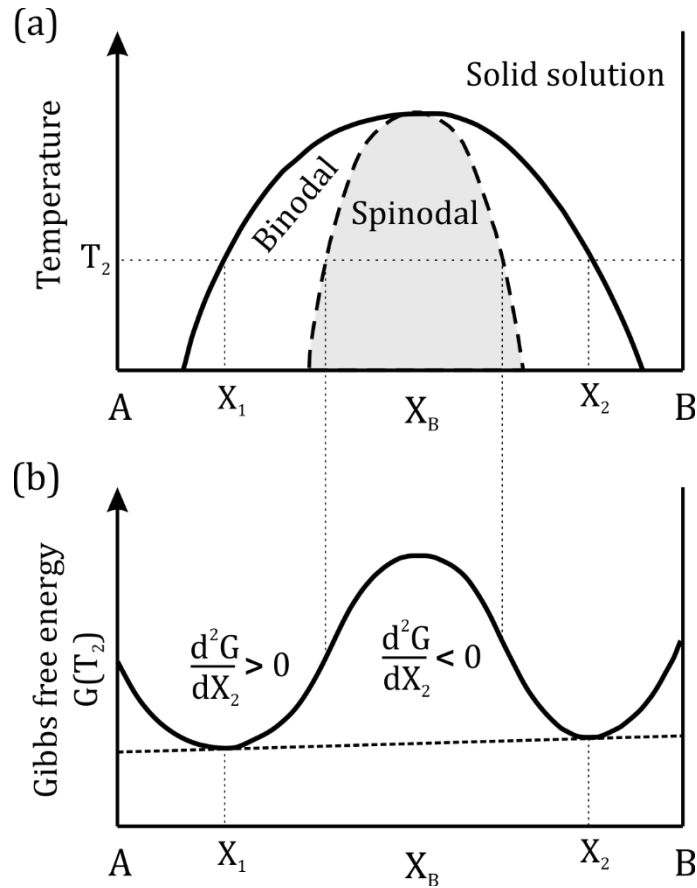

Figure 2.4: (a) Schematic phase diagram of a binary alloy presenting a miscibility gap and (b) the corresponding free energy curve at the temperature T_2. Modified from [29].

11

Spinodal decomposition possesses the following characteristics [31], as shown schematically in Figure 2.5:

- It occurs homogenously throughout the system (except near lattice defects) and it results in a finely disperse microstructure.
- The compositional fluctuations exhibit a certain wavelength during segregation, and the amplitude should increase continuously until a metastable state is reached.
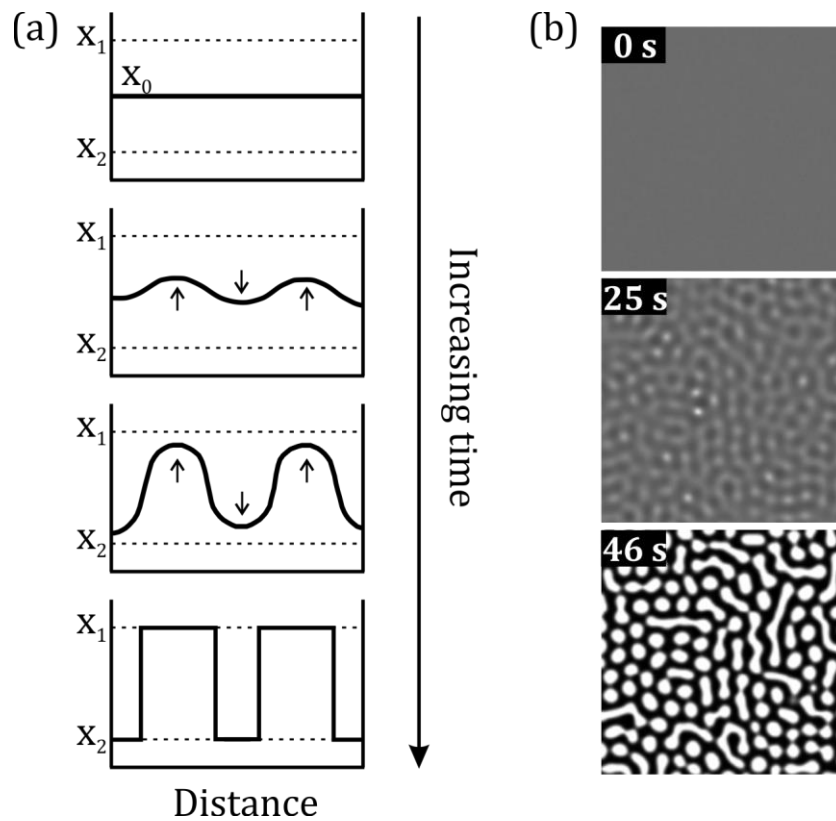- The interfaces between phases are diffuse.

Figure 2.5: Schematic representation of an alloy during spinodal decomposition (into X_1 and X_2) as a function of time in a (a) 1D composition profile [29] and (b) phase filed simulated 2D microstructure [32], obtained by solving a modified Cahn-Hilliard equation.

This mechanism of transformation was first proposed by Hillert [30], and later improved and expanded to three dimensions by Cahn [31,33] and Hilliard [34]. It occurs in

systems that present a miscibility gap in their phase diagram, e.g. Au-Ni, which is usually defined by two regions: spinodal and binodal as shown schematically in Figure 2.4 (a). Nucleation-free decomposition occurs only inside the spinodal region, while in the binodal region, a phase separation through nucleation and growth takes place. The line dividing them is called spinodal and it is defined by a zero curvature of the Gibbs free energy $\partial^2 G/\partial X^2 = 0$ (Figure 2.4). Cahn proposed that near the limit, yet still within the spinodal region, decomposition will be too slow so that the compositional fluctuations will reach a metastable state, and competing mechanisms like nucleation and growth will take over [31].

The kinetics describing the phase separation via spinodal decomposition are defined by the Cahn-Hilliard equation [34]:

$$\frac{dc}{dt} = D\nabla^2(c^3 - c - \gamma\nabla^2 c)$$

D is the diffusion coefficient, c is the concentration, and γ is the surface energy. As the time advances, the concentration approaches a sinusoidal composition profile with a wavelength (λ). The amplitude of the composition profile increases with time with a fixed λ until a metastable equilibrium is reached as shown schematically for one dimension in Figure 2.5 (a).

An important parameter that determines the rate of spinodal decomposition is λ, i.e. the smaller λ is, the faster the system decomposes. However, λ cannot be predetermined for a system (alloy composition) since it depends on the initial intrinsic compositional fluctuations and on the principle of selective amplification (fluctuations with $\sqrt{2}\,\lambda_{critical}$ will grow faster and dominate) [31]. Only an upper limit in the spinodal decomposition rate can be set, the critical wavelength ($\lambda_{critical}$), which depends on the interfacial energy and the coherency strain energy of the system. Therefore, below this $\lambda_{critical}$ decomposition cannot occur [29].

13

Once a wavelength dominates in the phase separation, this λ will persist and the amplitude will increase until the system has reached the final composition of the phases, X_1 and X_2 (Figure 2.5 (a)) [29]. The following stage is called coarsening, where a growth of the domains with composition X_1 and X_2 will take place in order to minimize the interfacial and strain energy of the system [33]. During coarsening, there is no wavelength defining the evolution of the domain growth.

Only systems that present a miscibility gap in their phase diagram can be candidates for spinodal decomposition. The system studied in this thesis, metastable (Ti,Al)N with a B1 structure, is one of the systems presenting a miscibility gap which is shown and described in the following Chapter 3.

2.3.3 Intercalation

The ability to accommodate an elements or molecule by insertion between layers in a layered material is called intercalation [35]. There are different chemical and physical methods for activating this insertion and diverse inorganic hosts (graphite, clays, carbides, etc.) [35–38]. Only one is of interest in this thesis: the thermal activation of intercalation in transition metal nitrides/carbides for MAX phase formation. First, a brief introduction into MAX phases is given, followed by the description of the process of intercalation as a mechanism of phase transformation.

MAX phases ($M_{n+1}AX_n$ phases, $n = 1, 2, 3$) are a class of hexagonally structured nitrides and carbides that present a characteristic layered structure with M_6X octahedral layers separated by A-element layers. M is an early transition metal (Ti, V, Cr, Zr, Nb, Mo, Hf, Ta), A is an A-group element (Al, Si, Ga, Ge, As, In, P), and X is carbon or nitrogen. The nomenclature depends on the amount of M layers separated by A layers, e.g. M_2AX ($n = 1$), M_3AX_2 ($n = 2$) or M_4AX_3 ($n = 3$) as shown in Figure 2.6 [39]. Their layered structure makes them a good candidate for intercalation.

Intercalation in MAX phases was proposed for the first time by Zhou *et al.* [40], and presented later by Riley *et al.* as a low temperature solid state method for MAX phase synthesis without the formation of intermediate phases [41,42]. In general, intercalation starts with a solid-state binary precursor ($M_{1-n}X_n$) and an A-element source. Through thermal activation, a spontaneous rearrangement of the precursor into a layered structure makes the insertion of the A-element possible, and finally the formation of a MAX phase [41]. Intercalation is a reversible process [40,43].
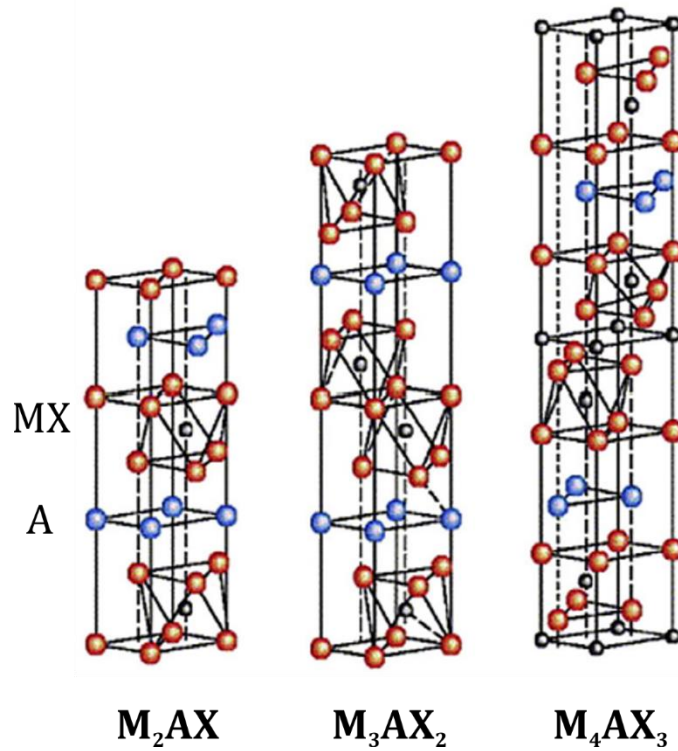

MX

A

M₂AX   **M₃AX₂**   **M₄AX₃**

Figure 2.6: Crystal structures of the different MAX phase stacking sequences: M₂AX, M₃AX₂, and M₄AX₃ from Högberg et al. [44] adapted from Barsoum [45].

In order for intercalation to occur, a proper selection of the binary precursor must be done in which a rapid and highly selective diffusion can take place. The precursor must have crystallographic similarities with the MAX phase structure, and it must allow an unrestricted motion of constituent elements through sufficient diffusion "pathways" [42]. Examples for precursors are MX binaries with NaCl (B1) structure, like TiC_x ($x < 1$) and TiN_x ($x < 1$), where the sub-stoichiometry in the non-metallic lattice

enhances the X-element diffusivity [4]. The structures present similarities in the shared edges between M_6X octahedral in MAX phases and the ones in the B1 structure [39,46].

Once the precursor exists, the next step is the thermal activation in the presence of an A-element source, where a sequence of steps must occur spontaneously. These steps start with (a) the initial random distribution of X-element vacancies, (b) ordering of the vacancies, (c) twinning of the precursor sublattice, and finally (d) intercalation of A-element [42]. A schematic view of the transformation is shown in Figure 2.7.
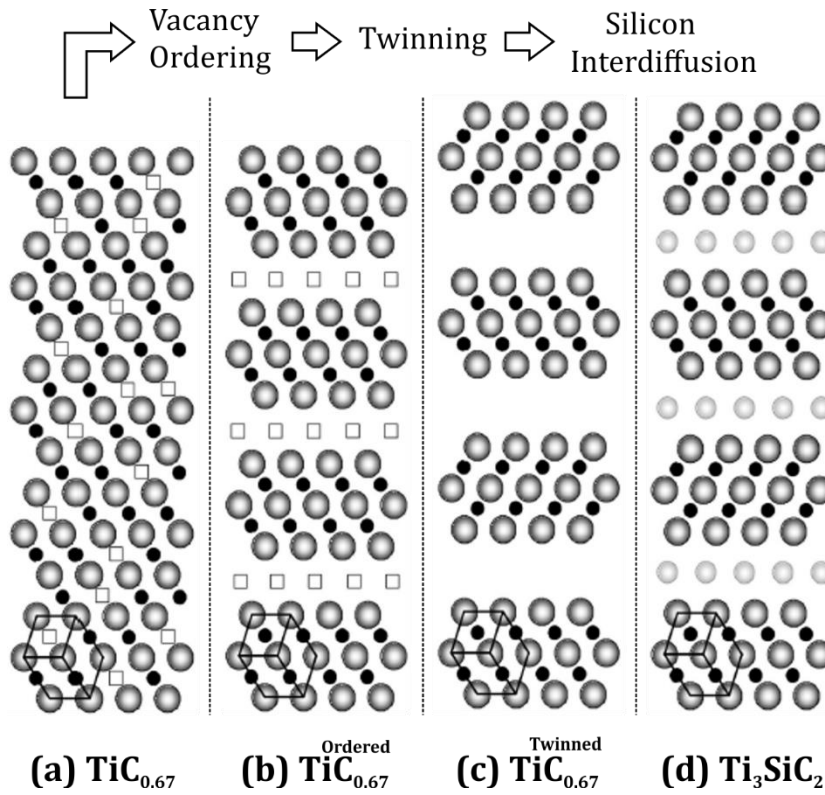

Figure 2.7: Proposed reaction mechanism of the intercalation of silicon into the customized solid state precursor, TiC0.67 by Riley et al. [42]*.*

MAX phase formation via intercalation has been reported in different ternary systems, e.g. Ti_3SiC_2, Ti_2AlC, Ti_3AlC_2 [47–49]. Until now it has only been shown in ternary systems containing carbon as the X-element.

3. Ti-Al-N system

The Ti-Al-N system has received considerable attention in the last three decades due to the technologically relevant materials obtained from this system either as bulk or as thin film. Various applications include TiN thin film diffusion barriers, AlN in electronic semiconductor devices, (Ti,Al)N wear-resistant coatings, high temperature composites like Ti_2AlN, Al_3Ti, AlN, and TiN enhancing Al-base alloys, TiN embedded in steels preventing grain growth, etc [4,7,39,50].

In order to obtain the desired material, it is important to understand and predict the phases formed in the system at different compositions, temperatures, pressures, etc. For that task, phase diagrams are of great help since they predict the thermodynamically stable phases for the different conditions. In the case of thin films, where it is possible to synthesize alloys far from thermodynamic equilibrium (like in the case of this thesis), additional data of the metastable phases is needed.

The prime material investigated in this thesis is the metastable *cubic* solid solution B1-$(Ti_{1-x}Al_x)N_y$ alloy with a rock salt structure deposited as thin film, in a very wide metal and non-metal compositional range ($0.28 \leq x \leq 0.63$ and $0.40 \leq y \leq 1.0$). To understand the thermal stability and the phase transformation of this alloy at high temperatures (up to 1400 °C) and ambient pressure, all available data was revised. Therefore, the chapter is divided in two parts. Firstly, the thermodynamic stable phases in the multicomponent Ti-Al-N system are examined in terms of composition and temperature variation at fixed pressure (1 atm). Secondly, the available thermodynamic data of the metastable *cubic* solid solution B1-$(Ti_{1-x}Al_x)N_y$ is presented. Additionally, as a guide for the reader, the most relevant phases in this work, stable and metastable, and their structure data are presented at the end of this chapter.
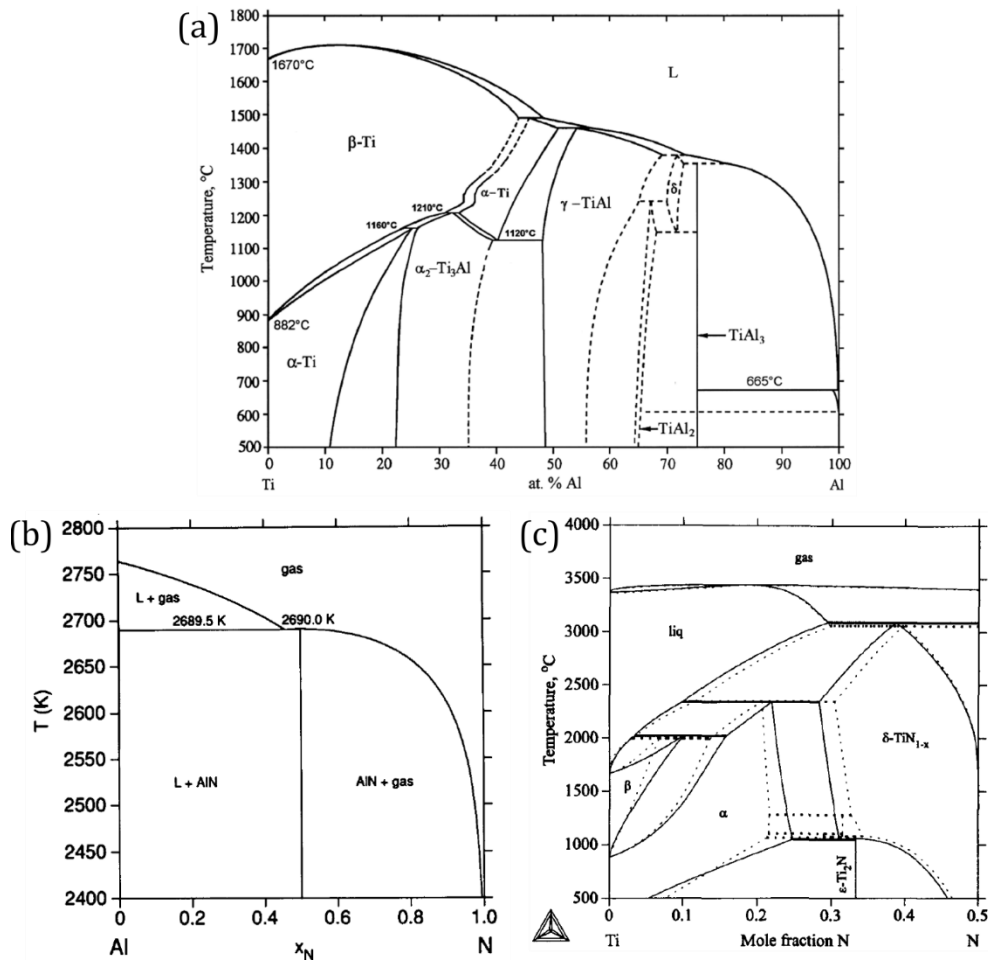
3.1 Stable phases in the Ti-Al-N system

Figure 3.1: (a) Ti-Al phase diagram by Kainuma et al. [51]*, (b) Al-N phase diagram assessed by Hillert and Jonsson* [52] *and (c) Ti-N phase diagram assessed by Chen and Sundman* [53].

The Ti-Al-N system presents a large variety of stable binary and ternary phases. The majority of the binary compounds are mixtures of Ti and Al, and only three of them contain nitrogen. The Ti-Al mixtures are intermetallic phases: Al_3Ti, $AlTi$, $AlTi_3$, Al_2Ti and Al_5Ti_2. Some have a wide compositional range of existence like $TiAl$ and $AlTi_3$, while others have a very narrow one like Al_3Ti and Al_2Ti, as shown in Figure 3.1 (a). Their crystal structures are varied, e.g. γ-$TiAl$ ($L1_0$), α_2-$AlTi_3$ (DO_{19}), Al_3Ti (DO_{22}).

18

The three binary phases containing nitrogen are AlN, TiN and Ti_2N. AlN has a hexagonal (*wurtzite*) structure and a very narrow compositional range as shown in Figure 3.1 (b) [52]. This phase is a wide-band-gap (6.3 eV) semiconductor which does not accommodate any excess nitrogen or aluminum under thermodynamic equilibrium. Ti_2N presents a tetragonal structure with a narrow compositional range and it is stable only at low temperatures as shown in Figure 3.1 (c) [53]. Finally, TiN belongs to the transition metal nitrides (TMN) with a rock salt (B1) structure, which can be seen as two face-centered cubic (*fcc*) structures with one unit cell shifted half an *a*-axis towards the other. One *fcc* lattice is occupied by Ti atoms and the other by N atoms. One main characteristic of TMNs is that they can accommodate a large quantity of nitrogen deficiency via nitrogen vacancies in the N lattice [4,54], making TiN stable over a large compositional range as it is shown in Figure 3.1 (c). TiN can also accommodate N overstoichiometry through metal vacancies [55].
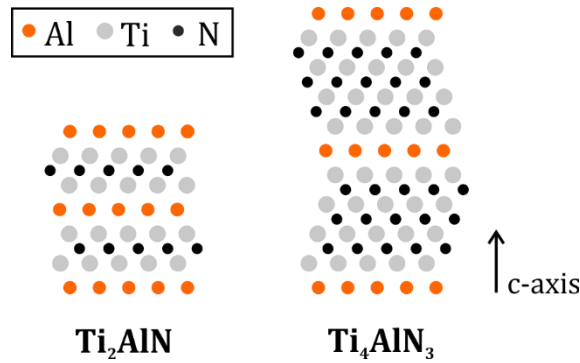

Figure 3.2: Schematic stacking sequence along c-axis of MAX phases Ti₂AlN and Ti₄AlN₃.

Only three ternary compounds are stable in the Ti-Al-N system: Ti_2AlN, Ti_3AlN and Ti_4AlN_3. Ti_3AlN has a $L1_2$-type structure and can be obtained after prolonged annealing at relatively low temperatures, i.e. 1000 °C [53]. Ti_2AlN and Ti_4AlN_3 belong to the MAX phases (for more details on MAX phases see Chapter 2 section Intercalation). Their structure is constituted by Ti_6N octahedral layers separated by Al layers, and depending on the amount *n* of Ti_6N layers separated by A layers, it will be Ti_2AlN (*n* = 1 layer) or Ti_4AlN_3 (*n* = 3 layers) [39]. The schematic view of their structure is shown in Figure 3.2.
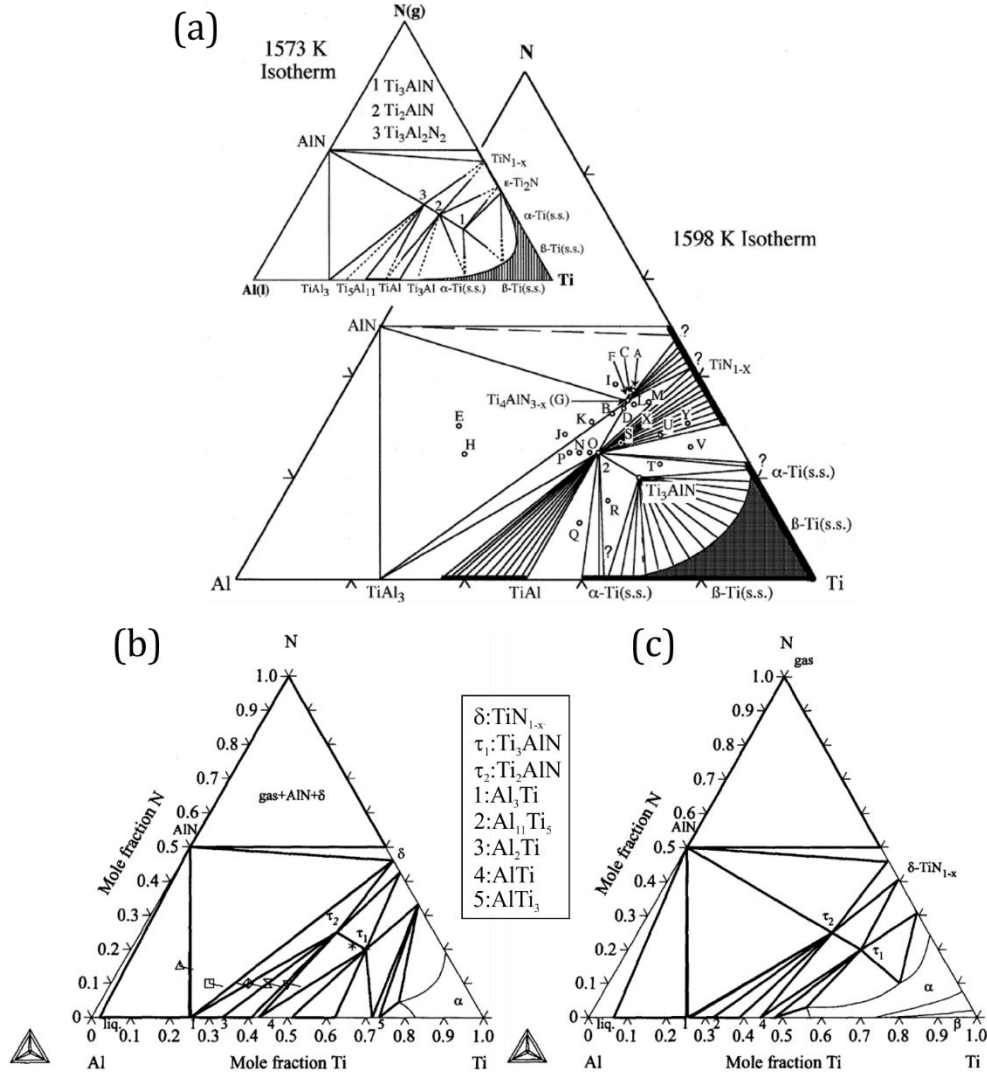
Figure 3.3: Isothermal sections of Ti-Al-N at (a) 1300 °C assessed by Procopio et al. [56]. Insert on the left corner is the old phase diagram reported by Chen and Sundman [53]. (b) 900 °C and (c) 1200 °C calculated by Chen and Sundman [53].

For the Ti-Al-N system both MAX phases have shown to accommodate N vacancies [57–59], making their compositional range broad. Among the ternary compounds Ti_2AlN exists over a large temperature and composition range, i.e. 700 to 1600 °C (e.g. see Figure 3.3) [53]; while Ti_4AlN_3 has a very narrow temperature range around 1300 °C, as shown by Procopio *et al.* in Figure 3.3(a) [56]. As side note, Ti_4AlN_3 was wrongly believed to be $Ti_3Al_2N_2$ until Barsoum *et al.* showed that it is the MAX phase Ti_4AlN_3 [60].

3.2 Metastable cubic solid solution $(Ti_{1-x}Al_x)N_y$

Metastable solid solution c-$(Ti_{1-x}Al_x)N_y$ alloys with a B1 structure can be obtained as thin films in a wide compositional range with an aluminum metal fraction x < 0.7 [4] and a nitrogen to metal ratio $0.37 \leq y \leq 1.02$ [55,61,62]. Their structure is similar to that of TiN, where two *fcc* sublattices are interpenetrated. One *fcc* lattice is randomly occupied by Ti and Al atoms, and the other by N atoms. Due to the technological relevance of this alloy as hard coating for cutting tools, extensive investigations on its thermal stability and phase transformations have being conducted. For the scope of this work, two relevant thermodynamic assessments are presented. The first is the quasi-binary TiN-AlN isostructural *cubic* phase diagram (N stoichiometric case) which has been optimized lately by Shulumba *et al.* (Figure 3.4) [13]. The second is the phase decomposition pattern of the metastable *cubic* $Ti_{1-x}Al_xN_{1-y}$ in the presence of nitrogen vacancies (N sub-stoichiometric case) calculated by Alling *et al.* via first principle calculations (Figure 3.5) [1].

The calculated phase diagram for c-$(Ti_{1-x}Al_x)N$ shows a miscibility gap, and three regions can be distinguished: spinodal, binodal and the solid solution (Figure 3.4) [13,63]. The first one corresponds to the spinodal region, where the metastable c-$(Ti_{1-x}Al_x)N$ is subject to nucleation-free, isostructural phase separation into c-TiN and the metastable c-AlN (spinodal decomposition). In the binodal region, separation is also expected, but the phases c-TiN and c-AlN are formed via nucleation and growth. Finally, the solid solution region can be observed at high temperatures. The miscibility gap has an asymmetric shape with the maximum located at high Al content (x ≈ 0.8) which is explained by the electronic structure mismatch between TiN and AlN, stronger in the Al-rich side [63]. Therefore, the driving force for segregation increases for alloys with high Al content. Furthermore, Shulumba *et al.* showed that lattice vibrations have a strong impact on the calculated B1-$(Ti_{1-x}Al_x)N$ phase diagram by lowering the maximum of the miscibility gap from 6560 to 2860 K and increasing the solubility of AlN in TiN as shown in Figure 3.4 [13].
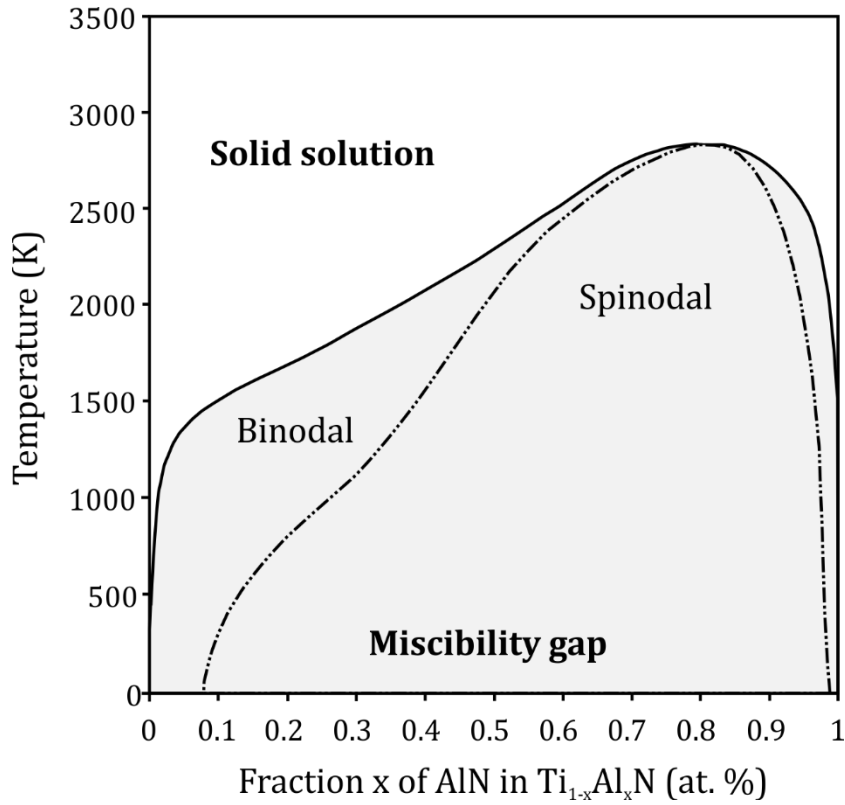
Figure 3.4: Calculated quasi-binary TiN-AlN phase diagram for B1-(Ti$_{1-x}$Al$_x$)N by Shulumba et al. [13]. *Adapted figure showing only the miscibility gap calculated with the SIFC TDEP method where the anharmonic vibrational entropy contribution is included. The dash-dotted lines correspond to the spinodal metastable region and the solid line to the binodal. Abbreviations: SIFC = symmetry-imposed force constants; TDEP = temperature-dependent effective potential method.*

Cubic AlN is a metastable phase with a B1 structure and a small volume mismatch with *c*-TiN in comparison to *w*-AlN with *c*-TiN, since a volume difference of 22.5 % between *c*-AlN and *w*-AlN exists [64]. Under specific circumstances (e.g. solid solution *c*-(Ti,Al)N inside the miscibility gap), spinodal decomposition can take place. The formation of *c*-AlN is energetically favorable as an intermediate step during the phase transformation of *c*-(Ti,Al)N into the stable phases *c*-TiN and *w*-AlN following the path:

$$c\text{-(Ti,Al)N} \rightarrow c\text{-TiN} + c\text{-AlN} \rightarrow c\text{-TiN} + w\text{-AlN}$$
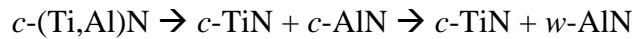
If enough energy is given to the system, *c*-AlN will eventually transform into the thermodynamic stable phase *w*-AlN via nucleation and growth [14,63]. This

transformation is not accounted for in the B1-$(Ti_{1-x}Al_x)N$ phase diagram presented by Shulumba *et al.* (Figure 3.4), nor in the following decomposition pattern map, since only isostructural phase separation is considered and of relevance to predict.

The effect of nitrogen substoichiometry on the phase stability of the metastable cubic B1 $(Ti_{1-x}Al_x)N_y$ ($y < 1$) alloys has been investigated by Alling *et al.* using static *ab initio* calculations [1]. They predicted the preferred isostructural decomposition pattern of c-$(Ti_{1-x}Al_x)N_y$ in the x-y compositional space as shown in Figure 3.5. The length of the arrows represents the magnitude of the driving force for nucleation-free phase separation, and the arrows point toward the preferred decomposition direction. A point represents no driving force for nucleation-free phase separation. The map can be divided in three major regions according to Alling *et al.*, which were schematically drawn in the map for a better visualization:

(1) High Al content, between N-rich and N-poor regions: Most energetically unstable compositional range. There are no reports of synthesis of stable or metastable cubic (Ti,Al)N alloys. Nevertheless, the use of epitaxial growth, pressure or a multilayer configurations could help obtain alloys in this range [65,66].

(2) Close to N stoichiometry and medium-high Al content: Nitrogen tends to stick preferably to aluminum due to unfavorable accommodation of N vacancies in AlN which presents a semiconducting bonding [1]. On the other hand, TiN can accommodate the N vacancies due to its broad stable composition range in the N deficient side (see Figure 3.1 (c)), as has been shown experimentally [67].

(3) The N-poor, Ti-rich region: Strong driving force for precipitation of metallic Al or Al-Ti mixtures and tendency of N to stick to Ti. AlN formation is not energetically favorable since the phase does not accommodate N vacancies (see comment on region (2)), and all compositions between Al metallic mixtures and AlN are unfavorable. Alling *et al.* also mention that the formation of Ti-Al alloys

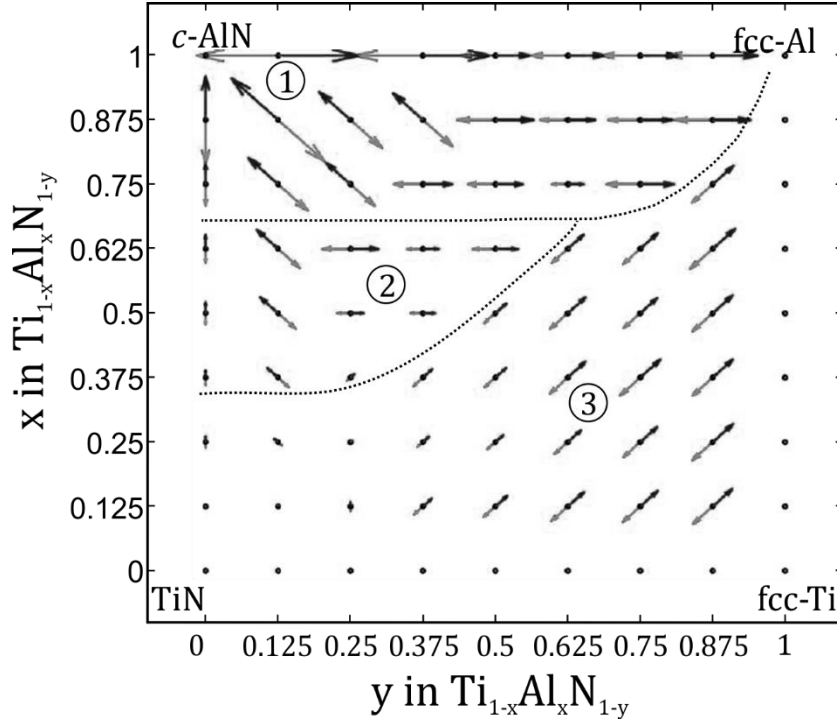or compounds has the same driving force as for stabilizing hexagonal MAX phases and cubic Ti_3AlN perovskite [1].

Figure 3.5: Energetically preferred decomposition pattern of $(Ti_{1-x}Al_x)N_y$ in x-y composition space calculated by Alling et al. [1]. The arrows point in the direction in which a phase separation would be most energetically favorable. Their length indicates the magnitude of this energy. Dot indicates no driving force for phase separation. Map modified from the original by adding a division of three regions.

3.3 Summary of relevant phases

The information presented in this chapter should serves as a guide to predict and understand the phase evolution of metastable cubic solid solution $(Ti_{1-x}Al_x)N_y$ thin films, when the composition of the alloys is varied and the material is subjected to high temperatures. The relevant phases for this thesis and their respective structures are listed below:

Phase	Crystal structure	ICDD #	Space group	Lattice parameter (Å)
(Ti,Al)N*	Cubic	Al-dependent	Fm3m (225)	4.120 < a < 4.241
TiN	Cubic	00-038-1420	Fm3m (225)	a = 4.241
AlN*	Cubic	00-025-1495	Fm3m (225)	a = 4.120
AlN	Hexagonal	00-025-1133	P63mc (186)	a = 3.111 c = 4.979
Ti₂AlN	Hexagonal	00-055-0434	P63/mmc (194)	a = 2.989 c = 13.614
Ti₄AlN₃	Hexagonal	04-010-5108	P63/mmc (194)	a = 2.988 c = 23.372
Ti₆Al₂N₄*	Hexagonal	This work	unknown	a = 2.988 c = 56.2
Al₃Ti	Tetragonal	01-072-5006	I4/mmm (139)	a = 3.853 c = 8.583
Al₅Ti₂	Tetragonal	03-065-9788	P4/mmm (123)	a = 3.905 c = 7.4

* Metastable phase.

4. Thin Films

According to literature, a thin film is broadly considered as a layer of material with a thickness that can vary from an atomic monolayer up to several microns [4–6,68]. It must show a difference of at least one order of magnitude between the lateral dimensions and the layer thickness, and it can be on a substrate (partially confined), confined between two materials or free-standing. Moreover, a multilayer is referred to as a stack of thin films. The process of synthesizing a thin film atom by atom from a source on a growth surface is called deposition, common methods of which are physical vapor deposition (PVD) and chemical vapor deposition (CVD) [5,69]. The method and deposition parameters produce distinct microstructures and, consequently, properties. A deep understanding of this strong process-microstructure-properties correlation must thus be developed to achieve the desired properties, rendering the characterization of the thin film a crucial task.

In this thesis, a PVD process called cathodic arc evaporation was used for depositing (Ti,Al)N thin films, which is currently used for coating cutting tools [2,3,70]. The main focus lies on the characterization of the film microstructure and hardness in as-deposited and annealed (up to 1400 °C) states. Therefore, the chapter is divided in two main sections: in the first one, the steps involved in the synthesis of a thin film by cathodic arc evaporation are described, as well as the employed experimental setup; the second part briefly introduces the characterization techniques used. Due to its relative novelty, atom probe tomography (APT) will be described in more detail as a nonstandard technique, as well as the different data analysis methods and graphical representations employed in this study.

4.1 Synthesis

In general, the synthesis of a thin film by a PVD process requires three main steps; the first is the creation of a material vapor from a source, followed by the transport of the vapor phase to the substrate and, finally, the film growth through condensation of vapor species and nucleation. All three steps can be controlled independently to some extent, making PVD techniques versatile tools to control the microstructure and properties of the deposited films.

4.1.1 Cathodic arc evaporation

Cathodic arc evaporation belongs to the PVD processes where the vapor phase of the desired material source (cathode target) is obtained by heating it with a high current (30 - 400 A), low voltage (tens of volts) arc discharge that moves along the cathode surface either controlled or randomly [5,69,70]. The arc spot (10^{-8} to 10^{-4} m diameter) carries high current densities (~ 10^8 to 10^{12} A/m^2) which erode the cathode by melting and vaporization as well as particle ejection. The ionized plasma generated by the process consists of electrons, multivalent ions, neutral vapor atoms and droplets, where the desired species are the metal ions and neutrals. A schematic view of a cathodic arc evaporation system is shown in Figure 4.1. The arc is usually ignited by a mechanical striker and confined to the cathode surface by a boundary shield. The vapor with multivalent ions is responsible for sustaining the arc. While the arc spot movement is governed, to a certain extent, on cathode composition, gas species and pressure, presence of magnetic fields, etc. with a typical velocity of ~ 100 m/s [5]. Furthermore, the ions ejected from the cathode surface are typically accelerated towards the substrate by applying a negative bias voltage to the substrate, thus controlling the energy of the condensing species.

The relatively high possible ionization of the material atoms in the plasma (30 - 100 %) [70], high kinetic energies (10 - 200 eV) [71], and multiple charge states of the ions [70]

are crucial parameters for the resulting microstructure and properties of the coating. These characteristics are responsible for relatively high deposition rates (e.g. 200 nm/min), a dense structure and good adhesion [3,7,70].
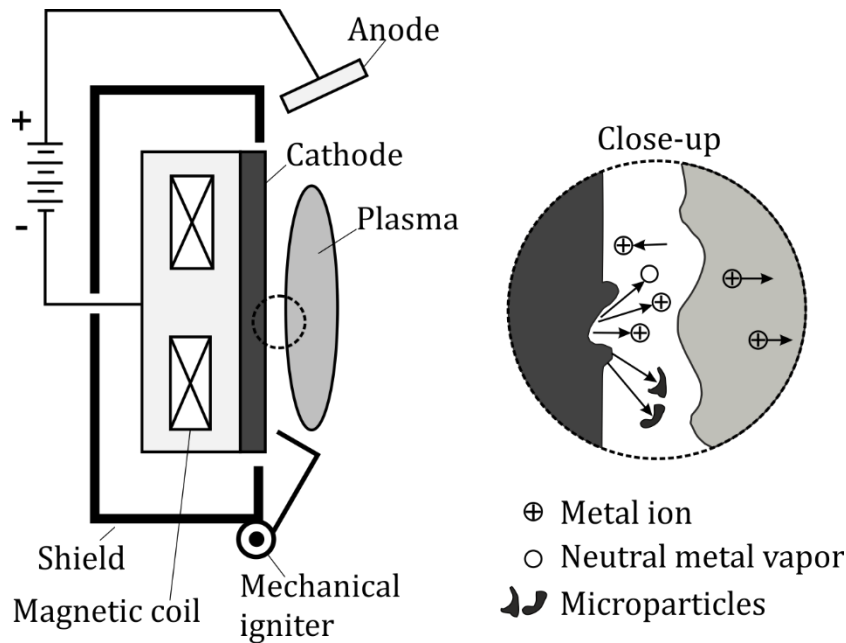

Figure 4.1: Schematic view of a cathodic arc deposition system with a model of the source emission. Adapted from Ohring [5].

Deposition of compound materials (nitrides, oxides, etc.) by cathodic arc evaporation is usually performed in a reactive atmosphere where some of the compound elements are evaporated from the cathode target, followed by their reaction with a gas (e.g. N_2, O_2) to form the desired compound. This variation of the technique is called reactive cathodic arc evaporation [69,70]. It is preferably used for deposition of compound materials since evaporation of a compound target does not necessarily result in a vapor phase with the same composition, but rather a dissociation of the vapor species into fragments of the compound [69]. It is one of the most common deposition processes used for refractory nitrides, carbonitrides, and carbides in the cutting tool industry [2,3,5].
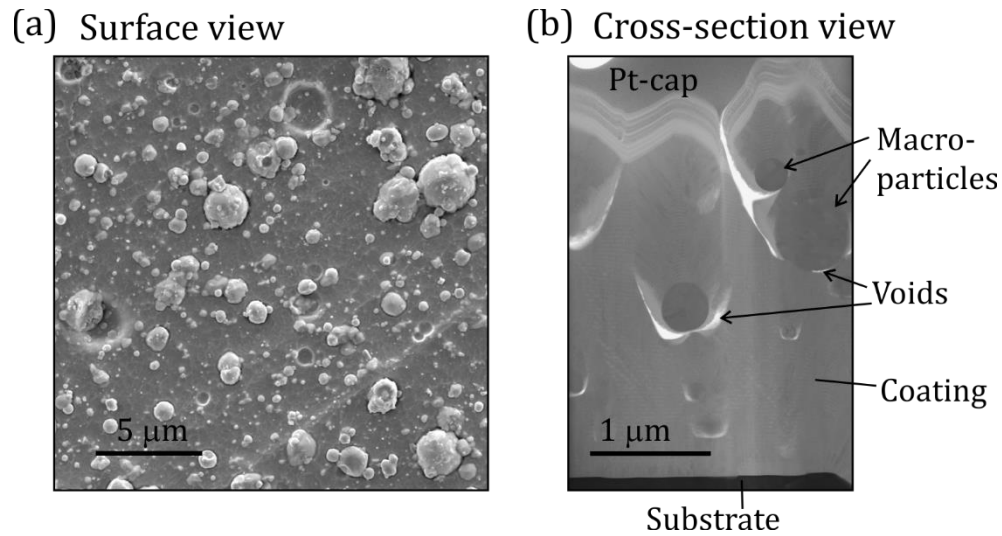
(a) Surface view

(b) Cross-section view

Figure 4.2: (a) SEM micrography of (Ti,Al)N film surface roughness due to macroparticles and (b) cross section in SE contrast of (Ti,Al)N thin film with embedded macroparticles.

One of the main disadvantages of this technique is the generation of macroparticles (droplets), which arise from the erosion of the cathode when the arc stays too long on one spot, locally melting the cathode [69–71]. The droplets arise from the ejection of liquid or solid particles due to thermal shock and hydrodynamic effects [5], resulting in a thin film with randomly embedded macroparticles. This leads to a disrupted film growth, an increase of the nucleation sites for new grains, a reduction in adhesion of the coating, an increase in surface roughness, and the creation of voids beneath and above them [3,72,73] as shown in Figure 4.2. Moreover, their composition tends to be more metallic compared to the reacted compound film (e.g. nitrides) [70], which can degrade the mechanical properties of the thin film. Size and density of the macroparticles can be controlled by the arc movement, deposition parameters or cathode target [69,71,74]. They can also be removed by the usage of a filter due to the differences in mass and properties, or by producing a diffuse arc [71,75]. However, the deposition rate drops substantially and it becomes less attractive for industrial scale deposition. Therefore, no filter is used during industrial scale depositions, nor for the thin films deposited in this thesis.

A second disadvantage of the cathodic arc evaporation process is the relatively high residual compressive stress caused by the high kinetic energy of the impinging ions, which generates lattice defects [4,76,77]. The compressive residual stresses are responsible for the increase in hardness since they also act as obstacles for dislocation movement and have a crack closing effect. Nevertheless, if the stresses are too high, delamination of the thin film can occur [4,78].

4.1.2 Film growth

The final step involved in the synthesis of a thin film is its growth. This consists in consecutive nucleation, island growth, coalescence of islands, competitive grain growth, formation of a continuous structure, recrystallization and film thickness growth [79,80]; making the evolution of the thin film structure a rather complex phenomenon. Therefore, a lot of effort has been put into understanding the correlation between deposition parameters and thin film microstructure, leading to the development and refinement of structure zone model (SZM) diagrams. SZMs should be a guideline to understand the mechanisms dominating the film growth, and thereby enable tuning of the deposition process parameters in order to obtain the desired microstructure and film properties.

There is no specific SZM for cathodic arc evaporated coatings, nevertheless a good approach is the model presented by Barna *et al.* for PVD thin films which is shown schematically in Figure 4.3 [79]. It was constructed by considering the role of impurities in addition to the most determinant atomic processes controlling the microstructure evolution: surface and bulk diffusion. Three main zones can be distinguished according to Barna *et al.*: *Zone I*, with low deposition temperatures, where porous and low density thins films are obtained with thin columns (1-10 nm) due to low surface and low bulk diffusion; *Zone T*, where surface diffusion is activated and a competitive columnar growth of the different crystal orientations takes place (here, texture changes with the film thickness); and *Zone II,* where surface and volume diffusion are active and high

due to the high deposition temperatures, leading to wide columnar growth with similar orientation.

Cathodic arc evaporation films are typically located in the intermediate zone (*zone T*) since they present a dense columnar microstructure [3,80]. A competitive columnar growth takes place at the beginning of the film growth and with increasing thickness, a dominant crystallographic orientation of the columns is observed [80].
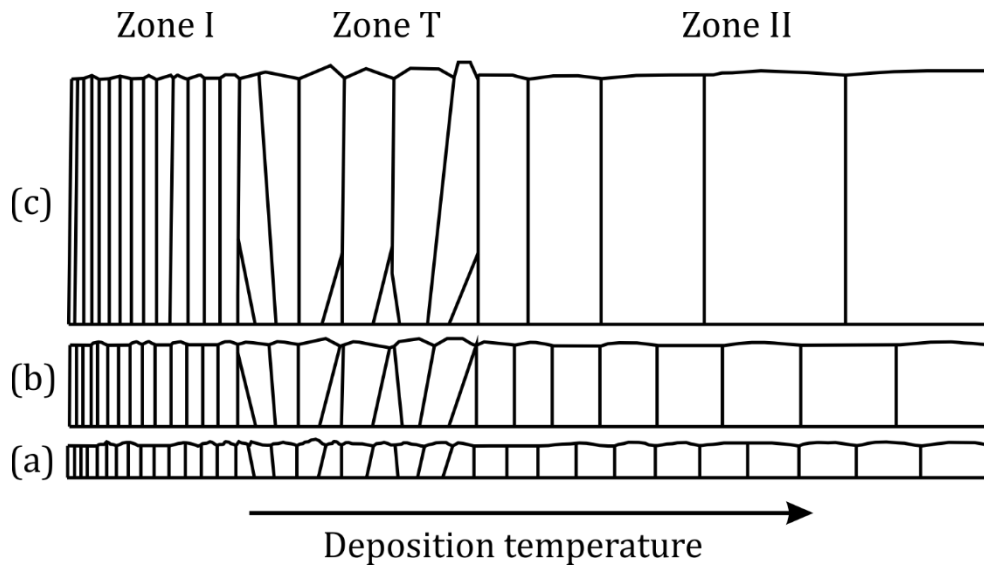

Figure 4.3: Structure zone model for PVD film growth for (a-c) different film thickness. Adapted from Barna et al. [79].

Surface and volume diffusion during film growth are primarily affected by the temperature. However, in the case of deposition of transition metal nitrides by PVD processes (cathodic arc evaporation), the synthesis temperature is low in comparison to the melting point of the material ($0.2 - 0.3 \, T_m$ of the material deposited) [4,70] and the energetic particle bombardment can be used to modify the adatom mobilities and nucleation rates during deposition [80]. These factors lead to kinetic limitations during growth of thin films far from thermodynamic equilibrium conditions. Therefore, by using PVD processes, it is possible to have controlled synthesis of metastable phases or artificial structures [4,80]. A good example, and the base of this thesis, is the deposition of metastable cubic solid solution *c*-(Ti,Al)N thin films with compositions inside the

31

miscibility gap, where in thermodynamic equilibrium a demixing into c-TiN and w-AlN would be expected [53].

The appropriate selection of the deposition parameters (substrate negative bias, gas atmosphere, deposition pressure, substrate temperature, etc.) is crucial to achieve the desired microstructure and film properties.

4.1.3 Experimental setup

The deposition configuration used during this thesis consists of three circular cathodes of 100 mm in diameter mounted next to each other, facing a rotating cylinder where the substrates are placed, as shown schematically in Figure 4.4. During deposition, the cylinder is set to rotate, maintain a growth temperature of ~ 450 °C and a deposition rate 0.1 μm/min, while the total gas pressure is kept at 2 Pa. A negative bias of - 30 V is used in all depositions unless stated otherwise. In order to study the effect of aluminum metal fraction when changing a deposition parameter, cathodes with different metal ratios (Ti:Al) were selected: 33:67, 45:55 and 100:0. Two different substrates were used: Fe foil and cemented carbide (ISO SNUN120408) comprising tungsten carbide (WC) with a 12 wt. % Co binder and less than 2 wt.% of other carbides, e.g. tantalum carbide. The first substrate was used for obtaining free-standing thin film since the Fe foils can be dissolved in HCl. The second one was selected so as to measure hardness and determine film-substrate interaction.

Three main deposition conditions were used in this thesis:

1. A mixed reactive gas atmosphere. Ar and N_2 gas were mixed in different ratios at a fixed total gas pressure, in order to reduce the nitrogen content of the deposited thin films.
2. An increase in negative bias voltage on the substrate. The kinetic energy of the ions arriving at the substrate was varied by changing the bias voltage in order to change the microstructure of the thin film.

3. A multilayer configuration. Deposition of (Ti,Al)N/TiN multilayers was implemented in order to have a predefined artificial structure and observe the effect of increasing interfaces.

For the (Ti,Al)N multilayer deposition, pure Ti cathodes were placed on the opposite side of the rotating cylinder (sample holder) in relation to the Ti:Al cathodes (Figure 4.4). This way, a multilayer configuration was obtained. The bilayer thickness was varied with the speed of the cylinder.
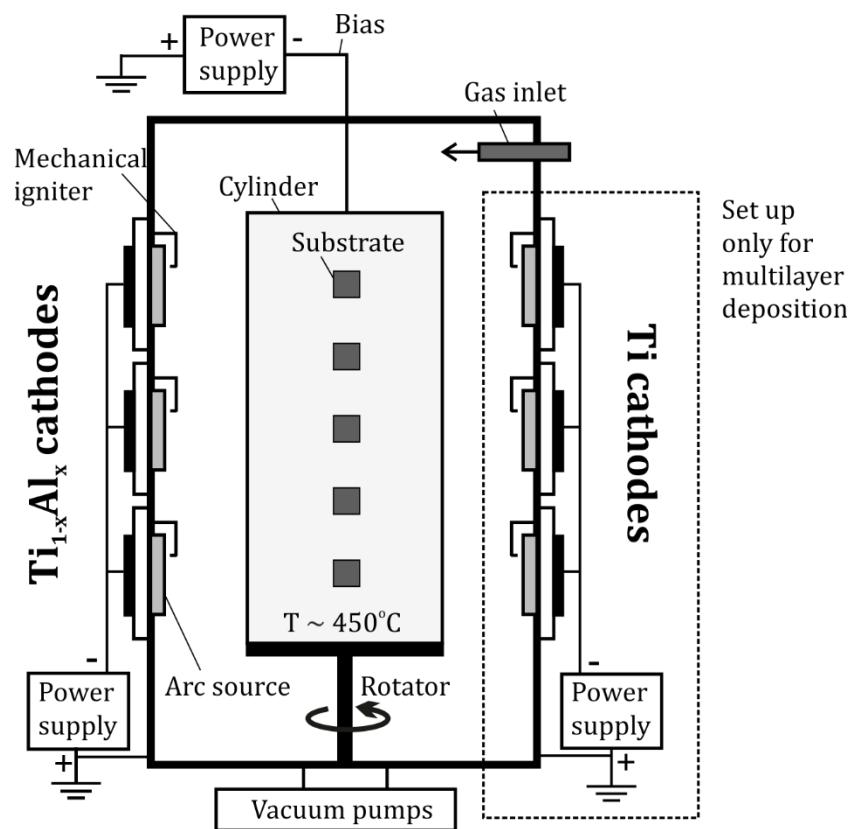
Figure 4.4: Schematic view of the deposition setup used for the synthesis of the thin films investigated in this thesis.

4.2 Characterization techniques

The characterization of thin films is not a trivial task. Challenges arise from the combination of the material and the limited dimensions of the film with the limitations and pre-requirements of the characterization technique. More specifically: the thickness of the thin film, the amount of material available for analysis, the change in microstructure along film thickness, the substrate used, the difficulty of quantitative chemical analysis (especially light elements) and structural analysis, the sample preparation and other challenges must be overcome for unambiguous characterization of the thin film microstructure and properties [81]. Therefore, it is of great relevance to choose the appropriate characterization techniques and to combine different techniques that cover different scales and information about the thin film.

The techniques used during this study are presented below with a description of the setup and parameters used. The main focus was on microstructure and hardness characterization of as-deposited and annealed thin films.

4.2.1 Differential scanning calorimetry

The thermal response of $(Ti,Al)N_y$ alloys and $(Ti,Al)N/TiN$ multilayers was measured in a differential scanning calorimeter (DSC) Netsch STA 449C operating with an argon flow of 50 ml/min. An alumina crucible holding 50 mg of the sample in powder form was used for each measurement. A zirconium oxygen getter was placed in the vicinity of the sample to avoid oxidation of the samples. First, samples were outgassed at 250 °C for one hour, directly followed by heating to 1400 °C with a rate of 20 °C/min. A second run was used as baseline and subtracted from the first measurement [82]. In some cases, a thermogravimetry (TG) measurement was coupled in order to obtain information about mass change attributed to phase transformations. Following the convention in the hard coating field, exothermic reactions are plotted upwards.

In addition, the DSC was used to heat powder samples to intermediate temperatures under the same conditions as stated above, to track the phase transformation sequence. A single heating cycle up to the desired temperature and 15 mg of powder were used. The maximum temperatures ranged from 700 to 1400 °C in 100 °C or 50 °C steps, when necessary.

Powder samples were obtained by deposition of the thin film material on Fe foils followed by a removal of the latter. First, the Fe foil was thinned mechanically by backside grinding, and then dissolved in hydrochloric acid (37 %). A magnet was used to confirm complete dissolution of the substrate. The recovered coating flakes were cleaned with distilled water and acetone and ground into a fine powder. The particles presented a flake-like shape approximately 30 - 80 μm long, fulfilling the criteria of a free-standing thin film. This Fe foil removal process has proven to yield a powder with the same stoichiometry and crystal structure as the deposited coating [83]. It also achieves a complete dissolution of the macroparticles generated during cathodic arc deposition, since the composition is of a more metallic nature.

4.2.2 X-ray diffraction

Phase analysis, preferred orientation (texture) and stress measurements were carried out in a PANalytical X´Pert PRO MPD and a PANalytical Empyrean diffractometer using Cu K_α radiation. A focusing, symmetric Bragg Brentano configuration was used for phase analysis. In this setup, only lattice planes parallel to the sample surface contribute to the diffraction peaks. Additional low-background optics were used in the PANalytical Empyrean diffractrometer. The diffractograms were recorded at room temperature either as-deposited or after annealing. A silicon zero diffraction plate was used as sample holder in order to reduce background signal. Stress measurements were performed on the 422 diffraction peak of *c*-(Ti,Al)N by using the $\sin^2\psi$ method. The elastic constants used to convert the strain measurements to stress are: $E = 460$ GPa and $\nu = 0.20$, obtained from *ab initio* calculations [19]. Pole figure measurements were

performed in the main reflections 111, 200 and 220 of the c-(Ti,Al)N structure with a resolution of three degrees for ψ and φ.

Phase analysis was performed in all as-deposited and annealed powder samples and coatings on cemented WC/Co-based substrates. Due to the predominant flake-like particle shape of the powder samples, preferred crystallographic orientation was measured in as deposited c-(Al,Ti)N$_y$ powder samples. This way, the effect of a reminiscent preferred orientation could be separated from the change in structure factor caused by the N vacancies accommodated in the B1 crystal structure. Stress measurements were performed only in the as-deposited c-(Ti,Al)N$_y$ coatings on WC/Co substrates where the applied substrate bias was varied, since a change in the residual compressive stresses was expected.

4.2.3 Transmission electron microscopy

Transmission electron microscopy (TEM), scanning TEM (STEM) and selected area diffraction (SAD) were used to characterize the microstructure and crystal structure of some samples in more detail. For samples in paper I to III, TEM imaging and selected area diffraction were performed in a JEOL JEM 2010 at an acceleration voltage of 200 kV. TEM/STEM analysis was carried out using a cold field emission gun JEOL JEM-ARM 200F at 200 kV equipped with a STEM Cs corrector (CESCOR, CEOS GmbH). A high angle annular dark-field (HAADF) detector was used for Z-contrast STEM imaging (paper II). Some of the FIB-prepared TEM thin lamellae received an additional thinning with an Ar Ion gun (Nanomill Mod. 1040, Fischione) for high-resolution imaging (paper II). The Ar ion beam current used was 125 pA for 20 min at a tilt angle of ± 10°.

For paper IV and V, cross sectional TEM samples were prepared through mechanical grinding and polishing, followed by Ar ion beam milling in a Gatan 691 precision ion polishing system until the sample was electron transparent (< 100 nm). These samples were investigated in an energy-filtered analytical transmission electron microscope

(EFTEM) using a cold field emission gun JEOL JEM-ARM 200 operated at an acceleration voltage of 200 kV. STEM imaging was performed in a FEI Tecnai G2 TF 20 UT microscope at an acceleration voltage of 200 kV using a high angle annular dark field detector.

4.2.4 Scanning electron microscopy

A scanning electron/focused ion beam (SEM/FIB) microscope, FEI Helios NanoLab600, was used for surface morphology imaging, cross section preparation, scanning transmission imaging (in SEM), energy dispersive X-ray analysis (EDS), and electron backscatter diffraction (EBSD). In situ lift-out techniques were used to prepare samples for transmission electron microscopy [84] and atom probe tomography (APT) [85] with a final cleaning step of 2 kV FIB milling. More details on APT sample preparation will be given in the respective section of this chapter.

Investigations of the chemical and phase distribution were performed by EDS and EBSD in some samples in paper III complementary to APT, due to the relatively large size of the inhomogeneities across the film thickness.

4.2.5 Nanoindentation

Hardness measurements of $(Ti,Al)N_y$ thin films on WC/Co-based substrates were performed with an UMIS nanoindentor using a Berkovich diamond tip. To avoid effects of surface topography on hardness measurements, the samples were prepared as tapered cross sections (taper angle ~ 10° relative to the sample surface) by mechanically grinding and polishing to a mirror-like finish using a 1 μm diamond suspension in the final step. A maximum load of 50 mN and 30 to 50 indents for each sample were used with fused silica as reference. The indentation depths for this amount of load were around 250 nm, which is less than 10 % of the film's thickness. Average hardness values were obtained using the Oliver and Pharr method [86].

The hardness behavior at high temperatures was obtained from post-annealing hardness measurements of coatings on WC/Co-based substrates (paper III and IV). The annealing was performed in a tube furnace at a vacuum of 7 x 10^{-4} Pa. Isothermal annealing treatments were performed at T_{max} = 700, 800, 900, 1000, 1100, and 1200 °C for 15 min with heating and cooling rates of 20 °C/min.

4.2.6 Elastic recoil detection analysis

Elemental composition of some as-deposited $(Ti,Al)N_y$ samples on WC/Co based substrates was measured by Time-of-Flight Energy (ToF-E) Elastic Recoil Detection Analysis (ERDA). The measurements were performed using a 36 MeV $^{127}I^{8+}$ ion beam with an incident angle of 67.5° relative to the surface normal and a spot size of 2 mm x 2 mm. Forward scattered recoil ions were detected with a time-of-flight energy detector at an angle of 45° with respect to the incoming ion beam [87]. The measured recoil ToF-E spectra were converted off-line into relative atomic concentration profiles using the CONTES code [88].

The technique requires a surface roughness in the nanometer range and inhomogeneities smaller than the ion beam spot cannot be detected. This is why the technique does not yield reliable results of samples containing high amounts of macroparticles, i.e. c-$(Ti,Al)N_y$ (y < 0.9). However, it was mainly use to cross-validate compositional measurements of the cubic solid solution phase with atom probe tomography for samples with low amount of macroparticles (paper I), i.e. $(Ti,Al)N_y$ (y > 0.9).

4.3 Atom Probe Tomography

Atom probe tomography (APT) is a powerful destructive technique that gives chemical and spatial information with near-atomic resolution (at least 0.04 nm in depth and 0.20 nm laterally) [89,90]. It combines a 3D visualization of atomic-scale microstructure with quantitative data analysis. One of the strengths of APT is the ability to measure all the elements (light to heavy) with an equivalent efficiency. A wide range of materials including metals, semiconductors, ceramics and limited biological or organic materials [91–93] can be measured [94–96]. The volume investigated is usually small (approx. 100 nm x 100 nm x 200 nm) meaning that the scientific questions to be solved with atom probe must be in the nanometer scale.

4.3.1 Principle of operation

The main principle is the controlled field evaporation (~ 10 - 50 V/nm) atom by atom from a very sharp tip (~ 50 nm radius) in ultra-high vacuum (~ 10^{-11} mbar) at cryogenic temperatures (> 15 K). Atoms at the surface of the tip are ionized and field evaporated with the combined effect of a laser or voltage pulse applied to the specimen and a static electric field that accelerates the ions toward a 2D detector. The experimental setup for atom probe tomography is shown in Figure 4.5.

The evaporation field (*F*) required for ionization depends on the elements, phases and their atomic bonding (crystal structure and bond type) and typically ranges from 10 to 50 V/nm. The field at the apex of an APT sample is calculated as follows [96]:

$$F = \frac{V}{k_f R}$$

where *V* is the applied high voltage, *R* the tip radius and k_f is a field factor that takes into account the tip shape and its electrostatic environment [97]. The evaporation field during the measurement can be estimated from the ratio of different charge states of an

ion by using the Kingham curves [98]. This can be combined with SEM images before and after run of the APT tip, in order to obtain tip shape information.
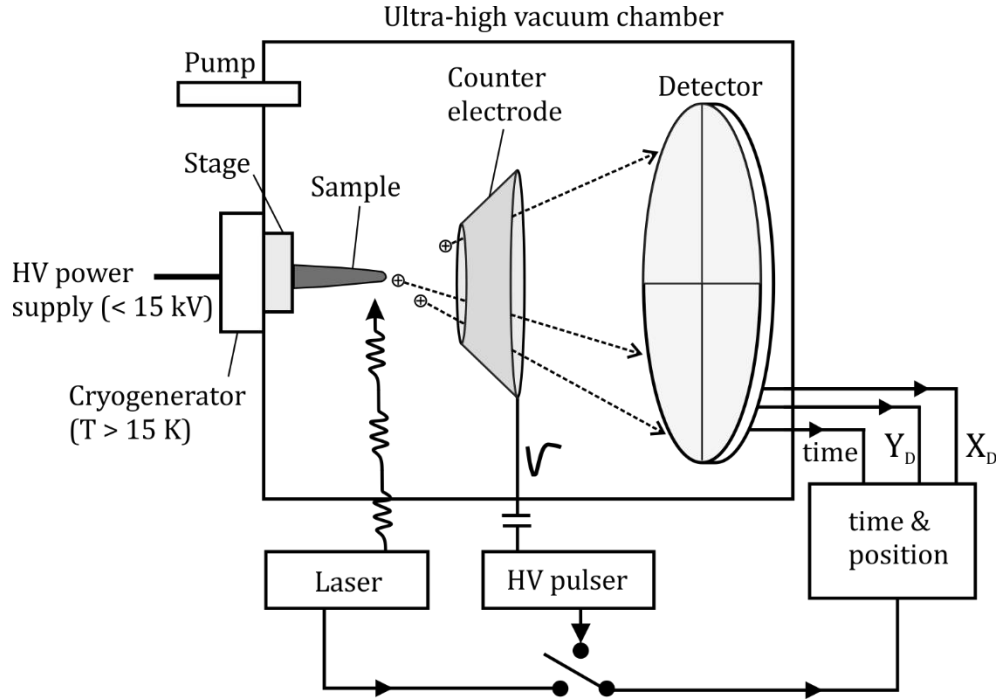

Figure 4.5: Experimental setup for local electrode atom probe tomography with a 2D detector, after [96].

Once the ions are field evaporated, they are accelerated towards a microchannel plate in front of the detector where the signal is amplified by converting a single ion into a cloud of electrons. These reach a delay-line detector and the positions in *x* and *y* are recorded. Since the ions are field evaporated by a controlled pulse and accelerated by a known electrostatic field, the time of flight (t_{flight}) of the ion can be used to determine its mass-to-charge ratio (*m/q*):

$$\frac{1}{2}m\,v^2 = q\,V \quad ; \quad v = \frac{L}{t_{flight}} \quad \overset{lead\ to}{\Longrightarrow} \quad \frac{m}{q} = 2\,V\left(\frac{t_{flight}}{L}\right)^2$$

where *v* is the velocity, *m* is the mass and *q* is the charge of the ion, *V* is the total voltage and *L* the flight length.

The collected time-of-flight information (independent of the ion position) during an APT measurement is generally represented as a histogram called mass-to-charge spectrum or mass spectrum (Figure 4.6). The units of *m/q* are commonly expressed in Daltons (Da). The elemental nature of the ions can be identified by measuring the mass-to-charge-state ratio, since every element has a characteristic number of isotopes with a fixed natural abundancy.
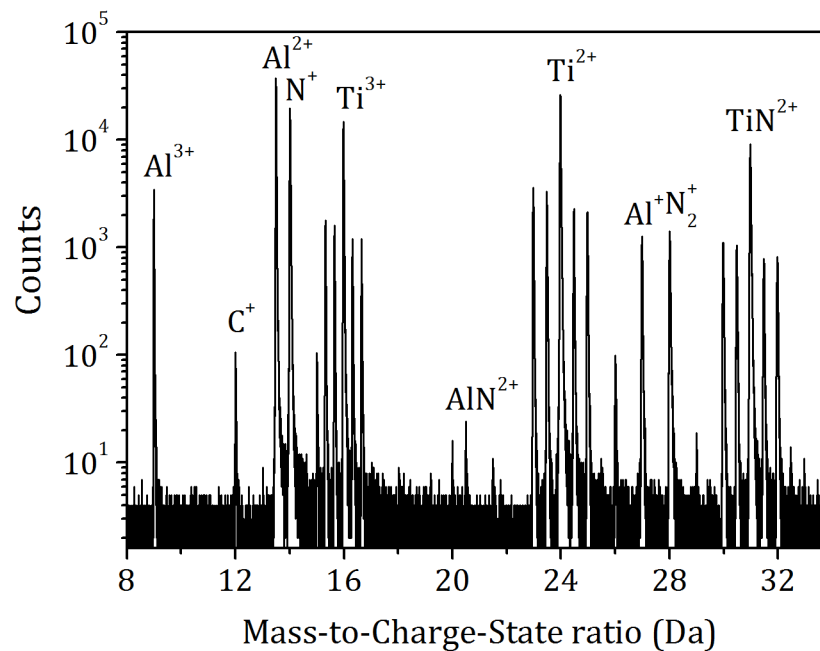
Figure 4.6: Mass-to-charge spectrum of a (Ti,Al)N sample.

The 3D reconstruction requires post-processing of the acquired data with specialized software based on an algorithm (protocol) that calculates the original position of the detected ions by a reverse-projection onto the surface of a virtual specimen. The basic protocol used in most software was published by Bas *et al.* [99]. It assumes that the tip is a truncated cone with a hemispherical cap, that the ions are projected along a straight trajectory (point-projection) and that the atoms are field evaporated layer-by-layer from the outermost shell inwards. That way, the *z* position of the ions can be calculated from the sequence of detection, and in combination with the detected *x, y* coordinates and the *time-of-flight,* a 3D reconstruction with chemical information can be made. Four fundamental parameters are required for a reconstruction: the evaporation field, the field

factor (tip geometry and electrostatic field dependency), the image compression factor (tip shape dependent) and the detection efficiency of the instrument.

The reconstruction of the APT tip is the first approach of a visual analysis of the data and depending on the type of information to be extracted, different algorithms and analysis tools are implemented. The tools used in this thesis are presented at the end of this chapter.

4.3.2 Limitations in APT

As any technique, APT has its limitations and it is important to have them in mind when performing data analysis and visualization. Artifacts in a reconstruction can arise due to the nature of the material such as presence of phases with different evaporation fields, grain boundaries, interfaces, clusters/segregations, bad thermal transport at cryogenic temperatures, etc. [96]. Also, a bad choice of measurement parameters, the specimen tip shape (no perfect hemisphere and shank angle) or a wrong choice of reconstruction parameters can lead to misleading results. Some of the main limitations encountered in this thesis and how they were mitigated are listed below.

Thermal tails in mass-to-charge peaks

They appear in laser mode when the heat from the laser pulse is not carried away fast enough. A longer cooling time of the tip can cause ions to be emitted shortly after the pulse (peak tail) and between pulses (background). Thermal tails can affect the accuracy of composition measurements since peaks may overlap or be completely hidden in the tail of another peak [96]. Tip shape (large shank angles) and measurement parameters (laser power and repetition rate, specimen temperature) can help to mitigate the effect.

Complex ion evaporation

The evaporation of complex ions (e.g. TiN^+, CN^+, N_2^+, Ti_2N^+) in compound materials containing nitrides, carbides and oxides is commonly observed (e.g. Figure 4.6). This process reduces the depth resolution of the atom probe [100]. It also leads to additional peaks in the mass spectrum, making unambiguous assignment more complicated and potentially causing peak overlap. Reduction in the laser power (in laser mode) decreases the amount of complex ions when measuring nitrides [101].

Multiple event detection

It is a common limitation in the delay-line position-sensitive detectors. It takes place when multiple events (i.e. ions) arrive close in time or/and in location. The extension of the signal loss is difficult to quantify since the exact number of ions emitted is unknown and some get lost in the detection efficiency of the detector [96]. In this work a range of 40 - 50 % of the detected ion events were multiple events, consistent with literature [102,103]. The amount can be reduced by increasing the laser power, nevertheless, this will increase the complex ion evaporation and degrade the compositional accuracy in nitrides [101].

Underestimation of N and C content

An underestimation of carbon and nitrogen contents of up to 5 at. % in carbides and in some nitride materials when using APT has been reported in literature [62,102]. The carbon deficiency was suggested to be strongly correlated with the detector dead time, the chemical bond and the carbon sites in the carbide lattice [102], which is similar in some nitrides, e.g. *w*-AlN [62]. Additionally, an overlap between complex and single carbon (nitrogen) isotope ion peaks contribute to the underestimation, e.g. C_2^+, C_4^{2+} and Ti^{2+}, or N^+ and N_2^{+2}. The N and C deficiency in the total composition of a given volume (not the spatial information) can be corrected in some cases by using isolated isotopes (if they are resolved in the mass spectrum) and calculating the concentration of the other

isotopes from the natural abundance [102], e.g. by using ^{13}C for calculating ^{12}C or $^{14.5}N_2$ to calculate the overlap between $^{14}N^+$ and $^{14}N_2^{2+}$. Cross-validation of compositional measurements with other techniques can also be of great help.

For an unambiguous interpretation and reconstruction of the APT data, it is important to use other techniques to adjust the reconstruction parameters and to validate the observations. SEM images before and after running an APT tip are of great help and a preceding characterization of the sample with other techniques like XRD, SEM, TEM is highly recommended.

4.3.3 Sample preparation

All APT tips in this thesis were prepared by a FIB-based wedge lift-out technique [85]. Due to the presence of compressive stress in the films, an additional rectangular cut around the region of interest was performed. This way, a release of stress is obtained and issues regarding bending fracture during lift-out are avoided.
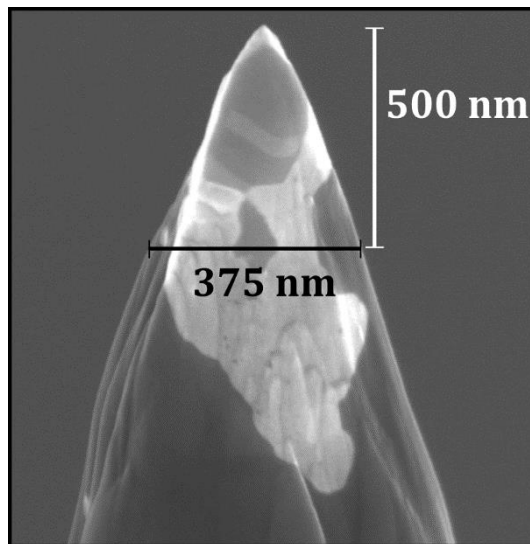
Figure 4.7: SEM image of an atom probe tip. Tilted view (52°).

The main requirements of an APT tip is a radius of 50 to 100 nm, smooth surface (free of cracks, grooves or protrusions) and an appropriate shank angle [96]. The majority of

the APT tips measured in this thesis fulfilled these requirements and were produced with a large shank angle, e.g. at a depth of 500 nm from the tip, a diameter of 350 - 400 nm was typically obtained (Figure 4.7). This was found to be most suitable for minimizing thermal tails and increasing the quality of the mass-to-charge spectrum (Figure 4.6).

4.3.4 APT measurement

APT measurements in this thesis were performed using a local electrode atom probe (Cameca LEAP 3000 X HR) in laser mode (10 ps pulse length, 532 nm wavelength), an evaporation rate of 5 atoms per 1000 pulses, and a laser repetition frequency of 200 kHz with a pulse energy of 0.5 nJ. The cryostat temperature was set to 60 K (base temperature). The detection efficiency of this instrument is of 37 % [96].

Data reconstruction was carried out with the commercial software package IVAS (version 3.6.8, Cameca) using voltage-based tip shape reconstruction. The reconstruction parameters such as evaporation field and the geometry factor (k_f) accounting for tip shape were obtained from the mass spectrum using Kingham curves [98] in combination with SEM images before and after run from which the length of the reconstructed tip could be estimated. A fixed image compression factor of 1.65 was used. For the majority of the *c*-(Ti,Al)N samples an evaporation field of 40 V/nm was obtained (consistent with literature [103]). k_f was set from 3.3 to 4.1 individually for each tip due to varying tip shank angles.

4.3.5 Visualization and data analysis

The most common data analysis and visualizations tools used in this thesis are presented in the following:

1D concentration profiles

Composition in APT is measured from the proportion of ions/atoms of each species in a volume (voxel). Therefore, a 1D profile is a plot of the composition along a volume also called region of interest (ROI) which can have a cuboid, sphere or cylinder shape. The ROI is divided into voxels with either a fixed amount of counts (ions) or a fixed volume from which the composition is calculated and plotted in a 1D concentration profile. Only statistical variations are considered in the uncertainty (error bar).

A critical step when calculating 1D concentration profiles is the selection of the voxel size. If it is too small, then the statistic will be low and it can even contain no ion counts. If the voxel is too large, fine details or composition fluctuations may be lost from the analysis. The selection of the voxel size involves a balance between positional error and statistical error.

Iso-concentration surfaces

An iso-concentration surface (isosurfaces) is a 3D visualization of an element distribution within the reconstructed tip. The analysis tool is based on isolating blocks with a specific composition (or ion density) and connecting them to a 3D surface within the reconstructed volume [96]. This helps to identify different phases, grain boundaries, precipitates and microstructure morphologies within the tip (Figure 4.8 (a,b)). Isosurfaces have no physical meaning, but are helpful for visualization or as a reference point for a proximity histogram calculation.

Proximity histograms

A proximity histogram (proxigram) is an algorithm that calculates a composition profile in 3D relative to a reference surface [104]. The first step is the creation of an isosurface which highlights the microstructure feature to be analyzed (Figure 4.8 (a, b)). Then, the composition is examined normal to the isosurface in layers (shells) at increasing/decreasing distances (Figure 4.8 (c)), therefore no restriction in the surface geometry is imposed. Then, from each shell a concentration distribution profile (histogram) of each element present is generated. Finally, the data extracted from the histograms (average composition) is plotted as a proxigram composition profile (Figure 4.8 (d)). Proxigram have no restrictions on the surface morphology (geometry) [104]. However, it is very sensitive to the choice of the isosurface concentration used to describe the feature of interest.
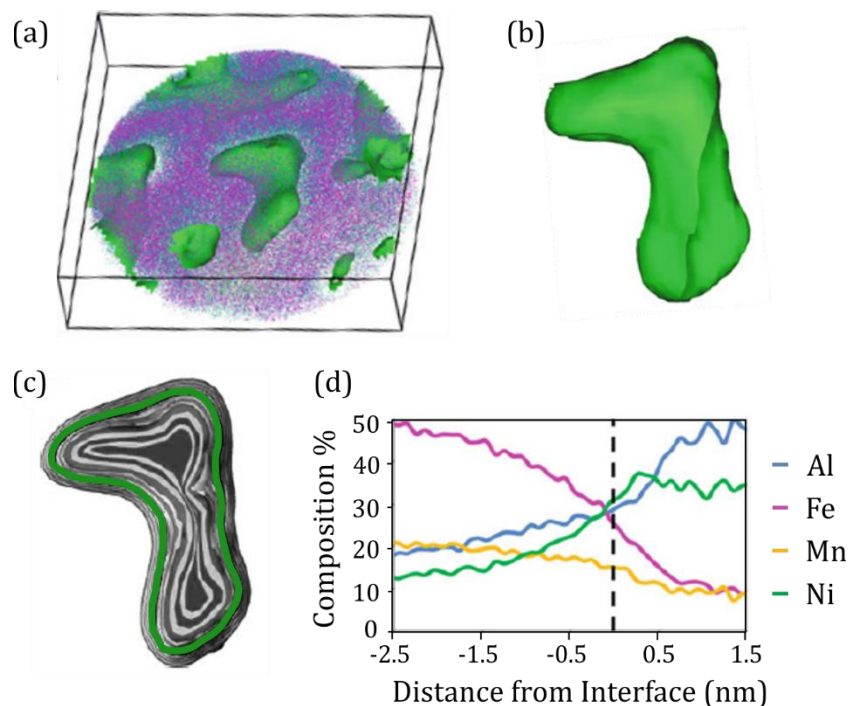
Figure 4.8: Proxigram analysis. (a) Several isoconcentration surfaces, (b) a specific surface selected for the analysis, (c) a 2D illustration of how the proxigram analysis measures the average composition normal to the surface and (d) the resulting proxigram composition profile. Adapted from [96].

Frequency distribution analysis

A FDA is a histogram obtained by dividing an APT dataset into small volumes (voxels) containing a fixed amount of n ions (e.g. n > 50) [96]. The procedure consists in: (1) dividing the data set into small volumes (voxel), (2) extracting the composition of each voxel, (3) plotting the composition of any element present (e.g. Ti, Al, N) or any desired ratio (e.g. Al metallic ratio, Al/(Ti+Al)). The selection of the number of ions per voxel is a critical step in FDA. Optimized voxels are needed to minimize convolution effects, since the amplitude of the measured compositional fluctuations (especially for spinodal decomposition) depend on the voxel dimension and the amount of ions per voxel [105].
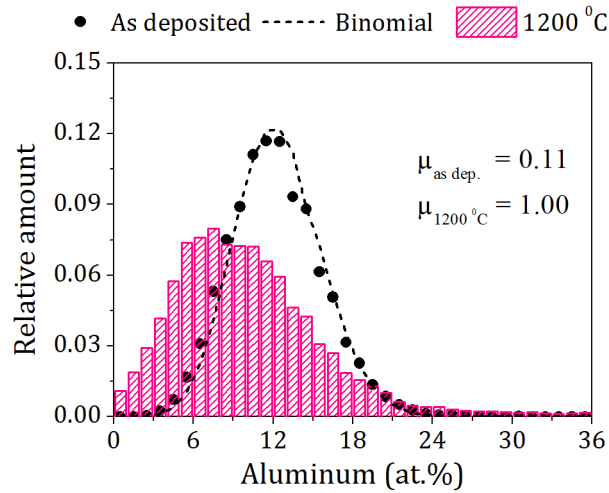
Figure 4.9: Aluminum composition histogram of as-deposited and 1200 °C annealed $(Ti_{0.74}Al_{0.26})N_{0.82}$. Calculated random distribution (binomial) is shown for comparison. Pearson coefficient of both measured distributions is given, where 0 indicates random distribution and 1 complete segregation [62].

Histograms were normalized to the total number of voxels of each analyzed volume for comparison purposes. For visual comparison, a random discrete distribution (binomial) distribution) was calculated by using the average composition of the analyzed volume. An example of an Al composition histogram from this work with its corresponding binomial distribution of an as-deposited sample and after annealing at 1200 °C is shown in Figure 4.9 [62].

Pearson coefficient

The Pearson coefficient (μ) is a qualitative indicator of the deviation of a measured chemical composition distribution (histogram) from a binomial (random) distribution. In order to calculate μ, the average composition of the volume analyzed, the total number of voxels and the measured composition histogram are needed. Pearson coefficient is calculated using the chi square statistics, χ_e^2, and normalized by the total number of voxels [96,106]. It ranges from 0 to 1, where 0 indicates a random distribution and 1 complete segregation. μ is a qualitative indicator of segregation, since it does not distinguish between different levels and morphologies of segregation. In this study, it was interesting for the as-deposited $(Ti,Al)N_y$ samples since chemical fluctuations can be investigated (paper I and II).

5. Summary of results

In this chapter, a summary of the most relevant results of this thesis is presented. Taken together, this work contributes mainly to the understanding of the effect of point defects on the phase transformations in *cubic* (Ti,Al)N alloys. It experimentally confirms theoretical predictions by Alling *et al.* on the effect of N vacancies on the decomposition pathway in c-(Ti,Al)N$_y$ (y < 1) [1]. Furthermore, this work increases the understanding of the predicted mechanism behind the early decomposition onset of (Ti,Al)N/TiN multilayers by surface-directed spinodal decomposition. The specific contributions to the field are presented in greater detail below.

Paper I. Impact of nitrogen vacancies on the high temperature behavior of (Ti$_{1-x}$Al$_x$)N$_y$ alloys

This is the first study of the thermal response and structural evolution in nitrogen deficient *cubic* solid solution (Ti$_{1-x}$Al$_x$)N$_y$ (y < 1) thin films for different Al metal ratios (x = 0.26, 0.48 and 0.60) and a N deficiency from y = 0.92 to 0.75. In order to reduce complexity, free-standing coatings were used in this investigation. The results show a substantial improvement of the thermal stability by reducing the nitrogen content for alloys with a Al metal fractions of x = 0.48 and 0.60. Alloys with x = 0.28 presented nucleation and growth of Al-Ti clusters inside the grains and w-AlN formation at grain boundaries. The decomposition paths shown in this study are consistent (with minor deviations) with predictions performed by Alling *et al.* on c-(Ti,Al)N$_y$ (y < 1) via static *ab initio* calculations [1].

The nitrogen deficiency is mainly accommodated through N vacancies in the c-(Ti$_{1-x}$Al$_x$)N$_y$ phase in as-deposited thin films. At elevated temperatures, alloys with Al metal fraction x = 0.48 and 0.60 show spinodal decomposition into c-AlN and c-TiN which is delayed with increasing N deficiency (Figure 5.1). As a consequence, the detrimental transformation of c-AlN into w-AlN is shifted to higher temperatures. It is

suggested that the mixing energy of the system is reduced by the presence of N vacancies, due to a reduction of the mixing enthalpy and an alteration of the entropy. Collectively, this reduces the miscibility gap and brings the spinodal line to lower temperatures.
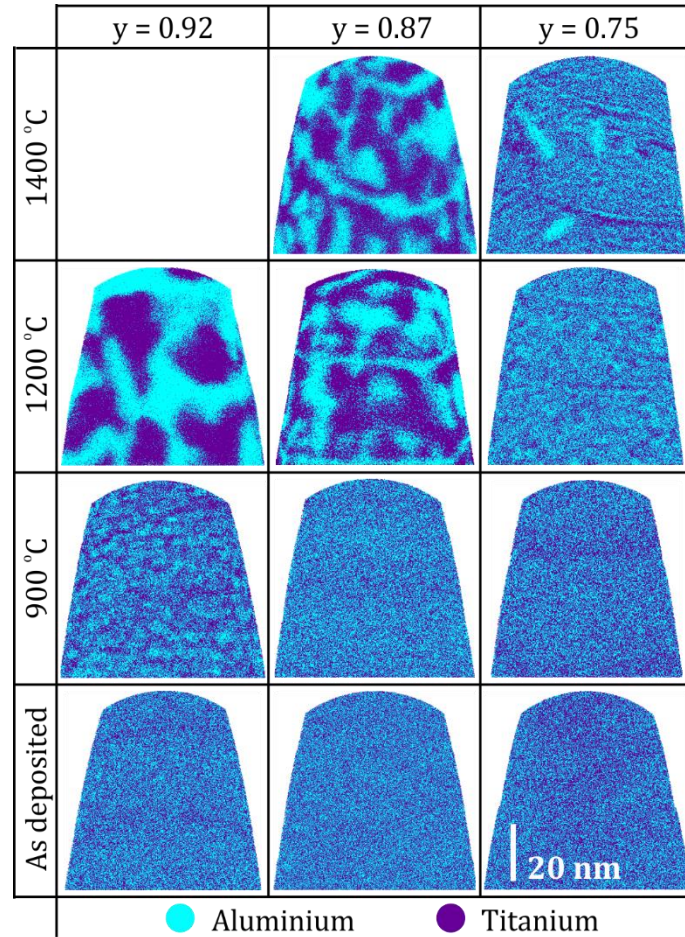
Figure 5.1: Reconstructed 3D APT tips of $(Ti_{0.52}Al_{0.48})N_y$, with y = 0.92, 0.87 and 0.75, in their as deposited state, and after heat treatments at 900 ˚C, 1200 ˚C and 1400 ˚C. Tips were extracted from single grains and no grain boundaries are present. Only Al and Ti ions are presented for clarity [62].

In addition, the suppressed spinodal decomposition leads to a concurrent phase separation into *c*-TiN and *w*-AlN via nucleation and growth. This happens preferably along grain boundaries at high temperatures and even inside the grains at high vacancy

concentrations (y = 0.75). The positive impact of N vacancies led to further studies on the potential application as hard coatings in cutting tools.

Paper II. Solid state formation of Ti_4AlN_3 in cathodic arc evaporated $(Ti_{1-x}Al_x)N_y$ alloys

As a complement to the first paper, the decomposition pathway in highly nitrogen-deficient solid solution *cubic* $(Ti_{1-x}Al_x)N_y$ ($0.58 \geq y \geq 0.40$) alloys was investigated for a wide range of Al metal fractions x = 0.28 to 0.63. This is the first study showing the formation of Ti_4AlN_3 (MAX phase) in thin films via solid state reaction in nitrogen deficient c-$(Ti_{1-x}Al_x)N_y$ alloys. A transformation mechanism from Ti_2AlN to Ti_4AlN_3 via intercalation is suggested and it is confirmed by the presence of an intermediate $Ti_6Al_2N_4$ phase (Figure 5.2). $Ti_6Al_2N_4$ has an intergrown structure whose unit cell consists of Ti_2AlN and Ti_4AlN_3 half unit cells.
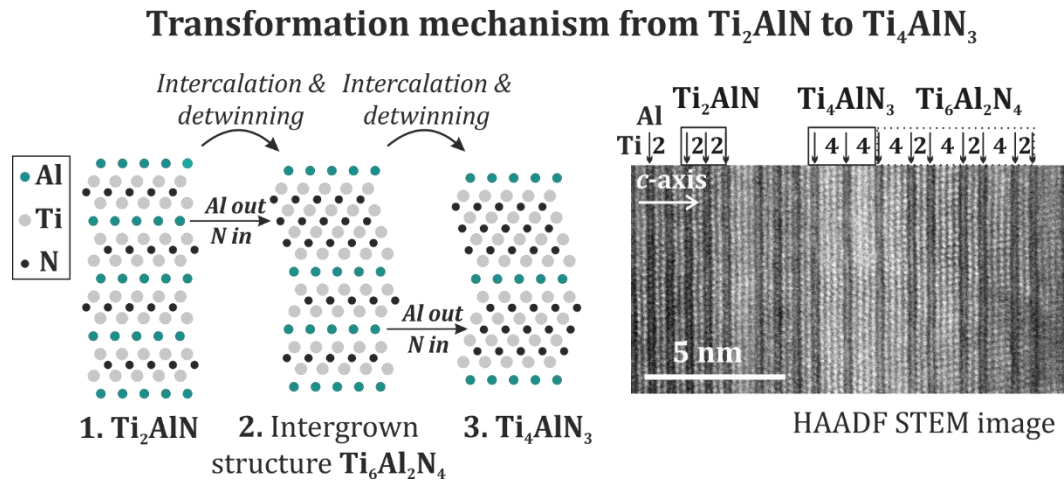
Figure 5.2: Graphical abstract [107]. *(Left side) Atomic scale model of the transformation mechanism from Ti_2AlN to Ti_4AlN_3 via intercalation and detwinning. (Right side) High resolution z-contrast STEM image displaying the coexistence of Ti_2AlN, Ti_4AlN_3, and $Ti_6Al_2N_4$ along the [1-210] direction in sample $(Ti_{0.52}Al_{0.48})N_{0.40}$ annealed at 1300 °C. Labels indicate the number of adjacent N-rich basal planes.*

Highly N-deficient single-phase c-$(Ti_{1-x}Al_x)N_y$ thin films were grown by cathodic arc deposition for a wide composition range (y = 0.40 to 0.58 with x < 0.55). In a first approach, free-standing thin films and heat treatments under Ar atmosphere were used

in this study. A general model of the solid state reaction path is suggested and phases such as Al_5Ti_2, Al_3Ti, c-TiN, w-AlN, Ti_2AlN and Ti_4AlN_3 are present. Their quantity can be varied with the as-deposited composition of the thin film. The phases observed are consistent with predictions performed by Alling *et al.* on N-poor c-$(Ti,Al)N_y$ [1]. In the reaction, it is shown that the formation of Ti_4AlN_3 takes place inside the preformed Ti_2AlN (MAX phase) grains by a thermally activated diffusion process above 1200 °C. The Ti_4AlN_3 formation mechanism proposed is the intercalation of Al layers for N layers along Ti_2AlN basal plane accompanied by a simultaneous detwinning process (Figure 5.2). This is confirmed by the presence of the intermediate $Ti_6Al_2N_4$ phase. This study extends the mechanism of intercalation to a ternary phase. In this case, the precursor is a MAX phase of a low *n* order (Ti_2AlN) and by fulfilling several conditions, a transformation to the next thermodynamically stable MAX phase with a higher *n* order (Ti_4AlN_3) takes place.

Paper III. (manuscript) Effect of nitrogen vacancies on phase stability and mechanical properties of arc deposited $(Ti_{0.52}Al_{0.48})N_y$ (y < 1) coatings

Based on the first paper, a medium Al metal fraction in the c-$(Ti_{1-x}Al_x)N_y$ was selected (x = 0.48), and the thermal stability in terms of w-AlN formation was studied for a larger N-to-metal range $0.92 \geq y \geq 0.46$. In this study, a typical cutting tool substrate (cemented carbide WC/co based) was used in order to investigate the film-substrate interaction in the presence of N vacancies. The results show a clear age hardening effect (due to spinodal decomposition) upshifted by 300 °C when reducing the N fraction in coatings with a $y \geq 0.75$ (Figure 5.3). This upshift is consistent with the enhanced thermal stability in terms of suppressing w-AlN formation. High N deficiency (y = 0.46) in the coating leads to a change of phase evolution and a strong interaction with WC and Co at elevated temperatures.

As deposited coatings present an increase in composition fluctuations, lattice defects and macroparticles when reducing the N content, which reduces the column width and changes the preferred orientation from 200 to 111 to 220 planes parallel to the substrate.
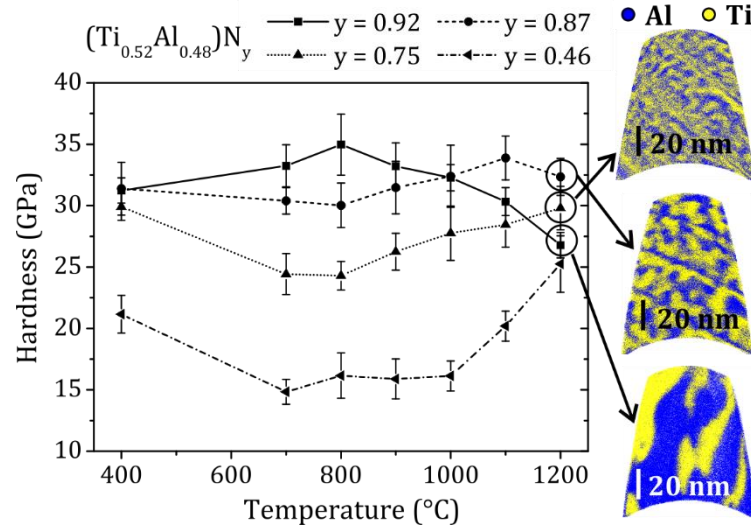
Figure 5.3: Graphical abstract [108]. *Ex situ hardness versus annealing temperature up to 1200 °C of ($Ti_{0.52}Al_{0.48}$)N_y samples with y = 0.92, y = 0.87, y = 0.75 and y = 0.46. APT reconstructions from the interior of a column of ($Ti_{0.52}Al_{0.48}$)N_y coatings annealed at 1200 °C for 15 min: y = 0.92, y = 0.87, and y = 0.75. Only Al and Ti ions are shown for clarity.*

At elevated temperatures, interdiffusion of substrate elements (Co and C) and nucleation and growth of *c*-TiN and *w*-AlN take place mainly along column boundaries for coatings with y ≥ 0.75. These processes seem not to be detrimental to the coatings hardness. Conversely, high N deficiency (y = 0.46) leads to significant diffusion of Co, C, W and Ta throughout the coating at elevated temperatures due to the increased amount on N vacancies and column boundaries. Substitution of N by C in the non-metal lattice, and substitution of W and Ta in the metal lattice is observed, e.g. formation of *c*-Ti(N,C), *c*-(Ti,W,Ta)(C,N). The overall hardness in sample y = 0.46 is lower than for coatings with y ≥ 0.75 (Figure 5.3). Nevertheless, an increase in hardness is observed above 1000 °C, and bond strengthening and solid solution hardening are suggested to be responsible for that. Base on this study, it is concluded that film-substrate interaction is a limiting factor for coating design by N deficiency. The most substantial improvement in hardness evolution was observed for y = 0.87.

Paper IV. Enhanced thermal stability and mechanical properties of nitrogen deficient titanium aluminum nitride (Ti$_{0.54}$Al$_{0.46}$N$_y$) thin films by tuning the applied negative bias voltage

Base on the third paper (manuscript), a fixed Al metal and N-to-metal fraction in the c-(Ti$_{1-x}$Al$_x$)N$_y$ was selected (x = 0.46 and y = 0.87), and the effect of point defects (interstitials and anti-sites) generated during film growth was investigated in terms of phase stability and hardness. The defect density was varied by applying a negative substrate bias from -30 to -80 V. The results show an improvement in the as-deposited hardness for the highly biased films (-80 V). At elevated temperatures, the hardness behavior shows age hardening shifted to higher hardness values and to lower temperatures by increasing the negative bias (Figure 5.4). Highly bias films present an increased driving force for phase separation at elevated temperatures.
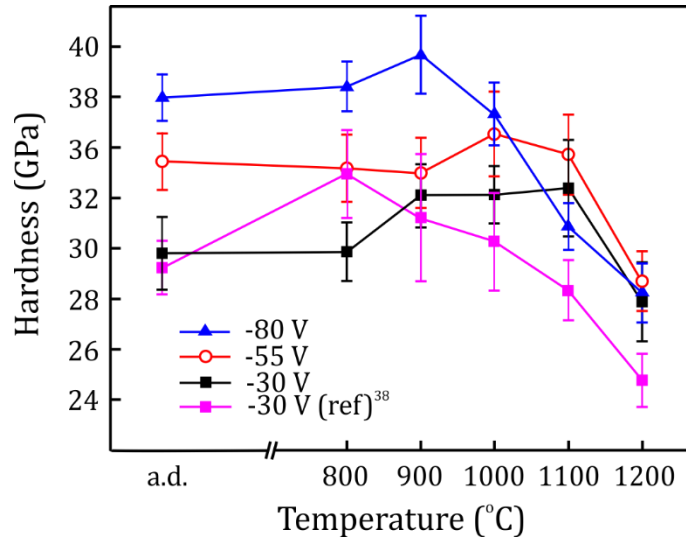
Figure 5.4: *Hardness at different temperatures of (Ti$_{0.54}$Al$_{0.46}$)N$_{0.87}$ films biased at - 30 V, - 55 V, and - 80 V and a reference sample* [108] *which contains a higher N content (y = 0.92)* [109].

The microstructure and the point defect density (interstitials and anti-sites) is modified in cathodic arc deposited c-(Ti$_{0.54}$Al$_{0.46}$)N$_{0.87}$ thin films by tuning the applied negative bias, since the kinetic energy of the impinging ions is altered. In the as-deposited state, films deposited with high bias (- 80V) show an increase in compressive stresses and

thus in hardness due to the increase in defect density. At elevated temperatures, it is shown that the defects caused by high ion energy bombardment (high bias) are more stable in the presence of N vacancies than the ones generated at low energy bombardment. This effect leads to a delayed annihilation of point defects (interstitials), an increase of the system´s internal energy and a retention of the hardness in high bias films (Figure 5.4). With a further increase in temperature, the release of the stored lattice strain energy in the system takes place and the decomposition of the c-$(Ti_{0.54}Al_{0.46})N_{0.87}$ into c-TiN and w-AlN is accelerated. Thus, a shift of the age hardening effect to lower temperatures is observed (Figure 5.4). In this study, it is shown that point defect concentration generated during deposition is critical in designing N deficient (Ti,Al)N coatings.

Paper V. Surface directed spinodal decomposition at TiAlN/TiN interfaces

This work investigates the mechanism behind the early onset of spinodal decomposition in arc evaporated $(Ti_{1-x}Al_x)N/TiN$ multilayers, and the positive effect of artificial interfaces on the hardness. Two compositions (x = 0.50 and 0.67) were investigated in a combined study of experiments and phase-field simulations. The results show that the decomposition is initiated at the multilayer interfaces, consistent with surface-directed spinodal decomposition (SDSD) (Figure 5.5). Regardless of the composition, the same decomposition onset temperature is observed since the internal interfaces are responsible for the SDSD.

SDSD consists in the formation of a layered microstructure parallel to the interface i.e. a dominant wave vector directed normal to the surface. Phase field simulations predicted the effect of composition, internal interfaces and intrinsic composition fluctuations (induced during growth) on the microstructure and thermal stability of the multilayer system. Decomposition is initiated at the interfaces by SDSD at similar temperatures, regardless of the composition, and at earlier temperatures compared to monolithic $(Ti_{1-x}Al_x)N$, whereas larger intrinsic fluctuations generate a more randomly oriented decomposition structure. Both mechanisms compete with each other and the resulting

microstructure is a combination of both effects. In the case of $(Ti_{0.34}Al_{0.66})N/TiN$ multilayers, the results show a clear SDSD at the interfaces which vanishes inside the layers due to a random decomposition (Figure 5.5). Moreover, the presence of interfaces generates coherency strains between TiN and $(Ti_{1-x}Al_x)N$ due to lattice mismatch. This effect prolongs the decomposition over a longer period of time and it decreases the driving force in comparison to the monolithic layers, resulting in a prolonged age hardening.
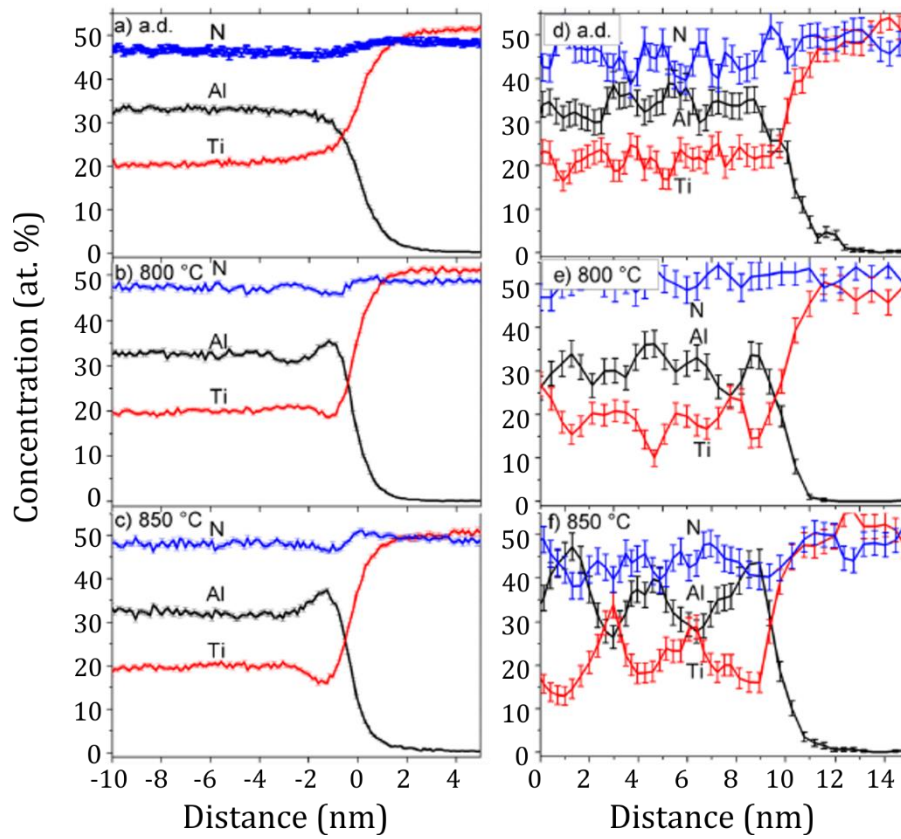
Figure 5.5: APT proxigrams from isosurfaces of a $(Ti_{0.34}Al_{0.66})N$ (left)/TiN (right) multilayer interfaces in (a) as-deposited state and annealed at (b) 800 °C and (c) 850 °C, showing Al, Ti, and N. (d)–(f) show 1D concentrations corresponding to a cylinder with a diameter of 5 nm of the same interfaces as in (a)-(c) [110].

6. Future work

Based on the results obtained in this thesis, an outlook of possible research trends is presented in this chapter.

Elastic properties and electronic structure of (Ti,Al)N$_y$ (y < 1) alloys

It has been shown previously that spinodal decomposition, hardness and age hardening of (Ti,Al)N alloys are strongly affected by the evolving elastic properties as a function of Al content [19,111] and of the Al distribution in the metal sublattice [112]. The increase in Al content increases the directional (covalent) character of the bonds, resulting in an increase in elastic anisotropy [19] and change in the electronic structure [112]. The elastic anisotropy results in a change in the nature of (Ti,Al)N decomposition and in the resulting microstructure as pointed out by Chan [31].

In this study, it is suggested that the introduction of nitrogen vacancies in the B1 structure of (Ti,Al)N alloys leads to a change in bonding toward a metallic situation [62]. The results are in accordance with prediction of Alling *et al.* via *ab initio* calculations [1]. Therefore, it is expected that the elastic properties change with the N content. New insight into the understanding of the spinodal decomposition and age hardening in N-deficient (Ti,Al)N$_y$ (y < 1) alloys can be obtained by the calculation of elastic properties and electronic structure.

Isostructural phase diagram of cubic (Ti,Al)N$_y$ (y < 1) alloys

Based on the results of this work, it is suggested that the enhanced thermal stability of (Ti,Al)N$_y$ (y < 1) via N vacancies is related to a reduction of the mixing enthalpy and an increase in the entropy. Collectively, this reduces the miscibility gap to lower temperatures. In order to prove this, the calculation of the isostructural phase diagram of cubic-(Ti,Al)N$_y$ for different N contents should be performed. Where vibrational

contributions including anharmonicity and temperature dependence of the mixing enthalpy should also be taken into account for a good approximation. The N content effect on the miscibility gap will lead to a deeper understanding of the effect of N vacancies on thermal stability of $(Ti,Al)N_y$ (y < 1), and to the selection of an optimized Al metal fraction.

It is important to note, that the calculation of an isostructural phase diagram of B1-$(Ti,Al)N_y$ is not a trivial task since two phases must be selected, i.e. c-AlN_y and c-TiN_z where y and z must not necessarily be equal. An alternative could be the calculation of a pressure-temperature diagram of the cubic solid solution $(Ti,Al)N_y$ phase.

Oxidation and wear behavior in (Ti,Al)N$_y$ (y < 1)

The improved thermal stability and hardness evolution of N-deficient c-$(Ti,Al)N_y$ (y < 1) thin films appear promising for an application as hard coating in cutting tools. In order to obtain a functional coating, further investigation of other properties must be studied such as cutting performance, wear resistance and oxidation resistance. These questions were beyond the scope of this thesis but should be investigated when considering industrial application of such coatings.

Point defect engineering combined with multilayering and alloying

As mentioned in the introduction, improving the thermal stability of (Ti,Al)N at elevated temperatures has become a key factor in hard coatings research in the last three decades. Some of the approaches were the use of multilayer configurations [3,25,113] or alloying elements (e.g. Cr, Hf, Ta) [24,83,114].

The addition of alloying elements have shown to delay the decomposition by the appearance of several intermediate phases and by changing the activation energy for diffusion [83,115]. The combination of alloying and N vacancies could lead to an enhancement of thermal stability in $(Ti,Al)N_y$ (y < 1) alloys, since alloying elements

like Cr or Ta are introduced in the metal sublattice and N vacancies in the non-metal sublattice.

In this study, the use of artificial interfaces by a multilayer stack (Ti,Al)N/TiN has been shown to prolong the spinodal decomposition over a longer period of time and to decrease the driving force for decomposition [110]. The generation of coherency strains due to the presence of interfaces is the main mechanism behind the enhanced age hardening. It appears interesting to explore the combined effect of artificial interfaces with N vacancies for a further improvement of the thermal stability and mechanical behavior of $(Ti,Al)N_y$ $(y < 1)$ alloys.

MAX phase formation via intercalation in thin films

In this study, the mechanism of intercalation was extended to a ternary phase, where the precursor is a MAX phase of a low *n* order which transforms into a MAX phase with a higher *n* order, i.e. Ti_2AlN into Ti_4AlN_3 [107]. In order for this transformation to take place, several conditions must be fulfilled (see paper II). According to the mechanism, the origin of the precursor MAX phase of low *n* order is independent of transformation mechanism. It is suggested that it is possible to obtain MAX phases of high *n* order in thin films which have not been previously obtained by direct nucleation and growth, like Ti_4GaC_3, Nb_4AlC_3 and V_4AlC_3. Exploring this possibility seems a promising path to continue research.

7. References

[1] B. Alling, A. Karimi, L. Hultman, I.A. Abrikosov, First-principles study of the effect of nitrogen vacancies on the decomposition pattern in cubic Ti1−xAlxN1−y, Appl. Phys. Lett. 92 (2008) 71903.

[2] K.-D. Bouzakis, N. Michailidis, G. Skordaris, E. Bouzakis, D. Biermann, R. M'Saoubi, Cutting with coated tools: Coating technologies, characterization methods and performance optimization, CIRP Ann. - Manuf. Technol. 61 (2012) 703.

[3] S. Paldey, S.C. Deevi, Single layer and multilayer wear resistant coatings of (Ti,Al)N: a review, Mater. Sci. Eng. A. 342 (2003) 58.

[4] L. Hultman, Thermal stability of nitride thin films, Vacuum. 57 (2000) 1.

[5] M. Ohring, Materials Science of Thin Films, 2nd editio, Academic Press, 1992.

[6] D.M. Mattox, Handbook of Physical Vapor Deposition (PVD) processing, Noyes Publications, 1998.

[7] B.F. Coll, P. Sathrum, R. Fontana, J.P. Peyre, D. Duchateau, M. Benmalek, Optimization of arc evaporated (Ti,Al)N film composition for cutting tool applications, Surf. Coatings Technol. 52 (1992) 57.

[8] O. Knotek, On structure and properties of sputtered Ti and Al based hard compound films, J. Vac. Sci. Technol. A Vacuum, Surfaces, Film. 4 (1986) 2695.

[9] H.A. Jehn, S. Hofmann, V.-E. Rückborn, W.-D. Münz, Morphology and properties of sputtered (Ti,Al)N layers on high speed steel substrates as a function of deposition temperature and sputtering atmosphere, J. Vac. Sci. Technol. A. 4 (1986) 2701.

[10] S. Hofmann, H.A. Jehn, Selective oxidation and chemical state of AL and Ti in (Ti, Al)N coatings, Surf. Interface Anal. 12 (1988) 329.

[11] D. McIntyre, J.E. Greene, G. Håkansson, J.-E. Sundgren, W.-D. Münz, Oxidation of metastable single-phase polycrystalline Ti0.5Al0.5N films: Kinetics and mechanisms, J. Appl. Phys. 67 (1990) 1542.

[12] B. Alling, A. V. Ruban, A. Karimi, L. Hultman, I.A. Abrikosov, Unified cluster expansion method applied to the configurational thermodynamics of cubic Ti1-xAlxN, Phys. Rev. B. 83 (2011) 104203.

[13] N. Shulumba, O. Hellman, Z. Raza, B. Alling, J. Barrirero, F. Mücklich, et al., Lattice Vibrations Change the Solid Solubility of an Alloy at High Temperatures, Phys. Rev. Lett. 117 (2016) 205502.

[14] P.H. Mayrhofer, A. Hörling, L. Karlsson, J. Sjölén, T. Larsson, C. Mitterer, et al., Self-organized nanostructures in the Ti-Al-N system, Appl. Phys. Lett. 83 (2003) 2049.

[15] R. Rachbauer, S. Massl, E. Stergar, D. Holec, D. Kiener, J. Keckes, et al., Decomposition pathways in age hardening of Ti-Al-N films, J. Appl. Phys. 110 (2011) 23515.

[16] M. Odén, L. Rogström, A. Knutsson, M.R. Terner, P. Hedström, J. Almer, et al., In situ small-angle x-ray scattering study of nanostructure evolution during decomposition of arc evaporated TiAlN coatings, Appl. Phys. Lett. 94 (2009) 53114.

[17] P.H. Mayrhofer, A. Hörling, L. Karlsson, J. Sjölén, T. Larsson, C. Mitterer, et al., Self-organized nanostructures in the Ti-Al-N system, Appl. Phys. Lett. 83 (2003) 2049.

[18] J.S. Koehler, Attempt to design a strong solid, Phys. Rev. B. 2 (1970) 547.

[19] F. Tasnádi, I.A. Abrikosov, L. Rogström, J. Almer, M.P. Johansson, M. Odén, Significant elastic anisotropy in Ti1−xAlxN alloys, Appl. Phys. Lett. 97 (2010) 231902.

[20] A. Hörling, L. Hultman, M. Odén, J. Sjölén, L. Karlsson, Mechanical properties and machining performance of Ti1-xAlxN-coated cutting tools, Surf. Coatings Technol. 191 (2005) 384.

[21] N. Norrby, L. Rogström, M.P. Johansson-Jõesaar, N. Schell, M. Odén, In situ X-ray scattering study of the cubic to hexagonal transformation of AlN in Ti1-xAlxN, Acta Mater. 73 (2014) 205.

[22] O. Knotek, M. Böhmer, T. Leyendecker, On structure and properties of sputtered Ti and Al based hard compound films, J. Vac. Sci. Technol. A. 4 (1986) 2695.

[23] I.A. Abrikosov, A. Knutsson, B. Alling, F. Tasnádi, H. Lind, L. Hultman, et al., Phase stability and elasticity of TiAlN, Materials (Basel). 4 (2011) 1599.

[24] H. Lind, R. Forsén, B. Alling, N. Ghafoor, F. Tasnádi, M.P. Johansson, et al., Improving thermal stability of hard coating films via a concept of multicomponent alloying, Appl. Phys. Lett. 99 (2011) 91903.

[25] A. Knutsson, M.P. Johansson, L. Karlsson, M. Odén, Machining performance and decomposition of TiAlN/TiN multilayer coated metal cutting inserts, Surf. Coatings Technol. 205 (2011) 4005.

[26] R. Rachbauer, D. Holec, P.H. Mayrhofer, Increased thermal stability of Ti-Al-N thin films by Ta alloying, Surf. Coatings Technol. 211 (2012) 98.

[27] N. Norrby, H. Lind, G. Parakhonskiy, M.P. Johansson, F. Tasnádi, L.S. Dubrovinsky, et al., High pressure and high temperature stabilization of cubic

AlN in Ti 0.60Al0.40N, J. Appl. Phys. 113 (2013) 53515.

[28] N. Norrby, M.P. Johansson-Jõesaar, M. Odén, Improved metal cutting performance with bias-modulated textured Ti0.50Al0.50N multilayers, Surf. Coatings Technol. 257 (2014) 102.

[29] D.A. Porter, K.E. Easterling, Phase Transformations in Metals and Alloys, Second, Chapman & Hall, 1992.

[30] M. Hillert, A Theory of Nucleation for Solid Metallic Solutions, Doctoral Thesis, Massachusets Institute of Technology, 1954.

[31] J.W. Cahn, On spinodal decomposition, Acta Metall. 9 (1961) 795.

[32] L. Rogström, J. Ullbrand, J. Almer, L. Hultman, B. Jansson, M. Odén, Strain evolution during spinodal decomposition of TiAlN thin films, Thin Solid Films. 520 (2012) 5542.

[33] J.W. Cahn, The later stages of spinodal decomposition and the beginnings of particle coarsening, Acta Metall. 14 (1966) 1685.

[34] J.W. Cahn, J.E. Hilliard, Free Energy of a Nonuniform System. I. Interfacial Free Energy, J. Chem. Phys. 28 (1958) 258.

[35] O. Mashtalir, M. Naguib, V.N. Mochalin, Y. Dall'Agnese, M. Heon, M.W. Barsoum, et al., Intercalation and delamination of layered carbides and carbonitrides, Nat. Commun. 4 (2013) 1716.

[36] M.S. Dresselhaus, G. Dresselhaus, Intercalation compounds of graphite, Adv. Phys. 30 (1981) 139.

[37] M.J. McKelvy, W.S. Glaunsinger, Molecular Intercalation Reactions in Lamellar Compounds, Annu. Rev. Phys. Chem. 41 (1990) 497.

[38] P. Podsiadlo, A.K. Kaushik, A.M. Waas, B.S. Shim, J. Xu, H. Nandivada, et al., Ultrastrong and Stiff Layered Polymer Nanocomposites, Science (80-.). 318 (2007) 80.

[39] M.W. Barsoum, The Mn-1AXn Phases : A New Class of Solids, Prog. Solid State Chem. 28 (2000) 201.

[40] Y. Zhou, Z. Sun, Crystallographic relations between Ti3SiC2 and TiC, Mater. Res. Innov. 3 (2000) 286.

[41] D.P. Riley, E.H. Kisi, The design of crystalline precursors for the synthesis of M n-1AXn phases and their application to Ti3AlC2, J. Am. Ceram. Soc. 90 (2007) 2231.

[42] D.P. Riley, E.H. Kisi, A new solid state synthesis methodology for ternary and higher order compounds, J. Aust. Ceram. Soc. 43 (2007) 102.

[43] J. Emmerlich, D. Music, P. Eklund, O. Wilhelmsson, U. Jansson, J.M. Schneider, et al., Thermal stability of Ti3SiC2 thin films, Acta Mater. 55 (2007)

1479.

[44] H. Högberg, L. Hultman, J. Emmerlich, T. Joelsson, P. Eklund, J.M. Molina-Aldareguia, et al., Growth and characterization of MAX-phase thin films, Surf. Coatings Technol. 193 (2005) 6.

[45] M.W. Barsoum, T. El-Raghy, The MAX Phases: Unique New Carbide and Nitride Materials, Am. Sci. 89 (2001) 334.

[46] M. Dahlqvist, B. Alling, J. Rosén, Stability trends of MAX phases from first principles, Phys. Rev. B. 81 (2010) 230102.

[47] R. Yu, Q. Zhan, L.L. He, Y.C. Zhou, H.Q. Ye, Si-induced twinning of TiC and formation of Ti3SiC2 platelets, Acta Mater. 50 (2002) 4127.

[48] S.S. Hwang, S.W. Park, T.W. Kim, Synthesis of the Ti3SiC2 by solid state reaction below melting temperature of Si, J. Alloys Compd. 392 (2005) 285.

[49] A. Abdulkadhim, T. Takahashi, D. Music, F. Munnik, J.M. Schneider, MAX phase formation by intercalation upon annealing of TiCx/Al (0.4 < x < 1) bilayer thin films, Acta Mater. 59 (2011) 6168.

[50] G.A. Slack, R.A. Tanzilli, R.O. Pohl, J.W. Vandersande, The intrinsic thermal conductivity of AlN, J. Phys. Chem. Solids. 48 (1987) 641.

[51] R. Kainuma, M. Palm, G. Inden, Solid-phase equilibria in the Ti-rich part of the Ti-Al system, Intermetallics. 2 (1994) 321.

[52] M. Hillert, S. Jonsson, An Assessment of the Al-Fe-N System, Metall. Trans. A. 23A (1992) 3141.

[53] Q. Chen, B. Sundman, Thermodynamic Assessment of the Ti-Al-N System, J. Phase Equilibria. 19 (1998) 146.

[54] L.E. Toth, Transition metal carbides and nitrides, Academic Press, 1971.

[55] M. to Baben, L. Raumann, D. Music, J.M. Schneider, Origin of the nitrogen over- and understoichiometry in Ti0.5Al0.5N thin films, J. Physics. Condens. Matter. 24 (2012) 155401.

[56] A.T. Procopio, T. El-Raghy, M.W. Barsoum, Synthesis of Ti4AlN3 and phase equilibria in the Ti-Al-N system, Metall. Mater. Trans. A. 31A (2000) 373.

[57] M.A. Pietzka, J.C. Schuster, Phase equilibria in the quarternary system Ti-Al-N-C, J. Am. Ceram. Soc. 79 (1996) 2321–2330.

[58] C.J. Rawn, M.W. Barsoum, T. El-Raghy, A. Procipio, C.M. Hoffmann, C.R. Hubbard, Structure of Ti4AlN3 - a layered Mn+1AXn nitride, Mater. Res. Bull. 35 (2000) 1785.

[59] D. Music, R. Ahuja, J.M. Schneider, Theoretical study of nitrogen vacancies in Ti4AlN3, Appl. Phys. Lett. 86 (2005) 31911.

[60] M.W. Barsoum, L. Farber, I. Levin, A. Procopio, T. El-Raghy, A. Berner, High-

Resolution Transmission Electron Microscopy of Ti4AlN3, or Ti3Al2N2 Revisited, J. Am. Ceram. Soc. 82 (1999) 2545.

[61] B.-Y. Shew, J.-L. Huang, The effects of nitrogen flow on reactively sputtered Ti-Al-N films, Surf. Coatings Technol. 71 (1995) 30.

[62] I.C. Schramm, M.P. Johansson Jõesaar, J. Jensen, F. Mücklich, M. Odén, Impact of nitrogen vacancies on the high temperature behavior of (Ti1−xAlx)Ny alloys, Acta Mater. 119 (2016) 218.

[63] B. Alling, A. V. Ruban, A. Karimi, O.E. Peil, S.I. Simak, L. Hultman, et al., Mixing and decomposition thermodynamics of c-Ti1−xAlxN from first-principles calculations, Phys. Rev. B. 75 (2007) 45123.

[64] Q. Xia, H. Xia, A.L. Ruoff, Pressure-induced rocksalt phase of aluminum nitride: A metastable structure at ambient condition, J. Appl. Phys. 73 (1993) 8198.

[65] A. Knutsson, Thermal stability and mechanical properties of TiAlN-based multilayer and monolithic coatings, Doctoral Thesis, Linköping University, 2012.

[66] J. Zalesak, D. Holec, I. Matko, M. Petrenec, B. Sartory, N. Koutná, et al., Peculiarity of self-assembled cubic nanolamellae in the TiN/AlN system: Epitaxial self-stabilization by element deficiency/excess, Acta Mater. 131 (2017) 391.

[67] C.-S. Shin, D. Gall, N. Hellgren, J. Patscheider, I. Petrov, J.E. Greene, Vacancy hardening in single-crystal TiNx(001) layers, J. Appl. Phys. 93 (2003) 6025.

[68] M. Birkholz, Thin Film Analysis by X-ray Scattering, Wiley-VCH Verlag GmbH & Co. KGaA, 2006.

[69] R.F. Bunshah, Vapor Deposition Technologies, in: R.F. Bunshah (Ed.), Haandb. Hard Coatings, Noyes Publications/William Andrew Publishing, 2001.

[70] H. Randhawa, Cathodic arc plasma deposition technology, Thin Solid Films. 167 (1988) 175.

[71] D.M. Sanders, A. Anders, Review of cathodic arc deposition technology at the start of the new millennium, Surf. Coatings Technol. 133−134 (2000) 78.

[72] L. Karlsson, L. Hultman, M.P. Johansson, J.-E. Sundgren, H. Ljungcrantz, Growth, microstructure, and mechanical properties of arc evaporated TiCxN1−x (0≤x≤1) films, Surf. Coatings Technol. 126 (2000) 1.

[73] A. Hörling, L. Hultman, M. Odén, J. Sjölén, L. Karlsson, Thermal stability of arc evaporated high aluminum-content Ti1−xAlxN thin films, J. Vac. Sci. Technol. A. 20 (2002) 1815.

[74] I. Zhirkov, A. Petruhins, J. Rosen, Effect of cathode composition and nitrogen pressure on macroparticle generation and type of arc discharge in a DC arc

source with Ti-Al compound cathodes, Surf. Coatings Technol. 281 (2015) 20.

[75] A. Anders, Energetic deposition using filtered cathodic arc plasmas, Vacuum. 67 (2002) 673.

[76] H. Oettel, R. Wiedemann, S. Preißler, Residual stresses in nitride hard coatings prepared by magnetron sputtering and arc evaporation, Surf. Coatings Technol. 74–75 (1995) 273.

[77] S.J. Bull, P.C. Evans, A.S. Saleh, Positron annihilation studies of defects in PVD TiN coatings, Surf. Coatings Technol. 78 (1996) 42.

[78] M. Ahlgren, H. Blomqvist, Influence of bias variation on residual stress and texture in TiAlN PVD coatings, Surf. Coatings Technol. 200 (2005) 157.

[79] P.. Barna, M. Adamik, Fundamental structure forming phenomena of polycrystalline films and the structure zone models, Thin Solid Films. 317 (1998) 27.

[80] I. Petrov, P.B. Barna, L. Hultman, J.E. Greene, Microstructural evolution during film growth, J. Vac. Sci. Technol. A. 21 (2003) S117.

[81] L. Hultman, J.E. Sundgren, Structure / Property Relationships For Hard Coatings, in: R.F. Bunshah (Ed.), Handb. Hard Coatings, Noyes Publications/William Andrew Publishing, 2001.

[82] G.W.H. Höhne, W. Hemminger, H.-J. Flammersheim, Differential Scanning Calorimetry, Springer Berlin Heidelberg, 2003.

[83] R. Forsén, M. Johansson, M. Odén, N. Ghafoor, Decomposition and phase transformation in TiCrAlN thin coatings, J. Vac. Sci. Technol. A. 30 (2012) 61506.

[84] R.M. Langford, M. Rogers, In situ lift-out : Steps to improve yield and a comparison with other FIB TEM sample preparation techniques, Micron. 39 (2008) 1325.

[85] K. Thompson, D. Lawrence, D.J. Larson, J.D. Olson, T.F. Kelly, B. Gorman, In situ site-specific specimen preparation for atom probe tomography, Ultramicroscopy. 107 (2007) 131.

[86] W.C. Oliver, G.M. Pharr, An improved technique for determining hardness and elastic modulus using load and displacement sensing indentation experiments, J. Mater. Res. 7 (1992) 1564.

[87] H.J. Whitlow, G. Possnert, C.S. Petersson, Quantitative mass and energy dispersive elastic recoil spectrometry: Resolution and efficiency considerations, Nucl. Instruments Methods Phys. Res. Sect. B. 27 (1987) 448.

[88] M.S. Janson, CONTES: Conversion of Time-Energy Spectra, a program for ERDA data analysis, Internal Report, Uppsala University, 2004.

[89] E. Cadel, F. Vurpillot, R. Lardé, S. Duguay, B. Deconihout, Depth resolution

function of the laser assisted tomographic atom probe in the investigation of semiconductors, J. Appl. Phys. 106 (2009) 44908.

[90] B. Gault, M.P. Moody, F. De Geuser, D. Haley, L.T. Stephenson, S.P. Ringer, Origin of the spatial resolution in atom probe microscopy, Appl. Phys. Lett. 95 (2009) 34103.

[91] T.J. Prosa, R.A. Alvis, T.F. Kelly, Observations of Cluster Ions Originating from Non-Traditional Atom Probe Materials, Microsc. Microanal. 14 (2008) 1236.

[92] T.F. Kelly, O. Nishikawa, J.A. Panitz, T.J. Prosa, Prospects for Nanobiology with Atom-Probe Tomography, Mater. Res. Bull. 34 (2009) 744.

[93] B. Gault, W. Yang, K.R. Ratinac, R. Zheng, F. Braet, S.P. Ringer, Atom Probe Microscopy of Self-Assembled Monolayers : Preliminary Results, Langmuir Lett. 26 (2010) 5291.

[94] T.F. Kelly, M.K. Miller, Invited review article: Atom probe tomography, Rev. Sci. Instrum. 78 (2007) 31101.

[95] R. Alvis, T.F. Kelly, Atom-Probe Microscopy LEAPs the Chasm to Mainstream Applications, Micros. Today. (2008) 6.

[96] B. Gault, M.P. Moody, J.M. Cairney, S.P. Ringer, Atom Probe Microscopy, 1st ed., Springer New York, 2012.

[97] R. Gomer, Field emission and field ionization, Cambridge, Harvard Univerversity Press, 1961.

[98] D.R. Kingham, The post-ionization of field evaporated ions: A theoretical explanation of multiple charge states, Surf. Sci. Lett. 116 (1982) 273.

[99] P. Bas, A. Bostel, B. Deconihout, D. Blavette, A general protocol for the reconstruction of 3D atom probe data, Appl. Surf. Sci. 87–88 (1995) 298.

[100] T.T. Tsong, Pulsed-laser-stimulated field ion emission from metal and semiconductor surfaces: A time-of-flight of the formation of atomic, molecular, and cluster ions, Phys. Rev. B. 30 (1984) 4946.

[101] L. Johnson, Inside The Miscibility Gap, Doctoral Thesis, Linköping University, 2012.

[102] M. Thuvander, J. Weidow, J. Angseryd, L.K.L. Falk, F. Liu, M. Sonestedt, et al., Quantitative atom probe analysis of carbides, Ultramicroscopy. 111 (2011) 604.

[103] L.J.S. Johnson, M. Thuvander, K. Stiller, M. Odén, L. Hultman, Spinodal decomposition of Ti0.33Al0.67N thin films studied by atom probe tomography, Thin Solid Films. 520 (2012) 4362.

[104] O.C. Hellman, J.A. Vandenbroucke, J. Rüsing, D. Isheim, D.N. Seidman, Analysis of Three-dimensional Atom-probe Data by the Proximity Histogram,

Microsc. Microanal. 6 (2000) 437.

[105] F. Danoix, P. Auger, D. Blavette, Hardening of Aged Duplex Stainless Steels by Spinodal Decomposition, Microsc. Microanal. 10 (2004) 349.

[106] K. Pearson, On the Theory of Contingency and Its Relation to Association and Normal Correlation, Biometric Series No. 1, Dulau and Co. Memories, London, 1904.

[107] I.C. Schramm, C. Pauly, M.P. Johansson Jõesaar, P. Eklund, J. Schmauch, F. Mücklich, et al., Solid state formation of Ti4AlN3 in cathodic arc deposited (Ti1-xAlx)Ny alloys, Acta Mater. 129 (2017) 268.

[108] I.C. Schramm, C. Pauly, M.P.J. Jõesaar, S. Slawik, S. Suarez, F. Mücklich, et al., Effects of nitrogen vacancies on phase stability and mechanical properties of arc deposited (Ti0.52Al0.48)Ny (y<1) coatings, Surf. Coatings Technol. 330 (2017) 77.

[109] K.M. Calamba, I.C. Schramm, M.P. Johansson-Jõesaar, J. Ghanbaja, J.F. Pierson, F. Mücklich, et al., Enhanced thermal stability and mechanical properties of nitrogen deficient titanium aluminum nitride (Ti0.54Al0.46Ny) thin films by tuning the applied negative bias voltage, J. Appl. Phys. 122 (2017) 65301.

[110] A. Knutsson, I.C. Schramm, K. Asp Grönhagen, F. Mücklich, M. Odén, Surface directed spinodal decomposition at TiAlN/TiN interfaces, J. Appl. Phys. 113 (2013) 114305.

[111] D.J. Seol, S.Y. Hu, Y.L. Li, J. Shen, K.H. Oh, L.Q. Chen, Computer simulation of spinodal decomposition in constrained films, Acta Mater. 51 (2003) 5173.

[112] P.H. Mayrhofer, D. Music, J.M. Schneider, Influence of the Al distribution on the structure, elastic properties, and phase stability of supersaturated Ti1-xAlxN, J. Appl. Phys. 100 (2006) 94906.

[113] G.B. Gaitan, J.C. Caicedo, A.G. Balogh, S. Gottschalk, Cutting tools performance enhancement by using a TiN/TiAlN multilayer coating system, Phys. Status Solidi Curr. Top. Solid State Phys. 4 (2007) 4260.

[114] R. Rachbauer, A. Blutmager, D. Holec, P.H. Mayrhofer, Effect of Hf on structure and age hardening of Ti-Al-N thin films, Surf. Coatings Technol. 206 (2012) 2667.

[115] R. Rachbauer, D. Holec, P.H. Mayrhofer, Increased thermal stability of Ti–Al–N thin films by Ta alloying, Surf. Coatings Technol. 211 (2012) 98.

Paper I

Impact of nitrogen vacancies on the high temperature behavior of $(Ti_{1-x}Al_x)N_y$ alloys

I.C. Schramm, M.P. Johansson Jõesaar, J. Jensen,

F. Mücklich and M. Odén
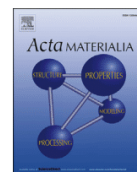
Full length article

Impact of nitrogen vacancies on the high temperature behavior of $(Ti_{1-x}Al_x)N_y$ alloys

I.C. Schramm [a, b, *], M.P. Johansson Jõesaar [a, c], J. Jensen [d], F. Mücklich [b], M. Odén [a]

[a] *Nanostructured Materials, Department of Physics, Chemistry and Biology (IFM), Linköping University, SE 58183 Linköping, Sweden*
[b] *Functional Materials, Department Materials Science, Saarland University, P.O. Box 151150, 66041 Saarbrucken, Germany*
[c] *SECO Tools AB, SE-73782 Fagersta, Sweden*
[d] *Thin Film Physics, Department of Physics, Chemistry and Biology (IFM), Linköping University, SE 58183 Linköping, Sweden*

ARTICLE INFO

ABSTRACT

Substoichiometric solid solution alloys of cubic $(Ti_{1-x}Al_x)N_y$ with x = 0.26, 0.48 and 0.60, and y ranging from 0.93 to 0.75 were grown by cathodic arc deposition. The influence of nitrogen deficiency on their thermal stability was studied by X-ray diffractometry, differential scanning calorimetry, scanning electron microscopy, and atom probe tomography. The nitrogen deficiency did not significantly affect the columnar growth nor the as deposited hardness. At elevated temperatures, alloys with x = 0.48 and 0.60 decompose isostructurally into cubic c-TiN and cubic c-AlN domains, which is consistent with spinodal decomposition. The decomposition is retarded by decreasing the nitrogen content, e.g. the formed isostructural domains in $(Ti_{0.52}Al_{0.48})N_{0.92}$ at 900 °C are similar in size to $(Ti_{0.52}Al_{0.48})N_{0.75}$ at 1200 °C. The formation of hexagonal w-AlN is shifted to higher temperatures by decreasing nitrogen content. Nucleation and growth of Al-Ti clusters in a Ti rich matrix were observed for the alloys with high Ti content, x = 0.26. These results suggest that nitrogen deficiency reduces the driving force for phase separation.

© 2016 Acta Materialia Inc. Published by Elsevier Ltd. All rights reserved.

1. Introduction

$Ti_{1-x}Al_xN$ alloys have been intensively studied due to their outstanding thermal stability and high temperature mechanical properties [1,2] related to an age hardening phenomenon. The as deposited metastable cubic (c)-$Ti_{1-x}Al_xN$ (B1 structure) phase separates isostructurally into coherent Ti rich (c-TiN) and Al rich (c-AlN) domains, through spinodal decomposition at high temperatures [3,4]. The lattice mismatch and differences in elastic properties generated between the domains collectively obstruct dislocation movements [4,5]. Loss of mechanical properties upon further annealing is a consequence of the transformation of metastable c-AlN into its stable wurzite B4 phase (w-AlN) during the coarsening stage of the domains [4,7]. Delaying the onset temperature for phase separation and suppressing the w-AlN transformation have been of great interest for this ternary system [8,9]. Nevertheless, the influence of nitrogen on the thermal

stability remains an open question and has only been addressed by Alling et al. for c-TiAlN$_y$ (y < 1) via static *ab initio* calculations [10].

Nitrogen vacancies (N_V) have been demonstrated to induce changes in the electronic structure, the bonding nature, and consequently the mechanical properties of transition metal nitrides (TMN) [11–13]. The B1 structures of TiN and TiAlN have been shown to accommodate a large fraction of N_V: $0.6 \leq y \leq 1.0$ in TiN$_y$[11–13] and $0.37 \leq y \leq 1.0$ in TiAlN$_y$[14,15]. The influence of N_V and other point defects on the thermal stability of TiN$_y$ was addressed by Tsetseris et al. via first principle calculations [16]. They showed that the N_V are stable up to 900 °C due to a high activation energy for migration and a slight repulsion toward segregation, consistent with positron annihilation spectroscopy observations [17]. In the case of the ternary (Ti,Al)N$_y$ system, only studies focusing on growth conditions have shown an influence of the nitrogen partial pressure [1,14,18]. In this work, we present a systematic study on cathodic arc deposited nitrogen deficient $(Ti_{1-x}Al_x)N_y$ coatings. The thermal response and structural evolution is evaluated with X-ray diffractometry, differential scanning calorimetry, scanning electron microscopy, and atom probe tomography. The effects of N_V are addressed in terms of driving force for phase separation, domains evolution, w-AlN formation, and co-

---

* Corresponding author. Nanostructured Materials, Department of Physics, Chemistry and Biology (IFM), Linköping University, SE 58183 Linköping, Sweden.
E-mail address: isasc@ifm.liu.se (I.C. Schramm).

occurring processes via nucleation and growth. Our results show substantial improvement of the thermal stability when reducing the nitrogen content for alloys in the metallic fraction range of x = 0.48–0.60.

2. Experimental details

Substoichiometric $(Ti_{1-x}Al_x)N_y$ coatings, y < 1, were grown using an industrial scale Metaplas MZR-323 reactive cathodic arc evaporation system in an atmospheric mixture of Ar and N_2 at a total gas pressure of 2 Pa, a substrate bias of −30 V, and a growth temperature of ~450 °C. Three circular cathodes, 100 mm in diameter, of $Ti_{1-x}Al_x$ (x = 0, 0.55 and 0.67) were mounted facing a rotating cylinder where Fe foils and polished WC/Co substrates were mounted. The cylinder was set to rotate at three revolutions per minute and the coatings were grown to a thickness of about 3 μm with a growth rate of about 5.5 μm/h. The nitrogen per metal fraction is y and it was controlled in the alloys by tuning the N_2 gas flow in the Ar/N_2 mixture during growth, from 366 to 85 standard cubic centimeters per minute.

Powder samples were obtained from the coated Fe foils and were used for all the microstructure analysis. The Fe foil was thinned mechanically and then dissolved in hydrochloric acid (37%). The recovered coating flakes were cleaned with distilled water and acetone and ground to a fine powder. This technique has proven to yield a powder with the same stoichiometry and crystal structure as the deposited coating [19].

The thermal response was measured in a Netsch STA 449C differential scanning calorimeter (DSC) operating with a 50 ml/min argon flow. Each measurement was performed with 50 mg of powder placed in an alumina crucible, outgassing for 1 h at 250 °C, followed by two heating cycles up to 1400 °C with a rate of 20 K per min. The second heating cycle was used for baseline correction. Additionally, single heating cycles were performed to different maximum temperatures, 800–1400 °C in steps of 100 °C, always starting with as deposited powder for each temperature. These cycles also started with an outgassing period and 15 mg powder were used.

X-ray diffractometry (XRD) was performed with a Panalytical X'Pert PRO MRD diffractometer using Cu K_{α} radiation and a Bragg Brentano configuration. The diffractograms were recorded at room temperature after annealing.

A dual beam, scanning electron microscope (SEM) and focused ion beam (FIB) instrument, was used for imaging surface morphology, prepare cross sections for microstructural overviews, and to produce of atom probe tomography (APT) tips. The powder particle flakes were sufficiently large and flat to carry out a standard lift out technique without deviations [20]. The APT tip shape was optimized to reduce the thermal tails and obtain high quality mass spectrum. Several tips were produced per sample at different depths.

APT was performed using a local electrode atom probe (Cameca LEAP 3000 X HR) in laser mode, with a sample ground temperature of 60 K, an evaporation rate of 0.5%, and a laser frequency of 200 kHz with an energy of 0.5 nJ. Data reconstruction was carried out with the software package IVAS (version 3.6.8, Cameca) using voltage mode. An evaporation field of 40 V/nm was obtained from the mass spectrum using Kingham curves [21]. The reconstruction parameter field factor (k) was chosen between 3.3 and 4.1 individually for each tip due to the variation in shank angle between tips. SEM images before and after run were used to determine k. In addition to the $(Ti_{0.52}Al_{0.48})N_y$ coatings, a reference standard w-AlN sample (Micro Analysis Consultants Ltd., Standard No:10578) was

also measured. The errors presented are the standard errors calculated by IVAS from the sampling distribution of each tip.

Elemental composition of as deposited samples on WC/Co substrates was measured by Time of Flight Energy Elastic Recoil Detection Analysis (ToF-E ERDA), using a 36 MeV $^{127}I^{8+}$ ion beam. The spectra were converted using the CONTES code.

Hardness measurements were performed with an UMIS nano-indentor using a Berkovich diamond tip. The samples were prepared as tapered cross sections (taper angle ~10°) by mechanically grinding and polishing to a mirror like finish using 1 μm diamond grits in the final step. Average hardness values were extracted using the Oliver and Pharr method [22], using a minimum of 50 indents for each sample with fused silica as reference.

3. Results

The results presented here correspond mainly to $(Ti_{0.52}Al_{0.48})N_y$ alloys with nitrogen per metal fraction y = 0.92, 0.87, and 0.75 and $(Ti_{0.74}Al_{0.26})N_{0.82}$. The results are very similar to $(Ti_{0.40}Al_{0.60})N_y$ and differences are pointed out.

3.1. As deposited state

All samples revealed a dense columnar microstructure with macroparticles evenly distributed in the coating as shown in Fig. 1. The average column width is 190 ± 20 nm regardless of the nitrogen content. Formation of macroparticles is common in arc deposited coatings [3], and their generation increases when coatings are grown with Ar/N_2 atmosphere, resulting in a larger surface topography similar to the results reported by Bujak et al. [18].

The nitrogen per metal fraction y and aluminum metal fraction x measured by APT and ERDA are shown in Table 1. Samples grown from the same cathode had aluminum metal fractions that were lower than the Al content of the cathode, e.g. x = 0.48 ± 0.01 and x = 0.55. This difference is expected from the preferential resputtering of Al atoms during deposition [23]. Impurity elements like oxygen, carbon, argon and gallium were also detected at a total content of less than 0.2 at.%. Oxygen and carbon are commonly detected in films grown in industrial scale vacuum chambers. Argon was incorporated during the deposition process and gallium during the APT sample preparation [20]. APT and ERDA results are consistent for the samples close to stoichiometry (y > 0.9) and the differences are within the error of ERDA as shown in Table 1. The higher amount of macroparticles and surface roughness in samples y < 0.9 introduced an error in the ERDA quantification. Nitrogen is underestimated due to the metallic nature of the macroparticles. This data is therefore discarded.

Chemical analysis by APT of the standard w-AlN reference sample yields an average composition of 53.6 ± 0.3 at.% Al and 46.3 ± 0.3 at.% N, i.e. an underestimation of the nitrogen content. Thuvander et al. showed that chemical bonding, detector dead time, and overlap between complex and single carbon isotope ions contributed to an erroneous carbon deficiency of up to 5 at.% in carbide materials using APT [24]. They suggested a nontrivial but strong correlation between carbon detection and the different chemical bonds caused by carbon occupying alike lattice sites, which is similar to our case. The semiconductor nature of w-AlN affects APT nitrogen detection, while the conducting c-TiAlN solid solutions do not display these artifacts, as confirmed by ERDA measurements. In case of the metastable c-AlN phase no standards exist that can confirm the nitrogen detection.

Powder X-ray diffractograms of samples $(Ti_{0.52}Al_{0.48})N_y$, y = 0.92, 0.87, and 0.75 only display peaks from the solid solution
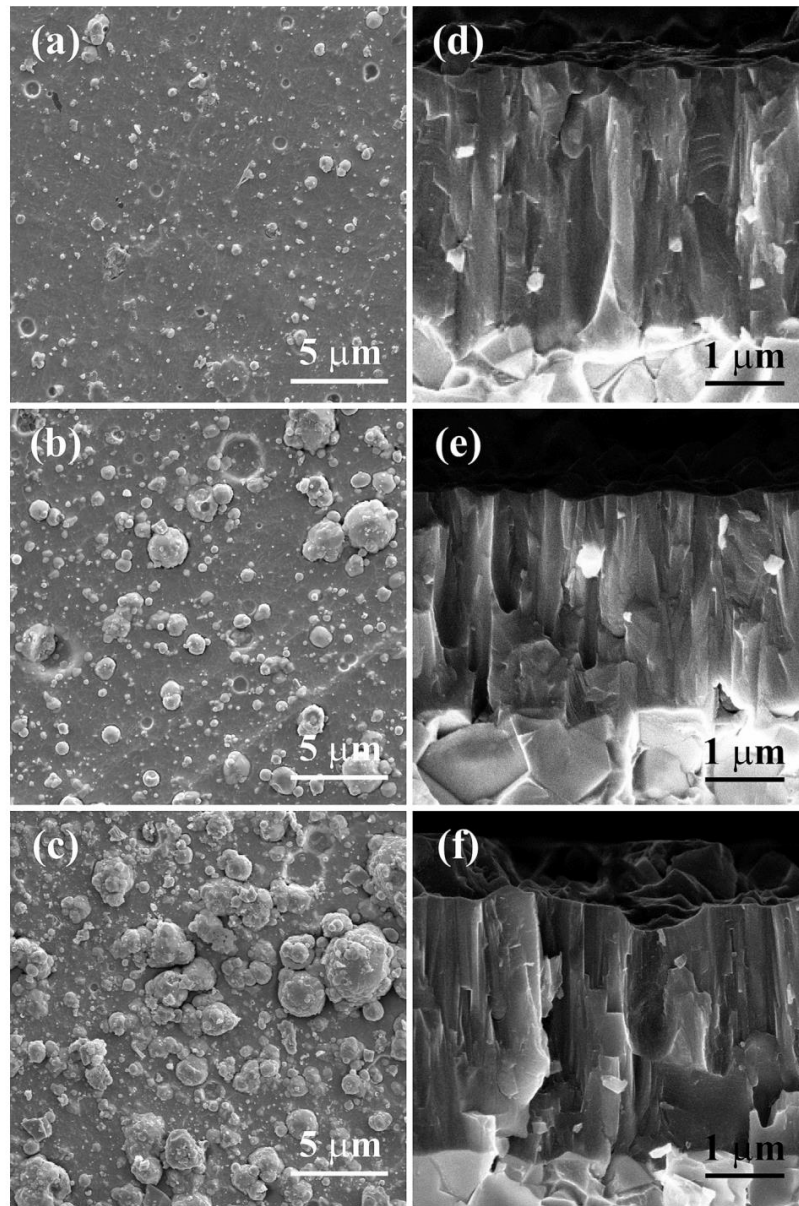
Fig. 1. SEM micrographs of (a–c) the surface morphology and corresponding (d–f) fractured cross sections of $(Ti_{0.52}Al_{0.48})N_y$ coatings with (a, d) y = 0.92, (b, e) y = 0.87 and (c, f) y = 0.75.

B1 structure in Fig. 2. The flake like shaped powder particles result in none random packing and a weak reminiscence of the preferred crystallographic orientations of the coatings. However, pole figure measurements yield a texture coefficient smaller than 1.5 for all samples. No macroscopic residual stress remains from the original coating in the powder form. Nevertheless, differences in lattice parameter, peak intensity ratio of the diffraction lines, and peak broadening are observed (Table 1). The lattice parameter extracted using the Nelson Riley method [25], shows a small change using sample y = 0.92 as reference. The change was of +0.12% and −0.05% for samples y = 0.87 and 0.75, respectively. The peak intensity ratio

111/200 increases by a factor of 3 when the nitrogen content is decreased, i.e. a gain from 0.14 to 0.44 when y is reduced from 0.92 to 0.75. This gain cannot be explained by the crystallographic texture in the powder samples. In addition, an increase of 25% in the peak intensity ratio 111/222 between sample y = 0.92 and y = 0.75 was measured, confirming changes in the structure factor. The peak broadening does not display a clear trend. Alloys $(Ti_{0.40}Al_{0.60})N_y$ and $(Ti_{0.74}Al_{0.26})N_{0.82}$ show similar behavior.

The hardness values of the as deposited coatings are similar for all samples with the same metallic ratio, i.e. for x = 0.48 and different nitrogen content: y = 0.92, 0.87 and 0.75 the values are

Table 1
Chemical composition obtained by atom probe and ERDA, and lattice parameter determined by XRD of the as deposited samples in powder form.

Name	Atom probe			XRD
	Nitrogen content	Nitrogen fraction	Aluminum (metal) fraction	Lattice parameter-Nelson-Riley method
	at.%	$y = N/(Al + Ti)$	$x = Al/(Al + Ti)$	Å
$(Ti_{0.52}Al_{0.48})N_{0.92}$	47.80 ± 0.27	0.92 ± 0.01	0.48 ± 0.01	4.1770 ± 0.0005
$(Ti_{0.52}Al_{0.48})N_{0.87}$	46.38 ± 0.16	0.87 ± 0.01	0.48 ± 0.01	4.1822 ± 0.0015
$(Ti_{0.52}Al_{0.48})N_{0.75}$	42.79 ± 0.57	0.75 ± 0.02	0.47 ± 0.01	4.1749 ± 0.0023
$(Ti_{0.40}Al_{0.60})N_{0.93}$	48.17 ± 0.25	0.93 ± 0.01	0.60 ± 0.01	4.1504 ± 0.0015
$(Ti_{0.40}Al_{0.60})N_{0.87}$	46.30 ± 0.24	0.87 ± 0.01	0.59 ± 0.01	4.1573 ± 0.0042
$(Ti_{0.40}Al_{0.60})N_{0.80}$	44.24 ± 0.33	0.80 ± 0.01	0.61 ± 0.01	4.1492 ± 0.0088
$(Ti_{0.74}Al_{0.26})N_{0.82}$	44.84 ± 0.70	0.82 ± 0.04	0.26 ± 0.03	4.2211 ± 0.0006
ERDA				
$(Ti_{0.52}Al_{0.48})N_{0.92}$	46.3 ± 1.4	0.88 ± 0.04	0.46 ± 0.03	–
$(Ti_{0.52}Al_{0.48})N_{0.75}$	37.7 ± 1.8	0.63 ± 0.04	0.44 ± 0.03	–
$(Ti_{0.40}Al_{0.60})N_{0.93}$	47.5 ± 1.5	0.91 ± 0.03	0.63 ± 0.04	–
$(Ti_{0.40}Al_{0.60})N_{0.80}$	39.2 ± 1.9	0.69 ± 0.04	0.57 ± 0.03	–
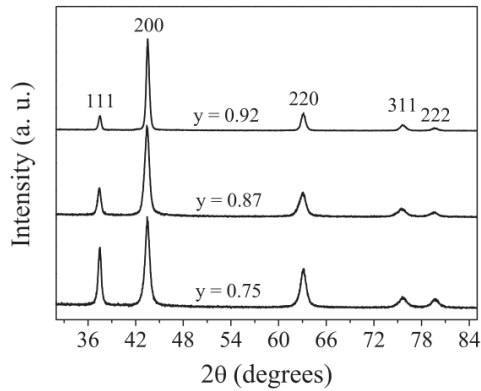
Fig. 2. X-Ray powder diffractograms from $(Ti_{0.52}Al_{0.48})N_y$ coatings in their as deposited state in a 2Θ range of 32°–85° showing the first five lattice planes (111, 200, 220, 311, 222).

31.2 ± 1.0, 31.4 ± 2.2 and 29.9 ± 1.1, respectively.

3.2. Phase evolution and thermal stability

X-ray diffractograms in Fig. 3(a–c) of samples with the same metallic ratio $x = 0.48$ but different nitrogen fractions show c-TiAlN solid solutions up to 900 °C with peaks slighted shifted to higher angles. The peak shifts have been reported as an effect of crystal recovery processes [4]. Only sample $y = 0.75$ retained the c-TiAlN peaks up to 1400 °C.

Above 900 °C samples $y = 0.92$ and 0.87 display c-TiN and c-AlN peaks. These peaks originate from phase separation into nm-sized coherent domains. Strains generated during decomposition shift the peaks to higher 2θ values [26]. The temperature range of the phase separation for each sample differs with the nitrogen content. It occurs at a lower temperature and shorter interval for $(Ti_{0.52}Al_{0.48})N_{0.92}$ than $(Ti_{0.52}Al_{0.48})N_{0.87}$. No distinct c-AlN peaks are observed when $y = 0.75$. However, all samples display w-AlN formation. The w-AlN peaks appear after the c-AlN peaks at 1100 °C for $y = 0.92$ and 1300 °C for $y = 0.87$. For $y = 0.75$, w-AlN peaks appear together with the c-TiN peaks at 1200 °C.

Similar peak evolution with nitrogen content was recorded for the alloys with higher aluminum fraction $(Ti_{0.40}Al_{0.60})N_y$. The phase separation starts at lower temperatures since this alloy composition is positioned nearer the maximum of the asymmetric miscibility gap [27].

In the alloy with higher titanium content $(Ti_{0.74}Al_{0.26})N_{0.82}$, the c-TiAlN solid solution peaks were stable up to 1200 °C as shown in Fig. 3(d). Above 1200 °C, the formation of w-AlN is apparent and accompanied by a shift to lower angles of the c-TiAlN peaks toward c-TiN. This suggests a nucleation and growth phase transformation mechanism (c-TiAlN → c-TiN + w-AlN) through a continuous depletion of Al from c-TiAlN rather than a formation of c-TiN and c-AlN domains.

The thermal response of $(Ti_{0.52}Al_{0.48})N_y$ presented in Fig. 4 show only exothermic reaction peaks and their maxima are marked T1 to T4. T1 and T2 correspond to recovery processes and defect annihilations [4,17,28]. T3 was only resolved for sample $y = 0.92$ at ~950 °C consistent with phase separation via spinodal decomposition. Peak T4 corresponds to w-AlN formation and a shift to higher temperatures is observed when decreasing the nitrogen content. The maximum heat flow is above 1400 °C for sample $y = 0.87$. The total mass of the samples remained nearly constant during the heating cycle and a change of less than 0.58% was recorded.

In Fig. 5 the temperature at which the w-AlN transformation has its maximum heat flow is shown as a function of nitrogen content. We have included literature data for monolithic $(Ti_{0.5}Al_{0.5})N_{1.0}$[29] and $(Ti_{0.5}Al_{0.5})N_{0.89}$[4]. The results show a consistent trend of increased temperature with reduced nitrogen content down to $y = 0.87$. Further nitrogen reduction leads to a strong drop of the maximum heat flow temperature.

SEM cross sectional micrographs of $(Ti_{0.52}Al_{0.48})N_y$ in their as deposited and 1200 °C annealed states are shown in Fig. 6. In the as deposited states, no segregation is observed. The annealed states display bright and dark contrast corresponding to Al rich and Ti rich domains, respectively. Phase separation inside the grains has taken place for samples $y = 0.92$ and 0.87, with less coarse domains when $y = 0.87$. No segregation was resolved for sample $y = 0.75$. Precipitation of an Al rich phase at grain boundaries with larger features is observed for the alloys with low nitrogen content, i.e. $y = 0.87$ and 0.75. This precipitation is consistent with w-AlN formation via nucleation and growth. In addition, porosity is observed in $y = 0.92$ at 1200 °C as a consequence of the volume expansion during the phase transformation from c-AlN to w-AlN.

Representative three dimensional (3D) APT tips of alloys with $x = 0.48$ and $y = 0.92$, 0.87, 0.75 are shown in Fig. 7. As deposited samples display a homogenous distribution of Al and Ti. At 900 °C, a phase separation into small Ti rich and Al rich domains is only observed in sample $y = 0.92$. At 1200 °C, a decomposed interconnected 3D structure is present in all samples. The segregation and coarsening are more pronounced with increasing nitrogen content. At 1400 °C, no further coarsening is observed in sample $y = 0.87$ and 0.75. Only elongated Al rich clusters embedded in a
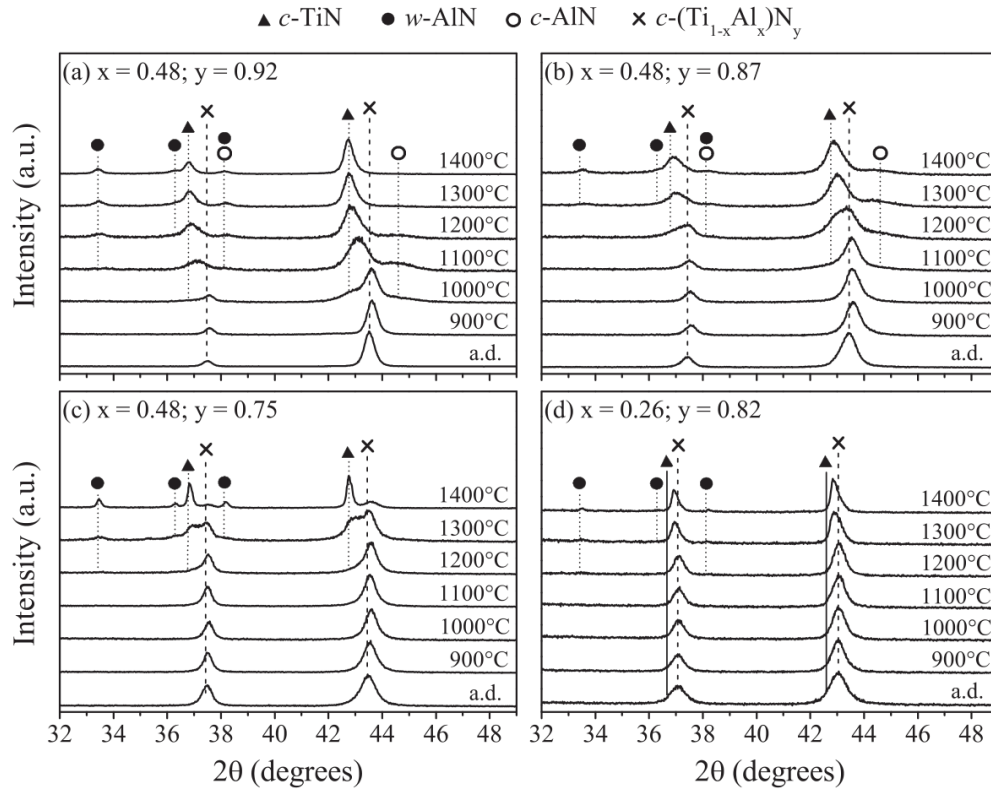
Fig. 3. X-ray diffractograms recorded after annealing at different temperatures of (a) $(Ti_{0.52}Al_{0.48})N_{0.92}$, (b) $(Ti_{0.52}Al_{0.48})N_{0.87}$, (c) $(Ti_{0.52}Al_{0.48})N_{0.75}$, and (d) $(Ti_{0.74}Al_{0.26})N_{0.82}$.

finely decomposed matrix are present in sample y = 0.75. The clusters have an average composition of 52.4 ± 1.4 at.% Al, 2.3 ± 0.6 at.% Ti, and 44.8 ± 1.3 at.% N. These values are similar to the composition of the w-AlN reference sample with a low Ti solubility.

A 1D concentration profile across an Al rich cluster in $(Ti_{0.52}Al_{0.48})N_{0.75}$ annealed at 1400 °C is shown in Fig. 8. Three regions can be seen: the matrix with small compositional fluctuations, the Al rich cluster, and an Al depleted zone. The results indicate a nucleation and growth process of AlN clusters from a spinodal decomposed structure.

Volume composition histograms of the main elements (Al, Ti, N) of as deposited samples $(Ti_{0.52}Al_{0.48})N_y$, at 900 °C and 1200 °C were obtained from the APT datasets divided into small volumes containing 80 ions. Their deviation from a random distribution (binomial distribution) was calculated using χ_e^2 statistics and then normalized to obtain the Pearson coefficients (μ), which are presented in Table 2. A μ of 0 indicates a random distribution while 1 is complete segregation. Pearson coefficient is a qualitative indicator

Fig. 4. Exothermal response of $(Ti_{0.52}Al_{0.48})N_y$, with y = 0.92, 0.87 and 0.75. The dashed curves in the upper part of the panel show the relative mass change.
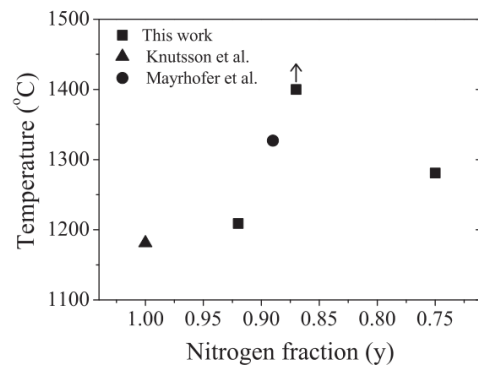
Fig. 5. Temperature of maximum heat flow during w-AlN formation (peak T4) as a function of nitrogen fraction for samples $(Ti_{0.52}Al_{0.48})N_y$ extracted from Fig. 3, monolithic $(Ti_{0.5}Al_{0.5})N_{1.0}$[25], and $(Ti_{0.5}Al_{0.5})N_{0.89}$[4]. The arrow indicates that maximum heat flow occurs for a temperature higher than 1400 °C for the sample with y = 0.87.
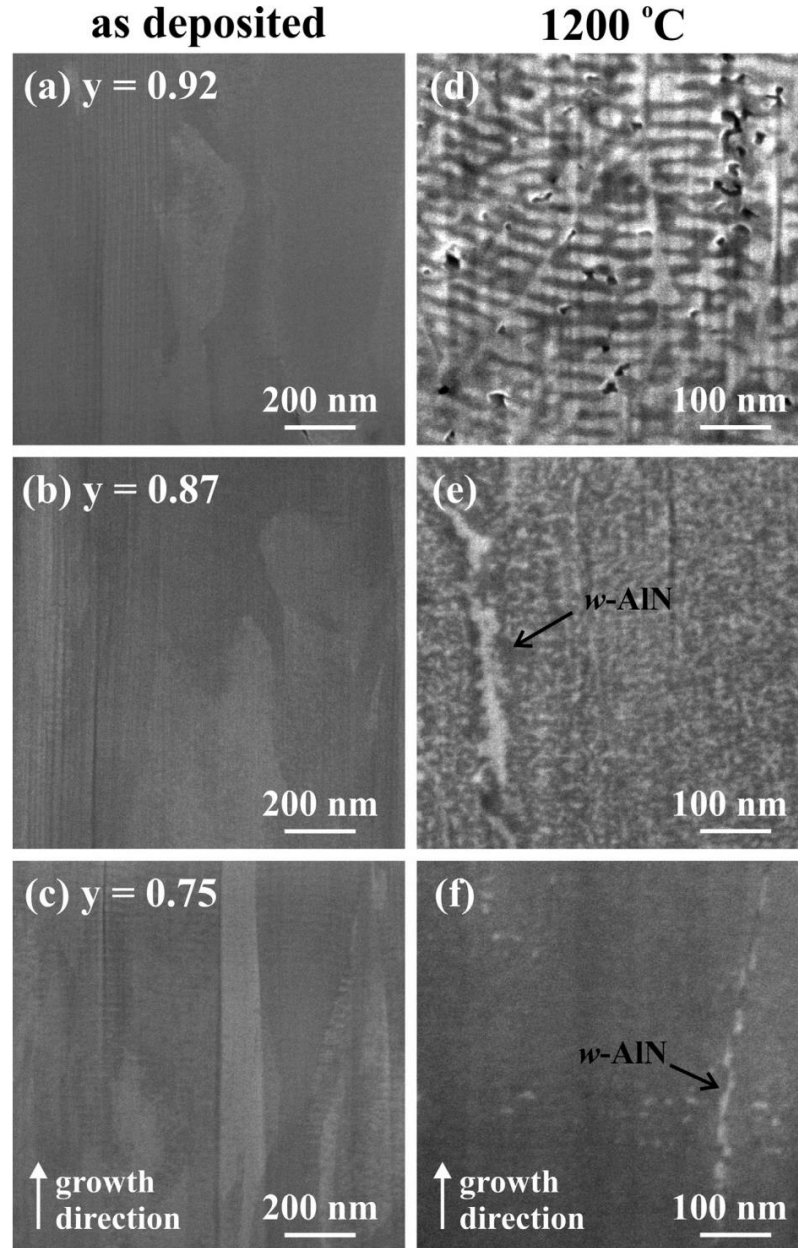
Fig. 6. SEM micrographs viewed with secondary electrons at a tilt of 52° using an in-lens detector of FIB prepared cross sections of $(Ti_{0.52}Al_{0.48})N_y$. (a–c) show as-deposited states and (d–f) 1200 °C annealing states for (a, d) y = 0.92, (b, e) y = 0.87 and (c, f) y = 0.75. The growth direction is the same in all panels and w-AlN is marked with black arrows.

and does not distinguish between different levels of segregation and morphological differences [30]. Volume composition histograms of samples annealed at 1200 °C are shown in Fig. 9. Additionally, calculated binomial distributions were plotted as reference for the measured data deviations.

All samples present an elemental distribution close to random in the as deposited state. Al and N deviate slightly from random when the nitrogen content is reduced, which is correlated to the more pronounced nitrogen compositional fluctuation close to the

artificial layers. Segregation on the metallic sublattice is apparent for y = 0.92 at 900 °C. At the same temperature nitrogen has redistributed for y = 0.87 and 0.75 to a more random and homogenous state. At 1200 °C, metal segregation is present in all samples and coarsening is apparent for sample y = 0.92. Sample y = 0.75 presents a symmetric widening of the metal distribution consistent with a phase separation via spinodal decomposition, i.e. the amplitude of the compositional variations is growing [31]. The nitrogen distribution remains random for low nitrogen content
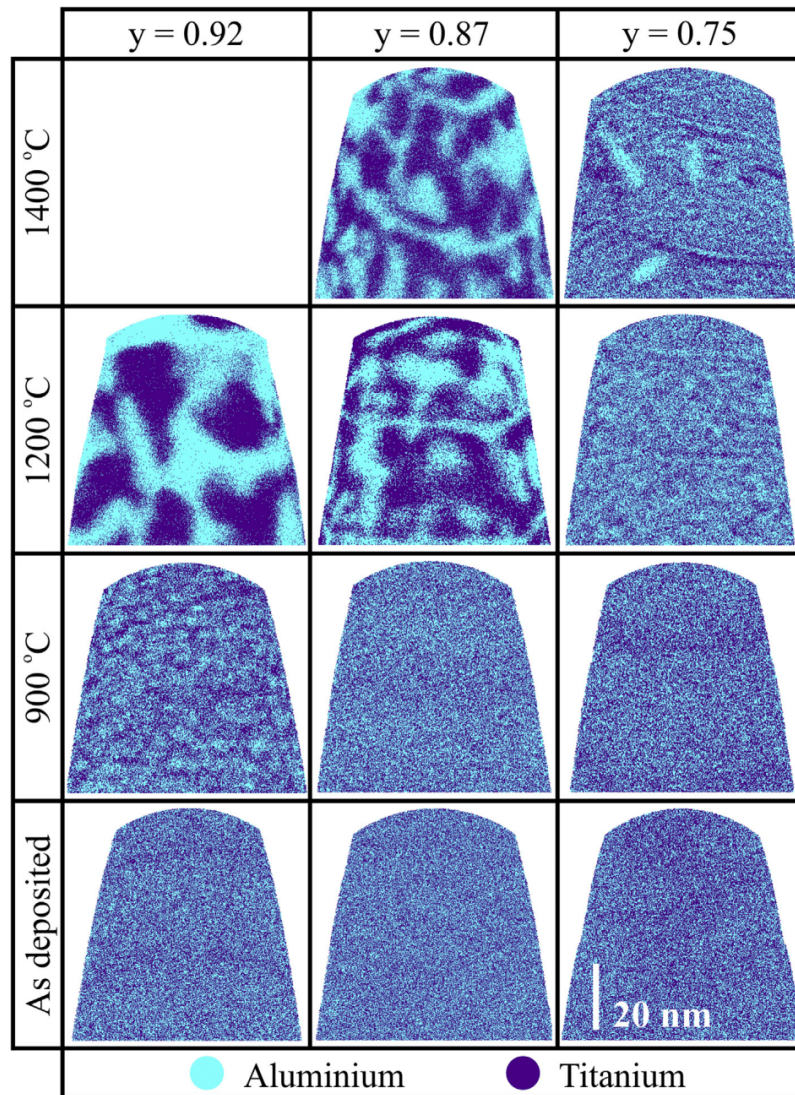
Fig. 7. Reconstructed 3D APT tips of $(Ti_{0.52}Al_{0.48})N_y$, with y = 0.92, 0.87 and 0.75, in their as deposited state, and after heat treatments at 900 °C, 1200 °C and 1400 °C. Tips were extracted from single grains and no grain boundaries are present. Only Al and Ti ions are presented for clarity.

samples at 1200 °C, while sample y = 0.92 displays an asymmetric distribution. The latter is an artifact caused by the underestimation of the nitrogen content in w-AlN.

Metal and nitrogen composition fractions inside Ti rich and Al rich domains were obtained from the APT datasets and plotted versus annealing temperature as shown in Fig. 10. For the not yet decomposed samples, global composition values were used. For samples showing segregation, proximity concentration histograms along the domains interfaces (proxigram) [30] were generated using an Al isoconcentration surface at 26.5 at.%. The upper row belongs to Al rich domains and the lower row to Ti rich domains. The nitrogen fraction in Al rich domains in $(Ti_{0.52}Al_{0.48})N_{0.92}$ at 1200 °C was corrected from y = 0.80 to y = 1.0, due to the presence mainly of w-AlN.

A partitioning on both sublattices occurs in all alloys. The metal segregation is consistent with spinodal decomposition and coarsening [31]. This decomposition is retarded by decreasing the nitrogen content, e.g. sample y = 0.75 at 1200 °C is in a similar decomposed state as sample y = 0.92 at 900 °C. Nitrogen partitioning is more complex as the temperature increases. First, nitrogen depletion in the Al rich domain and a slight enrichment in the Ti rich domains occur. Next, the Al rich domains become stoichiometric and the nitrogen deficiency is accommodated in the coarsened Ti rich domains (y = 0.92 at 1200 °C), similar to what was predicted by Alling et al. [10]. A global increase in nitrogen fraction is observed in sample y = 0.75 at 900 °C, possibly due to local variations.

Similar atom probe data analysis was performed on the
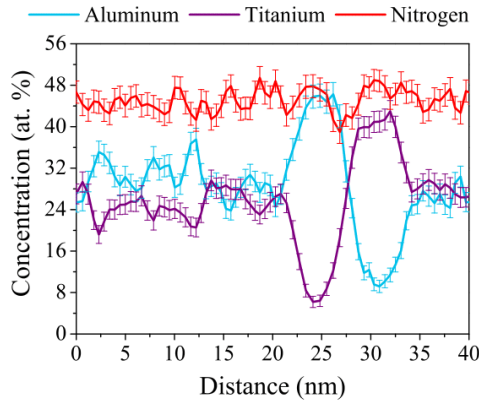
Fig. 8. 1D concentration profiles across an Al rich cluster in sample $(Ti_{0.52}Al_{0.48})N_{0.75}$ annealed at 1400 °C. A cylindrical region of interest of 5 nm in diameter was used.

Table 2
Pearson coefficient (μ) of aluminum, titanium and nitrogen for as deposited, 900 °C and 1200 °C of $(Ti_{0.52}Al_{0.48})N_y$ alloys: y = 0.92, 0.87 and 0.75.

Alloy	Annealing temperature	Aluminum	Titanium	Nitrogen
$(Ti_{0.52}Al_{0.48})N_{0.92}$	a.d.	0.22	0.09	0.06
	900 °C	0.99	0.72	0.17
	1200 °C	1.00	1.00	0.63
$(Ti_{0.52}Al_{0.48})N_{0.87}$	a.d.	0.16	0.12	0.17
	900 °C	0.27	0.12	0.09
	1200 °C	1.00	1.00	0.22
$(Ti_{0.52}Al_{0.48})N_{0.75}$	a.d.	0.26	0.11	0.26
	900 °C	0.23	0.12	0.10
	1200 °C	0.99	0.71	0.14

substoichiometric high titanium content c-$(Ti_{0.74}Al_{0.26})N_{0.82}$ alloy as shown in Fig. 11. In this case, Al rich clusters form in a Ti rich matrix when annealed at 1200 °C. The clusters are highlighted in Fig. 11(b) using 36 at.% Al isoconcentration surfaces. Their average composition is 64.1 ± 0.9 at.% Al, 26.1 ± 0.8 at.% Ti, and 9.5 ± 0.6 at.% N. These values suggest the formation of an Al-Ti compound and not w-AlN clusters. The matrix is aluminum depleted with a concentration of 13.1 ± 0.1 at.% Al, 42.6 ± 0.2 at.% Ti, and 43.8 ± 0.2 at.% N.

Aluminum volume composition histograms of as deposited $(Ti_{0.74}Al_{0.26})N_{0.82}$ and annealed at 1200 °C together with the

calculated binomial distributions are shown in Fig. 12. The as deposited state presents a random distribution, while a broadening of the Al distribution occurs at 1200 °C shifting the maximum to the left, with tailing on the right side of the peak. This indicates an Al depleted matrix with Al rich segregations consistent with a nucleation and growth process [30].

4. Discussion

4.1. As deposited state

All $(Ti_{1-x}Al_x)N_y$ alloys present a solid solution B1 structure, a columnar microstructure, and similar hardness values in their as deposited states. Local chemical fluctuation is present and more pronounced when the nitrogen content is reduced, mainly due to preferential resputtering of Al atoms during deposition [23] and intrinsic fluctuations [32].

Calculations of the lattice parameter performed by To Baben et al. [15] of the $(Ti_{0.5}Al_{0.5})N_y$ system and of the TiN_y system by Ashley et al. [13] have shown that the accommodation of sub-stoichiometry is done via nitrogen vacancies. The lattice parameter decreases linearly with decreasing nitrogen content, i.e. 0.65% for $(Ti_{0.5}Al_{0.5})N_{0.75}$ and 0.18% for $TiN_{0.8}$, which agree with experiments for $(Ti_{0.5}Al_{0.5})N_y$ [14,15] and TiN_y [11,12,17]. If other point defects (anti sites, interstitials) are present, an increased lattice parameter of at least 3% would be expected [13]. Our results showed a maximum change of 0.12% suggesting that the substoichiometry is accommodated mainly through nitrogen vacancies but with other additional point defects present that collectively affect the lattice parameter. The presence of different types of point defects in cathodic arc deposited transition metal nitride coatings has been confirmed experimentally [17,33]. However, their quantification is not yet possible because of the high density of other line defects and voids [33].

The 111/200 and 111/222 peak intensity ratio gain seen when reducing the nitrogen content stems mainly from a change in the structure factor toward a metallic face center cubic structure, caused by the introduction of nitrogen vacancies in the B1 structure. Similar trends were observed by Shew et al. [14] in $(Ti,Al)N_x$ coatings, although their XRD measurements were performed on coatings remaining on their substrates. Our results suggest a change in bonding towards a metallic situation although not strong enough to affect the hardness.
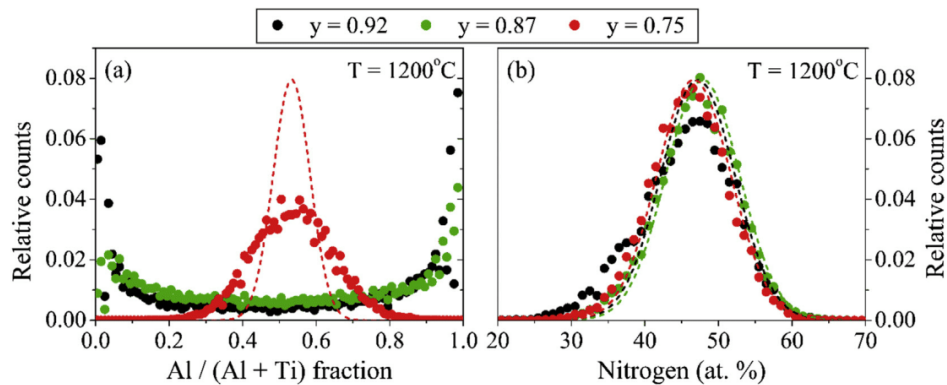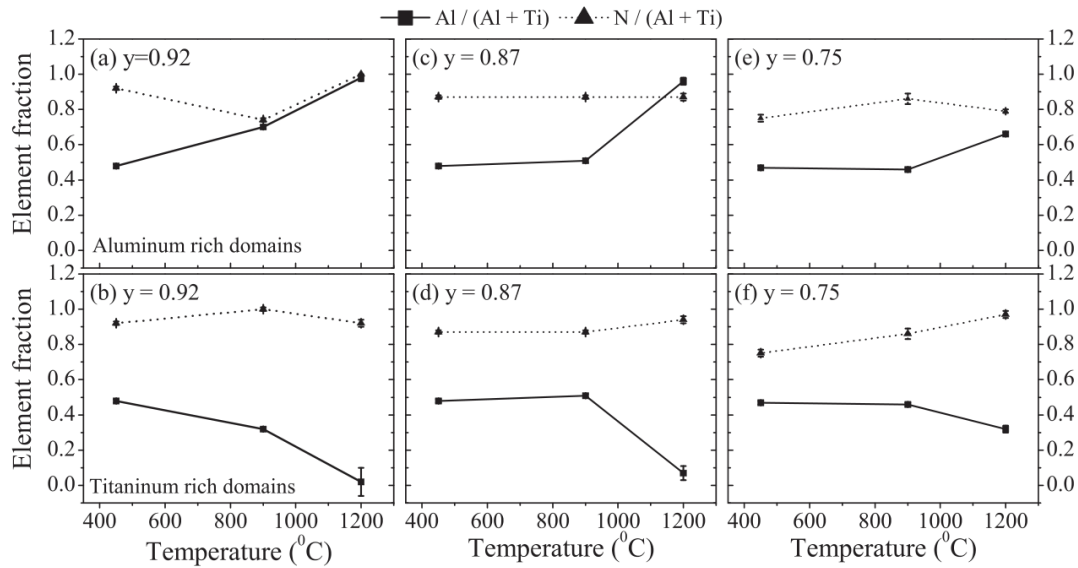

Fig. 9. Volume composition histograms of (a) the aluminum metal fraction and (b) nitrogen of alloys $(Ti_{0.52}Al_{0.48})N_y$ after annealing at 1200 °C, with y = 0.92, 0.87 and 0.75. The dots belong to observed data and the dashed lines to the corresponding calculated random distribution.

Fig. 10. Metal and nitrogen fractions inside aluminum and titanium rich domains extracted from APT datasets for $(Ti_{0.52}Al_{0.48})N_y$: (a–b) y = 0.92, (c–d) y = 0.87, and (e–f) y = 0.75.

4.2. Phase evolution and thermal stability

The high activation energy for migration and slight repulsion of nitrogen vacancies are suggested to be responsible for the thermal stability of substoichiometric TiN_x films based on first principle calculations [16]. These predictions are extended to the $TiAlN_y$ system where we observe at 900 °C a retention of the sub-stoichiometry for all samples, no mass change, and a minor change in the X-ray peak intensity 111/200 ratio. Nonetheless, crystal recovery through activation of defects migration and annihilation of different point defects take place at lower temperature [17,28], here seen as the exothermic peaks T1 and T2 in the thermal response, and as the composition redistribution inside the grains in APT results. The alloys close to stoichiometry, y > 0.9, are the only ones that simultaneously undergo phase separation at 900 °C.

Alling et al. [10] predicted the driving force for spontaneous decomposition across the entire compositional range: $0 \leq x \leq 1$ and $0 \leq y \leq 1$ of $(Ti_{1-x}Al_x)N_y$. Isostructural decomposition is favorable for alloy compositions with medium and high Al content, while alloys rich in Ti and low in nitrogen have a strong driving force for forming Al or Al-Ti phases. Our experimental results confirm these predictions with minor deviations. Alloys with x = 0.48 and 0.60 and y > 0.75 all display phase separation via spinodal decomposition. We also see co-occurring decomposition mechanisms into c-TiN and w-AlN. This takes place at grain boundaries via nucleation and growth in all alloys at 1200 °C. Only $(Ti_{0.52}Al_{0.48})N_{0.75}$, manifests this decomposition mechanism both inside the grains and at grain boundaries. The high Ti content alloy $(Ti_{0.74}Al_{0.26})N_{0.82}$ present nucleation and growth of Al-Ti clusters only inside the grains and w-AlN at grain boundaries.

Our data show that the onset temperature for phase separation is shifted to higher temperatures when reducing the nitrogen content in c-$(Ti_{1-x}Al_x)N_y$ coatings, with x = 0.48–0.60. This trend is consistent with a reduction in mixing enthalpy when decreasing the nitrogen content, as predicted by Alling et al. [10]. Furthermore,
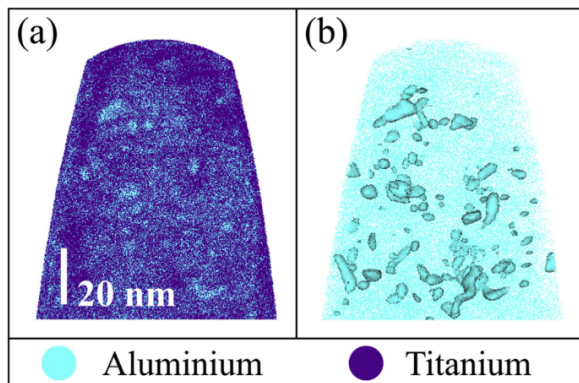
Fig. 11. 3D APT reconstructed tip of $(Ti_{0.74}Al_{0.26})N_{0.82}$ annealed at 1200 °C. (a) Only Al and Ti ions shown. (b) Al rich segregations are highlighted using Al isoconcentration surfaces at 36 at.% and Al ions.
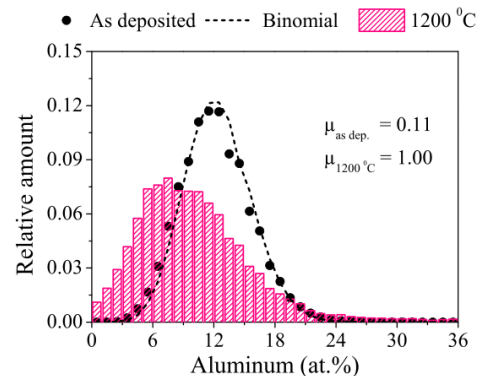
Fig. 12. Aluminum volume composition histogram of as-deposited and 1200 °C annealed $(Ti_{0.74}Al_{0.26})N_{0.82}$. Calculated random distribution (binomial) is shown for comparison.

first principle calculations performed by Shulumba et al. [34] showed a strong impact of anharmonic contributions (phonons) to the mixing energy. Phonons are related to the bonding nature of the crystal. Since N_V induced changes toward a metallic character, it is expected to affect the phonon dispersion and thus the mixing energy.

Competing mechanisms of phase separation was predicted by Cahn when approaching the spinodal [35], where a metastable state of the spinodal decomposition is reached and instead nucleation and growth take over. The steady state of compositional fluctuations observed by increasing the temperature from 1200 to 1400 °C in $(Ti_{0.52}Al_{0.48})N_{0.87}$ and $(Ti_{0.52}Al_{0.48})N_{0.75}$, and the co-occurring process of *w*-AlN nucleation inside the grains for sample y = 0.75 indicate that both alloys are above or very close to the spinodal [36]. At lower temperatures they are inside the spinodal. When the metal composition is shifted further away from the maximum of the miscibility gap and the N_V concentration is increased as for $(Ti_{0.74}Al_{0.26})N_{0.82}$ direct formation via nucleation and growth of Al-Ti precipitates takes place at elevated temperatures. This alloy composition is likely outside the spinodal even at lower temperatures.

In addition to the phase separation inside the grains, the higher temperature activates diffusion along grain and column boundaries, resulting in precipitation of *w*-AlN and *c*-TiN in these regions, consistent with the observations of Rachbauer et al. [37]. Moreover, Forsén et al. [38] showed that by adding Ti to CrAlN, a reduction of the driving force for phase separation in the interior of the grains promotes phase separation to occur in the grain boundaries. In our case, phase separation inside the grains is suppressed by reducing the nitrogen content. Instead *w*-AlN formation occurs at the grain boundaries. This yields a drop of the maximum heat flow temperature during *w*-AlN formation for sample y = 0.75.

Nitrogen demixing occurred regardless of the global nitrogen content during coarsening of Al rich and Ti rich domains. First, there is a preference of N toward Ti rich domains when the metal segregation is small. This is followed by N returning to Al rich domains once the domains are more pure or once formation of *w*-AlN has taken place. Similar behavior has previously been reported for overstoichiometric $(Ti_{0.46}Al_{0.54})N_{1.02}$ alloy where the authors noted segregation on both metal and nitrogen sublattices [39]. We propose non straight pathway of nitrogen partitioning to reach the equilibrium state: stoichiometric AlN and nitrogen vacancies located in the Ti rich domains [10]. It is caused by a higher diffusivity of N compared to Al and Ti in this material system [40], which is further enhanced by increasing the nitrogen vacancies. Non straight diffusion paths have been reported for other multicomponent materials systems with dissimilar diffusivities. For example, weld diffusion studies on ternary Fe-Si-C systems show strong differences in diffusivities between carbon and silicon leading to a complex path for carbon homogenization [41].

Nitrogen vacancies have been shown to impact the phase transformation of $(Ti_{1-x}Al_x)N_y$ even though the segregation occurs on the metal sublattice. Controlling the N_V concentration is a powerful tool to tune the thermal stability, as well as a mean to suppress the detrimental *w*-AlN formation, and should be considered when designing new alloys within this class of materials.

5. Conclusions

Solid solution $c\text{-}(Ti_{1-x}Al_x)N_y$ (x = 0.26, 0.48, and 0.60 and 0.93 > y > 0.75) single phase alloys with NaCl structure were grown by reactive cathodic arc deposition. The nitrogen deficiency was mainly accommodated as nitrogen vacancies. The vacancies did not alter the as deposited hardness or the columnar growth of the coatings. However, a lower nitrogen partial pressure during growth

resulted in a higher count of macroparticles in the coating.

Phase separation via spinodal decomposition occurred in most of the compositions investigated when the temperature was increased. A higher amount of nitrogen vacancies resulted in a shift of the onset of spinodal decomposition to higher temperatures. In addition, a metastable state of the phase separation was observed for alloys y = 0.87 and 0.75 where the decomposed microstructure did not coarsen further when the temperature was increased from 1200 °C to 1400 °C. We suggest that the mixing energy is reduced by the presence of nitrogen vacancies; primarily through a reduction of the mixing enthalpy and an alteration of the phonon dispersion causing increased entropy. Collectively this reduces the miscibility gap and brings the spinodal line to lower temperatures. As a consequence, the formation of *w*-AlN is shifted to higher temperatures, and this is beneficial for the high temperature mechanical properties of these alloys. An additional effect of the suppressed spinodal decomposition is that direct precipitation of *w*-AlN at grain boundaries and even inside the grains becomes favorable at high temperatures and high vacancy concentrations.

References

[1] H.A. Jehn, S. Hofmann, V.-E. Rückborn, W.-D. Münz, Morphology and properties of sputtered (Ti,Al)N layers on high speed steel substrates as a function of deposition temperature and sputtering atmosphere, J. Vac. Sci. Technol. A 4 (1986) 2701, http://dx.doi.org/10.1116/1.573709.
[2] L. Hultman, Thermal stability of nitride thin films, Vacuum 57 (2000) 1—30.
[3] A. Hörling, L. Hultman, M. Oden, J. Sjölen, L. Karlsson, Thermal stability of arc evaporated high aluminum-content Ti1−xAlxN thin films, J. Vac. Sci. Technol. A 20 (2002) 1815, http://dx.doi.org/10.1116/1.1503784.
[4] P.H. Mayrhofer, A. Hörling, L. Karlsson, J. Sjölén, T. Larsson, C. Mitterer, et al., Self-organized nanostructures in the Ti-Al-N system, Appl. Phys. Lett. 83 (2003) 2049—2051, http://dx.doi.org/10.1063/1.1608464.
[5] F. Tasnadi, I.A. Abrikosov, L. Rogström, J. Almer, M.P. Johansson, M. Oden, Significant elastic anisotropy in Ti1−xAlxN alloys, Appl. Phys. Lett. 97 (2010) 231902, http://dx.doi.org/10.1063/1.3524502.
[7] N. Norrby, L. Rogström, M.P. Johansson-Jöesaar, N. Schell, M. Odén, In situ X-ray scattering study of the cubic to hexagonal transformation of AlN in Ti1−xAlxN, Acta Mater. 73 (2014) 205—214, http://dx.doi.org/10.1016/j.actamat.2014.04.014.
[8] H. Lind, R. Forsén, B. Alling, N. Ghafoor, F. Tasnádi, M.P. Johansson, et al., Improving thermal stability of hard coating films via a concept of multicomponent alloying, Appl. Phys. Lett. 99 (2011) 091903, http://dx.doi.org/10.1063/1.3631672.
[9] N. Norrby, H. Lind, G. Parakhonskiy, M.P. Johansson, F. Tasnádi, L.S. Dubrovinsky, et al., High pressure and high temperature stabilization of cubic AlN in Ti0.60Al0.40N, J. Appl. Phys. 113 (2013) 053515, http://dx.doi.org/10.1063/1.4790800.
[10] B. Alling, A. Karimi, L. Hultman, I.A. Abrikosov, First-principles study of the effect of nitrogen vacancies on the decomposition pattern in cubic Ti1−xAlxN1−y, Appl. Phys. Lett. 92 (2008) 071903, http://dx.doi.org/10.1063/1.2838747.
[11] S.-H. Jhi, S.G. Louie, M.L. Cohen, J. Ihm, Vacancy hardening and softening in transition metal carbides and nitrides, Phys. Rev. Lett. 86 (2001) 3348—3351, http://dx.doi.org/10.1103/PhysRevLett.86.3348.
[12] C.-S. Shin, D. Gall, N. Hellgren, J. Patscheider, I. Petrov, J.E. Greene, Vacancy hardening in single-crystal TiNx (001) layers, J. Appl. Phys. 93 (2003) 6025—6028, http://dx.doi.org/10.1063/1.1568521.
[13] N.J. Ashley, R.W. Grimes, K.J. McClellan, Accommodation of non-stoichiometry in TiN1−x and ZrN1−x, J. Mater. Sci. 42 (2007) 1884—1889, http://dx.doi.org/10.1007/s10853-006-1321-z.

[14] B.-Y. Shew, J.-L. Huang, The effects of nitrogen flow on reactively sputtered Ti-Al-N films, Surf. Coat. Technol. 71 (1995) 30–36.

[15] M. to Baben, L. Raumann, D. Music, J.M. Schneider, Origin of the nitrogen over- and understoichiometry in Ti0.5Al0.5N thin films, J. Phys. Condens. Matter. 24 (2012) 155401, http://dx.doi.org/10.1088/0953-8984/24/15/155401.

[16] L. Tsetseris, N. Kalfagiannis, S. Logothetidis, S.T. Pantelides, Role of N Defects on thermally induced atomic-scale structural changes in transition-metal nitrides, Phys. Rev. Lett. 99 (2007) 125503, http://dx.doi.org/10.1103/PhysRevLett.99.125503.

[17] J.P. Schaffer, A.J. Perry, J. Brunner, Defects in hard coatings studied by positron annihilation spectroscopy and x-ray diffraction, J. Vac. Sci. Technol. A 10 (1992) 193–207, http://dx.doi.org/10.1116/1.578136.

[18] J. Bujak, J. Walkowicz, J. Kusiński, Influence of the nitrogen pressure on the structure and properties of (Ti,Al)N coatings deposited by cathodic vacuum arc PVD process, Surf. Coat. Technol. 180–181 (2004) 150–157, http://dx.doi.org/10.1016/j.surfcoat.2003.10.058.

[19] R. Forsén, M. Johansson, M. Odén, N. Ghafoor, Decomposition and phase transformation in TiCrAlN thin coatings, J. Vac. Sci. Technol. A 30 (2012) 061506, http://dx.doi.org/10.1116/1.4757953.

[20] K. Thompson, D. Lawrence, D.J. Larson, J.D. Olson, T.F. Kelly, B. Gorman, In situ site-specific specimen preparation for atom probe tomography, Ultra-microscopy 107 (2007) 131–139, http://dx.doi.org/10.1016/j.ultramic.2006.06.008.

[21] D.R. Kingham, The post-ionization of field evaporated ions: a theoretical explanation of multiple charge states, Surf. Sci. Lett. 116 (1982) A157.

[22] W.C. Oliver, G.M. Pharr, An improved technique for determining hardness and elastic modulus using load and displacement sensing indentation experiments, J. Mater. Res. 7 (1992) 1564–1583.

[23] A.O. Eriksson, J.Q. Zhu, N. Ghafoor, M.P. Johansson, J. Sjölen, J. Jensen, et al., Layer formation by resputtering in Ti–Si–C hard coatings during large scale cathodic arc deposition, Surf. Coat. Technol. 205 (2011) 3923–3930, http://dx.doi.org/10.1016/j.surfcoat.2011.02.007.

[24] M. Thuvander, J.J. Weidow, J. Angseryd, L.K.L. Falk, F. Liu, M. Sonestedt, et al., Quantitative atom probe analysis of carbides, Ultramicroscopy 111 (2011) 604–608, http://dx.doi.org/10.1016/j.ultramic.2010.12.024.

[25] J.B. Nelson, D.P. Riley, An experimental investigation of extrapolation methods in the derivation of accurate unit-Cell dimensions of crystals, Proc. Phys. Soc. 57 (1945) 160–177.

[26] L. Rogström, J. Ullbrand, J. Almer, L. Hultman, B. Jansson, M. Odén, Strain evolution during spinodal decomposition of TiAlN thin films, Thin Solid Films 520 (2012) 5542–5549, http://dx.doi.org/10.1016/j.tsf.2012.04.059.

[27] B. Alling, A.V. Ruban, A. Karimi, O.E. Peil, S.I. Simak, L. Hultman, et al., Mixing and decomposition thermodynamics of c-Ti1−xAlxN from first-principles

calculations, Phys. Rev. B 75 (2007) 045123, http://dx.doi.org/10.1103/PhysRevB.75.045123.

[28] K. Grönhagen, J. Ågren, M. Odén, Phase-field modelling of spinodal decomposition in TiAlN including the effect of metal vacancies, Scr. Mater. 95 (2015) 42–45, http://dx.doi.org/10.1016/j.scriptamat.2014.09.027.

[29] A. Knutsson, I.C. Schramm, K. Asp Grönhagen, F. Mücklich, M. Odén, Surface directed spinodal decomposition at TiAlN/TiN interfaces, J. Appl. Phys. 113 (2013) 114305, http://dx.doi.org/10.1063/1.4795155.

[30] B. Gault, M.P. Moody, J.M. Cairney, S.P. Ringer, Atom Probe Microscopy, first ed., Springer New York, 2012 http://dx.doi.org/10.1007/978-1-4614-3436-8.

[31] A. Knutsson, J. Ullbrand, L. Rogström, N. Norrby, L.J.S. Johnson, L. Hultman, et al., Microstructure evolution during the isostructural decomposition of TiAlN—a combined in-situ small angle x-ray scattering and phase field study, J. Appl. Phys. 113 (2013) 213518, http://dx.doi.org/10.1063/1.4809573.

[32] L.J.S. Johnson, M. Thuvander, K. Stiller, M. Odén, L. Hultman, Spinodal decomposition of Ti0.33Al0.67N thin films studied by atom probe tomography, Thin Solid Films 520 (2012) 4362–4368, http://dx.doi.org/10.1016/j.tsf.2012.02.085.

[33] J. Brunner, A.J. Perry, Lattice vacancies in TiN and HfN films: a study by positron annihilation, Thin Solid Films 153 (1987) 103–113.

[34] N. Shulumba, Vibrations in Solids: from First Principles Lattice Dynamics to High Temperature Phase Stability, Linköping University Electronic Press, Linköping, 2015, http://dx.doi.org/10.3384/diss.diva-122949.

[35] J.W. Cahn, On spinodal decomposition, Acta Metall. 9 (1961) 795–801, http://dx.doi.org/10.1016/0001-6160(61)90182-1.

[36] J.E. Morral, J.W. Cahn, Spinodal decomposition in ternary systems, Acta Metall. 19 (1971) 1037–1045.

[37] R. Rachbauer, S. Massl, E. Stergar, D. Holec, D. Kiener, J. Keckes, et al., Decomposition pathways in age hardening of Ti-Al-N films, J. Appl. Phys. 110 (2011) 023515, http://dx.doi.org/10.1063/1.3610451.

[38] R. Forsén, M.P. Johansson, M. Odén, N. Ghafoor, Effects of Ti alloying of AlCrN coatings on thermal stability and oxidation resistance, Thin Solid Films 534 (2013) 394–402, http://dx.doi.org/10.1016/j.tsf.2013.03.003.

[39] R. Rachbauer, S. Massl, E. Stergar, P. Felfer, P.H. Mayrhofer, Atom probe specimen preparation and 3D interfacial study of Ti-Al-N thin films, Surf. Coat. Technol. 204 (2010) 1811–1816, http://dx.doi.org/10.1016/j.surfcoat.2009.11.020.

[40] H. Matzke, Diffusion in carbides and nitrides: unsolved problems, Defect Diffus. Forum 83 (1992) 111–130, http://dx.doi.org/10.4028/www.scientific.net/DDF.83.111.

[41] L.S. Darken, Diffusion of carbon in austenite with a discontinuity in composition, Trans. Am. Inst. Min. Eng. 180 (1948) 430–438.
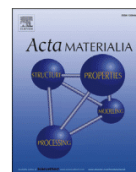
Paper II

Solid state formation of Ti_4AlN_3 in cathodic arc evaporated $(Ti_{1-x}Al_x)N_y$ alloys

I.C. Schramm, C. Pauly, M.P. Johansson Jõesaar, P. Eklund,

J. Schmauch, F. Mücklich and M. Odén

Full length article

Solid state formation of Ti_4AlN_3 in cathodic arc deposited $(Ti_{1-x}Al_x)N_y$ alloys

I.C. Schramm [a, b, *], C. Pauly [b], M.P. Johansson Jõesaar [a, c], P. Eklund [d], J. Schmauch [e], F. Mücklich [b], M. Odén [a]

[a] Nanostructured Materials, Department of Physics, Chemistry, and Biology, Linköping University, Linköping, Sweden
[b] Chair of Functional Materials, Department of Material Science, Saarland University, Saarbrücken, Germany
[c] SECO Tools AB, Fagersta, Sweden
[d] Thin Film Physics Division, Department of Physics, Chemistry, and Biology, Linköping University, Linköping, Sweden
[e] Experimental Physic, Department of Physics, Saarland University, Saarbrücken, Germany

ABSTRACT

Reactive cathodic arc deposition was used to grow substoichiometric solid solution cubic c-$(Ti_{1-x}Al_x)N_y$ thin films. The films were removed from the substrate and then heated in an argon environment to 1400 °C. Via solid state reactions, formation of MAX phase Ti_4AlN_3 was obtained. Additional phases such as Ti_2AlN, c-TiN, w-AlN, Al_5Ti_2 and Al_3Ti were also present during the solid state reaction. Ti_4AlN_3 formation was observed in samples with an Al metal fraction x < 0.63 and a nitrogen content 0.4 < y < 0.6. Regardless of the initial composition, formation of Ti_4AlN_3 started in Ti_2AlN crystal plates in the temperature range between 1200 and 1400 °C. Accompanying the onset of Ti_4AlN_3 was the presence of an intermediate structure identified as $Ti_6Al_2N_4$, consisting of alternating layers of intergrown Ti_2AlN and Ti_4AlN_3 phases with a half-unit-cell stacking. We suggest that the formation of Ti_4AlN_3 occurred via intercalation of aluminum and nitrogen along the basal plane accompanied by a simultaneous detwinning process. In addition we propose that this formation mechanism can be used to obtain MAX phases of high n order.

© 2017 Acta Materialia Inc. Published by Elsevier Ltd. All rights reserved.

1. Introduction

$M_{n+1}AX_n$ phases ("MAX" phases, $n = 1-3$) are nanolaminated hexagonal materials composed of a transition metal M-element (Ti, Zr, V, …), an A-element (Al, Si, Ge, …), and C or N (or both) as X-element [1]. The structure consists of M_6X octahedral layers separated by A-element layers. Depending on the number (n) of M layers separated by A layers the nomenclature will be M_2AX ($n = 1$), M_3AX_2 ($n = 2$) or M_4AX_3 ($n = 3$). Due to their layered structure, MAX phases present a rather complex interatomic bonding, where the M-A bonds are weaker than the M-X bonds. This results in materials with a combination of metal and ceramic properties which are elastically stiff, oxidation and thermal shock resistant, machinable, thermally and electrically conductive, etc. [1,2]. MAX phase materials are valuable in the shape of thin films for technical applications including electrical contacts, protective coatings, and low friction surfaces, among others. The technologies used to make thin film MAX phases can be divided in three main groups: physical vapor deposition, chemical vapor deposition, and solid state reaction synthesis [3,4]. Solid state reactions are further divided in two subgroups: one based on reactions between substrate and thin film, and the other on reactions of the coating. The most important example of the first subgroup is Ti_3SiC_2 formation as ohmic contacts on SiC [5–7]. The second type involves deposition of a M-A-X film of appropriate composition in a metastable state, amorphous [8–10] or multilayer [11–15], followed by annealing to form the MAX phase.

Two MAX phases have been reported experimentally in the Ti-Al-N system, Ti_2AlN and Ti_4AlN_3. The hypothetical Ti_3AlN_2 phase predicted to be metastable by DFT calculations performed by Holm et al. [16] has not been synthesized and is unlikely to exist [3,11]. Only Ti_2AlN has been obtained as a thin film via solid state reactions [11,12,17] and reactive sputter deposition [18–21]. Even though Ti_4AlN_3 was synthesized and characterized in the late 90's [22,23], it

has not been obtained as a thin film.

We report a method for obtaining Ti_4AlN_3 via solid state reactions of a nitrogen deficient monolithic *cubic* solid solution *c*-$(Ti_{1-x}Al_x)N_y$ thin film synthesized by cathodic arc deposition in an industrial system. We show that it is possible to form Ti_4AlN_3 for a large range of aluminum to titanium ratio and nitrogen compositions, and that the amount of Ti_4AlN_3 formed can be tuned. Formation of Ti_2AlN is required in order to achieve Ti_4AlN_3 since Ti_2AlN acts as a template above 1200 °C. Finally, our results suggest a route for formation of high *n* order MAX phases.

2. Experimental details

An industrial scale PVD cathodic arc deposition system, MZR-323 by Metaplas, Germany (now Oerlikon Metaplas GmbH), was used to grow nitrogen deficient $(Ti_{1-x}Al_x)N_y$ coatings. The nitrogen content of the coating was controlled by varying the N_2 ratio of an Ar/N_2 gas mixture between 25 and 33% during growth. The total gas pressure was fixed at 2 Pa, and a dc bias of - 30 V was used. Three circular cathodes of $Ti_{1-x}Al_x$ (x = 0, 0.55 and 0.67) with a diameter of 100 cm were mounted facing a rotating cylinder. The thin films were grown on Fe foils to a thickness of about 3 μm at a rate of 0.1 μm per minute and a temperature of ~450 °C.

Mechanical grinding of the coated Fe foils was followed by dissolution of remaining iron in concentrated HCl solution to obtain flake-like particles of the coating material. The coating flakes were recovered, cleaned with distilled water and acetone, and finally ground in a ceramic mortar. The powder preserved a flake-like shape, its crystal structure and composition were not affected by this process [24].

Powder annealing treatments under argon atmosphere were performed in a differential scanning calorimeter, STA 449C by Netsch, Germany. The annealing temperatures used were from 1000 to 1400 °C, with no isothermals and always using as-prepared powder for each temperature. Powder placed in an alumina crucible was heated at a rate of 20 K per min under an argon flow of 50 ml/min. Out gassing for 1 h at 250 °C was always performed just prior to the heating.

Powder X-ray diffractometry (XRD) was performed in an Empyrean diffractometer (PANalytical, The Netherlands) using Cu-K_α radiation in focusing Bragg-Brentano configuration with low background optics. Diffractograms were recorded at room temperature and a silicon zero diffraction plate was used to hold the powder.

Scanning electron and focused ion beam microscopy (SEM/FIB) (Helios NanoLab 600, FEI, United States) was used for scanning transmission imaging (in SEM), fabrication of site specific thin lamellas for transmission electron microscopy (TEM) and atom probe tomography (APT) tips. A standard lift out technique was used for the APT tips [25], and no deviation in the procedure was necessary because of the flake-like shape of the powder particles. STEM-in-SEM imaging in this instrument was performed at 30 kV.

3D chemical composition was obtained by local electrode atom probe tomography (LEAP 3000 X HR, Cameca, France) in laser mode. The laser was set to a frequency of 200 kHz and a pulse energy of 0.5 nJ. Measurements were carried out at a cryogenic temperature of 60 K and an evaporation rate of 5 ions per 1000 laser pulses. Data analysis was performed with the software package IVAS (version 3.6.14, Cameca). Reconstruction parameters were obtained individually for each tip by using Kingham curves [26] and post measurement SEM images. The evaporation field obtained was 40 V per nm and the image compression factor ranged from 3.4 to 4.0.

Transmission electron microscopy (TEM) and scanning TEM (STEM) were used to characterize the microstructure of the annealed powder in more detail. TEM analysis was performed using a JEM 2010 model of JEOL (Japan) at an acceleration voltage of 200 kV. TEM/STEM analysis was carried out using a cold field emission gun JEOL JEM-ARM 200F at 200 kV equipped with a STEM Cs corrector (CESCOR, CEOS GmbH, Germany). For STEM, the high angle annular dark-field (HAADF) detector was used. TEM thin lamellae were produced using the SEM/FIB and further thinning was performed with an Ar Ion gun (Nanomill Mod. 1040, Fischione, United States) at a beam current of 125 pA for 20 min at a tilt angle of ±10°.

3. Results

3.1. As-deposited state

Ternary composition map of the investigated $(Ti_{1-x}Al_x)N_y$ coatings is shown in Fig. 1. Samples are represented by dots and labeled A to F. For reference, the compositions corresponding to the MAX phases Ti_2AlN and Ti_4AlN_3, and horizontal lines representing fixed nitrogen/metal ratios are included. The notation $(Ti_{x-1}Al_x)N_y$ is obtained with x = Al/(Ti + Al) and y = N/(Ti + Al) where Ti, Al, and N are the elemental concentrations. The alloy compositions were measured by atom probe tomography. In addition to the main elements, small amounts of impurities are also present in the analysis, i.e. oxygen, carbon, argon, and gallium originating from the background pressure of the industrial deposition system and the FIB sample preparation [25]. The total impurities concentration is less than 1.0 at. %.

Chemical distribution of the main elements, Ti, Al and N, in as-deposited samples and their deviation from a random distribution were obtained using frequency distribution analysis and by calculating the Pearson coefficient (μ) [27], as shown in Table 1. The Pearson coefficient addresses qualitatively the composition deviation, where a value of 0 indicates a completely random distribution and 1 indicates complete segregation. For comparison, two samples grown under similar conditions from a previous publication [28], containing a higher nitrogen content and same metal fraction as sample C, are included and labeled with a star. Metal and nitrogen segregation were observed for all as-deposited samples, being more pronounced for samples with low nitrogen content. A
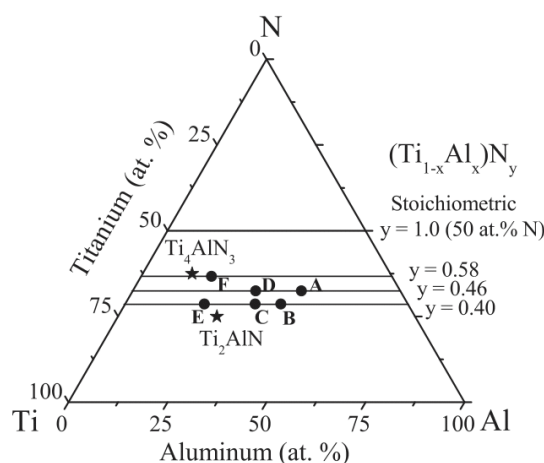

Fig. 1. Ternary composition map showing with dots the total alloy composition and their labeling from A to F. The position for the Ti_2AlN and Ti_4AlN_3 MAX phases are marked with stars. Horizontal lines represent fixed nitrogen contents given in the notation $(Ti_{1-x}Al_x)N_y$.

Table 1

Pearson coefficient of aluminum, titanium and nitrogen for as-deposited sample A, C and F. *Data from samples grown under similar conditions taken from Schramm et al. [28] for comparison. Value of 0 indicates random distribution and 1 complete segregation of the element.

Sample	Label	Pearson coefficient (μ)		
		Aluminum	Titanium	Nitrogen
$(Ti_{0.72}Al_{0.28})N_{0.58}$	F	0.98	0.18	0.89
$(Ti_{0.52}Al_{0.48})N_{0.92}$	*	0.22	0.09	0.06
$(Ti_{0.52}Al_{0.48})N_{0.75}$	*	0.26	0.11	0.26
$(Ti_{0.52}Al_{0.48})N_{0.40}$	C	0.99	0.27	0.88
$(Ti_{0.37}Al_{0.63})N_{0.46}$	A	0.99	0.34	0.97

stronger aluminum segregation is apparent, while Ti retains a close to random distribution with more titanium present in the global composition, i.e. sample F. These results are consistent with the c-$(Ti_{1-x}Al_x)N_y$ x-ray peak broadening seen in Fig. 2.

The x-ray diffractograms of nitrogen deficient flake-like powder $(Ti_{1-x}Al_x)N_y$ samples in their as-deposited state are shown in Fig. 2. Results indicate that all samples are solid solutions with a cubic B1 crystal structure c-$(Ti_{1-x}Al_x)N_y$, similar to what has been seen for coatings with higher N content [28,29]. No MAX phase peaks were detected in the low 2θ range between 5 and 30° (not shown). Increasing Ti content (reduction in x) corresponds to an increase of the lattice parameter, which shifts the c-$(Ti_{1-x}Al_x)N_y$ peaks to lower diffraction angles and consistent with previous results for y = 1 [30]. In samples A and B, x > 0.48, additional wurtzite w-AlN and cubic c-TiN diffraction peaks are present. w-AlN peaks are broad and shifted to lower angles since w-AlN also contains titanium. In addition, the 111 and 200 diffraction peaks for c-$(Ti_{1-x}Al_x)N_y$ display different intensity ratios depending on the N content. The 111 peak increases in intensity when the nitrogen content is reduced, which is consistent with a change in the structure factor caused by a reduced N lattice site occupancy when nitrogen vacancies are present [28,31]. The structure factor change is observed as a gain in the XRD peak intensity ratio 111 to 200 and the variation of the 111 to 222 ratio. These changes are stronger than what the weak crystallographic texture gives.

3.2. High temperature reactions

In order to trace the phase transformation route, flake-like powder samples were annealed at different temperatures from 1000 to 1400 °C. Fig. 3 shows room temperature x-ray
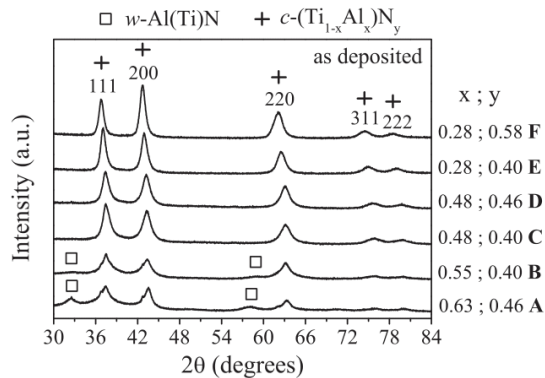
Fig. 2. X-Ray powder diffractograms of as-deposited $(Ti_{1-x}Al_x)N_y$ coatings. The aluminum content ranges from x = 0.28 to 0.63 and nitrogen fraction from y = 0.40 to 0.58. The total 2θ range measured is 5°–85°.
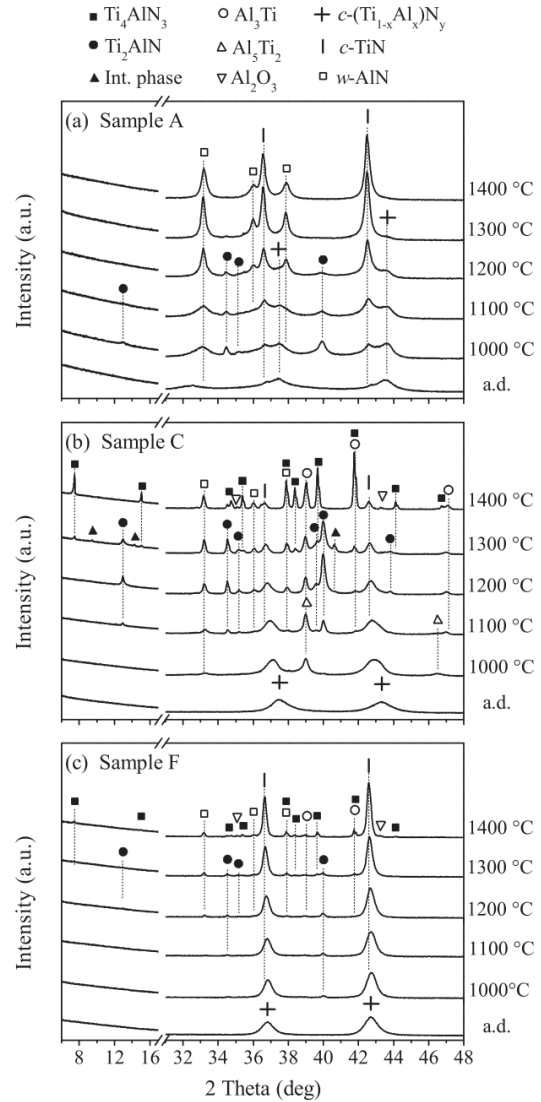
Fig. 3. X-ray powder diffractograms recorded after annealing at 1000 °C−1400 °C for (a) $(Ti_{0.27}Al_{0.63})N_{0.46}$, (b) $(Ti_{0.52}Al_{0.48})N_{0.40}$, and (c) $(Ti_{0.72}Al_{0.28})N_{0.58}$.

diffractograms recorded after annealing and only samples presenting substantial differences are shown.

Sample A, $(Ti_{0.27}Al_{0.63})N_{0.46}$, with a high Al content shows the highest phase fraction of Ti_2AlN at 1000 °C. As-deposited w-Al(Ti)N peaks shift toward w-AlN positions due to the low solubility of Ti atoms, corroborated by the formation of c-TiN simultaneously. When annealed at higher temperatures, the intensity of Ti_2AlN and c-$(Ti_{0.27}Al_{0.63})N_{0.46}$ peaks decrease and completely disappear at 1300 °C. At 1400 °C, only c-TiN and w-AlN peaks are present.

1000 °C XRD results of sample C, $(Ti_{0.52}Al_{0.48})N_{0.40}$, shows formation of intermetallic Al_5Ti_2 and a shift of c-$(Ti_{0.52}Al_{0.48})N_{0.40}$ peaks toward c-TiN position by Al depletion. Further annealing leads to the transformation of Al_5Ti_2 to Al_3Ti, further purification of c-TiN, formation of w-AlN, and a dominant presence of Ti_2AlN. Between 1200 and 1400 °C, Ti_2AlN and Ti_4AlN_3 coexist with the additional presence of a third intermediate phase, accompanied by

a decrease in c-TiN and an increase in Al$_3$Ti peaks. Finally at 1400 °C, Ti$_2$AlN and the intermediate phase are gone, and Ti$_4$AlN$_3$ is the dominant phase. Secondary phases, Al$_3$Ti, c-TiN, w-AlN, and small amounts of Al$_2$O$_3$, are also present.

Sample F, with a low Al content and an alloy composition close to Ti$_4$AlN$_3$, shows Ti$_2$AlN at 1000 °C and a shift of c-(Ti$_{0.72}$Al$_{0.28}$)N$_{0.58}$ peaks towards c-TiN position by Al depletion. Further annealing results in w-AlN and Al$_3$Ti formation. Similar to sample C, Ti$_2$AlN and Ti$_4$AlN$_3$ coexist between 1200 and 1400 °C. However, in this case only small quantities are observed. At 1400 °C, c-TiN is the majority phase coexisting with small additions of Ti$_4$AlN$_3$, Al$_3$Ti, and w-AlN.

A similar phase transformation path is seen in all samples (Table 2) except for sample A, in which no Ti$_4$AlN$_3$ and Al$_3$Ti phases were detected. Formation of c-TiN, w-AlN, Al$_3$Ti, and Ti$_2$AlN always occurred below 1200 °C and Al$_5$Ti$_2$ appeared as precursor for Al$_3$Ti. The formation temperature of Ti$_2$AlN depends on the initial composition of the alloy (Ti$_{1-x}$Al$_x$)N$_y$ but is below 1000 °C for all samples in this study. The end amount of c-TiN and w-AlN is affected by the initial metallic ratio of the coating, x, where more Al results in larger amounts of w-AlN, while Al$_3$Ti and Ti$_2$AlN become more dominant when reducing the nitrogen content. Coexistence of Ti$_2$AlN and Ti$_4$AlN$_3$ occurred in a temperature range between 1200 and 1400 °C, for alloy composition x < 0.63, with a strong correlation between the amount of Ti$_2$AlN at 1200 °C and the amount of Ti$_4$AlN$_3$ at 1400 °C. Additionally, an intermediate phase appeared in the same temperature range, which was only resolved when the MAX phase fraction was high.

3.3. Transformation of Ti$_2$AlN to Ti$_4$AlN$_3$

To elucidate the origin of the coexistence of Ti$_2$AlN and Ti$_4$AlN$_3$ local studies of the microstructure and chemical composition were conducted by STEM-in-SEM, TEM, and APT. This was done on sample C, which presented the largest amount of MAX phases in this temperature range.

Bright field STEM-in-SEM micrographs of sample C, annealed at 1200, 1300, and 1400 °C are shown in Fig. 4. MAX phase plates are seen in all samples. The plates are oriented arbitrarily with respect to the growth direction of the coatings and surrounded by secondary phases: w-AlN, Al$_3$Ti, and c-TiN. The MAX plates display a layered contrast, which is less pronounced when the annealing temperature is increased. At 1400 °C, TEM and SAED (Fig. 5) reveal well-defined micrometer-sized Ti$_4$AlN$_3$ single crystal plates.

The layer contrast in the MAX plates was investigated further by APT and shown in Fig. 6. In the left column in Fig. 6 (a–c), slices (10 nm thick) of the reconstructed APT tips are shown. For clarity, only aluminum and nitrogen ions are presented. Arrows drawn inside the tips indicate the location and direction of 1D composition profiles presented in the right column, Fig. 6 (d–f). Based on the

composition, the different regions in the 1D profiles were labeled with the corresponding phases. As a reference, the nominal stoichiometric composition of the MAX phases of interest are listed in Table 3.

Annealing sample C at 1200 and 1300 °C (Fig. 6) results in layers in the MAX plate that corresponds to chemical fluctuations of Al and N, while Ti presents a nearly constant concentration around 52 at. %. Based on the Al to N ratio, three main compositions are identified: Ti$_2$AlN, Ti$_4$AlN$_3$, and an intermediate phase. Ti to Al ratio for Ti$_2$AlN and Ti$_4$AlN$_3$ showed stoichiometric values of 2.00 ± 0.03 and 4.00 ± 0.02, respectively, while a nitrogen deficiency was observed which decreased with annealing temperature from δ = 0.20 to 0.04 for Ti$_2$AlN$_{1-\delta}$ and from δ = 0.35 to 0.22 for Ti$_4$AlN$_{3-\delta}$. Substoichiometry is expected and can be accommodated in MAX phases [3,32,33]. The intermediate phase displays a composition of Al and N between Ti$_2$AlN and Ti$_4$AlN$_3$ and it is similar in composition to the MAX phase Ti$_3$AlN$_2$. Moreover at 1400 °C, the internal layering has almost disappeared and only Ti$_4$AlN$_3$ is left with some slight compositional variation corresponding to reminiscence of the layers.

3.4. Identification of intergrown structure Ti$_6$Al$_2$N$_4$

The intermediate phase observed in Figs. 3 and 6 is an intergrown structure of the two MAX phases Ti$_2$AlN and Ti$_4$AlN$_3$. High resolution STEM and more detailed XRD of sample C after annealing at 1300 °C are shown in Fig. 7. The recorded low angle x-ray diffraction peaks are listed in Table 4. Fig. 7 (b) shows a high resolution z-contrast micrograph of a MAX phase plate. A varying basal plane stacking sequence is observed. The bright layers display titanium atom columns and the dark layers aluminum.

The X-ray peaks in Fig. 7 (a) are inconsistent with the hypothetical metastable Ti$_3$AlN$_2$ MAX phase [16], since we observe peaks at 2θ = 4.62 and 14.22°, which would correspond to the forbidden 0001 and 0003 peaks of any M$_3$AX$_2$ structure. Instead, these peaks originate from an intergrown structure, Ti$_6$Al$_2$N$_4$, which has the same chemical composition as Ti$_3$AlN$_2$ but a different crystal structure. The unit cell of Ti$_6$Al$_2$N$_4$ can be described as a half unit cell of Ti$_2$AlN and a half unit cell of Ti$_4$AlN$_3$ repeated three times, and c lattice parameter of 56.2 Å which is the sum of the c lattice parameters of Ti$_2$AlN and Ti$_4$AlN$_3$, multiplied by 1.5. Even though the symmetry of the P6$_3$/mmc space group to which regular MAX phases belong is broken, the intergrown structure belongs to the MAX phase family because of its hexagonal lattice and layered structure [34].

Fig. 7(b) shows different stacking sequences of half unit cell layers of Ti$_4$AlN$_3$ and Ti$_2$AlN. The different structures have different sequences: the combination of two Ti layers between Al layers corresponds to Ti$_2$AlN, the sequence of four Ti layers between Al layers corresponds to Ti$_4$AlN$_3$, and a mix of both corresponds to

Table 2
Phase identification by X-ray diffraction after annealing at different temperatures.

Sample	Phases present at room temperature after annealing (no dwell time)			
	1000 °C	1200 °C	1300 °C	1400 °C
A (Ti$_{0.37}$Al$_{0.63}$)N$_{0.46}$	211; TiAlN; TiN, AlN	211; TiAlN; TiN; AlN	TiAlN; TiN; AlN	TiN; AlN
B (Ti$_{0.45}$Al$_{0.55}$)N$_{0.40}$	211; Al$_5$Ti$_2$; TiAlN; TiN; AlN	211; Al$_3$Ti; TiAlN; TiN; AlN; Al$_2$O$_3$	211; 413; IntP; Al$_3$Ti; TiN; AlN; Al$_2$O$_3$	413; Al$_3$Ti; TiN; AlN; Al$_2$O$_3$
C (Ti$_{0.52}$Al$_{0.48}$)N$_{0.40}$	Al$_5$Ti$_2$; TiAlN; TiN; AlN	211; IntP; Al$_3$Ti; TiN; AlN; Al$_2$O$_3$	211; 413; IntP; Al$_3$Ti; TiN; AlN; Al$_2$O$_3$	413; Al$_3$Ti; TiN; AlN; Al$_2$O$_3$
D (Ti$_{0.52}$Al$_{0.48}$)N$_{0.46}$	211; Al$_5$Ti$_2$; TiAlN; TiN; AlN	211; IntP; Al$_3$Ti; TiN; AlN; Al$_2$O$_3$	211; 413; IntP; Al$_3$Ti; TiN; AlN; Al$_2$O$_3$	413; Al$_3$Ti; TiN; AlN; Al$_2$O$_3$
E (Ti$_{0.72}$Al$_{0.28}$)N$_{0.40}$	211; Al$_5$Ti$_2$; TiAlN; TiN	211; Al$_3$Ti; TiN; AlN	211; 413; IntP; Al$_3$Ti; TiN; AlN	413; Al$_3$Ti; TiN; AlN; Al$_2$O$_3$
F (Ti$_{0.72}$Al$_{0.28}$)N$_{0.58}$	211; TiAlN; TiN	211; Al$_3$Ti; TiN; AlN	211; 413; Al$_3$Ti; TiN; AlN; Al$_2$O$_3$	413; Al$_3$Ti; TiN; AlN; Al$_2$O$_3$

Key: TiAlN − c-(Ti$_{1-x}$Al$_x$)N$_y$; TiN − c-TiN; AlN − w-AlN; 211 − Ti$_2$AlN; 413 − Ti$_4$AlN$_3$; IntP − Intermediate phase.
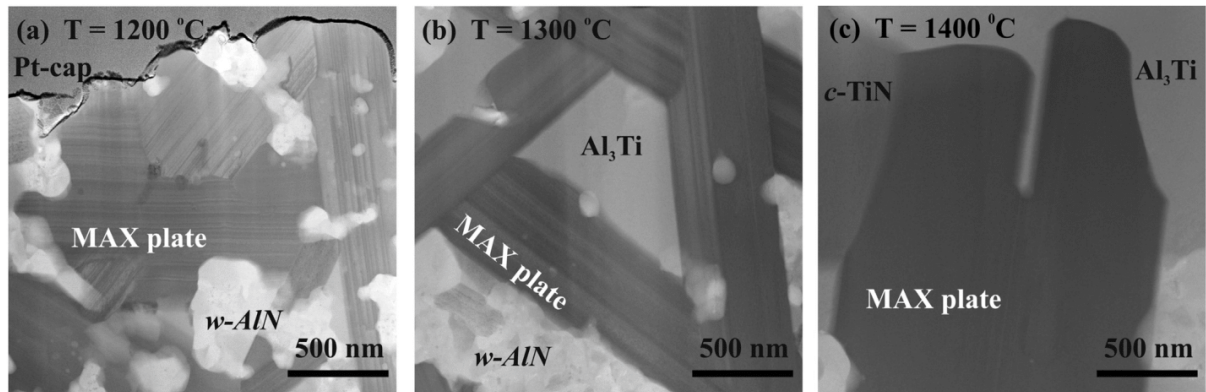
Fig. 4. Bright field STEM-in-SEM micrographs of sample C at different post annealing states: (a) 1200 °C, (b) 1300 °C, and (c) 1400 °C. MAX phase plates and secondary phases are labeled for guidance.
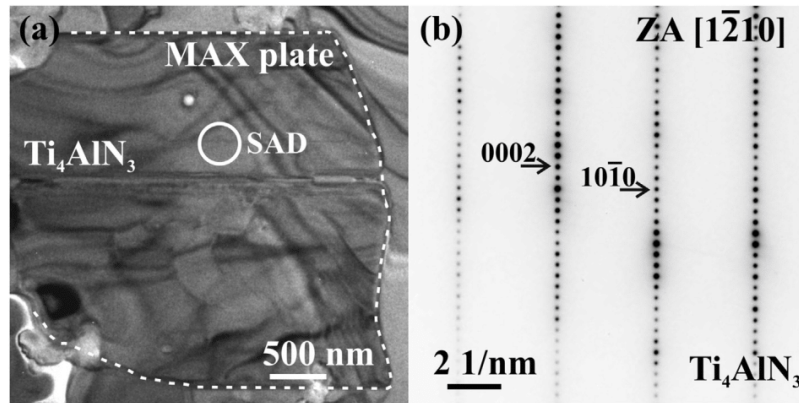
Fig. 5. (a) TEM micrograph of sample C post annealing at 1400 °C. Circumference of the MAX plate is marked by dashed line. (b) Selected area diffraction pattern from a Ti_4AlN_3 crystal.

$Ti_6Al_2N_4$. Three Ti layers between Al layers were not found, which is also consistent with the XRD observations. We also note that when Ti_2AlN, Ti_4AlN_3, and $Ti_6Al_2N_4$ coexist, it occurs within the same grain. Pure crystallites of Ti_4AlN_3 were found only at 1400 °C.

4. Discussion

4.1. As-deposited state

Single-phase c-$(Ti_{1-x}Al_x)N_y$ thin films with B1 structure and composition values y = 0.40 to 0.58 and x < 0.55 were grown by cathodic arc deposition. Alloys with x ≥ 0.55 also contained w-AlN. $(Ti_{1-x}Al_x)N_y$ system is known to accommodate high N deficiencies via formation of nitrogen vacancies in the B1 structure, at least in the range $0.37 \leq y \leq 1.0$ [28,29,35]. The asymmetric miscibility gap of the TiN-AlN pseudo-binary phase diagram with its maximum located at high Al content, x ≈ 0.63, provides a stronger driving force for segregation for the Al rich samples [36,37]. In this case, it is sufficient to cause AlN segregation during growth that results in a two phase microstructure consisting of c-$(Ti_{1-x}Al_x)N_y$ and w-AlN(Ti), i.e. samples A and B in this study. Similarly, there is a driving force for precipitation of metallic Al and Al-Ti mixtures in highly nitrogen deficient c-$(Ti_{1-x}Al_x)N_y$ solid solutions [31], which

is seen to occur in samples B to F at elevated temperatures by the formation of Al_5Ti_2.

4.2. High temperature reactions

A general model of the solid state reaction path is suggested based on the XRD data recorded after annealing between 1000 °C and 1400 °C. The phase evolution with increasing annealing temperature can be summarized as follows:

(1) Solid solution c-$(Ti_{1-x}Al_x)N_y$ becomes Al depleted and formation of the intermetallic Al_5Ti_2 takes place. Similar observations were made by annealing Ti/AlN [11,38,39] and Al/TiN multilayers [40], where the fast diffusion of N compared to Ti and Al and the preferential diffusion of N towards Ti lead to Al_3Ti formation. In this system, an intermediate intermetallic phase, Al_5Ti_2, is formed that transforms to Al_3Ti at higher temperatures.

(2) Al_5Ti_2 transforms to Al_3Ti and the decreasing amount of c-$(Ti_{1-x}Al_x)N_y$ evolves toward c-TiN accompanied by the formation of nitrogen deficient Ti_2AlN and w-AlN. The increase in annealing temperature enhances the species mobility which promotes formation of more complex unit cells like
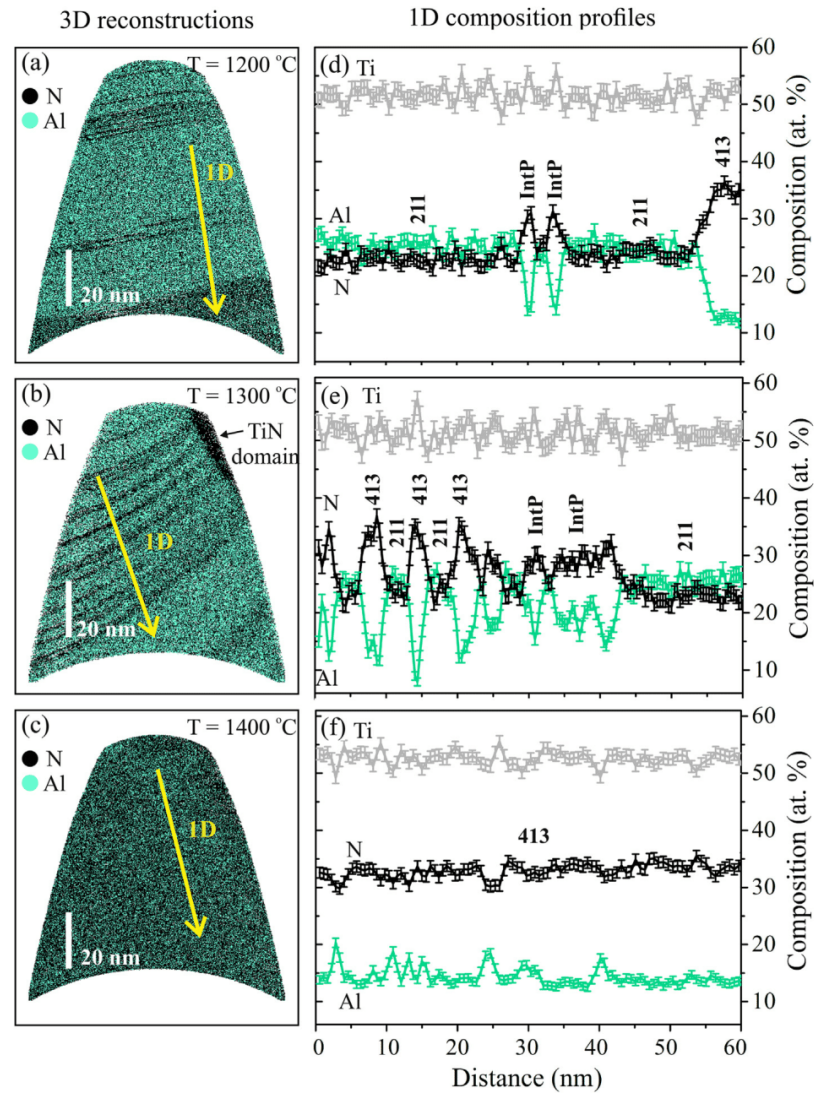
Fig. 6. Left column (a—c): 10 nm thick slices of reconstructed 3D atom probe tips of sample C after annealing at 1200 °C, 1300 °C and 1400 °C, respectively. Only Al and N ions are presented for clarity. Right column (d—f): 1D concentration profiles extracted from the corresponding APT reconstructions, exact location is highlighted with arrows. The different composition regions in the 1D profiles are labeled with the corresponding phases. Line curvature in (b) is a reconstruction artifact. Key: 211 — Ti_2AlN; 413 — Ti_4AlN_3; IntP — Intermediate phase.

Table 3
Nominal stoichiometric composition of the possible MAX phases in the Ti-Al-N system.

MAX phase	Nominal composition		
	Titanium (at. %)	Aluminum (at. %)	Nitrogen (at. %)
Ti_2AlN	50.0	25.0	25.0
Ti_3AlN_2	50.0	16.7	33.3
Ti_4AlN_3	50.0	12.5	37.5

MAX phases [3,41]. Imanaka et al. showed that the activation energy of Ti_2AlN growth is similar to the nitrogen diffusion in Ti [42], which confirms that nitrogen mobility and local chemical concentration control the phase formation [11,12,41—43]. Besides the diffusivity of the species, c-$(Ti_{1-x}Al_x)N_y$ likely acts as a precursor for Ti_2AlN formation [20,41] due to similarities in the shared edges between M_6X octahedral in MAX phases and the ones in the B1 structure of MX binaries [1,44]. w-AlN formation is common as a competing phase in transition metal nitrides containing Al [44].

(3) Ti_2AlN transforms into Ti_4AlN_3, with the presence of $Ti_6Al_2N_4$ during transformation, Al_3Ti fraction increases while c-TiN decreases, and w-AlN remains stable. Diffusion of Al from Ti_2AlN at high temperatures favors Ti_4AlN_3 formation and leads to the appearance of the intergrown structure $Ti_6Al_2N_4$. Annealing temperatures used in this study are above the melting point of Al_3Ti, ~1375 °C [45]. Melting of Al_3Ti
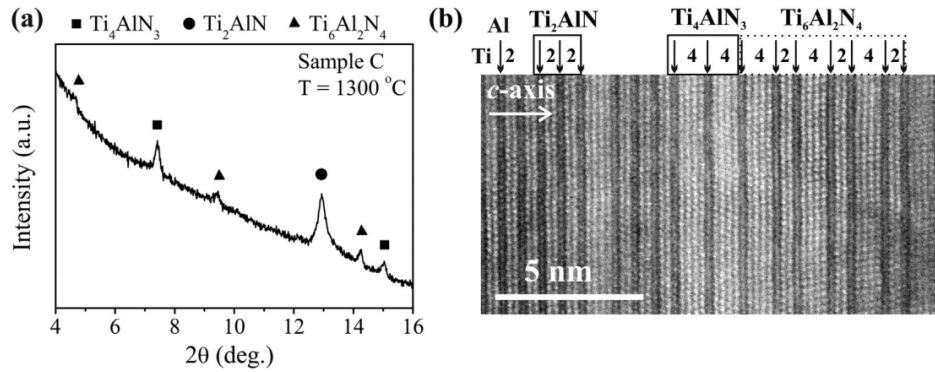
Fig. 7. (a) Low angle x-ray diffractogram of sample C annealed at 1300 °C. (b) High resolution z-contrast STEM image displaying the coexistence of Ti_2AlN, Ti_4AlN_3, and $Ti_6Al_2N_4$ along [1−210] direction. Labels indicate the number of adjacent N-rich basal planes.

Table 4
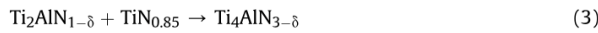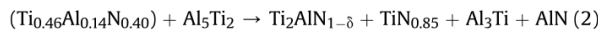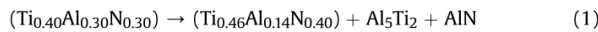X-ray powder diffraction data collected and shown in Fig. 7 (a).

2θ measured	d-spacing (Å)	hkil	Phase
4.630 ± 0.011	19.095	0003	$Ti_6Al_2N_4$
7.417 ± 0.003	11.913	0002	Ti_4AlN_3
9.419 ± 0.010	9.391	0006	$Ti_6Al_2N_4$
12.951 ± 0.002	6.837	0002	Ti_2AlN
14.227 ± 0.009	6.219	0009	$Ti_6Al_2N_4$
15.025 ± 0.011	5.894	0004	Ti_4AlN_3

enhances the diffusion rate of the species similar to what has been observed by Lee et al. in the Ti-Al-N system [46] and by Kisi et al. in the Ti-Al-C system [47]. The result is an accelerated formation of Ti_4AlN_3. Moreover, w-AlN is a stable phase that is not likely to take part in the reaction once formed [44].

As an example, we propose a reaction path for sample C based on X-ray diffractograms and atom probe data. Compositions were taken from APT measurements which cannot be assumed to be representative for the entire sample. Therefore, the reaction path is of qualitative nature and meant to give an idea of how the phases interact at different stages of the reaction.

$$(Ti_{0.40}Al_{0.30}N_{0.30}) \rightarrow (Ti_{0.46}Al_{0.14}N_{0.40}) + Al_5Ti_2 + AlN \qquad (1)$$

$$(Ti_{0.46}Al_{0.14}N_{0.40}) + Al_5Ti_2 \rightarrow Ti_2AlN_{1-\delta} + TiN_{0.85} + Al_3Ti + AlN \quad (2)$$

$$Ti_2AlN_{1-\delta} + TiN_{0.85} \rightarrow Ti_4AlN_{3-\delta} \qquad (3)$$

The formation of small quantities of Al_2O_3 at high temperatures was observed in most of the samples. The presence of oxygen below 0.6 at. %, in as-deposited state cannot fully explain the presence of Al_2O_3. Instead we attribute the additional Al_2O_3 to residual O_2 and H_2O in the DSC chamber/argon not captured by the zirconium trap used during all annealing treatments.

Sample A does not follow the suggested transformation path, due to the decomposition of Ti_2AlN into c-TiN and w-AlN above 1000 °C. We suggest that the large amount of w-AlN(Ti) present in the as-deposited state is responsible for the absence of Al_3Ti and the instability of Ti_2AlN at high temperatures. Beckers et al. showed that reactively sputtered Ti_2AlN thin films decomposed already at ~800 °C by the out diffusion of Al and the formation of c-TiN$_x$ by Ti_2N detwinning [48].

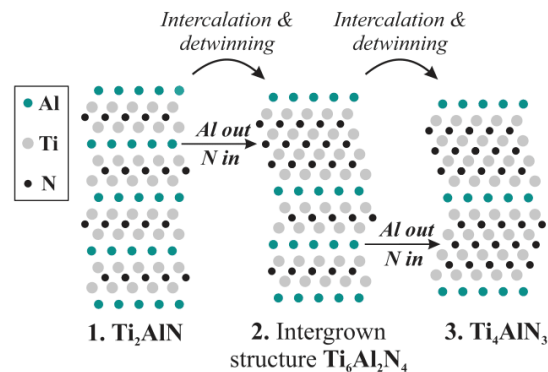### 4.3. Formation mechanism of Ti_4AlN_3

The progression of chemically modulated layers inside the MAX plates at different temperatures suggests a thermally activated diffusion mechanism, where nitrogen layers replace Al layers in the Ti_2AlN crystal. During the phase transformation an intergrown structure, $Ti_6Al_2N_4$, forms as a consequence of a specific stacking of Ti_4AlN_3 and Ti_2AlN units.

The Ti_4AlN_3 formation mechanism proposed here is based on a transformation from a MAX phase of a low n order to a higher order via deintercalation of the Al layers along the basal planes with concurrent introduction of N layers and detwinning. Two schematics describing the proposed mechanism are shown in Fig. 8 and Fig. 9.

The atomistic model in Fig. 8 describes several sequential steps of the formation of Ti_4AlN_3 from Ti_2AlN:

1. Intercalation of basal plane Al layers for N layers and detwinning.
2. Mixed half unit cells of Ti_2AlN and Ti_4AlN_3, forming an intergrown structure $Ti_6Al_2N_4$.
3. Further intercalation of Al layers for N layers and detwinning until the entire crystal is Ti_4AlN_3.

The deintercalation process in the Ti_2AlN crystals is highly likely to trap some layers of Ti_2AlN inside the Ti_4AlN_3 crystals after the

Fig. 8. Atomic scale model of the transformation mechanism from Ti_2AlN to Ti_4AlN_3 via intercalation and detwinning.
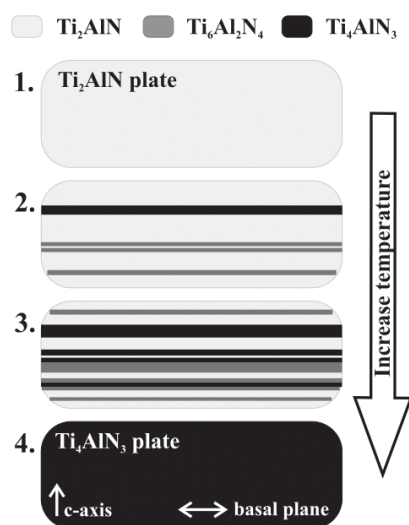
Fig. 9. Large scale view of the transformation mechanism of Ti$_2$AlN into Ti$_4$AlN$_3$.

transformation is completed, which explains the remaining chemical fluctuation in Ti$_4$AlN$_3$ even after being heated to 1400 °C.

For a direct correlation with the experimental observations, our transformation model is schematically illustrated at a larger scale in Fig. 9. It shows the microstructure evolution during the transformation:

1. Starting material is a Ti$_2$AlN plate.
2. Intercalation of Al layers for N layers along basal plane leads to the formation of Ti$_4$AlN$_3$ layers and Ti$_6$Al$_2$N$_4$ layers inside the Ti$_2$AlN crystal. They are visible as nm-scale layers inside the grains (see Fig. 4).
3. Progressing intercalation during temperature increase. Ti$_4$AlN$_3$ and Ti$_6$Al$_2$N$_4$ layers become more dominant and frequent.
4. Ti$_4$AlN$_3$ dominates completely and the entire plate is now transformed.

MAX phase formation via a periodic intercalation of the A-element into a M$_{1-n}$X$_n$ preordered matrix is a mechanism proposed by Zhou et al. [49] and presented later by Riley et al. as a low temperature solid state synthesis method for MAX phase formation in bulk materials [50,51]. The suggested mechanism starts with a binary precursor, M$_{1-n}$X$_n$, in which a sequence of vacancy ordering, twinning, and intercalation of A-element leads to the formation of a MAX phase. Intercalation is a reversible mechanism and is thermally activated [49,52]. MAX phase formation via intercalation has been reported in different ternary systems, e.g. Ti$_3$SiC$_2$, Ti$_2$AlC, Ti$_3$AlC$_2$ [13,53,54]. It is important to note that the precursor used is a binary phase rich in X-element vacancies, and intercalation has only been shown in systems with carbon as the X element.

The presented results extend the mechanism of intercalation to a ternary phase, where the precursor is a MAX phase of a low n order, i.e. Ti$_2$AlN. By de-intercalation of Al layers concurrently with introduction of N layers and detwinning, a MAX phase of higher n order is formed, i.e. Ti$_4$AlN$_3$. Similar observations have been done in other transition metal carbide systems, where a full or a partial transformation was observed by annealing thin films or bulk material. In the Ti-Al-C system, Kisi et al. [47] and Wu et al. [55] showed a full conversion of Ti$_2$AlC into Ti$_3$AlC$_2$, while in the same system Lane et al. [56–58] and Zhang et al. [59] presented the

intergrown phase Ti$_5$Al$_2$C$_3$ in coexistence with Ti$_3$AlC$_2$ by annealing Ti$_2$AlC. In all these cases, the temperatures used were above 1400 °C with annealing times between 1 and 8 h. Further, in the systems Ti-Si-C and Ti-Ge-C, presence of intergrown phases were observed to coexist with their related MAX phases, i.e. Ti$_7$Si$_2$C$_5$ with Ti$_3$SiC$_2$ and Ti$_4$SiC$_3$ by Palmquist et al. [34], and Ti$_7$Si$_2$C$_5$ and Ti$_5$Si$_2$C$_3$ with Ti$_2$SiC, Ti$_3$SiC$_2$ and Ti$_4$SiC$_3$ by Högberg et al. [60]. Scabarozi et al. [61] demonstrated that Ti$_7$Si$_2$C$_5$ can be synthesized as a phase pure epitaxial thin film. In ternary systems containing nitrogen, Lee et al. were able to obtain full transformation of Ti$_2$AlN into Ti$_4$AlN$_3$ by annealing a powder mixture at 1300 °C for 20 days, which at the time (1997) was wrongly believed to be Ti$_3$Al$_2$N$_2$ [46]. In our study, we were able to obtain full transformation of Ti$_2$AlN into Ti$_4$AlN$_3$ by annealing up to 1400 °C with no dwell time.

In order for this transformation to take place, several conditions must be fulfilled: (1) the ternary system M-A-X must have at least two M$_{1+n}$AX$_n$ phases thermodynamically stable, (2) the MAX phase to be transformed into a higher n order must be stable at the temperature where the transformation takes place, and (3) high annealing temperature must be applied, i.e. above 900 °C. Moreover, transformation occurs from a low n order MAX phase to the next thermodynamic stable MAX phase with higher n order. The full transformation takes place if sufficient amount of X element and energy is supplied to the system, and it can be accelerated by the melt of an A-rich phase [46,47].

We suggest that with the transformation mechanism we propose, it is possible to obtain MAX phases of high n order in thin films which has not been obtained previously by direct nucleation and growth, like Ti$_4$GaC$_3$, Nb$_4$AlC$_3$ and V$_4$AlC$_3$.

5. Conclusions

Formation of MAX phase Ti$_4$AlN$_3$ in flake-like powder was possible via solid state reactions in a nitrogen deficient cubic solid solution (Ti$_{1-x}$Al$_x$)N$_y$. The as-deposited composition where Ti$_4$AlN$_3$ was obtained ranged from x = 0.28 to 0.55 and y = 0.40 to 0.58. Phases like Ti$_2$AlN, w-AlN, c-AlN, Al$_5$Ti$_2$, and Al$_3$Ti were present and their quantity varied with the as-deposited composition of the thin film, as was the case for Ti$_4$AlN$_3$ too.

We have showed that formation of Ti$_4$AlN$_3$ takes place inside the preformed MAX phase Ti$_2$AlN single crystal plates by a thermal activated diffusion process. The mechanism of transformation suggested is the intercalation of Al layers for N layers along the basal plane accompanied by a simultaneous detwinning process of the Ti$_2$AlN crystals, leading to the formation of a MAX phase of higher n order, Ti$_4$AlN$_3$. Therefore, a prerequisite for obtaining large quantities of Ti$_4$AlN$_3$ is the formation and stability of Ti$_2$AlN above 1200 °C. During the transformation from Ti$_2$AlN to Ti$_4$AlN$_3$, an intermediate Ti$_6$Al$_2$N$_4$ phase was observed and characterized to be an intergrown structure whose unit cell consists of Ti$_2$AlN and Ti$_4$AlN$_3$ half unit cells. This phase confirms intercalation as the formation mechanism of Ti$_4$AlN$_3$.

References

[1] M.W. Barsoum, The Mn-1AXn phases: a new class of solids, Prog. Solid State Chem. 28 (2000) 201, http://dx.doi.org/10.1016/S0079-6786(00)00006-6.

[2] M.W. Barsoum, T. El-Raghy, The MAX Phases: unique new carbide and nitride materials, Am. Sci. 89 (2001) 334.

[3] P. Eklund, M. Beckers, U. Jansson, H. Högberg, L. Hultman, The Mn + 1AXn phases: materials science and thin-film processing, Thin Solid Films 518 (2010) 1851, http://dx.doi.org/10.1016/j.tsf.2009.07.184.

[4] P. Eklund, J. Rosen, P.O.Å. Persson, Layered ternary Mn+1AXn phases and their 2D derivative MXene: an overview from a thin-film perspective, J. Phys. D. Appl. Phys. 50 (2017) 113001, http://dx.doi.org/10.1088/1361-6463/aa57bc.

[5] B. Pécz, L. Tóth, M.A. di Forte-Poisson, J. Vacas, Ti3SiC2 formed in annealed Al/ Ti contacts to p-type SiC, Appl. Surf. Sci. 206 (2003) 8.

[6] M. Gao, S. Tsukimoto, S.H. Goss, S.P. Tumakha, T. Onishi, M. Murakami, et al., Role of interface layers and localized states in TiAl-based Ohmic contacts to p-type 4H-SiC, J. Electron. Mater 36 (2007) 277, http://dx.doi.org/10.1007/s11664-006-0078-0.

[7] H. Fashandi, M. Andersson, J. Eriksson, J. Lu, K. Smedfors, C.M. Zetterling, et al., Single-step synthesis process of Ti3SiC2 ohmic contacts on 4H-SiC by sputter-deposition of Ti, Scr. Mater 99 (2015) 53–56, http://dx.doi.org/10.1016/j.scriptamat.2014.11.025.

[8] A. Abdulkadhim, M. to Baben, T. Takahashi, V. Schnabel, M. Hans, C. Polzer, et al., Crystallization kinetics of amorphous Cr2AlC thin films, Surf. Coat. Technol. 206 (2011) 599–603, http://dx.doi.org/10.1016/j.surfcoat.2011.06.003.

[9] A. Abdulkadhim, M. to Baben, V. Schnabel, M. Hans, N. Thieme, C. Polzer, et al., Crystallization kinetics of V2AlC, Thin Solid Films 520 (2012) 1930–1933, http://dx.doi.org/10.1016/j.tsf.2011.09.037.

[10] V. Vishnyakov, O. Crisan, P. Dobrosz, J.S. Colligon, Ion sputter-deposition and in-air crystallisation of Cr2AlC films, Vacuum 100 (2014) 61–65, http://dx.doi.org/10.1016/j.vacuum.2013.07.045.

[11] C. Höglund, M. Beckers, N. Schell, J. Borany, Topotaxial growth of Ti2AlN by solid state reaction in AlN/Ti(0001) multilayer thin films, Appl. Phys. Lett. 90 (2007) 174106, http://dx.doi.org/10.1063/1.2731520.

[12] V. Dolique, M. Jaouen, T. Cabioc'h, F. Pailloux, P. Guerin, V. Pelosin, Formation of (Ti,Al)N/Ti2AlN multilayers after annealing of TiN/TiAl(N) multilayers deposited by ion beam sputtering, J. Appl. Phys. 103 (2008) 83527, http://dx.doi.org/10.1063/1.2894589.

[13] A. Abdulkadhim, T. Takahashi, D. Music, F. Munnik, J.M. Schneider, MAX phase formation by intercalation upon annealing of TiCx/Al (0.4 < x < 1) bilayer thin films, Acta Mater 59 (2011) 6168–6175, http://dx.doi.org/10.1016/j.actamat.2011.06.029.

[14] R. Grieseler, T. Kups, M. Wilke, M. Hopfeld, P. Schaaf, Formation of Ti2AlN nanolaminate films by multilayer-deposition and subsequent rapid thermal annealing, Mater. Lett. 82 (2012) 74–77, http://dx.doi.org/10.1016/j.matlet.2012.05.055.

[15] M. Hopfeld, R. Grieseler, T. Kups, M. Wilke, P. Schaaf, Thin film synthesis of Ti3SiC2 by rapid thermal processing of magnetron-sputtered Ti-C-Si multilayer systems, Adv. Eng. Mater 15 (2013) 269–275, http://dx.doi.org/10.1002/adem.201200180.

[16] B. Holm, R. Ahuja, S. Li, B. Johansson, Theory of the ternary layered system Ti-Al-N, J. Appl. Phys. 91 (2002) 9874–9877, http://dx.doi.org/10.1063/1.1476076.

[17] T. Cabioch, M. Alkazaz, M.F. Beaufort, J. Nicolai, D. Eyidi, P. Eklund, Ti2AlN thin films synthesized by annealing of (Ti+Al)/AlN multilayers, Mater. Res. Bull. 80 (2016) 58–63, http://dx.doi.org/10.1016/j.materresbull.2016.03.031.

[18] T. Joelsson, A. Flink, J. Birch, L. Hultman, Deposition of single-crystal Ti2AlN thin films by reactive magnetron sputtering from a 2Ti:Al compound target, J. Appl. Phys. 102 (2007) 74918, http://dx.doi.org/10.1063/1.2785958.

[19] P.O.Å. Persson, S. Kodambaka, I. Petrov, L. Hultman, Epitaxial Ti2AlN(0001) thin film deposition by dual-target reactive magnetron sputtering, Acta Mater 55 (2007) 4401–4407, http://dx.doi.org/10.1016/j.actamat.2007.04.006.

[20] M. Beckers, C. Höglund, C. Baehtz, R.M.S. Martins, P.O.Å. Persson, L. Hultman, et al., The influence of substrate temperature and Al mobility on the micro-structural evolution of magnetron sputtered ternary Ti-Al-N thin films, J. Appl. Phys. 106 (2009) 64915, http://dx.doi.org/10.1063/1.3208065.

[21] Z. Zhang, H. Jin, J. Pan, H.L. Seng, G.T.W. Goh, et al., Temperature-dependent microstructural evolution of Ti2AlN thin films deposited by reactive magnetron sputtering, Appl. Surf. Sci. 368 (2016) 88–96, http://dx.doi.org/10.1016/j.apsusc.2016.01.229.

[22] M.W. Barsoum, L. Farber, I. Levin, A. Procopio, T. El-Raghy, A. Berner, High-resolution transmission electron microscopy of Ti4AlN3, or Ti3Al2N2 revisited, J. Am. Ceram. Soc. 82 (1999) 2545–2547, http://dx.doi.org/10.1111/j.1151-2916.1999.tb02117.x.

[23] A.T. Procopio, T. El-Raghy, M.W. Barsoum, Synthesis of Ti4AlN3 and phase equilibria in the Ti-Al-N system, Metall. Mater. Trans. A 31A (2000) 373.

[24] R. Forsen, M. Johansson, M. Oden, N. Ghafoor, Decomposition and phase transformation in TiCrAlN thin coatings, J. Vac. Sci. Technol. A 30 (2012) 61506, http://dx.doi.org/10.1116/1.4757953.

[25] K. Thompson, D. Lawrence, D.J. Larson, J.D. Olson, T.F. Kelly, B. Gorman, In situ site-specific specimen preparation for atom probe tomography, Ultramicroscopy 107 (2007) 131, http://dx.doi.org/10.1016/j.ultramic.2006.06.008.

[26] D.R. Kingham, The post-ionization of field evaporated ions: a theoretical explanation of multiple charge states, Surf. Sci. Lett. 116 (1982) 273.

[27] B. Gault, M.P. Moody, J.M. Cairney, S.P. Ringer, Atom Probe Microscopy, first ed., Springer, New York, 2012 http://dx.doi.org/10.1007/978-1-4614-3436-8.

[28] I.C. Schramm, M.P. Johansson Jöesaar, J. Jensen, F. Mücklich, M. Odén, Impact of nitrogen vacancies on the high temperature behavior of (Ti1−xAlx)Ny alloys, Acta Mater 119 (2016) 218–228, http://dx.doi.org/10.1016/j.actamat.2016.08.024.

[29] M. to Baben, L. Raumann, D. Music, J.M. Schneider, Origin of the nitrogen over- and understoichiometry in Ti0.5Al0.5N thin films, J. Phys. Condens. Matter 24 (2012) 155401, http://dx.doi.org/10.1088/0953-8984/24/15/155401.

[30] F. Tasnadi, I.A. Abrikosov, L. Rogström, J. Almer, M.P. Johansson, M. Oden, Significant elastic anisotropy in Ti1−xAlxN alloys, Appl. Phys. Lett. 97 (2010) 231902, http://dx.doi.org/10.1063/1.3524502.

[31] B. Alling, A. Karimi, L. Hultman, I.A. Abrikosov, First-principles study of the effect of nitrogen vacancies on the decomposition pattern in cubic Ti1−xAlxN1−y, Appl. Phys. Lett. 92 (2008) 71903, http://dx.doi.org/10.1063/1.2838747.

[32] C.J. Rawn, M.W. Barsoum, T. El-Raghy, A. Procipio, C.M. Hoffmann, C.R. Hubbard, Structure of Ti4AlN3-a layered Mn+1AXn nitride, Mater. Res. Bull. 35 (2000) 1785–1795, http://dx.doi.org/10.1016/S0025-5408(00)00383-4.

[33] D. Music, R. Ahuja, J.M. Schneider, Theoretical study of nitrogen vacancies in Ti4AlN3, Appl. Phys. Lett. 86 (2005) 31911, http://dx.doi.org/10.1063/1.1854744.

[34] J.P. Palmquist, S. Li, P.O.Å. Persson, J. Emmerlich, O. Wilhelmsson, H. Högberg, et al., Mn+1AXn phases in the Ti-Si-C system studied by thin-film synthesis and ab initio calculations, Phys. Rev. B - Condens. Matter Mater. Phys. 70 (2004) 165401, http://dx.doi.org/10.1103/PhysRevB.70.165401.

[35] B.-Y. Shew, J.-L. Huang, The effects of nitrogen flow on reactively sputtered Ti-Al-N films, Surf. Coat. Technol. 71 (1995) 30–36.

[36] B. Alling, A.V. Ruban, A. Karimi, O.E. Peil, S.I. Simak, L. Hultman, et al., Mixing and decomposition thermodynamics of c-Ti1−xAlxN from first-principles calculations, Phys. Rev. B 75 (2007) 45123, http://dx.doi.org/10.1103/PhysRevB.75.045123.

[37] N. Shulumba, O. Hellman, Z. Raza, B. Alling, J. Barrirero, F. Mücklich, et al., Lattice vibrations change the solid solubility of an alloy at high temperatures, Phys. Rev. Lett. 117 (2016) 205502, http://dx.doi.org/10.1103/PhysRevLett.117.205502.

[38] T. Yasumoto, K. Yamakawa, N. Iwase, N. Shinosawa, Reaction between AlN and metal thin films during high temperature annealing, J. Ceram. Soc. Jpn. 101 (1993) 969–973.

[39] X. He, S. Yang, K. Tao, Y. Fan, Investigation of the interface reactions of Ti thin films with AlN substrate, J. Mater. Res. 12 (1996) 846–851.

[40] L. Hultman, S. Benhenda, G. Radnoczi, J.-E. Sundgren, J.E. Greene, I. Petrov, Interfacial reactions in single-crystal-TiN (100)/Al/polycrystalline-TiN multilayer thin films, Thin Solid Films 215 (1992) 152–161.

[41] O. Wilhelmsson, J.P. Palmquist, E. Lewin, J. Emmerlich, P. Eklund, P.O.Å. Persson, et al., Deposition and characterization of ternary thin films within the Ti-Al-C system by DC magnetron sputtering, J. Cryst. Growth 291 (2006) 290–300, http://dx.doi.org/10.1016/j.jcrysgro.2006.03.008.

[42] Y. Imanaka, M.R. Notis, Interface reactions between titanium thin films aluminium nitride substrates, J. Am. Ceram. Soc. 82 (1999) 1547–1552, http://dx.doi.org/10.1007/BF02387808.

[43] L. Hultman, Thermal stability of nitride thin films, Vacuum 57 (2000) 1–30.

[44] M. Dahlqvist, B. Alling, J. Rosén, Stability trends of MAX phases from first principles, Phys. Rev. B 81 (2010) 230102, http://dx.doi.org/10.1103/PhysRevB.81.220102.

[45] F. Zhang, S.L. Chen, Y.A. Chang, U.R. Kattner, A thermodynamic description of the Ti-Al system, Intermetallics 5 (1997) 471–482, http://dx.doi.org/10.1016/S0966-9795(97)00030-7.

[46] H.D. Lee, W.T. Peertuskey, New ternary nitride in the Ti-Al-N system, J. Am. Ceram. Soc. 80 (1997) 604–608, http://dx.doi.org/10.1111/j.1151-2916.1997.tb02874.x.

[47] E.H. Kisi, E. Wu, J.S. Zobec, J.S. Forrester, D.P. Riley, Inter-conversion of Mn+1AXn phases in the Ti-Al-C system, J. Am. Ceram. Soc. 90 (2007) 1912–1916, http://dx.doi.org/10.1111/j.1551-2916.2007.01710.x.

[48] M. Beckers, N. Schell, R.M.S. Martins, A. Mücklich, W. Möller, Phase stability of epitaxially grown Ti2AlN thin films, Appl. Phys. Lett. 89 (2006) 101–103, http://dx.doi.org/10.1063/1.2335681.

[49] Y. Zhou, Z. Sun, Crystallographic relations between Ti3SiC2 and TiC, Mater. Res. Innov. 3 (2000) 286–291.

[50] D.P. Riley, E.H. Kisi, The design of crystalline precursors for the synthesis of M n-1AXn phases and their application to Ti3AlC2, J. Am. Ceram. Soc. 90 (2007) 2231–2235, http://dx.doi.org/10.1111/j.1551-2916.2007.01728.x.

[51] D.P. Riley, E.H. Kisi, A new solid state synthesis methodology for ternary and higher order compounds, J. Aust. Ceram. Soc. 43 (2007) 102.

[52] J. Emmerlich, D. Music, P. Eklund, O. Wilhelmsson, U. Jansson, J.M. Schneider, et al., Thermal stability of Ti3SiC2 thin films, Acta Mater 55 (2007)

1479—1488, http://dx.doi.org/10.1016/j.actamat.2006.10.010.

[53] R. Yu, Q. Zhan, L.L. He, Y.C. Zhou, H.Q. Ye, Si-induced twinning of TiC and formation of Ti3SiC2 platelets, Acta Mater 50 (2002) 4127—4135, http://dx.doi.org/10.1016/S1359-6454(02)00248-3.

[54] S.S. Hwang, S.W. Park, T.W. Kim, Synthesis of the Ti3SiC2 by solid state reaction below melting temperature of Si, J. Alloys Compd. 392 (2005) 285—290, http://dx.doi.org/10.1016/j.jallcom.2004.08.089.

[55] E. Wu, E. Herold Kisi, Synthesis of Ti3AlC2 from Ti/Al4C3/C studied by in situ neutron diffraction, J. Am. Ceram. Soc. 89 (2006) 710—713, http://dx.doi.org/10.1111/j.1551-2916.2005.00745.x.

[56] N.J. Lane, M. Naguib, J. Lu, L. Hultman, M.W. Barsoum, Structure of a new bulk Ti5Al2C3 MAX phase produced by the topotactic transformation of Ti2AlC, J. Eur. Ceram. Soc. 32 (2012) 3485—3491.

[57] N.J. Lane, M. Naguib, J. Lu, P. Eklund, L. Hultman, M.W. Barsoum, Comment on "Ti5Al2C3: a New ternary carbide belonging to MAX phases in the Ti-Al-C system", J. Am. Ceram. Soc. 95 (2012) 3352—3354, http://dx.doi.org/10.1111/j.1551-2916.2012.05299.x.

[58] N.J. Lane, S.C. Vogel, Elád N. Caspi, M.W. Barsoum, High-temperature neutron diffraction and first-principles study of temperature-dependent crystal structures and atomic vibrations in Ti3AlC2, Ti2AlC, and Ti5Al2C3, J. Appl. Phys. 113 (2013) 183519, http://dx.doi.org/10.1063/1.4803700.

[59] H. Zhang, X. Wang, Y. Ma, L. Sun, L. Zheng, Y. Zhou, Crystal structure determination of nanolaminated Ti5Al2C3 by combined techniques of XRPD, TEM and ab initio calculations, J. Adv. Ceram. 1 (2012) 268—273, http://dx.doi.org/10.1007/s40145-012-0034-9.

[60] H. Högberg, P. Eklund, J. Emmerlich, J. Birch, L. Hultman, Epitaxial Ti2GeC, Ti3GeC2, and Ti4GeC3 MAX-phase thin films grown by magnetron sputtering, J. Mater. Res. 20 (2005) 779—782, http://dx.doi.org/10.1557/JMR.2005.0105.

[61] T.H. Scabarozi, J.D. Hettinger, S.E. Lofland, J. Lu, L. Hultman, J. Jensen, et al., Epitaxial growth and electrical-transport properties of Ti 7Si2C5 thin films synthesized by reactive sputter-deposition, Scr. Mater 65 (2011) 811—814, http://dx.doi.org/10.1016/j.scriptamat.2011.07.038.

Paper III

Effect of nitrogen vacancies on phase stability
and mechanical properties of arc deposited
$(Ti_{0.52}Al_{0.48})N_y$ (y < 1) coatings

I.C. Schramm, C. Pauly, M.P. Johansson Jõesaar, S. Slawik, S. Suárez,
F. Mücklich and M. Odén.

Effects of nitrogen vacancies on phase stability and mechanical properties of arc deposited $(Ti_{0.52}Al_{0.48})N_y$ (y < 1) coatings

I.C. Schramm[1,2*], C. Pauly[2], M.P. Johansson Jõesaar[1,3], S. Slawik[2], S. Suarez[2], F. Mücklich[2], M. Odén[1]

* Corresponding author: isasc@ifm.liu.se

1. Nanostructured Materials, Department of Physics, Chemistry and Biology (IFM), Linköping University, SE 58183, Linköping, Sweden
2. Functional Materials, Department Materials Science, Saarland University, P.O Box 151150, 66041 Saarbrucken, Germany
3. SECO Tools AB, SE-73782 Fagersta, Sweden

Nitrogen sub-stoichiometric $(Ti_{0.52}Al_{0.48})N_y$ ($0.92 \geq y \geq 0.46$) coatings were grown in a mixed Ar/N_2 atmosphere by cathodic arc deposition on cemented carbide (WC/Co-based) substrates. The coatings present a columnar structure with decreasing column widths from 250 to 60 nm, due to a corresponding reduced N content, accompanied by changes in preferred orientation from 200 to 111 to 220. Among these, coatings prepared with $0.92 \geq y \geq 0.75$ exhibit spinodal decomposition and consequently age hardening at elevated temperatures. A reduced N content upshifts the hardness maximum by more than 300 °C. For these samples, the high temperature treatment resulted in interdiffusion of substrate elements, Co and C, mainly along column boundaries. Nevertheless, no detrimental effect in the hardness could be correlated. Conversely, a low N content sample (y = 0.46) presents significant lattice diffusion of substrate elements Co, C, W, and Ta in the coating. In this case, the substrate elements are present throughout the coating, forming additional phases such as c-Ti(C,N), c-Co(Al,Ti,W), and c-(Ti,W,Ta)(C,N), with an observed increased hardness from 16 to 25 GPa. We suggest that the substitution of nitrogen by carbon and the solution of W and Ta in c-TiN are responsible for the observed hardening. Our investigation shows the potential of sub-stoichiometric $(Ti_{1-x}Al_x)N_y$ coatings for high temperature applications such as cutting tools and puts forth corresponding criteria for N content selection.

Keywords: TiAlN, Thin Films, Nitrogen vacancies, Spinodal decomposition, age hardening.

1. Introduction

The control over microstructure and composition during the synthesis of transition metal nitride (TMN) thin films are key factors in tuning their physical properties for high temperature applications [1,2]. (Ti,Al)N coatings, typically deposited by physical vapor deposition, exhibit excellent wear and oxidation properties in addition to high thermal stability. These attributes make it one of the most commonly used TMN materials in cutting tool applications [2–4]. The (Ti,Al)N system has a miscibility gap in its quasi-binary phase diagram TiN-AlN [5,6]. Spinodal decomposition of the as-deposited metastable *cubic* solid solution (Ti,Al)N phase separates into coherent c-TiN- and c-AlN-rich nanometer-sized domains [7], resulting in age hardening [8]. The 3D interconnected segregated network with differing elastic properties leads to coherency strain and a Koehler-type hardening at high annealing temperatures [8–10]. A drawback is that any further increase in temperature leads to coarsening of the segregated domains, transformation of the metastable c-AlN into its stable wurtzite phase, w-AlN, and a decline in mechanical properties [8,11,12]. Suppressing or delaying w-AlN formation in (Ti,Al)N thin films at high temperatures has been a challenge in the last decades. The use of other alloying elements, layered structures, external pressure and stresses are some of the proposed solutions [13–17].

Recently, it has been shown in two studies that changing the N content in medium Al content $(Ti_{1-x}Al_x)N_y$ alloys can change the onset temperature for spinodal decomposition. To Baben *et al.* showed that for $y > 1$ the presence of metal vacancies is responsible for an increase in diffusivity by 12 orders of magnitude in comparison to the stoichiometric case ($y \approx 1$), leading to a spinodal decomposition at low temperatures < 800 °C while for $y \approx 1$ nucleation and growth products only are observed above > 1100 °C [18]. We recently showed that small amounts of N vacancies ($y = 0.92$) enhance the decomposition similar to the $y > 1$ case, while a further increase ($0.92 > y \geq 0.75$) decreases the driving force for phase separation. Spinodal decomposition took place above > 1100 °C for $y = 0.75$ and no coarsening of the microstructure was observed between 1200 and 1400 °C [19]. These results were obtained from coating material detached from the substrate to see the effect of N vacancies on the phase evolution of (Ti,Al)N. In order to further explore the potential of these coatings for applications such as cutting tools the influences of the substrate must be included.

94

We present a systematic study on N deficient cathodic arc-evaporated $(Ti_{0.52}Al_{0.48})N_y$ coatings with $0.92 \geq y \geq 0.46$, and invoke high temperature interaction with WC/Co-based substrates. We report the microstructure and phase evolution, which are largely influenced by interdiffusion between the substrate and coating, along with hardness evolution as a function of high temperature annealing. We show that besides diffusion of Co and C along grain boundaries, the reduction of driving force for separation of $(Ti_{0.52}Al_{0.48})N_y$ via N vacancies is still present for the nitrogen content range $0.92 > y \geq 0.75$, and accordingly age hardening is observed. For even lower N contents in the coating (y = 0.46) substantial interdiffusion occurs resulting in formation of phases containing Co, C, W, Ta, Ti, Al and N, and a general decrease in hardness is observed.

2. Experimental details

Nitrogen deficient coatings were grown using an industrial scale reactive cathodic arc deposition system, Metaplas MZR-323 (now Oerlikon Metaplas GmbH), at a total gas pressure of 2 Pa, a substrate bias of -30 V and a growth temperature of ~ 450 °C. The N content of the coating was tuned by varying the % N_2 of an Ar/N_2 gas mixture between 33 and 100 % during growth. The substrates used is commercial grade of cemented carbide (ISO SNUN120408) comprising 12 wt.% Co binder balanced with tungsten carbide (WC) and less than 2 wt.% of other carbides, e.g., tantalum carbide. The substrates, polished to a mirror-like surface finish, were mounted on a one-axis rotational drum fixture. Three circular (100 mm in diameter) arc sources fitted with $Ti_{0.45}Al_{0.55}$ cathodes were mounted in a straight line, bottom to top, on the chamber wall, facing the fixture. For more details see Ref. [20]. During deposition the fixture was rotated at 3 rpm, resulting in a deposition rate of 0.1 µm/min, and a total coating thickness of about 3 µm.

Isothermal annealing treatments were performed at T_{max} = 700, 800, 900, 1000, 1100, and 1200 °C for 15 min in a vacuum tube furnace held at 8 x 10^{-4} Pa. The heating and cooling rates were set to 20 °C/min. A Zirconium oxygen getter was placed in the vicinity of the sample to further avoid oxidation of the samples.

X-ray diffractometry (XRD) was performed in a PANalytical Empyrean diffractometer using Cu-K_α radiation in a focusing Bragg Brentano configuration and low background optics. For phase analysis, diffractograms were recorded at room temperature and a silicon zero diffraction plate was used as sample holder. In this setup, only lattice planes parallel to the sample surface contribute to

the diffraction peaks. Residual stress measurements in the as-deposited samples were performed with parallelizing polycapillary optics in point focus and recording the 422 diffraction line of c-(Ti,Al)N at different chi-tilts. The $\sin^2\psi$ method was used to extract the stress values. The elastic constants used were: E = 460 GPa and υ = 0.20, obtained from *ab initio* calculations [10]. Crystallite size was obtained from the 200 diffraction line of c-(Ti,Al)N recorded under specular conditions (no chi-tilt) in the as-deposited samples by using the Scherrer´s equation.

A focused ion beam/scanning electron microscope (FIB/SEM), FEI Helios Nanolab 600, was used for cross sectional and surface views of the coatings, energy dispersive X-ray analysis (EDS), electron backscatter diffraction (EBSD), macroparticles analysis, and preparation of TEM lamellas and atom probe tips. Needle-shaped specimens for atom probe were produced using a standard lift-out technique [21] with a final cleaning step of 2 kV FIB milling.

Transmission electron microscopy (TEM) and selected area diffraction (SAD) were used to characterize the crystal structure of phases present in the annealed coatings in more detail. TEM analysis was performed using a JEOL JEM 2010F at an acceleration voltage of 200 kV.

Atom probe tomography (APT) was performed using a local electrode atom probe (Cameca LEAP 3000X HR) in laser mode (10 ps, 532 nm) and a controlled evaporation rate of 0.5 % on samples held at 60 K. The laser was set to a repetition frequency of 200 kHz and an energy per pulse of 0.5 nJ. Data reconstruction was carried out with the software package IVAS (version 3.6.14, Cameca) using an evaporation field of 40 V/nm, an image compression factor of 1.65 and a field factor between 3.3 and 4.0 depending on the tip shank angle. Parameters were obtained by using Kingham curves [22] and tip SEM images before and after the APT run. 3D morphology and chemical composition were extracted from annealed samples while as-deposited data was obtained from previous work on the same material [19,23].

Hardness measurements were performed with an UMIS nanoindentor using a Berkovich diamond tip and fused silica as reference material. The average hardness for each sample was evaluated from the load-displacement curves using the Oliver and Pharr method [24], a minimum of 40 indents per sample. To avoid effects of surface topography on hardness measurements, samples were mechanically polished at a taper angle of ~ 10° relative to the original surface. Measurements were

then carried out close to the original surface [25]. The indentation depth was less than 10 % of the coating thickness.

3. Results and Discussion

The chemical compositions shown in Figure 1 were obtained by APT. The notation used is $(Ti_{1-x}Al_x)N_y$, where x is the atomic aluminum metal fraction, Al/(Al+Ti), and y is the nitrogen to metal ratio, N/(Al+Ti). The metal ratio was close to $x \approx 0.48$ for all samples while y varied from 0.92 to 0.46. The four samples were labeled according to the average N content as y = 0.92, y = 0.87, y = 0.75 and y = 0.46. The main contribution to the error is from intrinsic chemical fluctuations in the as-deposited state as shown by frequency distribution analysis and Pearson coefficient in previous work [19,23]. Impurity elements like oxygen, argon and gallium were also detected with an overall content of less than 0.5 at. % in all samples. These impurities and their amounts are typical for the industrial scale vacuum chamber and atom probe sample preparation [21].
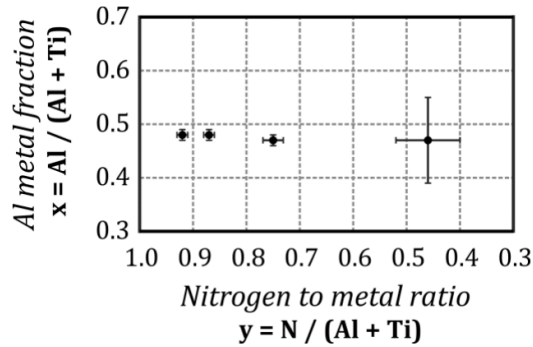

Figure 1. Composition map of as-deposited coatings investigated.

Results are discussed and divided into three sections. First, the as-deposited state of the samples is described, followed by the phase evolution during high temperature annealing. Finally, the hardness vs. annealing temperature is presented. In addition, the phase evolution is divided into a high/medium N content range ($0.92 \geq y \geq 0.75$) and a low N content one (y = 0.46).

3.1 As-deposited state

X-ray diffractograms of all as-deposited samples are shown in Figure 2. The diffraction peaks of the cemented carbide (WC/Co) substrate are marked with vertical lines. Regardless of N content, all samples reveal a cubic solid solution c-(Ti$_{0.52}$Al$_{0.48}$)N$_y$ B1 crystal structure. Samples y = 0.75 and 0.46 showed additional hexagonal h-Ti peaks due to the increased presence of macroparticles, which is a consequence of the reduced N content in the process [19,26]. The cubic B1 structure of (Ti,Al)N is known to accommodate a large fraction of nitrogen deficiency, $1.0 > y \geq 0.37$ [19,27,28]. The lattice parameters, extracted using the Nelson and Riley method [29], show similar values for all samples with a maximum difference of 0.6 %, consistent with nitrogen vacancies accommodating the substoichiometry [19,28,30]. The crystallite sizes obtained by the Scherrer equation were 50 ± 5 nm. An influence of N-content on crystallite size could not be established. Instead the values are consistent with the thickness of the artificial layers (~ 40 nm) caused by rotation during growth, see Fig. 3(d). These layers have significantly different electron density [31] and thereby limit the coherent scattering length.
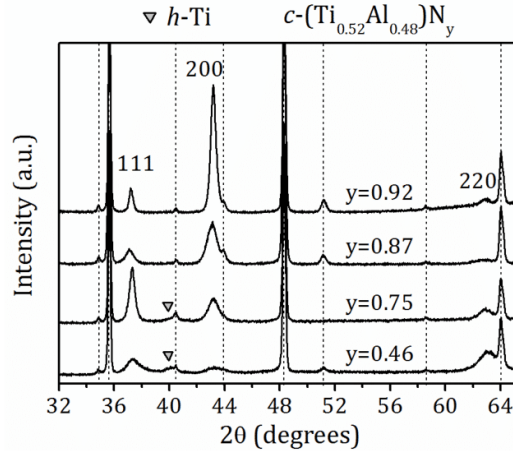

Figure 2. X-ray diffractograms of as-deposited coatings (Ti$_{0.52}$Al$_{0.48}$)N$_y$ with y = 0.92, y = 0.87, y = 0.75 and y = 0.46. Vertical lines correspond to substrate cemented carbide (WC/Co-based) peaks.

As observed in Fig. 2, the dominant diffraction peak intensity from the c-(Ti$_{0.52}$Al$_{0.48}$)N$_y$ coatings changes preferred orientation from 200 to 111 to 220 accompanied by peak broadening with decreasing N content. The peak broadening is related to the increase in chemical fluctuations as confirmed by APT (Fig. 1) [19,23,32], while the change in orientation is a superposition of effects. An increased N vacancy concentration in the B1 structure leads to a change in the structure factor and thus an increase of the 111/200 diffraction peak intensity ratio in powder X-ray diffraction

[19]. The measured ratios show a dominant 200 diffraction peak for the compositional range $1 > y \geq 0.58$, and a change to a dominant 111 diffraction peak for $y < 0.58$ [19,23]. In the present study, the coatings were deposited on cemented carbide (WC/Co-based) substrates and the 111 diffraction peak is dominant already for sample $y = 0.75$. We suggest that the peak intensity variation recorded for the coatings is a superposition of the effect from a change in the structure factor and a change in preferred orientation when decreasing the N content in c-$(Ti_{0.52}Al_{0.48})N_y$.

It has been reported that the change in preferred orientation of magnetron sputtered TiN films from 001 to 111 when reducing the N_2 partial pressure or when reducing the N_2^+/Ti flux ratio is mainly caused by the change in surface energy, adatoms bonding and adatom diffusion [33,34]. Typical sputter deposition conditions leads to a 111 preferred orientation since the diffusion of Ti adatoms is slow on (111) surfaces. However, the excess of atomic N reduces the Ti diffusion length and lowers the potential on the (001) surface leading to a change in preferential growth to 001 based on *ab initio* studies performed by Gall et al. [33]. In cathodic arc evaporated c-$(Ti_{1-x}Al_x)N$, Hörling *et al.* showed a change in the texture from 111 to 200 by increasing the Al content [11]. This is correlated to a strong dependency of the Al composition on the elastic properties, where an increase in Al content leads to a more covalent nature of the bonds and a greater elastic anisotropy [10]. In addition, a change in adatom surface diffusion occurs when Al-substitution occurs in TiN surfaces [35,36]. Therefore, we suggest that the preferred orientation change in N-deficient c-$(Ti_{0.52}Al_{0.48})N_y$ ($y < 1$) results from the changes in adatom bonding and mobility, since less N gradually changes the bonding toward a metallic character [37] as an Ar/N_2 mixtures were varied during deposition [33].

The residual stresses for samples $y = 0.92$, 0.87 and 0.75 are -0.9 $\pm$ 0.1 GPa, -2.8 $\pm$ 0.4 GPa and -1.7 $\pm$ 0.1 GPa, respectively. The rather small differences in stress values between samples are expected since the deposition conditions are similar. In contrast, a change in the applied bias potential has a more pronounced effect [13]. The amount of macroparticles (quantification is given below) increases when the N content is reduced. Voids are often formed in the vicinity of macroparticles [25,38] that cause stress relaxation. Hence, a direct correlation between changes in stress and N vacancy concentration could not be established.

Fig. 3 shows fractured, cross-sectional view SEM micrographs of samples $y = 0.92$, $y = 0.75$ and $y = 0.46$, respectively. In Fig. 3 (a, b), a dense columnar structure with an average column width

of about 250 nm was observed for the y = 0.92 sample and about 200 nm for the y = 0.75 sample. A more disruptive columnar growth is seen in coatings with lower N content (y = 0.75 in Fig. 3 (b)) caused by the increased number of macroparticles [19,26,38]. A further reduction of the N content, sample y = 0.46 in Fig. 3(c), led to a transition from dense columnar to a glassy-type structure. This microstructure consists of a fine columnar structure, as shown in the dark field STEM-in-SEM micrograph in Fig. 3 (d), having an average column width of about 60 nm. The preferential re-sputtering of Al during rotational deposition is responsible for the layering seen in Fig. 3 (d) [39].
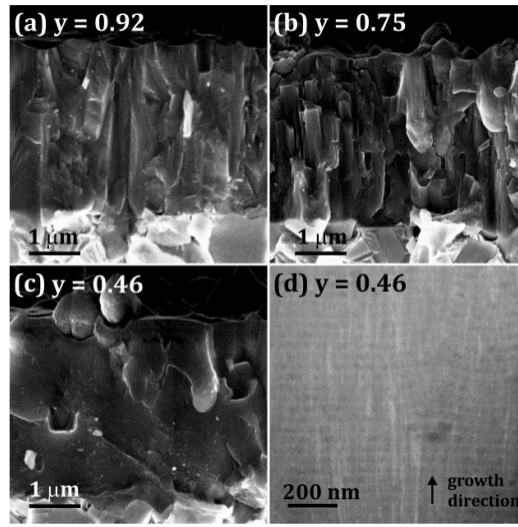

Figure 3. SEM micrographs of fractured cross sections of as-deposited $(Ti_{0.52}Al_{0.48})N_y$ samples (a) y = 0.92, (b) y = 0.75, and (c) y = 0.46 on cemented carbide (WC/Co-based) substrate. (d) Dark field STEM-in-SEM micrograph of sample y = 0.46.

A transition from a dense columnar microstructure to a glassy appearance in c-$(Ti_{0.52}Al_{0.48})N_y$ coatings has been reported for magnetron sputtered $(Ti_{0.5}Al_{0.5})N_y$ (y < 1) coatings when reducing the N_2 flux [27], for arc evaporated $(Ti_{0.5}Al_{0.5})N$ coatings when increasing substrate bias [13], and for arc evaporated TiC_xN_{1-x} coatings when increasing the C content [40]. The increase of built-in defects and change in adatom mobility during deposition lead to an increased probability for re-nucleation causing a breakdown of the column structure [41,42].

Characterization of the macroparticles was performed by analyzing their surface coverage and morphology by SEM [43]. The particles are mostly spherically shaped with an average diameter

of ~1 μm for sample y = 0.92 and 0.87 and they increased in size by reducing the N content further to ~2 μm for samples y = 0.75 and 0.46. Also, larger irregularly shaped particles, with an apparent diameter of up to ~4 μm were seen for sample y = 0.75 and of ~5 μm for sample y = 0.46. The area fraction of macroparticles was found to increase from 5 % to 22 % to 42 % to 54 % with decreasing N-to-metal ratio. The increased amount of macroparticles when the N_2 gas fraction is reduced is consistent with previous publications [26,27,44,45], and with the appearance of *h*-Ti peaks in Fig. 2 for sample y = 0.75 and 0.46.

3.2 Phase evolution and substrate interaction

3.2.1 Samples with N content 0.92 ≥ y ≥ 0.75

X-ray diffractograms of the samples y = 0.92, 0.87 and 0.75 obtained after annealing up to 1200 °C are shown in Fig. 4. All samples exhibit a peak shift to higher 2θ values when annealing from as-deposited to 700 °C which is related to the relaxation of the in plane compressive stresses and recovery processes [8,38]. Further in temperature, samples y = 0.92 (a) and y = 0.87 (b) show spinodal decomposition of *c*-(Ti,Al)N into *c*-TiN and *c*-AlN. This is recognized by an initial broadening of *c*-(Ti,Al)N peaks (for small chemical fluctuations) followed by the appearance of broad *c*-TiN and *c*-AlN peaks [8,46] as it is highlighted by arrows Fig. 4 (a) and (b) and confirmed by APT results in Fig. 5. A more detailed analysis of the spinodal decomposition is given elsewhere [19]. The decomposition temperature range changes as a function of N content. A reduction in N leads to a shift of the phase separation to higher temperatures and prolonged temperature range, i.e. no additional diffraction peaks except those expected for a solid solution *c*-(Ti,Al)N phase are present up to 900 °C and 1100 °C for the (a) y = 0.92 and (b) y = 0.87 samples, respectively. The spinodal decomposition is followed by the transformation of *c*-AlN into *w*-AlN. *w*-AlN peaks are present in sample y = 0.92, 0.87 and 0.75 at 1000 °C, 1200 °C and 1200 °C, respectively. In addition, sample y = 0.75 shows growing intensities of diffraction peaks corresponding to *c*-TiN at T_{max} ≥ 1000 °C coexisting with *c*-(Ti,Al)N, which suggests nucleation and growth of *c*-TiN and *w*-AlN concurrent to spinodal decomposition of *c*-(Ti,Al)N into *c*-TiN and *c*-AlN, similar to the results obtained in substrate-free $(Ti_{0.52}Al_{0.48})N_y$ coatings [19]. The reduction of the driving force for segregation when reducing the N content has previously been discussed in terms of a decreased mixing enthalpy, and an increased entropy caused by a change in phonon dispersion in the presence of N vacancies [19]. The coexistence of *c*-(Ti,Al)N, *c*-TiN and *w*-AlN diffraction peaks in sample

101

y = 0.75 was also observed by to Baben et al. for y ≈ 1, where the enhanced thermal stability via reduction of point defects (metal vacancies) led to concurrent precipitation and growth above > 1100 °C [18].
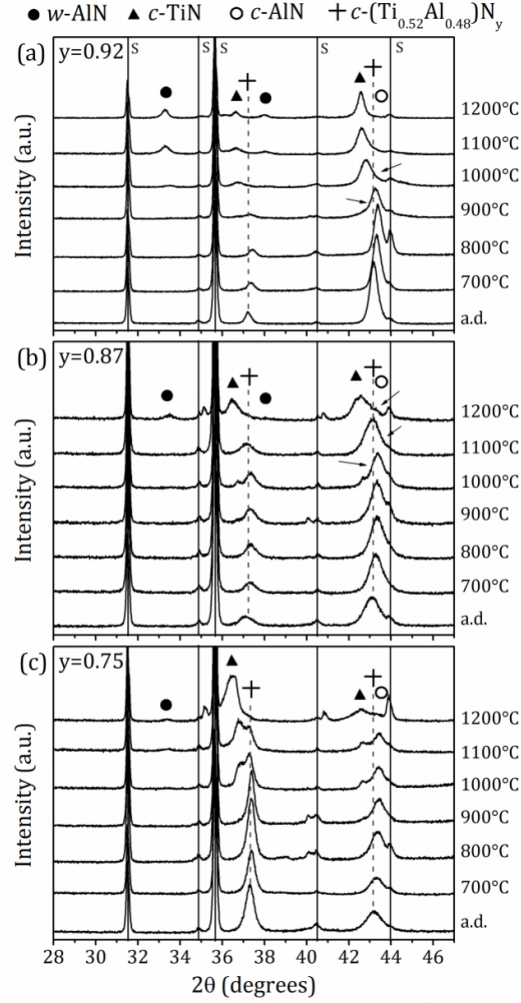

Figure 4. X-ray diffractograms recorded after different annealing temperatures of $(Ti_{0.52}Al_{0.48})N_y$ samples (a) y = 0.92 (b) y = 0.87, and (c) y = 0.75. Vertical lines correspond to substrate cemented carbide (WC/Co) peaks, labeled as "S". Arrows highlight the spinodal decomposition.

Figure 5 shows the effect of decreasing the N content on the microstructure after annealing at 1200 °C. The APT reconstructed tips extracted from the interior of a single column show the coarsest and most decomposed microstructure for sample y = 0.92 followed by samples y = 0.87

and y = 0.75. The reduced driving force for spinodal decomposition in nitrogen-deficient c-(Ti$_{0.52}$Al$_{0.48}$)N$_y$, activates competing phase separation processes such as segregation by nucleation and growth of the stable binary c-TiN and w-AlN phases at the column boundaries [18,19,47–49]. Such column boundary phases (CBP) are highlighted in Fig. 5 (b, c) and Fig. 6 (a) for clarity. The increased presence of macroparticles and column breakdown when the N content is reduced results in an increased volume fraction of column boundaries and consequently of CBP, which is dominant in sample y = 0.75 as confirmed by XRD (Fig. 4 (c)) with the appearance of c-TiN peaks concurrent to the spinodal decomposition.

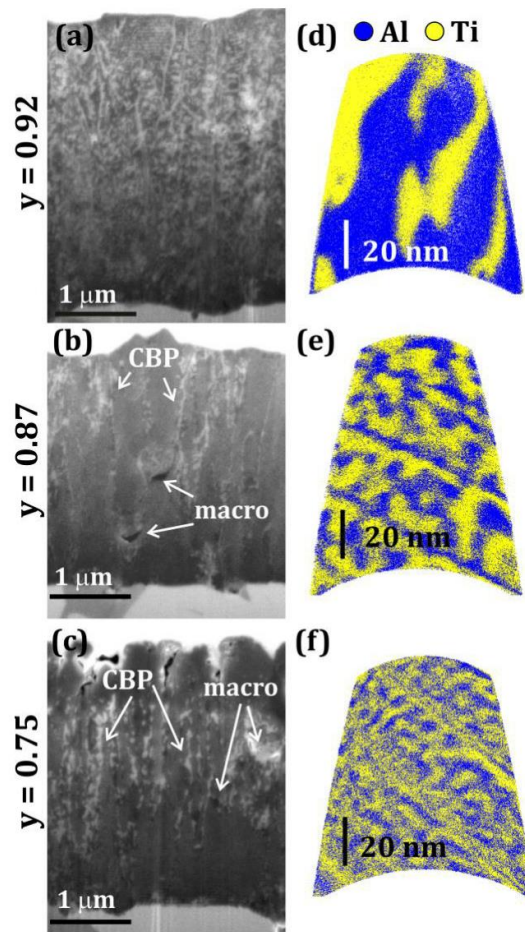*Figure 5. (a - c) SEM micrograph cross sections of (Ti$_{0.52}$Al$_{0.48}$)N$_y$ coatings annealed at 1200˚C for 15 min: (a) y = 0.92, (b) y = 0.87, and (c) y = 0.75. (d - f) Corresponding APT reconstructions from the interior of a column showing only Al and Ti ions for clarity. Key: macro = macroparticle, CPB = column boundary phase.*
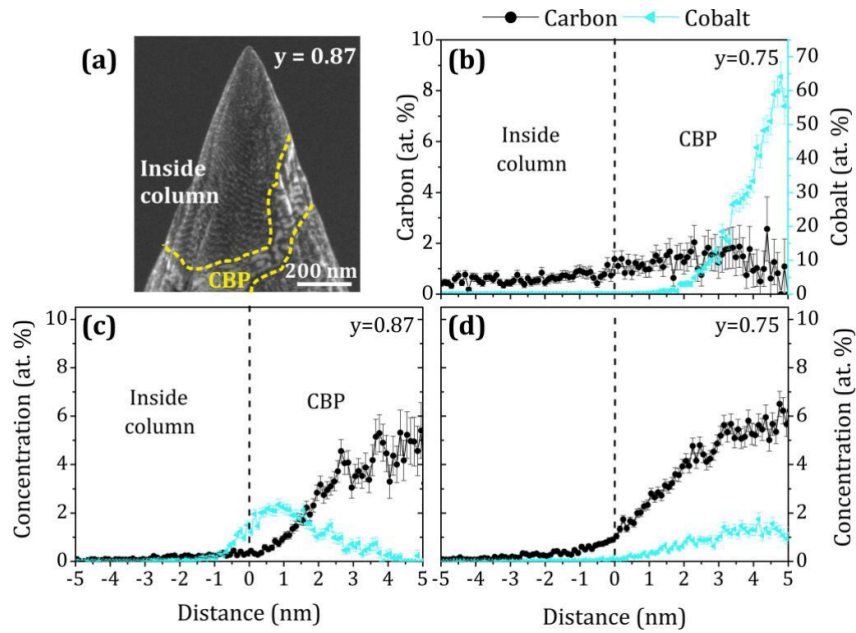
Figure 6. (a) SEM micrograph of an APT tip before run where the column boundary phase (CBP) is highlighted with dotted lines. 1D line profiles of Co and C composition across the column boundary is shown for (a, c) y = 0.87, and (b, d) y = 0.75. Note the different scales.

Interdiffusion of substrate elements occurred during the high temperature anneals. Figure 6 shows APT reconstruction of samples y = 0.87 and y = 0.75 after annealing at 1200 °C. Cobalt and carbon are now present in the films. Their concentrations inside the columns are less than 0.2 at. % for C and 0.1 at. % for Co. However, up to 6 at. % C and up to 65 at. % Co are found in the column boundaries, especially in Ti-rich regions. Some examples of the Co and C concentration profiles inside the CBP are shown in Fig. 6 (b - d). Hörling et al. reported Co diffusion in (Ti,Al)N coatings deposited on WC/Co substrates after annealing at 1250 °C, associated with diffusion along column boundaries and formation of Co-rich islands on the coating surface [38]. Similar observations have been made for other substrate/coating systems, e.g. Choi et al. [50] observed enrichment of substrate elements Fe and V at the grain boundaries in a (Ti,Al)N/CrN multilayer coating, when annealing a coated high speed steel at 1000 °C and Thuvander et al. [51] detected WC/Co substrate elements in as-deposited Ti-Si-Al-C-N coatings close to the substrate/coating interface when grown at 600 °C. Column boundaries are low-density regions and they are expected to be preferred diffusion paths. The low amounts of substrate elements inside the columns compared to the boundaries supports this. An effect of substrate elements on the spinodal decomposition inside the

columns is therefore not expected and the phase evolution follows the trends observed for isolated coating material [19].

3.2.2 Sample with N content y = 0.46

The phase evolution of a highly N-deficient $(Ti_{0.52}Al_{0.48})N_{0.46}$ coating is shown by X-ray diffractograms in Fig. 7, where a different phase formation path is observed compared to the coatings containing more nitrogen ($0.92 \geq y \geq 0.75$). Identification of the peaks and phases was supported by local measurements of the chemical compositions by APT and EDS shown in Fig. 8 and 9.
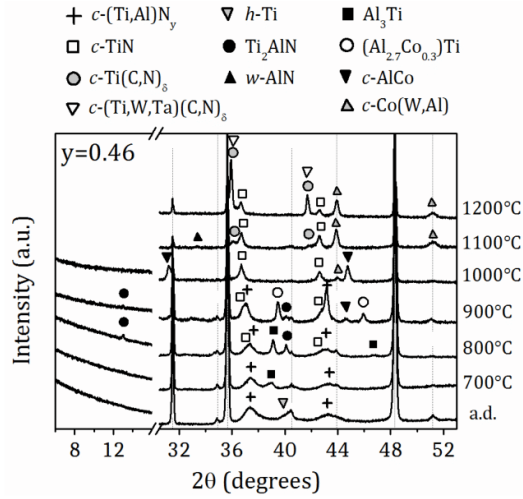

Figure 7. X-ray diffractograms of sample y = 0.46 in the as-deposited state and after annealing at temperatures up to 1200 °C. Vertical lines correspond to substrate peaks, cemented carbide (WC/Co).

A reduction of N in $(Ti,Al)N_y$ increases the driving force for the formation of a metallic Al-Ti mixture [37], which leads to metal segregation, already in the as-deposited state (Fig. 1), as well as the formation of Al_3Ti and the Al depletion of $(Ti,Al)N_y$ when annealed above 700 °C. The formation of Al_3Ti is enhanced by the fast diffusion of N compared to metal atoms [52], preferential diffusion of N to Ti-rich regions [53], and the presence of N vacancies [54]. A further increase in the annealing temperature resulted in the formation of the MAX phase Ti_2AlN (between 700 – 900 °C), which is a diffusion-controlled process with an activation energy similar to that of N diffusion in Ti [55,56]. In addition, *h*-Ti diffraction peaks from macroparticles seen in the as-deposited coating disappear when heated above 700 °C. The reason for this is expected to be

twofold: in-diffusion of N to the macroparticle to form TiN, and out-diffusion of Ti from the macroparticle. The latter acts as a supply of Ti to the surrounding system.

Up to 800 °C the solid state reaction path is similar to what was observed for N-deficient c-$(Ti_{0.52}Al_{0.48})N_y$ powders (y = 0.40 and 0.46) annealed in an Ar atmosphere [23]. Above this temperature, the presence of substrate elements in the coating is observed. The greater amount of N vacancies and the increase in temperature led to a concentration gradient providing enough driving force for the diffusion of substrate elements into the coating, as well as the appearance of new competing phases such as cubic c-AlCo. MAX phase formation is sensitive to element mobility and concentration gradients [57,58], and its destabilization was expected.

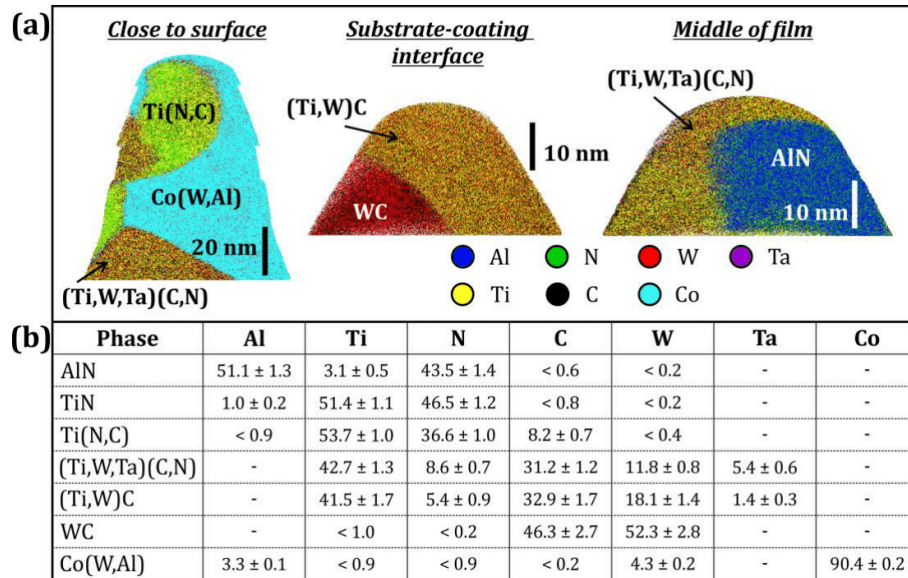| Phase	Al	Ti	N	C	W	Ta	Co
AlN	51.1 ± 1.3	3.1 ± 0.5	43.5 ± 1.4	< 0.6	< 0.2	-	-
TiN	1.0 ± 0.2	51.4 ± 1.1	46.5 ± 1.2	< 0.8	< 0.2	-	-
Ti(N,C)	< 0.9	53.7 ± 1.0	36.6 ± 1.0	8.2 ± 0.7	< 0.4	-	-
(Ti,W,Ta)(C,N)	-	42.7 ± 1.3	8.6 ± 0.7	31.2 ± 1.2	11.8 ± 0.8	5.4 ± 0.6	-
(Ti,W)C	-	41.5 ± 1.7	5.4 ± 0.9	32.9 ± 1.7	18.1 ± 1.4	1.4 ± 0.3	-
WC	-	< 1.0	< 0.2	46.3 ± 2.7	52.3 ± 2.8	-	-
Co(W,Al)	3.3 ± 0.1	< 0.9	< 0.9	< 0.2	4.3 ± 0.2	-	90.4 ± 0.2

Figure 8. Sample y = 0.46 annealed at 1200 °C. (a) Some examples of APT reconstructed tips extracted at different positions along the film thickness, from left to right: close to surface, at the substrate interface and middle of the film. (b) Table with selected phase compositions measured by APT. Impurity elements (O, Ar, Ga) are below 0.3 at. %.

The large number of column boundaries and N vacancies lead to an enhanced diffusion of substrate elements along column boundaries and through the grains, not just of Co and C, but also elements like W and Ta as observed in the EDS map in Fig. 9 (b). Above 1000 °C, cobalt segregates as solid solution fcc Co(W,Al), carbonitrides are formed, and the substitution of W and Ta in the metal sublattice of Ti(C,N) takes place, i.e. c-(Ti,W,Ta)(C,N), as confirmed by APT measurements in

Fig. 8. Substitutions in the metal and nonmetal sublattices of TiN are possible due to the greater amount of N vacancies, the complete miscibility of TiN and TiC already at room temperature [59,60], and its ability to accommodate many different elements as substitutional solutes in the metal lattice [1,61–63]. Weak *w*-AlN peaks are observed at 1100 °C.
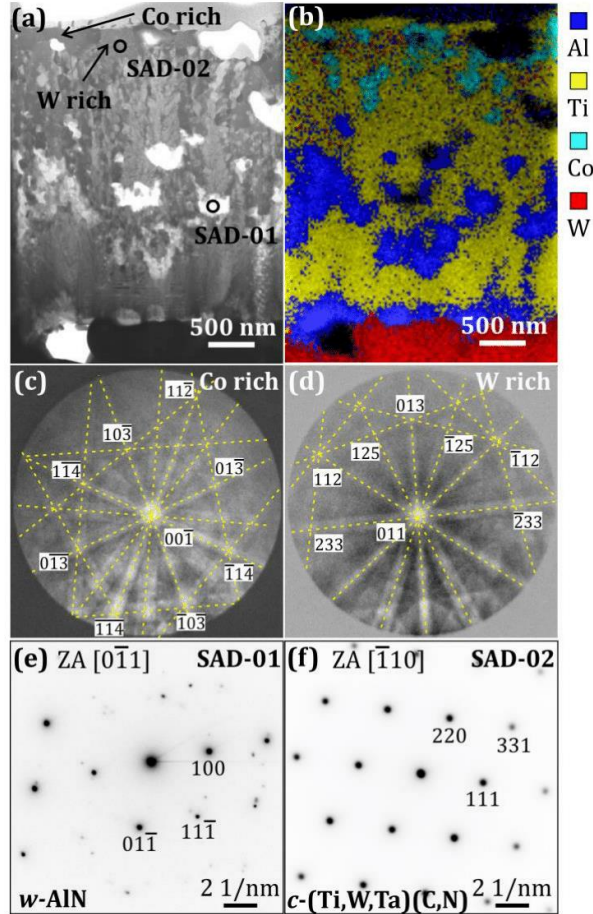

Figure 9. (a) STEM micrograph and, (b) corresponding EDS map of sample y = 0.46 annealed at 1200 °C. EBSD Kikuchi patterns indexed as fcc structures: (c) Co rich grain and (d) W rich grain. Selected area diffraction patterns from (e) w-AlN and (f) c-(Ti,W,Ta)(C,N) grain.

Investigation of the chemical and phase distributions through the thickness of sample y = 0.46 after annealing at 1200 °C was performed by SEM, EDS, EBSD and APT, and the data is shown in Figs. 8 and 9. Given the size of the inhomogeneities in this sample, the volume of a single APT tip is not representative and several tips from different positions along the film thickness were

extracted and measured, some examples are presented in Fig. 8 (a). In addition, previous APT measurements of carbides and carbonitrides [64], and *w*-AlN [19] have shown underestimation of maximum 5 at. % of C or N. This is related to the chemical bonding, overlap of isotopes, high number of multiple events, and detector dead time. Therefore, underestimation of N and C in APT compositions of phases present in this sample (y = 0.46) annealed at 1200 °C, and projection effects in the EDS map must be taken into account during the interpretation of Fig. 8 (b) and Fig. 9 (b), respectively. Despite these uncertainties, it is possible to find trends for the elemental composition of the present phases.

Most of the phases detected by APT are carbonitrides with different N to C ratios as shown in Fig. 8 (b). The more carbon present in the phase, the more W and Ta are observed, while phases with a high amount of N tend to contain less substrate elements. Carbides with a high W content (18 at. %) were found close to the substrate interface, i.e. Ti(W)C (Fig. 8 (a)). These trends are consistent with the high driving force for diffusion of substrate elements through the coating in the presence of N vacancies and the complete miscibility of TiN and TiC [1,59,60]. A Co-rich phase had completely penetrated the coating and was present near the surface.

Figure 9 shows segregations which are rich in Co and W close to the coating surface of sample y = 0.46 after annealing at 1200 °C. These segregations have large enough grains to give high quality Kikuchi patterns for EBSD analysis. Two different grain types were captured, one rich in Co and one rich in W. Both types were indexed as fcc structures and shown in Fig. 9 (c, d). The first corresponds to the solid solution *c*-Co(W,Al) phase with W and Al contents of 4.3 and 3.3 at. %, respectively. A solubility of up to 10 at. % of W and Al is possible according to the ternary Co-W-Al phase diagram of Sato et al. [65]. For the W rich grains, EDS composition measurements yielded the same composition as one of the carbonitride phases measured by APT, *c*-(Ti,W,Ta)(C,N). The lattice parameter of this phase obtained from the selected area diffraction (SAD) pattern in Fig. 9 (f) is ~ 0.443 nm, which is close to that of *c*-Ti(C,N). After this 1200 °C anneal, also a small amount of *w*-AlN was detected by SAD (Fig. 9 (e)) and APT measurement, which was not resolved in XRD.

3.3 Mechanical properties

Hardness values of all samples annealed up to 1200 °C are shown in Fig. 10. The as-deposited hardness was about 31 GPa for samples $0.92 \geq y \geq 0.75$ and substantially lower (21 GPa) for sample $y = 0.46$. We suggest that this hardness drop is dominated by the increased presence of macroparticles as the N content of the c-$(Ti_{0.52}Al_{0.48})N_y$ coatings is reduced, followed by vacancy softening and texture effects. The macroparticle composition tends to be more metallic (see Fig. 7) compared to the nitride coating which in turn leads to an overall softening of its mechanical properties. Nitrogen vacancies have shown to affect the mechanical properties of transition metal nitrides depending on their defect configuration. In case of highly N-deficient TMN, vacancy softening is more likely to occur [1,66]. Finally, as observed by comparing samples $y = 0.92$, 0.87 and 0.75, no texture effects on coating hardness could be detected.
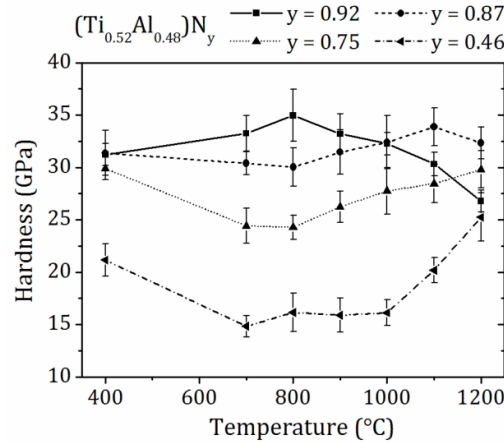

Figure 10. Ex situ hardness versus annealing temperature up to 1200 °C of $(Ti_{0.52}Al_{0.48})N_y$ samples with $y = 0.92$, $y = 0.87$, $y = 0.75$ and $y = 0.46$.

Due to the pronounced effect of macroparticles and the differences in phase evolution between sample $y = 0.46$ and samples $0.92 \geq y \geq 0.75$, the hardness behavior at high temperatures is not comparable. Annealing at 700 °C results in a hardness drop for sample $y = 0.75$, $y = 0.87$ maintains its as-deposited hardness, and sample $y = 0.92$ shows age hardening. Softening of (Ti,Al)N-coatings has been attributed to migration, redistribution and annihilation of lattice defects [67,68] causing a residual stress relaxation [38,46,69,70]. This is consistent with the observed XRD peak shifts to higher 2θ at this temperature. Recrystallization is not expected to occur since no change

in texture is observed [69]. Age hardening is observed in all three samples, and a 300 °C upshift by reducing the N content is consistent with the reduction of driving force for segregation in c-$(Ti_{0.52}Al_{0.48})N_y$ coatings and the suppression of w-AlN formation inside the columns via N vacancies. The preferential nucleation and growth of w-AlN and c-TiN at grain boundaries present no detrimental impact on the hardness for samples y = 0.87 and y = 0.75 in our study, nor for sample y ≈ 1 of to Baben et al. [18]. In contrast to that, sample y = 0.92 shows a decrease in hardness when c-AlN transforms into w-AlN along the entire coating. [8,18]. Instead, a retention of the age hardening effect at higher temperatures is observed for y = 0.87 and y = 0.75 despite the additional diffusion of Co and C along column boundary.

For sample y = 0.46 the drop in hardness from 21 to 15 GPa, between 400 and 1000 °C, is ascribed to defect rearrangement and annihilation mechanisms, accompanied by the formation of phases like, Al_3Ti, Ti_2AlN and c-AlCo. The hardness of Al_3Ti and c-AlCo has been reported to be between 4 to 7 GPa [71,72], which lowers the hardness while Ti_2AlN and (Ti,Al)N make the material harder. The reported hardness for single-crystal Ti_2AlN is 16 GPa [73]. Above 1000 °C, an increase in hardness from 16 to 25 GPa is correlated with the formation of carbonitrides and the dissolution of most of the phases present at lower temperatures. Substitution of N by C in TiC_xN_{1-x} leads to a more covalent bonding, and thus to a bond strengthening [74], while substitution of W and Ta in the metal lattice of the carbonitrides generates a solid solution hardening effect [1]. Phase distribution, precipitation at grain boundaries, crystal structure and grain size, may also play a role in the hardness enhancement at high temperatures, but the strong diffusion of substrate elements and interaction with the coating increase the complexity of data interpretation to a level where these effects cannot be separated.

Based on our investigation, the N fraction that yielded the most substantial improvement of the mechanical properties (age hardening effect) and the lowest effect of column boundaries was sample y = 0.87. We have shown that a reduction of the N content in c-$(Al,Ti)N_y$ coatings is a key factor in suppressing the w-AlN formation inside the columns and in improving its hardness, as well as for controlling the substrate-coating interaction. We suggest N deficiency as a tool for tuning the phase transformation and improving the mechanical properties of TMN coatings.

Conclusions

The N deficiency in as-deposited $(Ti_{0.52}Al_{0.48})N_y$ (y < 1) coatings has proven to be instrumental in changing the microstructure, the phase transformation and the hardness in the presence of cemented carbides (W/Co-based) substrates. In as-deposited state, a reduction in the N content led to an increase in compositional fluctuations, lattice defects and volume fraction of macroparticles, which modified the microstructure from columnar to glassy-like structure, and changed the preferred orientation from 200 to 111 to 220.

Coatings prepared with a N fraction of 0.92 ≥ y ≥ 0.75, revealed a spinodal decomposition mechanism and a corresponding age hardening effect. By reducing N content, a shift to higher temperatures of the age hardening effect by more than 300 °C is consistent with the reduction in driving force for spinodal decomposition of $(Ti_{0.52}Al_{0.48})N_y$ coatings. Nucleation and growth of w-AlN and c-TiN, and segregation of Co and C at the column boundaries seems not to be detrimental to the coating hardness. The nitrogen fraction of y = 0.87 yielded the most substantial improvement. The phase evolution during annealing follows the trends observed in our previous study on isolated coating material.

Coatings with a low N content (y = 0.46) presented an increase in hardness from 16 to 25 GPa and extensive diffusion of substrate elements at elevated temperatures which strongly affects the phase evolution. Above 1000 °C, diffusion along column boundaries results in the formation of a Co rich phase dissolving some W and Al. W and Ta tend to form a solid solution with Ti on one sublattice of a NaCl-structured phase, while having a solid solution of N and C on the other sublattice, e.g. c-Ti(N,C), c-(Ti,W,Ta)(C,N). These phases are responsible for the enhanced hardness. We conclude that the film-substrate interaction is a limiting factor for coating design by N deficiency.

Acknowledgments

References

[1]   H. Holleck, Material selection for hard coatings, J. Vac. Sci. Technol. A Vacuum, Surfaces, Film. 4 (1986) 2661.

[2]   L. Hultman, Thermal stability of nitride thin films, Vacuum. 57 (2000) 1.

[3]   O. Knotek, On structure and properties of sputtered Ti and Al based hard compound films, J. Vac. Sci. Technol. A Vacuum, Surfaces, Film. 4 (1986) 2695.

[4]   H.A. Jehn, S. Hofmann, V.-E. Rückborn, W.-D. Münz, Morphology and properties of sputtered (Ti,Al)N layers on high speed steel substrates as a function of deposition temperature and sputtering atmosphere, J. Vac. Sci. Technol. A. 4 (1986) 2701.

[5]   B. Alling, A. V. Ruban, A. Karimi, L. Hultman, I.A. Abrikosov, Unified cluster expansion method applied to the configurational thermodynamics of cubic Ti1-xAlxN, Phys. Rev. B. 83 (2011) 104203.

[6]   N. Shulumba, O. Hellman, Z. Raza, B. Alling, J. Barrirero, F. Mücklich, et al., Lattice Vibrations Change the Solid Solubility of an Alloy at High Temperatures, Phys. Rev. Lett. 117 (2016) 205502.

[7]   A. Knutsson, J. Ullbrand, L. Rogström, N. Norrby, L.J.S. Johnson, L. Hultman, et al., Microstructure evolution during the isostructural decomposition of TiAlN—A combined in-situ small angle x-ray scattering and phase field study, J. Appl. Phys. 113 (2013) 213518.

[8]   P.H. Mayrhofer, A. Hörling, L. Karlsson, J. Sjölén, T. Larsson, C. Mitterer, et al., Self-organized nanostructures in the Ti-Al-N system, Appl. Phys. Lett. 83 (2003) 2049.

[9]   J.S. Koehler, Attempt to design a strong solid, Phys. Rev. B. 2 (1970) 547.

[10]   F. Tasnádi, I.A. Abrikosov, L. Rogström, J. Almer, M.P. Johansson, M. Odén, Significant elastic anisotropy in Ti1−xAlxN alloys, Appl. Phys. Lett. 97 (2010) 231902.

[11]   A. Hörling, L. Hultman, M. Odén, J. Sjölén, L. Karlsson, Mechanical properties and machining performance of Ti1-xAlxN-coated cutting tools, Surf. Coatings Technol. 191 (2005) 384.

[12]   N. Norrby, L. Rogström, M.P. Johansson-Jõesaar, N. Schell, M. Odén, In situ X-ray scattering study of the cubic to hexagonal transformation of AlN in Ti1-xAlxN, Acta Mater. 73 (2014) 205.

[13]   M. Ahlgren, H. Blomqvist, Influence of bias variation on residual stress and texture in TiAlN PVD coatings, Surf. Coatings Technol. 200 (2005) 157.

[14]   A. Knutsson, M.P. Johansson, L. Karlsson, M. Odén, Thermally enhanced mechanical properties of arc evaporated Ti 0.34Al0.66 N/TiN multilayer coatings, J. Appl. Phys. 108 (2010) 44312.

[15]   H. Lind, R. Forsén, B. Alling, N. Ghafoor, F. Tasnádi, M.P. Johansson, et al., Improving thermal stability of hard coating films via a concept of multicomponent alloying, Appl. Phys. Lett. 99 (2011) 91903.

[16]   R. Rachbauer, D. Holec, P.H. Mayrhofer, Increased thermal stability of Ti-Al-N thin films by Ta alloying, Surf. Coatings Technol. 211 (2012) 98.

[17]   N. Norrby, H. Lind, G. Parakhonskiy, M.P. Johansson, F. Tasnádi, L.S. Dubrovinsky, et al., High pressure and high temperature stabilization of cubic AlN in Ti0.60Al0.40N, J. Appl. Phys. 113 (2013) 53515.

[18]   M. to Baben, M. Hans, D. Primetzhofer, S. Evertz, H. Ruess, J.M. Schneider, Unprecedented thermal stability of inherently metastable titanium aluminum nitride by point defect engineering, Mater. Res. Lett. (2016) 1–12.

[19]   I.C. Schramm, M.P. Johansson Jõesaar, J. Jensen, F. Mücklich, M. Odén, Impact of nitrogen vacancies on the high temperature behavior of (Ti1−xAlx)Ny alloys, Acta Mater. 119 (2016) 218.

[20]   L. Rogström, M.P. Johansson, N. Ghafoor, L. Hultman, M. Odén, Influence of chemical composition and deposition conditions on microstructure evolution during annealing of arc evaporated ZrAlN thin film, J. Vac. Sci. Technol. A. 30 (2012) 31504.

[21]   K. Thompson, D. Lawrence, D.J. Larson, J.D. Olson, T.F. Kelly, B. Gorman, In situ site-specific specimen preparation for atom probe tomography, Ultramicroscopy. 107 (2007) 131.

[22]   D.R. Kingham, The post-ionization of field evaporated ions: A theoretical explanation of multiple charge states, Surf. Sci. Lett. 116 (1982) 273.

[23]   I.C. Schramm, C. Pauly, M.P. Johansson Jõesaar, P. Eklund, J. Schmauch, F. Mücklich, et al., Solid state formation of Ti4AlN3 in cathodic arc deposited (Ti1-xAlx)Ny alloys, Acta Mater. 129 (2017) 268.

[24]   W.C. Oliver, G.M. Pharr, An improved technique for determining hardness and elastic modulus using load and displacement sensing indentation experiments, J. Mater. Res. 7 (1992) 1564.

[25]   L. Karlsson, L. Hultman, M.P. Johansson, J.-E. Sundgren, H. Ljungcrantz, Growth, microstructure, and mechanical properties of arc evaporated TiCxN1−x (0≤x≤1) films, Surf. Coatings Technol. 126 (2000) 1.

[26]   J. Bujak, J. Walkowicz, J. Kusiński, Influence of the nitrogen pressure on the structure and

properties of (Ti,Al)N coatings deposited by cathodic vacuum arc PVD process, Surf. Coatings Technol. 180–181 (2004) 150.

[27] B.-Y. Shew, J.-L. Huang, The effects of nitrogen flow on reactively sputtered Ti-Al-N films, Surf. Coatings Technol. 71 (1995) 30.

[28] M. to Baben, L. Raumann, D. Music, J.M. Schneider, Origin of the nitrogen over- and understoichiometry in Ti0.5Al0.5N thin films, J. Physics. Condens. Matter. 24 (2012) 155401.

[29] J.B. Nelson, D.P. Riley, An experimental investigation of extrapolation methods in the derivation of accurate unit-Cell dimensions of crystals, Proc. Phys. Soc. 57 (1945) 160.

[30] N.J. Ashley, R.W. Grimes, K.J. McClellan, Accommodation of non-stoichiometry in TiN1-x and ZrN1-x, J. Mater. Sci. 42 (2007) 1884.

[31] M. Odén, L. Rogström, A. Knutsson, M.R. Terner, P. Hedström, J. Almer, et al., In situ small-angle x-ray scattering study of nanostructure evolution during decomposition of arc evaporated TiAlN coatings, Appl. Phys. Lett. 94 (2009) 53114.

[32] B.D. Cullity, S.R. Stock, Elements of X-Ray Diffraction, Third, Prentice Hall PTR, 2001.

[33] D. Gall, S. Kodambaka, M.A. Wall, I. Petrov, J.E. Greene, Pathways of atomistic processes on TiN(001) and (111) surfaces during film growth: An ab initio study, J. Appl. Phys. 93 (2003) 9086.

[34] S. Mahieu, D. Depla, Reactive sputter deposition of TiN layers: modelling the growth by characterization of particle fluxes towards the substrate, J. Phys. D. Appl. Phys. 42 (2009) 53002.

[35] B. Alling, P. Steneteg, C. Tholander, F. Tasnádi, I. Petrov, J.E. Greene, et al., Configurational disorder effects on adatom mobilities on Ti1-xAlxN(001) surfaces from first principles, Phys. Rev. B - Condens. Matter Mater. Phys. 85 (2012) 245422.

[36] C. Tholander, B. Alling, F. Tasnádi, J.E. Greene, L. Hultman, Effect of Al substitution on Ti, Al, and N adatom dynamics on TiN(001), (011), and (111) surfaces, Surf. Sci. 630 (2014) 28.

[37] B. Alling, A. Karimi, L. Hultman, I.A. Abrikosov, First-principles study of the effect of nitrogen vacancies on the decomposition pattern in cubic Ti1−xAlxN1−y, Appl. Phys. Lett. 92 (2008) 71903.

[38] A. Hörling, L. Hultman, M. Odén, J. Sjölén, L. Karlsson, Thermal stability of arc evaporated high aluminum-content Ti1−xAlxN thin films, J. Vac. Sci. Technol. A. 20 (2002) 1815.

[39] A.O. Eriksson, J.Q. Zhu, N. Ghafoor, M.P. Johansson, J. Sjölen, J. Jensen, et al., Layer formation by resputtering in Ti–Si–C hard coatings during large scale cathodic arc deposition, Surf. Coatings Technol. 205 (2011) 3923.

[40] L. Karlsson, L. Hultman, J.-E. Sundgren, Influence of residual stresses on the mechanical

properties of TiCxN1-x (x = 0, 0.15, 0.45) thin films deposited by arc evaporation, Thin Solid Films. 20371 (2000) 167.

[41]   G. Håkansson, J.-E. Sundgren, D. McIntyre, J.E. Greene, W.-D. Münz, Microstructure and physical properties of polycrystalline metastable Ti0.5Al0.5N alloys grown by D.C. magnetron sputter deposition, Thin Solid Films. 153 (1987) 55.

[42]   I. Petrov, P.B. Barna, L. Hultman, J.E. Greene, Microstructural evolution during film growth, J. Vac. Sci. Technol. A. 21 (2003) S117.

[43]   A.O. Eriksson, I. Zhirkov, M. Dahlqvist, J. Jensen, L. Hultman, J. Rosen, Characterization of plasma chemistry and ion energy in cathodic arc plasma from Ti-Si cathodes of different compositions, J. Appl. Phys. 113 (2013) 163304.

[44]   M. Li, F. Wang, Effects of nitrogen partial pressure and pulse bias voltage on (Ti,Al)N coatings by arc ion plating, Surf. Coatings Technol. 167 (2003) 197–202. doi:10.1016/S0257-8972(02)00895-2.

[45]   C. Chokwatvikul, S. Larpkiattaworn, S. Surinphong, Effect of Nitrogen Partial Pressure on Characteristic and Mechanical Properties of Hard Coating TiAlN Film, J. Met. Mater. Miner. 21 (2011) 115–119.

[46]   L. Rogström, J. Ullbrand, J. Almer, L. Hultman, B. Jansson, M. Odén, Strain evolution during spinodal decomposition of TiAlN thin films, Thin Solid Films. 520 (2012) 5542.

[47]   J.W. Cahn, On spinodal decomposition, Acta Metall. 9 (1961) 795.

[48]   R. Rachbauer, S. Massl, E. Stergar, D. Holec, D. Kiener, J. Keckes, et al., Decomposition pathways in age hardening of Ti-Al-N films, J. Appl. Phys. 110 (2011) 23515.

[49]   R. Forsén, N. Ghafoor, M. Odén, Coherency strain engineered decomposition of unstable multilayer alloys for improved thermal stability, J. Appl. Phys. 114 (2013) 244303.

[50]   P.P. Choi, I. Povstugar, J.P. Ahn, A. Kostka, D. Raabe, Thermal stability of TiAlN/CrN multilayer coatings studied by atom probe tomography, Ultramicroscopy. 111 (2011) 518.

[51]   M. Thuvander, G. Östberg, M. Ahlgren, L.K.L. Falk, Atom probe tomography of a Ti–Si–Al–C–N coating grown on a cemented carbide substrate, Ultramicroscopy. (2015) 1.

[52]   H. Matzke, Diffusion in Carbides and Nitrides: Unsolved Problems, Defect Diffus. Forum. 83 (1992) 111.

[53]   X. He, S. Yang, K. Tao, Y. Fan, Investigation of the interface reactions of Ti thin films with AlN substrate, J. Mater. Res. 12 (1996) 846–851.

[54]   K. Shinozuka, M. Susa, M. Takayuki, K. Nagata, Nitrogen Diffusion in δ-TiN and α-Ti(N) at High Pressures, Defect Diffus. Forum. 143–147 (1997) 1237–1242.

[55]   Y. Imanaka, M.R. Notis, Interface reactions between titanium thin films Aluminium Nitride Substrates, J. Am. Ceram. Soc. 82 (1999) 1547.

[56] C. Höglund, M. Beckers, N. Schell, J. Borany, Topotaxial growth of Ti2AlN by solid state reaction in AlN⁄Ti(0001) multilayer thin films, Appl. Phys. Lett. 90 (2007) 174106.

[57] O. Wilhelmsson, J.P. Palmquist, E. Lewin, J. Emmerlich, P. Eklund, P.O.Å. Persson, et al., Deposition and characterization of ternary thin films within the Ti-Al-C system by DC magnetron sputtering, J. Cryst. Growth. 291 (2006) 290.

[58] V. Dolique, M. Jaouen, T. Cabioc'h, F. Pailloux, P. Guérin, V. Pélosin, Formation of (Ti,Al)N⁄Ti2AlN multilayers after annealing of TiN⁄TiAl(N) multilayers deposited by ion beam sputtering, J. Appl. Phys. 103 (2008) 83527.

[59] C. Agte, K. Moers, Methoden zur Reindarstellung hochschmelzender Carbide, Nitride und Boride und Beschreibung einiger ihrer Eigenschaften, Zeitschrift Für Anorg. Und Allg. Chemie. 198 (1931) 233.

[60] W. Lengauer, S. Binder, K. Aigner, P. Ettmayer, A. Guillou, J. Debuigne, et al., Solid state properties of group IVb carbonitrides, J. Alloys Compd. 217 (1995) 137.

[61] H. Randhawa, Cathodic arc plasma deposition technology, Thin Solid Films. 167 (1988) 175.

[62] R. Forsén, M. Johansson, M. Odén, N. Ghafoor, Decomposition and phase transformation in TiCrAlN thin coatings, J. Vac. Sci. Technol. A. 30 (2012) 61506.

[63] R. Rachbauer, D. Holec, P.H. Mayrhofer, Increased thermal stability of Ti–Al–N thin films by Ta alloying, Surf. Coatings Technol. 211 (2012) 98.

[64] M. Thuvander, J. Weidow, J. Angseryd, L.K.L. Falk, F. Liu, M. Sonestedt, et al., Quantitative atom probe analysis of carbides, Ultramicroscopy. 111 (2011) 604.

[65] J. Sato, T. Omori, K. Oikawa, I. Ohnuma, R. Kainuma, K. Ishida, Cobalt-Base High-Temperature Alloys, Science (80-.). 312 (2006) 90.

[66] S.-H. Jhi, S.G. Louie, M.L. Cohen, J. Ihm, Vacancy hardening and softening in transition metal carbides and nitrides, Phys. Rev. Lett. 86 (2001) 3348.

[67] K. Grönhagen, J. Ågren, M. Odén, Phase-field modelling of spinodal decomposition in TiAlN including the effect of metal vacancies, Scr. Mater. 95 (2015) 42.

[68] F. Tasnádi, A. V. Lugovskoy, M. Odén, I.A. Abrikosov, Non-equilibrium vacancy formation energies in metastable alloys — A case study of Ti0.5Al0.5N, Mater. Des. 114 (2017) 484.

[69] H. Oettel, R. Wiedemann, S. Preißler, Residual stresses in nitride hard coatings prepared by magnetron sputtering and arc evaporation, Surf. Coatings Technol. 74 (1995) 273.

[70] J.P. Schaffer, A.J. Perry, J. Brunner, Defects in hard coatings studied by positron annihilation spectroscopy and x-ray diffraction, J. Vac. Sci. Technol. A. 10 (1992) 193.

[71] T. Hausöl, V. Maier, C.W. Schmidt, M. Winkler, H.W. Höppel, M. Göken, Tailoring Materials Properties by Accumulative Roll Bonding, Adv. Eng. Mater. 12 (2010) 740.

[72] R. Webler, M. Ziener, S. Neumeier, P.J. Terberger, R. Vaßen, M. Göken, Evolution of microstructure and mechanical properties of coated Co-base superalloys during heat treatment and thermal exposure, Mater. Sci. Eng. A. 628 (2015) 374.

[73] J. Joelsson, a. Höfling, J. Birch, L. Hultman, Single-crystal Ti2AlN thin films, Appl. Phys. Lett. 86 (2005) 1–3. doi:10.1063/1.1882752.

[74] L. Karlsson, L. Hultman, M.P. Johansson, J.-E. Sundgren, H. Ljungcrantz, Growth, microstructure, and mechanical properties of arc evaporated TiCxN1−x (0 ≤ x ≤ 1) films, Surf. Coatings Technol. 126 (2000) 1.

Paper IV

Enhanced thermal stability and mechanical properties
of nitrogen deficient titanium aluminum nitride
$(Ti_{0.54}Al_{0.46}N_y)$ thin films
by tuning the applied negative bias voltage

K.M. Calamba, I.C. Schramm, M.P. Johansson Jõesaar,

J. Ghanbaja, J.F. Pierson, F. Mücklich and M. Odén.

Enhanced thermal stability and mechanical properties of nitrogen deficient titanium aluminum nitride (Ti$_{0.54}$Al$_{0.46}$N$_y$) thin films by tuning the applied negative bias voltage

K. M. Calamba,[1,2,a)] I. C. Schramm,[1,3] M. P. Johansson Jõesaar,[1,4] J. Ghanbaja,[2] J. F. Pierson,[2] F. Mücklich,[3] and M. Odén[1]

[1]*Nanostructured Materials, Department of Physics, Chemistry and Biology (IFM), Linköping University, Linköping SE 58183, Sweden*
[2]*Institut Jean Lamour (UMR CNRS 7198), Université de Lorraine, Nancy 54011, France*
[3]*Functional Materials, Department Materials Science, Saarland University, Saarbrucken 66041, Germany*
[4]*SECO Tools AB, Fagersta SE-73782, Sweden*

Aspects on the phase stability and mechanical properties of nitrogen deficient (Ti$_{0.54}$Al$_{0.46}$)N$_y$ alloys were investigated. Solid solution alloys of (Ti,Al)N were grown by cathodic arc deposition. The kinetic energy of the impinging ions was altered by varying the substrate bias voltage from -30 V to -80 V. Films deposited with a high bias value of -80 V showed larger lattice parameter, finer columnar structure, and higher compressive residual stress resulting in higher hardness than films biased at -30 V when comparing their as-deposited states. At elevated temperatures, the presence of nitrogen vacancies and point defects (anti-sites and self-interstitials generated by the ion-bombardment during coating deposition) in (Ti$_{0.54}$Al$_{0.46}$)N$_{0.87}$ influence the driving force for phase separation. Highly biased nitrogen deficient films have point defects with higher stability during annealing, which cause a delay of the release of the stored lattice strain energy and then accelerates the decomposition tendencies to thermodynamically stable *c*-TiN and *w*-AlN. Low biased nitrogen deficient films have retarded phase transformation to *w*-AlN, which results in the prolongment of age hardening effect up to 1100 °C, i.e., the highest reported temperature for Ti-Al-N material system. Our study points out the role of vacancies and point defects in engineering thin films with enhanced thermal stability and mechanical properties for high temperature hard coating applications. *Published by AIP Publishing.* [http://dx.doi.org/10.1063/1.4986350]

I. INTRODUCTION

Investigation on the thermal stability of transition metal nitride thin films is of importance because it is a key factor in determining their distinctive physical properties, e.g., hardness, wear resistance, and electrical properties.[1–3] Among the metal nitrides, titanium aluminum nitride (Ti,Al)N based coating has remained as an outstanding material system partly due to its excellent high temperature resistance combined with an age hardening behavior resulting in good wear resistance.[2,4] The latter is based on a spinodal decomposition of the metastable cubic (*c*) solid solution *c*-(Ti,Al)N[5] into isostructurally coherent *c*-TiN and *c*-AlN rich domains at elevated temperatures.[6,7] The latter generates a hardness enhancement and hence improved mechanical properties of the *c*-(Ti,Al)N due to fluctuating strain fields[8] caused by coherency strains[9] and elastic stiffness differences[10,11] that obstruct dislocation motion. At even higher thermal loads, however, the *c*-AlN transform into its most stable phase, i.e., wurtzite *w*-AlN,[12] which is detrimental for the mechanical properties of the coating.[13] Suppressing or delaying the *w*-AlN formation is therefore expected to enhance the thermal stability and the mechanical properties of (Ti,Al)N thin film and extend its operational envelope to higher temperatures.

Ab initio calculations on *c*-Ti$_{1-x}$Al$_x$N$_{1-y}$ ($0 \leq x$, $y \leq 1$) have shown that nitrogen vacancies (V$_N$) has significant effect on the driving force for decomposition and the preferred decomposition direction.[14] This was experimentally confirmed by Schramm *et al.*,[15] where the presence of V$_N$ enhanced the phase stability, i.e., delaying the onset of decomposition of cathodic arc evaporated (Ti,Al)N$_y$ ($y < 1$). It was shown that the onset of *w*-AlN phase transformation in (Ti$_{0.52}$Al$_{0.48}$)N$_{0.87}$,[15] occurred at about 1200 °C, which is about 300 °C higher than what typically is reported for stoichiometric (Ti$_{0.5}$Al$_{0.5}$)N thin films.[16,17] Primary decomposition occurs on the metal sublattice, and Baben *et al.*[18] also reports an improved thermal stability of close to stoichiometric (Ti,Al)N$_y$ ($y \approx 1$) as compared to over-stoichiometric (Ti,Al)N$_y$ ($y > 1$). The faster decomposition in over-stoichiometric ($y > 1$) films is attributed to an enhanced diffusivity in the presence of metal vacancies. It has to be noted that in addition to vacancies, structural modifications in the film such as lattice strain also play a decisive role in determining its thermal stability since it is correlated to the energetic balance during the decomposition process of cubic ternary transition metal nitride.[19,20] Another approach to control the structure and properties of coatings is through the substrate bias condition.[21–23] It is well known that the bias determines the kinetic energy of the ions bombarding the growing film. In this context, cathodic arc deposition is

---

a)Electronic mail: katherine.calamba@liu.se.

122, 065301-1

advantageous since its plasma typically comprises a high degree of ionized metal vapor, and therefore, tuning the negative bias is an effective means to change the arrival energy of the condensing species[24] and hence also the microstructure and its point defect density (interstitials and anti-sites).[25]

In this study, the influence of such point defects in combination with nitrogen vacancies on the thermal stability of cathodic arc deposited $Ti_{0.54}Al_{0.46}N_{0.87}$ thin films were investigated. The Ti/Al ratio and amount of nitrogen vacancies was fixed at a level found by Schramm *et al.*[15] to yield substantially improved phase stability. The substrate bias voltage was varied from -30 V to -80 V in reference to the anode potential. At elevated temperatures, high biased films presented an enhanced phase separation while low biased films showed the highest phase stability. It is noteworthy that the age hardening effect of these coatings is retained to a temperature higher than ever before reported for Ti-Al-N materials. This paper also highlights the interplay between nitrogen vacancies and microstructure on transformation kinetics, which is of relevance for the understanding of metastable transition metal nitrides' thermal stability and mechanical properties.

II. MATERIAL AND METHODS

$(Ti_{1-x}Al_x)N_y$ films were deposited using an industrial scale (Metaplas MZR-323) reactive cathodic arc deposition system. A powder metallurgical manufactured $Ti_{0.45}Al_{0.55}$ cathode with a diameter of 100 mm was used as a target. Fe foils (Goodfellow Cambridge, Ltd., FE000400) and polished cemented carbide (WC-Co) inserts (12 wt. % Co, ISO SNUN120408) were used as substrates. The substrates were cleaned in an alkaline solution prior to inserting the substrates in the deposition chamber. In the chamber, they were mounted on a rotating cylinder fixture (3 rpm) facing the cathode. Pure N_2 was used to obtain $(Ti_{1-x}Al_x)N$ reference samples with compositions close to stoichiometric value[15] while an atmosphere mixture of 40% $N_2/(Ar + N_2)$ was used to synthesize the nitrogen deficient coatings. During deposition, a total gas pressure of 2 Pa was used for both conditions. The flow rates of N_2 and Ar were set to 120 sccm and 180 sccm, respectively, to obtain the 40% $N_2/(Ar + N_2)$ mixture, and the gasses were introduced through pipes positioned vertically in the chamber. An arc current of 13.7 A was required to achieve stable deposition conditions, which resulted in plasma heating of the substrates. To improve coating adhesion, additional heating was supplied by a heater positioned on the chamber wall. Collectively this resulted in a deposition temperature of 550 °C. Thin films were grown to a thickness of about 3 μm with a deposition rate of 250 nm/min. All deposition conditions were kept constant between depositions for each deposition atmosphere, except for the substrate bias voltage that was set to -30 V, -43 V, -55 V, -68 V, or -80 V for the different coatings.

A differential scanning calorimeter (DSC, Netsch STA 449C) was used to examine the thermal response of the as-deposited films. Powder samples were used in the analysis and extracted from the coatings deposited on the Fe foils. Powder samples were obtained by first thinning of the Fe foil by mechanical grinding its backside and then dissolving it

in concentrated (37%) HCl.[26] DSC measurements were performed with two heating cycles, in which the second cycle was used as baseline correction. The sample mass used per run was 30 mg. The powder samples were initially outgassed for 1 h at 250 °C after which the measurement started by heating up the sample to 1400 °C in 50 sccm flow of Ar. The heating and cooling rates were kept constant at 20 °C/min.

X-ray diffractograms of the powdered samples and coatings on substrates recorded with a PANalytical X'Pert PRO MRD diffractometer and were used for phase analysis. Residual stress measurements of the coatings on substrates were obtained using a PANalytical Empyrean diffractometer. The $\sin^2\psi$ method was used to determine the strain state in the coating using the 422 diffraction line. The elastic constants used to convert the strain measurements to stress are $E = 460$ GPa and $\nu = 0.20$, obtained from *ab initio* calculations.[10] All x-ray diffractometry measurements were performed using Cu K_α radiation.

Isothermal annealing of the thin films deposited on the WC-Co substrates was performed in a tube furnace under vacuum with a base pressure of 7×10^{-4} Pa. The samples were held for 15 min at the maximum temperature of either 800 °C, 900 °C, 1000 °C, 1100 °C, or 1200 °C. The heating and cooling rates were set to 20 °C/min.

Morphological and microstructural characterizations of the thin films were performed using a scanning electron microscope (SEM) (FEI Helios nanolab 600), scanning transmission electron microscope (STEM), energy-filtered analytical transmission electron microscopes (EFTEM) (JEOL ARM 200 Cold FEG), and analytical transmission electron microscope (TEM) (Fei Tecnai G^2 TF 20 UT). The analytical TEM was used to obtain the selected area electron diffraction (SAED) images. A focus ion beam (FIB) integrated in the SEM was used for producing cross section cuts. Both TEMs were operated at an acceleration voltage of 200 kV. Cross sectional TEM samples were prepared through mechanical grinding and polishing, followed by sputter etching (Gatan 691 precision ion polishing system) until the sample was electron transparent (<100 nm).

The 3D chemical composition was obtained from a local electrode atom probe (Cameca LEAP 3000 X HR) operated in the laser mode with a wavelength of 532 nm, a pulse frequency of 200 kHz, and a pulse energy of 0.5 nJ. The evaporation rate was set to 5 atoms per 1000 laser pulses, and the sample was set to a ground temperature of 60 K. Data reconstruction was performed in the IVAS package (version 3.6.8, Cameca) using the voltage mode. The reconstruction parameters were obtained using Kingham curves[27] and SEM images of the tip before and after run, where an evaporation field of 40 V per nm and a field factor between 3.5 and 3.8 were obtained. Atom probe tomography (APT) tips were produced using the FIB equipment via the standard lift out technique.[28]

The hardness values of the coatings were measured using UMIS nanoindenter equipped with a Berkovich diamond tip. Depth-sensing indentation was performed on polished tapered cross-sections of the coatings using a maximum load of 50 mN. The indentation depths for this amount of load were around 250 nm, which is less than 10% of the film's thickness.

TABLE I. Composition of $(Ti_{1-x}Al_x)N_y$ films in an atmosphere mixture of 40% $N_2/(Ar + N_2)$ at different negative bias voltages.

Bias voltage (V)	$x = Al/(Al + Ti)$	$y = N/(Al + Ti)$
−30	0.46 ± 0.01	0.87 ± 0.02
−43	0.46 ± 0.01	0.87 ± 0.01
−55	0.46 ± 0.02	0.87 ± 0.03
−68	0.46 ± 0.01	0.86 ± 0.01
−80	0.46 ± 0.01	0.87 ± 0.02

The average hardness values were extracted from the load-displacement curves using the Oliver and Pharr method.[29] At least 30 indents for were used for each samples, and fused silica was used as reference to compute the contact area of the tip versus penetration depth.

III. RESULTS

The chemical composition of as-deposited $(Ti_{1-x}Al_x)N_y$ films deposited in an atmosphere mixture of 40% $N_2/(Ar + N_2)$ at different negative bias voltages is shown in Table I. The composition values were obtained via APT, and only the main elements (Al, Ti, and N) were used for the values of $x = Al/(Al + Ti)$ and $y = N/(Al + Ti)$. These films are referred as the nitrogen deficient samples. The total content of impurity elements such as O, C, and Ar is less than 0.5 at. %. Results show that the chemical composition of the thin films is not altered with the variation of the bias voltage.

The X-ray diffraction patterns of the nitrogen deficient $(Ti_{0.54}Al_{0.46})N_{0.87}$ films at different bias voltage are shown in Fig. 1(a). The XRD peaks at 37.16°, 43.15°, and 62.66° correspond to the c-(Ti,Al)N 111, 200, and 220 diffraction peaks, respectively. The other peaks originate from the WC-Co substrate. XRD reveals that the bias voltage does not alter the phase composition and all as-deposited $(Ti_{0.54}Al_{0.46})N_{0.87}$ thin films have of a single phase with cubic NaCl-structure. Diffractograms show that an increase in the bias voltage leads to a small shift to lower 2θ values. Peak shifts are mainly caused by strain or by compositional changes.[30] APT measurements show that the elemental compositions of the films are not altered by bias voltage; thus, the observed shifts are attributed to changes in compressive stress. The measured compressive residual stresses of the films biased at −30 V, −55 V, and −80 V are −2.8 ± 0.4 GPa, −2.9 ± 0.8 GPa, and

−5.6 ± 1 GPa, respectively. The increase in compressive stress is accompanied with line broadening, which indicates increasing microstrains. The high compressive residual stress in the as-deposited films with increased negative bias voltage has been observed for several materials synthesized by cathodic arc deposition.[21,23,31] In addition, a clear decrease in the 200 peak intensity and a change of preferred orientation to (111) and (220) are observed as a consequence of increasing the negative substrate bias voltage. The X-ray diffractograms of the $(Ti_{0.54}Al_{0.46})N$ reference samples [Fig. 1(b)] also show that they also crystallize in the cubic structure in the as-deposited state [Fig. 1(b)]. These films also exhibit peak shifts and line broadening when the applied bias voltage is increased, similar with the nitrogen deficient samples. The relative intensity of the 220 peak is more pronounced under high biasing conditions. The peak intensity ratio I^{111}/I^{200} of the nitrogen deficient coatings is higher as compared to the reference samples.

The surface morphologies of the as-deposited $(Ti_{0.54}Al_{0.46})N_{0.87}$ films with two different bias voltages (−30 V and −80 V) are presented in Figs. 2(a) and 2(b). SEM micrographs reveal that macroparticle density and diameter decrease with increasing biased voltage resulting in smoother surfaces. The corresponding microstructures of the films biased at −30 V and −80 V are shown in Figs. 2(c) and 2(d), respectively. Cross sectional TEM micrographs show that highly biased films have finer columnar structure. The sample biased at −80 V has a column width of $0.21 \pm 0.04 \mu m$ while that biased at −30 V has a width of $0.57 \pm 0.12 \mu m$. The measured column widths are typical for (Ti,Al)N films deposited via arc technique and their decrease with increasing bias has been also observed in previously.[32,33] The SAED patterns of the coatings biased at −30 V and −80 V confirm that the films all have cubic structure in the as deposited state, in agreement with the XRD results.

The heat flow responses of $(Ti_{0.54}Al_{0.46})N_y$ samples synthesized at different bias voltages were evaluated by DSC as shown in Fig. 3. The $(Ti_{0.54}Al_{0.46})N_{0.87}$ coating biased at −30 V has a broad peak (T_1) at 900 °C (in 600 °C to 1100 °C range) while the sample biased at −80 V has peak at 800 °C (in 500 °C to 1000 °C range). These peaks correspond to several exothermic reactions, including recovery processes of lattice point defect complexes at different activation energies and phase separation via spinodal decomposition of
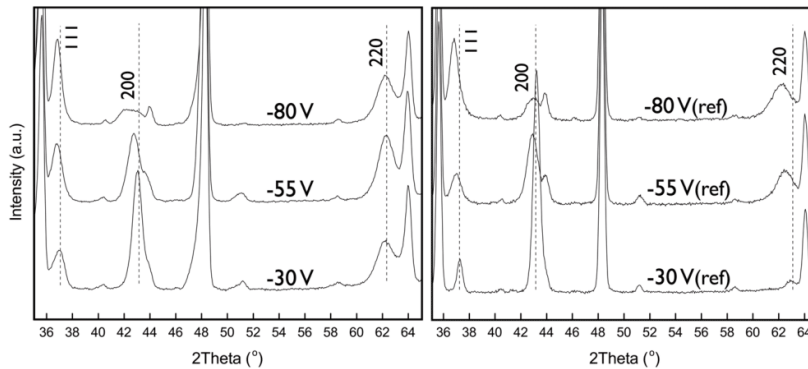

FIG. 1. X-ray diffractograms of as-deposited $(Ti_{0.54}Al_{0.46})N_y$ (a) nitrogen deficient and (b) reference coatings at different negative bias voltages. The unmarked peaks originate from the WC-Co substrate.

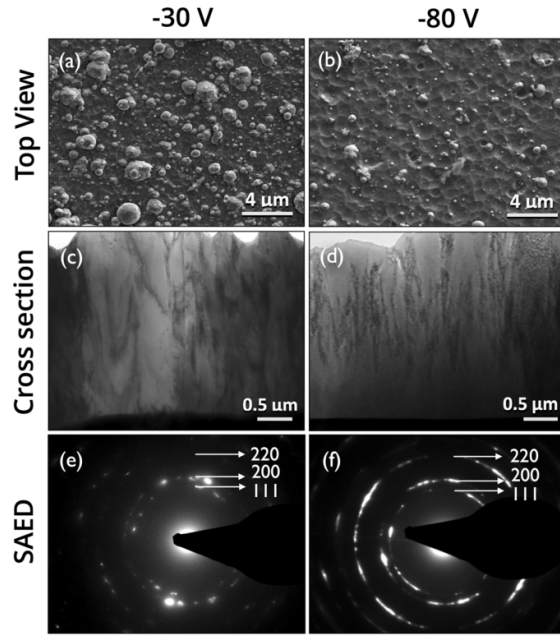FIG. 2. Top-view SEM micrographs of as-deposited $(Ti_{0.54}Al_{0.46})N_{0.87}$ films with negative bias voltages of (a) $-30\,V$ and (b) $-80\,V$, the cross-sectional TEM images of (c) $-30\,V$ and (d) $-80\,V$, and SAED of (e) $-30\,V$ and (f) $-80\,V$.

c-(Ti,Al)N.[34,35] The $(Ti_{0.54}Al_{0.46})N$ reference samples have resolved the T_2 peak corresponding to spinodal decomposition.[35,36] The $(Ti_{0.54}Al_{0.46})N$ reference samples biased at $-30\,V$ and $-80\,V$ and the nitrogen deficient samples biased at $-80\,V$ show another peak (T_3) at around $1200\,°C$ corresponding to the transformation of the c-AlN into w-AlN. This peak is not clearly observed in the nitrogen deficient sample biased at $-30\,V$ and is expected to occur at higher temperature starting from $1200\,°C$, where a weak peak is observed. The T_1 to T_3 peaks are labeled in reference to the XRD result shown in Fig. 4. The peak at $1100\,°C$ is an instrumental artifact caused by a phase transition in the furnace. The thermal response of the coatings reveals that highly biased nitrogen deficient samples have transformed to w-AlN
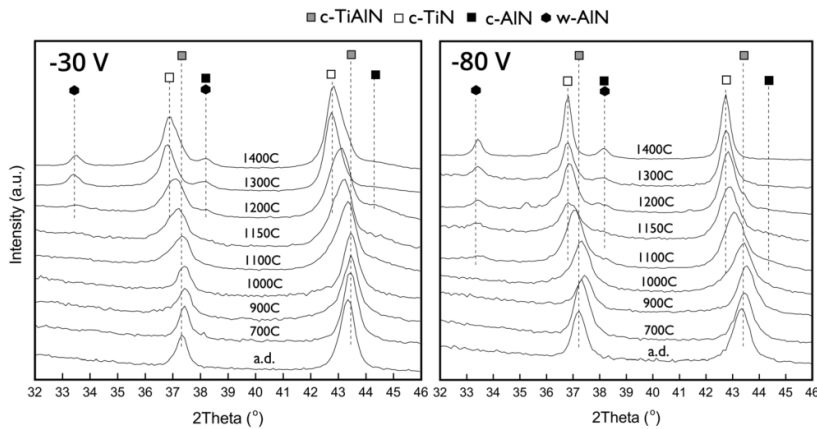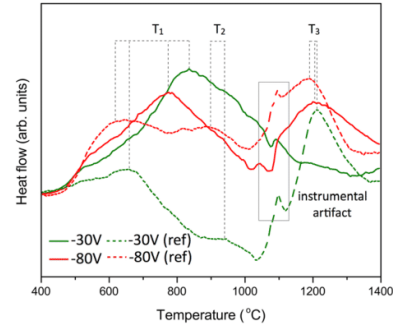

FIG. 3. Exothermal response of $(Ti_{0.54}Al_{0.46})N_{0.87}$ (solid line) and reference coatings (dashed line) at applied bias voltages of $-30\,V$ (green) and $-80\,V$ (red).

at earlier temperature in comparison to samples grown at lower bias voltage. There is no significant difference on the critical temperatures (T_1 to T_3) for phase transformation between the reference samples with different applied negative biases, similar to what was previously reported.[8]

The as-deposited $(Ti_{0.54}Al_{0.46})N_{0.87}$ films were annealed at different temperatures to examine their phase transformation at elevated temperatures. Figure 4 shows their x-ray diffractograms measured at room temperature after annealing. The sample biased at $-30\,V$ presents similar diffractograms in its as-deposited state and after annealing at $1000\,°C$. This indicates that the material still consists primarily of a solid solution of c-(Ti,Al)N, and only a slight shift to higher angles takes place between 700 and $1000\,°C$ due to crystal recovery processes that cause stress relaxation.[13] The recovery is due to the rearrangement of defects and not due to recrystallization[25] since there has been no change in texture even at elevated temperatures. The c-(Ti,Al)N peaks broaden above $1000\,°C$, indicating the formation of c-AlN domains and Ti-enriched c-(Ti,Al)N domains via spinodal decomposition.[7] Well resolved diffraction peaks from both phases are observed at $1200\,°C$. Further annealing causes the c-AlN peaks to vanish while the w-AlN peaks increase in the intensity since metastable c-AlN transforms to its most stable form at high thermal loadings.[12] The sample biased at $-80\,V$ exhibits
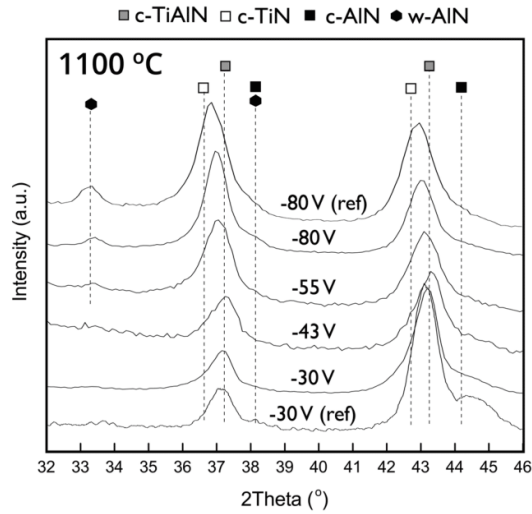

FIG. 4. X-ray diffractograms of $(Ti_{0.54}Al_{0.46})N_{0.87}$ biased at $-30\,V$ and $-80\,V$ after different annealing temperatures.

■ c-TiAlN ☐ c-TiN ■ c-AlN ● w-AlN

FIG. 5. X-ray diffractograms of $(Ti_{0.54}Al_{0.46})N_{0.87}$ with bias voltages of -30 V, -43 V, -55 V, and -80 V and reference coatings with bias voltages of -30 V (Ref. 15) and -80 V annealed at $1100 \,^\circ$C.

peak shifting to higher angles between 700 and 900 °C (due to crystal recovery processes) and peak broadening at 1000 °C (due to spinodal decomposition). The peak corresponding to w-AlN starts to appear at 1100 °C and becomes more distinct at higher temperatures. A similar trend is observed between samples biased at -30 V and -80 V, but the latter exhibits phase transformation at earlier temperatures.

A more detailed view of the bias voltage effect on the phase transformations of c-$(Ti_{0.54}Al_{0.46})N_{0.87}$ is shown in Fig. 5 at two temperatures, 1100 °C and 1200 °C. At 1100 °C, broadening of c-(Ti,Al)N peaks starts to occur for sample -30 V, wherein the peaks shift to left and small bump occurs to the right. The reference coating biased at -30 V heated at this temperature has a higher c-AlN peak intensity as compared to nitrogen deficient coatings. The w-AlN peaks are only resolved for samples with bias voltage -55 V and above, and the peaks become more pronounced by increasing the bias. The increase in w-AlN peak intensity with bias voltage is observed in both nitrogen deficient and reference coatings. However, the reference coating has higher w-AlN peak intensity as compared to the nitrogen deficient coating signifying that it is in a more advanced decomposed state.

The microstructure of $(Ti_{0.54}Al_{0.46})N_{0.87}$ coating grown with a bias of -55 V and heat-treated at 900 °C is shown in Fig. 6(a). The STEM micrograph in Fig. 6(b) shows bright and dark contrast, which arises from compositional segregation. The EFTEM images in Figs. 6(c) and 6(d) confirm segregation on the metal sublattice resulting from the chemical fluctuation during the deposition[37] while segregation on the N-sublattice cannot be detected. The artificial layers caused by rotating the samples during deposition can also be seen. They arise due to preferential resputtering of the lighter elements.[38,39] The observed segregation at 900 °C is less pronounced compared to coatings with stoichiometric N-content,[39] which indicates a higher phase stability.

Figure 7 shows the cross sectional SEM micrographs of the samples biased at -30 V, -55 V, and -80 V then
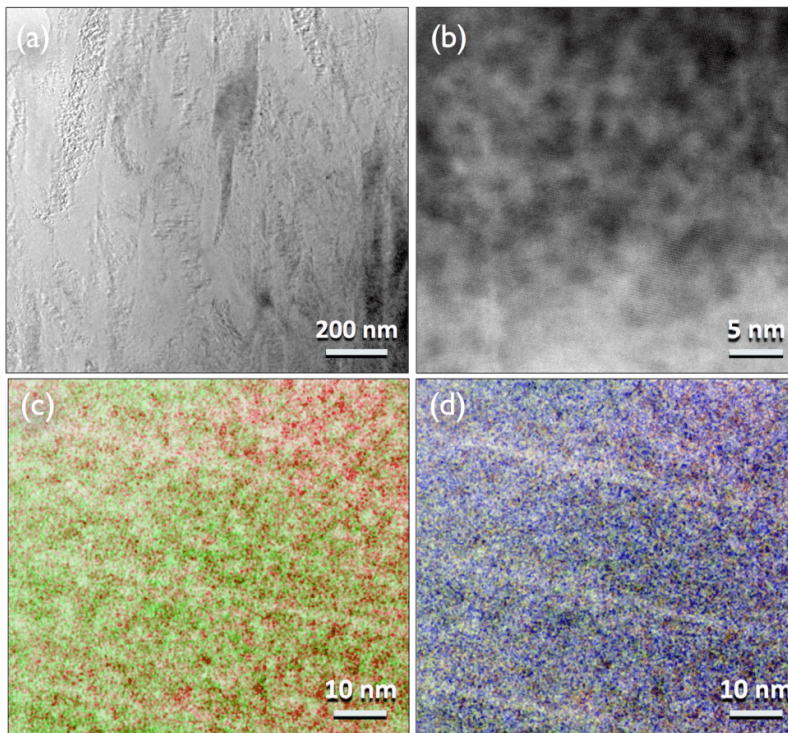

FIG. 6. (a) TEM (b) STEM, (c) EFTEM [Ti(red), Al(green)], and (d) EFTEM [Ti(red), Al(green), N(blue)] micrographs of $(Ti_{0.54}Al_{0.46})N_{0.87}$ grown with a bias voltage of -55 V and heated at 900 °C.
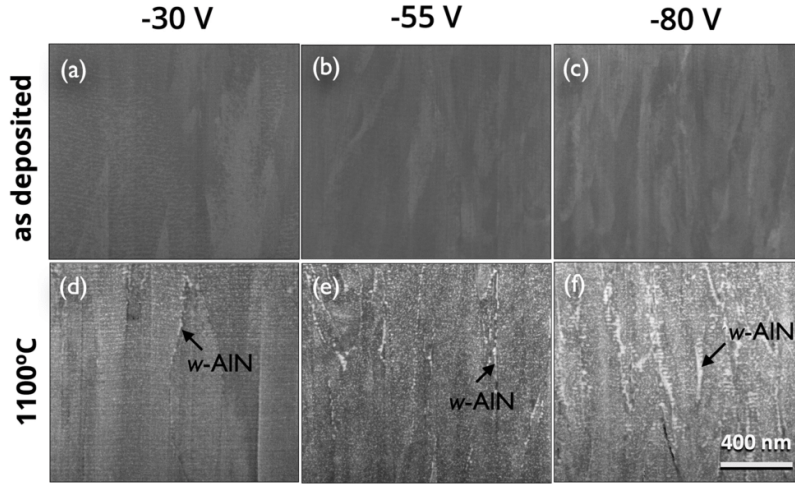
FIG. 7. Cross-sectional HRSEM micrographs of $(Ti_{0.54}Al_{0.46})N_{0.87}$ in as-deposited state with negative bias voltages of (a) -30 V, (b) -55 V, and (c) -80 V and heated at $1100\,^{\circ}$C with negative bias voltages of (d) -30 V, (e) -55 V, and (f) -80 V.

post-annealed at $1100\,^{\circ}$C, i.e., the critical temperature where w-AlN were observed in some samples from the XRD result. It can be observed that large w-AlN domains are growing mainly at grain boundaries. Sample biased at -80 V presents a higher amount of grain boundaries in comparison to the lower biased samples. Therefore, it is expected that highly biased samples have a larger volume fraction of w-AlN, as also observed from the XRD result. The high-resolution TEM images of samples biased at -30 V and -80 V and their corresponding SAED patterns are shown in Fig. 8. When the coatings are heated at $1100\,^{\circ}$C, the sample biased at -30 V retains its c-(Ti,Al)N structure while the -80 V sample has segregated to c-TiN and w-AlN.

3D-APT data from $(Ti_{0.54}Al_{0.46})N_{0.87}$ coatings biased at -30 V and -80 V and annealed at $1100\,^{\circ}$C are presented in Fig. 9. Figures 9(a) and 9(b) show elemental contrast overviews of the reconstructed tips. For clarity, only Al and Ti elements are shown. The morphology of the segregated aluminum- and titanium-rich domains is displayed in Figs. 9(c) and 9(d), where aluminum iso-concentration surfaces were drawn for the same reconstructed tips at an Al value of 26 at. %. Both biased samples presented a 3D interconnected segregation network. For the sample biased at -30 V, the

domains are rounded while at -80 V the domains are slightly elongated. The segregated domains of the reference coatings have similar morphology as the nitrogen deficient coatings (figure not shown). There is no significant difference of the size of the domains between coatings with different N-stoichiometry and applied negative bias. The composition profiles across the interfaces of the decomposed Al- and Ti-rich domains were obtained by using proximity concentration histogram perpendicular to the surface as described by Gault *et al.*[40] Elemental composition of the samples annealed at $1100\,^{\circ}$C is obtained from the concentration profiles across the Al-rich and Ti-rich clusters. Table II shows that the composition of the domains for the two samples. The composition of the domains is similar in the two samples.

The hardness evolution of the biased $(Ti_{0.54}Al_{0.46})N_{0.87}$ films as a function of annealing temperature is shown in Fig. 10. For the as-deposited state, the hardness increases with applied negative bias voltage. The hardness values of the films are retained until $800\,^{\circ}$C. Age hardening is observed for all samples when annealed above this temperature. The occurrence of hardness enhancement has been prolonged when the coatings have lesser bias. A significant drop in hardness is observed when the samples are further annealed
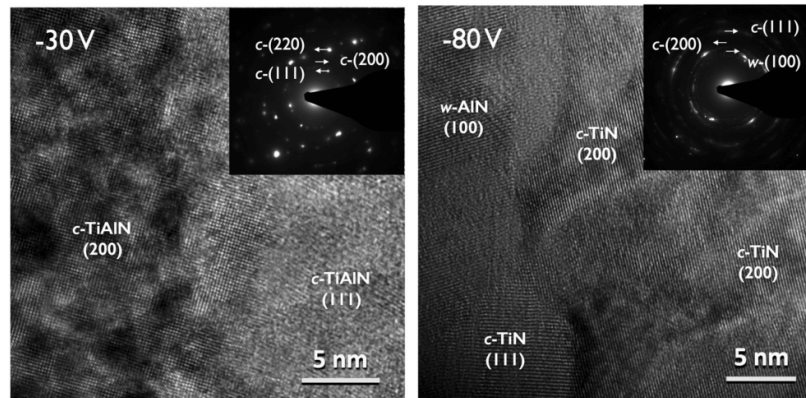

FIG. 8. HR-TEM of $(Ti_{0.54}Al_{0.46})N_{0.87}$ heated at $1100\,^{\circ}$C and biased at (a) -30 V and (b) -80 V and SAED of (c) -30 V and (d) -80 V.
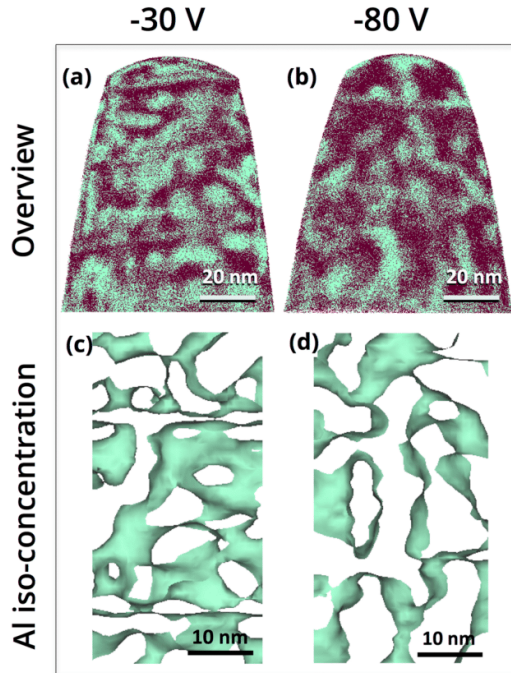
FIG. 9. An overview of the 3D reconstructed tip [Ti(red), Al(green)] of $(Ti_{0.54}Al_{0.46})N_{0.87}$ films annealed at 1100 °C with bias voltage of (a) −30 V and (b) −80 V and the Al iso-concentration surfaces for (c) −30 V and (d) −80 V.

FIG. 10. Hardness at different temperatures of $(Ti_{0.54}Al_{0.46})N_{0.87}$ films biased at −30 V, −55 V, and −80 V and the reference sample.[41]

to higher temperatures. The hardness drops at 1200 °C for the low biased samples (−30 V and −55 V) while the more highly biased sample (−80 V) decreases at 1000 °C. The indentation results show that the sample with the lowest bias had the most prolonged age hardening. The reference coating biased at −30 V has hardness value comparable to the nitrogen deficient $(Ti_{0.54}Al_{0.46})N_{0.87}$ in the as-deposited state; however, the former exhibits age hardening at lower temperature of around 800 °C and its hardness started to drop at 900 °C. The $(Ti_{0.54}Al_{0.46})N_{0.87}$ coating biased at −55 V showed the optimal mechanical behavior since the hardness values are relatively high and age hardening occurred at higher temperature and retained for a longer temperature range.

IV. DISCUSSION

Previous studies have shown that the presence of nitrogen vacancies significantly improves the phase stability of (Ti,Al)N-alloys, in which spinodal decomposition is retarded

TABLE II. Elemental composition inside Ti- and Al-rich domains of $(Ti_{0.54}Al_{0.46})N_{0.87}$ films biased at −30 V and −80 V annealed at 1100 °C.

Bias voltage (V)	Al (at. %)	Ti (at. %)	N (at. %)
−30 (Al-rich)	50.9 ± 0.4	2.2 ± 0.1	46.7 ± 0.4
−80 (Al-rich)	48.3 ± 0.4	4.4 ± 0.2	46.8 ± 0.4
−30 (Ti-rich)	3.3 ± 0.1	48.2 ± 0.3	48.2 ± 0.3
−80 (Ti-rich)	4.5 ± 0.1	46.2 ± 0.3	48.9 ± 0.3

and w-AlN formation is shifted to higher temperatures.[14,15] These results suggest defect engineering as a route for new and improved materials. However, the synthesis method used may affect the defect structure. It has been reported that cathodic arc deposition introduces self-interstitials and anti-sites in the film[25] and one key deposition parameter affecting such point defect generation is the substrate bias voltage.[23,25] In this study, we build on the concept of vacancy improved thermal stability and include the effect of point defects generated during growth. We kept other parameters constant to isolate the effect of bias voltage, which included a constant coating composition. We will divide the discussion of our findings in three parts: address the effect of bias voltage on the growth of nitrogen deficient (Ti,Al)N, discuss how it affects the coatings' thermal stability, and describe the effect of microstructural evolution on their mechanical properties.

A. Microstructure of as-deposited films

The microstructure of nitrogen deficient (Ti,Al) coatings is significantly affected when the growth-conditions are altered by changing the bias voltage. When applying a negative bias voltage to the substrate during arc deposition, positively charged metal ions are attracted towards the growing film surface, wherein additional kinetic energy and momentum transfer change the film forming conditions. This alters the morphology and grain size of the films because energetic ions directly associated with high bias voltage enhance surface diffusion, recrystallization, and resputtering.[42,43] The $(Ti_{0.54}Al_{0.46})N_{0.87}$ coatings grown with higher bias voltage results in finer columnar structure since enhanced energy of incoming ions generates more point defects, which increases the nucleation rates and defect density of the coatings during growth.[44] When the defect density is high, the local epitaxial growth of individual columns is interrupted by the occurrence of repeated nucleation.[45,46]

As-deposited $(Ti_{0.54}Al_{0.46})N_y$ coatings grown at different bias voltages all show single-phase solid solution NaCl-structure. The correlation of the peak intensity ratio and

applied negative bias voltage from the XRD results is due to a change in crystallographic texture and not an alteration of the films' stoichiometry. The change in preferred orientation from (001) to (111) and (110) by increasing the bias is a consequence of increasing ion bombardment. In general, the lowest overall energy condition resulting from the competition of surface energy, strain energy, and stopping energy of different lattice planes determines the preferred orientation of a multi-component fcc crystal with NaCl-type structure.[47,48] High bombardment energy of incoming and adsorbed spices would favor (111) and (110) growth, which have the lowest strain energy and lowest stopping energy, respectively. The preference of (110) is also attributed to an ion channeling effect,[49] in which the planes with lower resputtering rate becomes dominant since they survive the high ion bombardment best.

The cathodic arc deposition technique involves bombardment of high energetic ions during the film growth and thus the intrinsic stress of the coatings can be very high. Compressive residual stresses are generated when the number of atoms per unit volume of the film increases through implantation of incoming ions without any atomic rearrangement.[50] For (Ti,Al)N, residual stresses are mainly caused by interstitials and anti-sites (occupation of metal ions or atoms on the lattice sites of nitrogen and nitrogen on the metal lattice sites), which increase the compressive strain fields of the surrounding lattice.[25] The anti-site and interstitial defect concentrations increase with bias voltage or the energy of the incoming ions because it enhances the collision cascade. Consequently, applying a high bias voltage increases the strain energy stored in the system[51] and may affect the diffusion kinetics and evolution of the microstructure when exposed to high temperature. The films deposited with a high applied bias of $-80\,\mathrm{V}$ have the highest compressive residual stress, which causes the interplanar distances parallel and perpendicular to the growth direction to differ.[42] Dispersion of the lattice parameter can result in considerable changes in the activation of processes such as vacancy and interstitial migration when the coatings are subjected to different temperatures. In Sec. IV B, the role of point defects on the observed changes during annealing will be discussed with respect to the thermal stability of nitrogen deficient (Ti,Al)N.

B. Thermal stability of $Ti_{1-x}Al_xN_y$

Nitrogen deficient $(Ti_{0.54}Al_{0.46})N_{0.87}$ coatings have shown enhanced phase stability, wherein phase transformation from c-AlN to w-AlN occurs at higher temperatures as compared to the same transition in stoichiometric films.[16,17,19,52,53] For $(Ti_{0.54}Al_{0.46})N_y$ where y < 1, *ab initio* calculations indicate that nitrogen vacancies is the fundamental reason for the lack of nitrogen in the coatings.[54] The delayed phase transformation to w-AlN of these coatings is mainly attributed to the reduction of mixing enthalpy and the alteration of the phonon dispersion in the presence of nitrogen vacancies.[15] It is expected that the miscibility gap is reduced when nitrogen vacancies are present and as a consequence, the spinodal line is suppressed to lower temperatures.

Stress relaxation and phase transformation occur when the coatings are subjected to increasing temperatures as indicated by the heat flow responses of the DSC curve. A system under such condition seeks to minimize its total energy during which atoms tend to rearrange into configuration giving lower stress provided that they have sufficient time and mobility. The relaxation is attained through migration, redistribution, and annihilation of stress-generating lattice defects.[23,55] The primary defects present in (Ti,Al)N coatings annealed above their deposition temperature are the less mobile point defects, which are the metal interstitials and vacancies.[55] Nitrogen interstitials have low activation energy, and thus, they easily migrate through diffusion to nitrogen vacancies, inner boundaries, or to the surface when annealed at low temperatures ($<500\,^\circ\mathrm{C}$).[56] Metal and nitrogen vacancies affect significantly the thermal stability of TiAlN, but in different ways. The low onset temperature for spinodal decomposition of overstoichiometric $(Ti,Al)N_y$ is attributed to their existing metal vacancies, which enhance diffusion on the metal sublattice.[18] Diffusion requires energy to overcome the energy barriers for vacancy formation and changing atomic positions. Decomposition is then favored in the presence of metal vacancies because only the activation energy for changing atomic positions is needed. In $(Ti_{0.54}Al_{0.46})N_{0.87}$, nitrogen vacancies are prevalent in the system rather than metal vacancies. The presence of nitrogen vacancies in the $(Ti_{0.54}Al_{0.46})N_{0.87}$ material system may also allow diffusion of substitutional metal atoms such that temporary anti-site occupation occurs. However, the formation of anti-lattice sites is associated with high-energy barriers and actually less likely to occur. Nitrogen vacancies also have high activation energy for migration and exhibits slight repulsion, which delays decomposition.[15,56] Thus, nitrogen vacancy concentration in $(Ti_{0.54}Al_{0.46})N_{0.87}$ would contribute to the thermal stability enhancement of in contrast to metal vacancies.

In-situ XRD diffraction study on $Ti_{0.5}Al_{0.5}N$ coatings has shown that increasing the negative bias voltage delays the lattice strain reduction resulting in an accelerated phase decomposition of the material, i.e., w-AlN formation already occurs at $850\,^\circ\mathrm{C}$.[16] Strain reduction happens when the inherent structural defects undergo thermally activated rearrangement and then annihilated or migrate to lower energy sites. The larger size of T_1 peak from the DSC curve of the $(Ti_{0.54}Al_{0.46})N_{0.87}$ coatings biased at $-30\,\mathrm{V}$ as compared to the coatings biased at $-80\,\mathrm{V}$ indicates that many point defects were already annihilated at lower temperatures at lower biasing condition. This signifies that the defects caused by high ion energy bombardment in the presence of N vacancies are more stable than that by low ion energy bombardment,[57,58] contrary to the stoichiometric case $(Ti_{0.35}Al_{0.65})N$ observed by Rogström *et al.*,[8] perhaps by forming more complex defect structures that are more stable. The film biased at $-80\,\mathrm{V}$ has delayed the lattice strain reduction to higher temperature; thus, there are considerable amount of defects that cause the internal energy of the system to increase and consequently accelerate the decomposition tendencies of c-(Ti,Al)N to its most stable form, i.e., c-TiN and w-AlN.

Koller *et al.*[59] have presented the idea that microstructure affects the phase separation of the thin film coatings. It was suggested that under-dense column boundaries caused by lowly biased coatings accelerates decomposition because they provide higher diffusion and reduce retarding forces against volume changes. In this study, the applied negative bias voltage was increased to obtain more dense films. However, the high biased coatings have shown to exhibit decomposition at earlier temperature. *In-situ* x-ray scattering studies have indicated that the size of the Al-rich domains also affects the transformation rate of *c*-AlN to *w*-AlN in $Ti_{1-x}Al_xN$.[8,12] In the case of $(Ti_{0.54}Al_{0.46})N_{0.87}$, the size of the Al-rich domains of both low and high biased films is similar, but later has shown earlier transformation of *c*-AlN to *w*-AlN. Thus, the accelerated decomposition of the highly biased nitrogen deficient (Ti,Al)N is not attributed to the grain density nor domain size changes.

C. Mechanical properties

In this study, defects and residual stresses have been shown to be beneficial to the film's physical properties (e.g., high hardness) in the as-deposited state. The high grain boundary density, high residual stress, and reduction of crystallite size of the $(Ti_{0.54}Al_{0.46})N_{0.87}$ film biased at $-80\,V$ contribute to its higher as-deposited hardness value as compared to film biased at $-30\,V$. A significant increase in hardness is observed when the coatings are subjected to high temperatures. The age hardening observed for the coatings are due to the changes in the microstructure caused by spinodal deposition of *c*-(Ti,Al)N into coherent *c*-TiN and *c*-AlN domains. This mechanism creates composition fluctuation and differences in elastic properties, which prevents dislocations to propagate and thus resists plastic deformation,[7,36,53] known as coherency and Kohler hardening.[10,60]

Further annealing to higher temperatures causes the transformation of *c*-AlN to *w*-AlN. This transformation is detrimental to the film's mechanical properties as it causes the hardness values to significantly drop. The high rate of phase transformation of the coatings biased at $-80\,V$ is attributed to their high density of grain and column boundaries, which serve as high diffusion paths.[17] The grain size modification of the thin films induced by biasing may play lesser role on their spinodal decomposition; however, it has a considerable effect on other phenomena, such as nucleation. The formation of *w*-AlN at grain boundaries is enhanced when the decomposition is suppressed inside the grains.[15,61] The phase transformation would cause an increase in unit cell volume up to around 20%, which obliterates the coherency and increase the likelihood of dislocation movements.[36] It is essential to observe that the critical temperatures for the hardness drop vary with bias voltage. The low biased samples had hardness drop at higher temperatures, which signifies higher phase stability since they have prolonged age hardening effect of the (Ti,Al)N system.

V. CONCLUSIONS

The microstructure and thermal stability of nitrogen deficient $(Ti_{0.54}Al_{0.46})N_{0.87}$ films with different applied bias voltage were investigated. In the as-deposited state, the

highly biased film showed improvements in hardness, morphology, and microstructure because of the enhanced ion bombardment that caused high compressive stresses and densification. At elevated temperature, this ternary material with nitrogen vacancies has shown high thermal stability, in which the phase transformation of *c*-AlN to *w*-AlN is suspended to higher temperatures compared to reference samples with compositions close to stoichiometric value. Adding the factor of bias voltage to the nitrogen deficient film has influenced the thermal stability of the material in addition to nitrogen vacancies. The highly biased films have enhanced the driving force for phase separation because of the delayed annihilation of point defects at high temperature, resulting in an increase in internal energy of the system. The low biased film has delayed phase transformation to *w*-AlN, thus improving the mechanical properties of the coatings, i.e., age hardening effect has been prolonged to the highest reported temperature. Point defect concentration generated during deposition plays a critical role in designing (Ti,Al)N films with desired thermal stability and mechanical properties suitable for hard coating applications.

[1]J. E. Sundgren and H. Hentzell, J. Vac. Sci. Technol., A **4**, 2259 (1986).
[2]P. Jindal, A. Santhanam, U. Schleinkofer, and A. Shuster, Int. J. Refract. Met. Hard Mater. **17**, 163 (1999).
[3]J. Musil, Surf. Coat. Technol. **125**, 322 (2000).
[4]S. PalDey and S. Deevi, Mater. Sci. Eng., A **342**, 58 (2003).
[5]N. Shulumba, O. Hellman, Z. Raza, B. Alling, J. Barrirero, F. Mücklich, I. A. Abrikosov, and M. Odén, Phys. Rev. Lett. **117**, 205502 (2016).
[6]M. Oden, L. Rogström, A. Knutsson, M. Terner, P. Hedström, J. Almer, and J. Ilavsky, Appl. Phys. Lett. **94**, 053114 (2009).
[7]A. Hörling, L. Hultman, M. Odén, J. Sjölén, and L. Karlsson, Surf. Coat. Technol. **191**, 384 (2005).
[8]L. Rogström, J. Ullbrand, J. Almer, L. Hultman, B. Jansson, and M. Odén, Thin Solid Films **520**, 5542 (2012).
[9]F. Wang, I. A. Abrikosov, S. I. Simak, M. Odén, F. Mücklich, and F. Tasnádi, Phys. Rev. B **93**, 174201 (2016).
[10]F. Tasnádi, I. A. Abrikosov, L. Rogström, J. Almer, M. P. Johansson, and M. Odén, Appl. Phys. Lett. **97**, 231902 (2010).
[11]N. Shulumba, O. Hellman, L. Rogström, Z. Raza, F. Tasnádi, I. A. Abrikosov, and M. Odén, Appl. Phys. Lett. **107**, 231901 (2015).
[12]N. Norrby, L. Rogström, M. P. Johansson-Jõesaar, N. Schell, and M. Odén, Acta Mater. **73**, 205 (2014).
[13]P. H. Mayrhofer, A. Hörling, L. Karlsson, J. Sjölén, T. Larsson, C. Mitterer, and L. Hultman, Appl. Phys. Lett. **83**, 2049 (2003).
[14]B. Alling, A. Karimi, L. Hultman, and I. A. Abrikosov, Appl. Phys. Lett. **92**, 071903 (2008).
[15]I. C. Schramm, M. P. Johansson Jõesaar, J. Jensen, F. Mücklich, and M. Odén, Acta Mater. **119**, 218 (2016).
[16]C. Wüstefeld, D. Rafaja, M. Dopita, M. Motylenko, C. Baehtz, C. Michotte, and M. Kathrein, Surf. Coat. Technol. **206**, 1727 (2011).

[17]R. Rachbauer, S. Massl, E. Stergar, D. Holec, D. Kiener, J. Keckes, J. Patscheider, M. Stiefel, H. Leitner, and P. Mayrhofer, J. Appl. Phys. **110**, 023515 (2011).

[18]M. to Baben, M. Hans, D. Primetzhofer, S. Evertz, H. Ruess, and J. M. Schneider, Mater. Res. Lett. **5**, 158 (2017).

[19]F. Rovere, D. Music, S. Ershov, H.-G. Fuss, P. H. Mayrhofer, and J. M. Schneider, J. Phys. D: Appl. Phys. **43**, 035302 (2010).

[20]P. H. Mayrhofer, F. D. Fischer, H. J. Böhm, C. Mitterer, and J. M. Schneider, Acta Mater. **55**, 1441 (2007).

[21]M. Pfeiler, K. Kutschej, M. Penoy, C. Michotte, C. Mitterer, and M. Kathrein, Surf. Coat. Technol. **202**, 1050 (2007).

[22]H. Ljungcrantz, L. Hultman, J. E. Sundgren, and L. Karlsson, J. Appl. Phys. **78**, 832 (1995).

[23]M. Ahlgren and H. Blomqvist, Surf. Coat. Technol. **200**, 157 (2005).

[24]A. Anders, Appl. Phys. Lett. **80**, 1100 (2002).

[25]H. Oettel, R. Wiedemann, and S. Preißler, Surf. Coat. Technol. **74**, 273 (1995).

[26]N. Norrby, H. Lind, G. Parakhonskiy, M. P. Johansson, F. Tasnádi, L. S. Dubrovinsky, N. Dubrovinskaia, I. A. Abrikosov, and M. Odén, J. Appl. Phys. **113**, 053515 (2013).

[27]D. R. Kingham, Surf. Sci. **116**, 273 (1982).

[28]K. Thompson, D. Lawrence, D. J. Larson, J. D. Olson, T. F. Kelly, and B. Gorman, Ultramicroscopy **107**, 131 (2007).

[29]W. C. Oliver and G. M. Pharr, J. Mater. Res. **7**, 1564 (1992).

[30]B. D. Cullity, S. R. Cullity, and S. Stock, *Elements of X-Ray Diffraction* (Prentice Hall, New Jersey, 2001).

[31]C. Wüstefeld, D. Rafaja, V. Klemm, C. Michotte, and M. Kathrein, Surf. Coat. Technol. **205**, 1345 (2010).

[32]N. Norrby, M. P. Johansson-Jõesaar, and M. Odén, Surf. Coat. Technol. **257**, 102 (2014).

[33]O. Piot, C. Gautier, and J. Machet, Surf. Coat. Technol. **94**, 409 (1997).

[34]A. Knutsson, M. Johansson, L. Karlsson, and M. Odén, J. Appl. Phys. **108**, 044312 (2010).

[35]P. H. Mayrhofer, C. Mitterer, L. Hultman, and H. Clemens, Prog. Mater. Sci. **51**, 1032 (2006).

[36]I. A. Abrikosov, A. Knutsson, B. Alling, F. Tasnádi, L. Hind, L. Hultman, and M. Odén, Materials **4**, 1599 (2011).

[37]L. J. S. Johnson, M. Thuvander, K. Stiller, M. Odén, and L. Hultman, Thin Solid Films **520**, 4362 (2012).

[38]A. O. Eriksson, J. Q. Zhu, N. Ghafoor, M. P. Johansson, J. Sjölen, J. Jensen, M. Odén, L. Hultman, and J. Rosén, Surf. Coat. Technol. **205**, 3923 (2011).

[39]A. Knutsson, J. Ullbrand, L. Rogström, N. Norrby, L. Johnson, L. Hultman, J. Almer, M. J. Jöesaar, B. Jansson, and M. Odén, J. Appl. Phys. **113**, 213518 (2013).

[40]B. Gault, M. P. Moody, J. M. Cairney, and S. P. Ringer, *Atom Probe Microscopy* (Springer Science & Business Media, 2012), Vol. 160.

[41]I. C. Schramm, C. Pauly, M. P. Johansson Jõesaar, S. Suarez, F. Mücklich, and M. Odén, "Effects of N vacancies on phase stability and mechanical properties of arc deposited $(Ti_{0.52}Al_{0.48})N_y$" (unpublished).

[42]S. M. Rossnagel and J. J. Cuomo, Vacuum **38**, 73 (1988).

[43]A. Raveh, I. Zukerman, R. Shneck, R. Avni, and I. Fried, Surf. Coat. Technol. **201**, 6136 (2007).

[44]J. Almer, M. Odén, L. Hultman, and G. Håkansson, J. Vac. Sci. Technol., A **18**, 121 (2000).

[45]I. Petrov, P. Barna, L. Hultman, and J. Greene, J. Vac. Sci. Technol., A **21**, S117 (2003).

[46]I. Petrov, L. Hultman, J. E. Sundgren, and J. Greene, J. Vac. Sci. Technol., A **10**, 265 (1992).

[47]J. Zhao, X. Wang, Z. Chen, S. Yang, T. Shi, and X. Liu, J. Phys. D: Appl. Phys. **30**, 5 (1997).

[48]J. Pelleg, L. Z. Zevin, S. Lungo, and N. Croitoru, Thin Solid Films **197**, 117 (1991).

[49]L. S. Yu, J. M. Harper, J. J. Cuomo, and D. A. Smith, J. Vac. Sci. Technol., A **4**, 443 (1986).

[50]M. M. M. Bilek, D. R. McKenzie, and W. Moeller, Surf. Coat. Technol. **186**, 21 (2004).

[51]D. Rafaja, C. Wüstefeld, C. Baehtz, V. Klemm, M. Dopita, M. Motylenko, C. Michotte, and M. Kathrein, Metall. Mater. Trans. A **42**, 559 (2011).

[52]P. H. Mayrhofer, C. Mitterer, and H. Clemens, Adv. Eng. Mater. **7**, 1071 (2005).

[53]A. Hörling, L. Hultman, M. Odén, J. Sjölén, and L. Karlsson, J. Vac. Sci. Technol., A **20**, 1815 (2002).

[54]M. T. Baben, L. Raumann, D. Music, and J. M. Schneider, J. Phys.: Condens. Matter **24**, 155401 (2012).

[55]L. Hultman, Vacuum **57**, 1 (2000).

[56]L. Tsetseris, N. Kalfagiannis, S. Logothetidis, and S. T. Pantelides, Phys. Rev. Lett. **99**, 125503 (2007).

[57]L. Karlsson, A. Hörling, M. P. Johansson, L. Hultman, and G. Ramanath, Acta Mater. **50**, 5103 (2002).

[58]P. H. Mayrhofer and C. Mitterer, Surf. Coat. Technol. **133–134**, 131 (2000).

[59]C. M. Koller, R. Hollerweger, C. Sabitzer, R. Rachbauer, S. Kolozsvari, J. Paulitsch, and P. H. Mayrhofer, Surf. Coat. Technol. **259**, 599 (2014).

[60]J. S. Koehler, Phys. Rev. B **2**, 547 (1970).

[61]R. Forsén, M. P. Johansson, M. Odén, and N. Ghafoor, Thin Solid Films **534**, 394 (2013).

Paper V

Surface directed spinodal decomposition

at TiAlN/TiN interfaces

A. Knutsson, <u>I.C. Schramm</u>, K. Asp Grönhagen,

F. Mücklich and M. Odén

Surface directed spinodal decomposition at TiAlN/TiN interfaces

A. Knutsson,[1] I. C. Schramm,[1,2] K. Asp Grönhagen,[1] F. Mücklich,[2] and M. Odén[1,a)]

[1]*Nanostructured Materials, Department of Physics, Chemistry, and Biology (IFM), Linköping University, Linköping SE-581 83, Sweden*
[2]*Functional Materials, Materials Science and Engineering Department (MSE), Saarland University, P.O. Box 151150, 66041 Saarbrücken, Germany*

In contrast to the monolithic c-Ti$_{1-x}$Al$_x$N, the isostructural spinodal decomposition to c-AlN and c-TiN in c-Ti$_{1-x}$Al$_x$N/TiN multilayers has almost the same onset temperature for the compositions x = 0.50 and 0.66. Differential scanning calorimetry also shows that the decomposition initiates at a lower temperature compared to the monoliths with the same Al-content. Z-contrast scanning transmission electron microscopy imaging reveals a decomposed structure of the multilayers at temperatures where the monoliths remain in solid solution. In the multilayers, the decomposition is initiated at the internal interfaces. The formation of an AlN-rich layer followed by a TiN-rich area parallel to the interface in the decomposed Ti$_{0.34}$Al$_{0.66}$N/TiN coating, as observed in atom probe tomography, is consistent with surface directed spinodal decomposition. Phase field simulations predict this behavior both in terms of microstructure evolution and kinetics. Here, we note that surface directed spinodal decomposition is affected by the as-deposited elemental fluctuations, coherency stresses, and alloy composition. © 2013 American Institute of Physics. [http://dx.doi.org/10.1063/1.4795155]

I. INTRODUCTION

Spinodal decomposition of binary alloys is well understood[1–3] and its theoretical description has been confirmed in numerous experimental studies on polymers,[4,5] metals,[6–8] and ceramics.[9–11] Cubic (c)- Ti$_{1-x}$Al$_x$N coatings are unstable and spinodally decompose to c-TiN and c-AlN at elevated temperatures for alloy compositions inside the spinodal.[9,11–13] Spinodal decomposition is characterized by chemical composition fluctuations with diffuse domain boundaries extended over large volumes,[10,11,13–16] and ab initio calculations show a miscibility gap and a positive Gibbs' free energy.[9,17,18] The isostructural decomposition includes beside spinodal decomposition also coarsening of the formed nm-sized domains. The decomposition is followed by transformation of c-AlN to hexagonal (h)-AlN, possibly through an intermediate state, where h-AlN is semicoherent with c-TiN.[10,11,13–16,19,20] The attractive age hardening seen at elevated temperatures is associated with the isostructural part of the decomposition.[9,11–13] Recent studies on how to influence the decomposition behavior of Ti$_{1-x}$Al$_x$N coatings have addressed effects from annealing conditions,[11] composition,[21] growth induced stresses,[21] additional alloying elements,[22–26] and pressure.[27–29] Multilayers of aluminum containing transition metal nitrides offer the opportunity to study in detail spinodal decomposition in the vicinity of an internal interface and the resulting microstructure. Ti$_{1-x}$Al$_x$N/TiN is particularly interesting because the multilayers provide coatings with good mechanical properties[12] and cutting performance.[30,31] The kinetics of the spinodal decomposition and the resulting microstructure can be significantly affected by the presence of an interface or a surface.[32–35] The characteristic of the interface-controlled decomposition is the formation of a

layered microstructure parallel to the interface, i.e., a dominant wave vector directed normal to the interface or surface. This phenomenon is referred to as surface directed spinodal decomposition (SDSD), and has been observed in polymers[36–39] and metals,[40] but not reported in post deposition annealed thin ceramic films. Adibi *et al.*[41] showed compositionally modulated platelets during growth of Ti$_{0.50}$Al$_{0.50}$N, but reports on a similar behavior based on formation from a solid solution are lacking in the literature.

We have earlier shown that a multilayer structure of Ti$_{1-x}$Al$_x$N/TiN promotes spinodal decomposition, i.e., decomposition starts at a lower temperature.[12] This work investigates, the mechanism behind the earlier onset and how it is affected by the composition and SDSD, which influences the thermal stability of the coating. Furthermore, an evolving layered structure may result in interesting mechanical properties.[42,43] We show how the microstructure and thermal stability is affected by the composition, growth induced elemental fluctuations, and internal interfaces. We have used differential scanning calorimetry (DSC), x-ray diffractometry (XRD), analytical scanning transmission electron microscopy (STEM), and atom probe tomography (APT) in combination with 2-dimensional (2D) phase field simulations to characterize and understand the decomposed microstructure and the kinetics.

II. EXPERIMENTAL DETAILS

The coatings were grown using an industrial reactive cathodic arc evaporation system from Sulzer/Metaplas (MZR-323). The deposition was performed in a N$_2$-atmosphere of 2 Pa, with a substrate bias of −40 V and substrate temperature of 400 °C. Cemented carbide substrates [ISO SNUN120408, chemical composition (wt. %) WC 94 − Co 6] polished to a mirror-like surface finish and Fe-foils were mounted on a one axis rotating drum. Three circular 63 mm cathodes of Ti$_{1-x}$Al$_x$ (x = 0.50 or 0.66) were mounted facing the three

a)Author to whom correspondence should be addressed. Electronic mail: magod@ifm.liu.se.

other cathodes on the opposite side of the drum with composition of $Ti_{1-x}Al_x$ (x = 0, 0.50, or 0.66). Two μm thick $Ti_{0.34}Al_{0.66}N/TiN$ and $Ti_{0.50}Al_{0.50}N/TiN$ multilayers and $Ti_{0.34}Al_{0.66}N$, $Ti_{0.50}Al_{0.50}N$, and TiN monolithic coatings were then grown by evaporating from the appropriate combination of cathodes. For more details on deposition conditions, see Refs. [15] and [44].

X-Ray -2θ diffractograms were recorded over a 2θ range of 20° to 80° with a Panalytical X'Pert PRO MRD X-ray diffractometer using Cu Kα radiation.

For thermal analysis a DSC (Netsch STA 449C) operating in a 50 ml/min argon flow with a heating rate of 20 K/min was used. Samples were prepared by dissolving coated Fe foil substrates in 64% hydrochloric acid. The resulting mm-sized coating flakes were rinsed with acetone and distilled water, ground to a fine powder, and placed in an alumina crucible. For more details on the sample preparation, see Ref. [30]. Before starting the high temperature anneals the powder samples were out-gassed for 3 h at 250 °C at 50 mPa. At least 60 mg of powder was used for each anneal and an anneal cycle consisted of heating to the maximum temperature 1300 °C, directly followed by cooling to room temperature (RT). Baseline correction was executed by repeating an identical heating cycle directly after the first one. The onset of the decomposition was extracted from the thermograms by fitting Gaussian functions to all the observed peaks.

A 200 kV Fei Tecnai G^2 TF 20 UT microscope was used for STEM-imaging using a high angle annular dark field detector with a camera length of 190 mm. Cross sectional TEM/STEM samples of the coatings were prepared by mechanical grinding and polishing followed by Ar-ion beam milling to electron transparency by an Gatan precision ion polish system.

APT was performed using a local electrode atom probe (Cameca LEAP 3000X-HR) in laser mode with a wavelength of 532 nm, pulse duration of 150 ps, repetition rate of 200 kHz and energy of 0.5 nJ. The target evaporation rate was 0.5% ions/pulse and the specimen base temperature was kept at 65 K. The APT needle-shaped specimens was prepared using a focused ion beam (FEI Helios nanolab 600) employing a micromanipulator (Omniprobe 100.7) and a lift-out technique.[45] To reduce the preparation-inherent Gallium ion implantation, the final milling step was made at 2 keV. Reconstruction and analysis of the data were carried out with the software package IVAS (version 3.6.3, Cameca). For reconstruction purposes, an evaporation field of 40 V/nm, image compression factor of 1.65, and a field factor of 3.3 were used. On average, 11×10^6 ions were collected from each tip. Data were depicted as 1D concentration profiles and proximity histograms (proxigrams) for easier correlation with the phase field simulation and TEM results.

The specimens for the TEM and APT investigation were annealed with a heating rate of 20 K/min in a protective argon flow of 50 ml/min using the same setup used for the DSC measurements. The annealing procedure chosen was such that the early stages of spinodal decomposition could be captured, i.e., 700, 800, 850 and 900 °C with no isothermal time period. When the set temperatures were reached the samples were instantaneously cooled by a 150 ml/min helium and argon gas mixture flow.

III. SIMULATIONS

The microstructure evolution in $Ti_{1-x}Al_xN$ was predicted with a phase-field model.[21] In the model $Ti_{1-x}Al_xN$ is approximated as a pseudo binary system consisting of AlN and TiN. The concentration of N is homogenous and constant during the simulations. Hence, only metal diffusion on the metal sub-lattice is considered. The total Gibbs' free energy of the system is given by

$$\Delta G = \frac{1}{V_m} \int_\Omega (\Delta G_m(x_k) + \kappa |\Delta x_k|^2 + \Delta E_{el}) d\Omega, \qquad (1)$$

where V_m is the assumed constant molar volume, G_m is the molar free energy, x_k is the molar fraction, κ is the gradient energy coefficient, and E_{el} is the elastic energy. It is assumed that some clustering of AlN and TiN occur already during deposition as discussed. Thus, G_m is chosen to reflect the degree of clustering at 2000 K given in Ref. [46]. The implementation of the elastic energy term, using results from DFT calculations of the elastic constants[47] and lattice constants,[21] is described in detail in Ref. [21].

In contrast to the previous work, on phase field simulations of $Ti_{1-x}Al_xN$,[21] here we consider a multilayer stack consisting of TiN enclosing a 30 nm thick slab of $Ti_{0.34}Al_{0.66}N$ or $Ti_{0.50}Al_{0.50}N$. The system will give rise to initial strains across the interfaces, which are calculated from the elastic constants and the lattice constants in the following way: the growth direction (GD) is in the (001) soft direction and if it is assumed that the stress in GD = 0, the biaxial plane stress in in-plane (IP) for the TiN layer is

$$\sigma_\parallel^{TiN} = \frac{a - a_{TiN}}{a_{TiN}} \left(C_{11}^{TiN} + C_{12}^{TiN} - \frac{(C_{12}^{TiN})^2}{C_{11}^{TiN}} \right), \qquad (2)$$

where a is the lattice constant in the strained TiN layer, a_{TiN}, is the equilibrium lattice constant for the unstrained system and C_{11}^{TiN} and C_{12}^{TiN} are the elastic constants. The stress in the $Ti_{1-x}Al_xN$ is governed by the same equation, and the resulting lattice constant is given by force equilibrium in IP. Knowing the strained lattice constant a, the strains in IP and GD in the TiN layer were calculated as

$$\varepsilon_{IP}^{TiN} \frac{a - a_{TiN}}{a_{TiN}}, \qquad (3)$$

and

$$\varepsilon_{GD}^{TiN} = -\frac{2C_{12}^{TiN}}{C_{11}^{TiN}} \varepsilon_{IP}^{TiN}. \qquad (4)$$

The strains in IP and GD for the $Ti_{1-x}Al_xN$ layer were calculated in the same way. Since, the initial elemental fluctuations have a pronounced effect on the decomposition, two simulations with different initial fluctuations, large $x \pm 0.035$ and small $x \pm 0.0001$, were performed for both compositions. The initial fluctuation imitates the growth-induced elemental variations in the system[48] and is set as an initial random noise term. The transition from the TiN layer to the $Ti_{1-x}Al_xN$ layer is modeled as a gradual change to avoid a mathematically

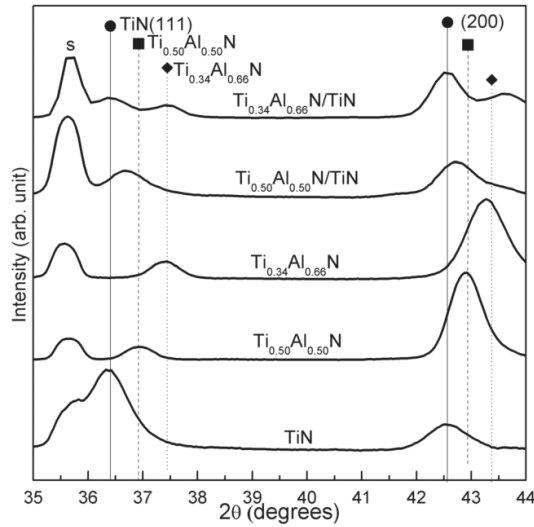FIG. 1. X-ray diffractograms from the monolithic $Ti_{1-x}Al_xN$ and multilayer $Ti_{1-x}Al_xN/TiN$ coatings in their as-deposited state showing only cubic phases. S indicates peak corresponding to the substrate.

sharp change in strains at the boundary. Periodic boundary conditions are applied in the IP direction, while zero flux boundary conditions and constant strains are applied in GD.

The numerical simulations were carried out using FlexPDE,[46] a commercial software for solving partial differential equations. The system of partial differential equations is solved in the following order. First, two simultaneous partial differential equations for the X- and Y- displacements acting on the simulation box are solved. Then, the Cahn-Hilliard

equation is solved by treating it as a system where the chemical potential is computed initially, followed by the composition. A 2D square computational domain of 40×40 nm is used and the temperature is ramped, as in the experiments, from RT to 850 °C by 20 K/min and then back to RT.

IV. RESULTS

A. Experimental results

Figure 1 shows x-ray diffractograms from the TiN, $Ti_{0.34}Al_{0.66}N$, and $Ti_{0.50}Al_{0.50}N$ monolithic and multilayer coatings in their as-deposited state. When Al is introduced in the coating the 111 and 200 peaks are shifted toward higher scattering angles in comparison to TiN, while remaining in the NaCl-type (B1) structure, i.e., $Ti_{1-x}Al_xN$ is a solid solution with a shorter lattice parameter compared to TiN.[21,49] The multilayer coatings show 200 and 111 peaks corresponding to both TiN and $Ti_{1-x}Al_xN$, which is expected for multilayer coatings with these layer periods.[12]

Figure 2 shows Z-contrast cross sectional STEM micrographs of the $Ti_{0.34}Al_{0.66}N$ multilayer coating annealed to (a) 700, (b) 800, (c) 850, and (d) 900 °C using identical annealing conditions as used for the thermograms. All images were acquired at the same magnification and camera length. The brighter areas at top and bottom of the images correspond to the TiN layer while the darker center area is $Ti_{0.34}Al_{0.66}N$. At 700 °C the $Ti_{0.34}Al_{0.66}N$ appears to be homogenous, in contrast to the other annealing temperatures where a decomposed structure is seen. Average compositional wavelengths of 2.3 nm, 2.8 nm, and 3.2 nm were extracted inside the decomposed $Ti_{0.34}Al_{0.66}N$ layer for the 800, 850, and 900 °C anneals, respectively. This was performed using the autocorrelation function in the software

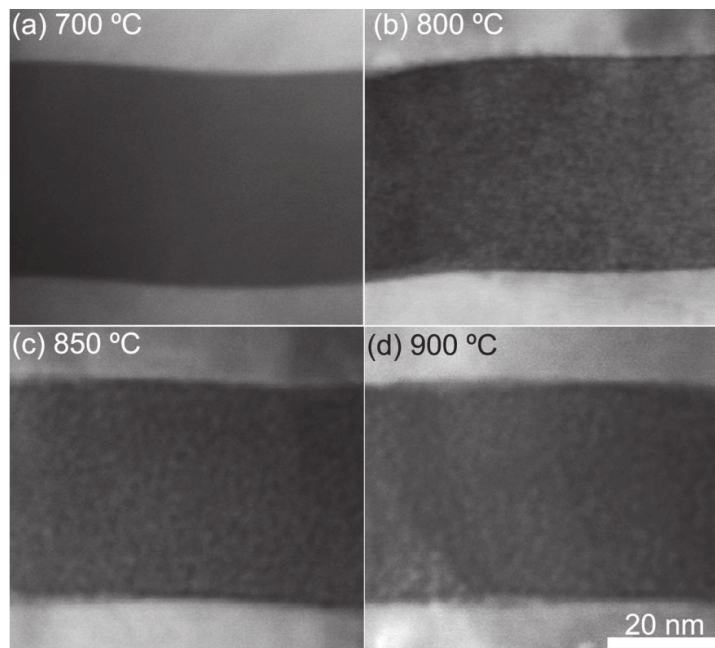FIG. 2. Elemental Z-contrast STEM micrographs of the $Ti_{0.34}Al_{0.66}N/TiN$ coating annealed to (a) 700, (b) 800, (c) 850, and (d) 900 °C. A decomposed structure is observed in (b) and (c). All images were acquired using the same camera length and magnification.
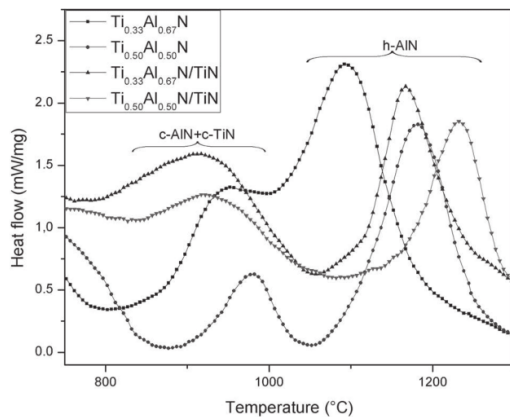
FIG. 3. Exothermal responses from DSC measurements of the multilayer and monolithic $Ti_{0.34}Al_{0.66}N$ and $Ti_{0.50}Al_{0.50}N$ coatings showing peaks corresponding to the spinodal decomposition and the subsequent phase transformation.

Gatan DigitalMicrograph. This technique to determine domain size is expected to slightly overestimate the size due to possible projection errors when imaging the thin TEM foil. A thin dark layer enriched with Al along the multilayer interface is revealed in all the decomposed coatings. This is in contrast to the monolithic coatings annealed at 800 °C, which appear homogeneous when viewed under identical STEM-conditions. Thus, no decomposition is detected for monolithic $Ti_{0.50}Al_{0.50}N$ and $Ti_{0.34}Al_{0.66}N$ at 800 °C in accordance with the thermograms showing a higher onset temperature for the coatings.

Figure 3 shows the heat flow responses of the monolithic and multilayer $Ti_{0.34}Al_{0.66}N$ and $Ti_{0.50}Al_{0.50}N$ coatings. All coatings were found to have the same basic thermal response from the decomposition, with one peak located between 750 and 1050 °C attributed to spinodal decomposition followed by a peak located in the 1050–1300 °C regime assigned as transformation from c-AlN to h-AlN.[9,12] The monolithic $Ti_{0.34}Al_{0.66}N$ coating exhibits a lower onset temperature of the spinodal decomposition (817 °C) compared to the $Ti_{0.50}Al_{0.50}N$ (875 °C). The multilayer coatings, on the other hand, have their spinodal decomposition located in a more

narrow range with onset temperatures of 751 °C for the $Ti_{0.34}Al_{0.66}N/TiN$ and 767 °C for the $Ti_{0.50}Al_{0.50}N/TiN$.

Figure 4(a) depicts a background corrected APT mass spectrum of the $Ti_{0.34}Al_{0.66}N/TiN$ multilayer heat-treated at 850 °C. The mass spectrum and the detected ions are comparable to earlier publications,[48,50] but with smaller thermal tails. Similar spectra were collected for the as-deposited and 800 °C annealed $Ti_{0.34}Al_{0.66}N/TiN$ coatings. Figure 4(b) illustrates a reconstructed tip showing two $Ti_{0.34}Al_{0.66}N$ layers enclosing a TiN layer. For the best visualization only 3% of the Al and Ti ions are presented in the reconstruction. The interfaces are represented by isosurfaces with a 35 at. % Ti threshold value. The red cylinder, with a diameter of 5 nm, represents an example of the volume used for the 1-D concentration profiles in Figure 5.

Proxigrams of isosurfaces of a $Ti_{0.34}Al_{0.66}N/TiN$ interface, in the as-deposited, annealed at 800 °C, and annealed at 850 °C, are shown in (Figures 5(a)–5(c)). In the TiN layer (right), the Al concentration approaches zero for all states. In the as-deposited state, the transition from TiN to $Ti_{0.34}Al_{0.66}N$ layer is seen as a smooth increase followed by a constant concentration for all elements. This is in contrast to the annealed states showing an enrichment of the Al concentration close to the interface in comparison to inside the $Ti_{0.34}Al_{0.66}N$ layer. At 800 °C a Ti-enrichment is also observed after the first Al increase. The maximum Al concentration at the interface enrichment is increased from 35 at. % to 38 at. % when the annealing temperature is increased from 800 to 850 °C. The 1D concentration profiles in (Figures 5(d)–5(f)) correspond to the same interface presented in (Figures 5(a)–5(c)). The enrichment of AlN at the interface in the annealed states is also observed in the 1D concentration profiles. However, in contrast to the proxigrams, the decomposition is observed further into the $Ti_{0.34}Al_{0.66}N$ layer, i.e., an inverse relationship between the Al and Ti concentrations. These chemical fluctuations are averaged out in the proxigrams and therefore not seen. The number of AlN-rich maxima decreasing from five to three between 800 and 850 °C is consistent with domain coarsening. The observed inverse relationship between the N- and Al-concentration seen in the proxigrams is discussed in Ref. 48 where it is attributed to the vacancies on the N sublattice and the calculated negative curvature of the formation energy surface.[51]
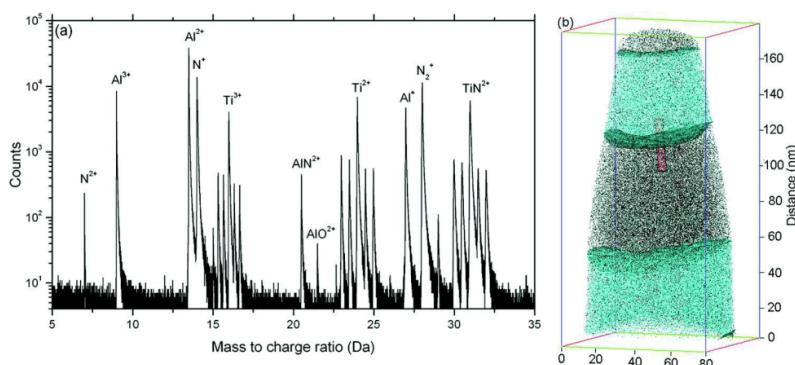

FIG. 4. (a) APT mass spectrum and (b) a reconstructed APT tip of the $Ti_{0.34}Al_{0.66}N/TiN$ multilayer in as deposited state. In (b) light blue corresponds to Al and dark blue to Ti. The red cylinder in (b) represents an example of the volumes used for the 1-D concentration profiles in Figures 5(d)–5(f).
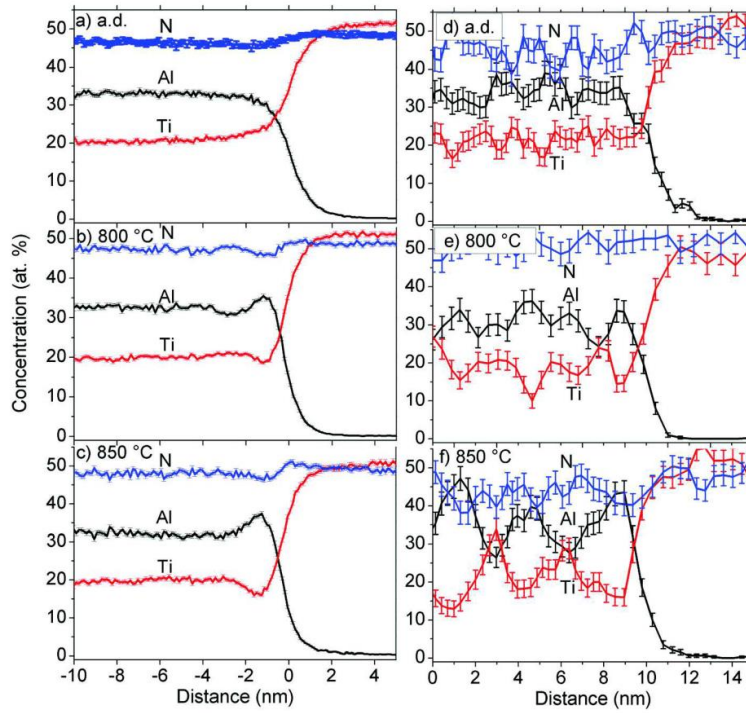
FIG. 5. APT proxigrams from isosurfaces of a $Ti_{0.34}Al_{0.66}N$ (left)/TiN (right) multilayer interfaces in (a) as-deposited state and annealed at (b) 800 °C and (c) 850 °C, showing Al, Ti, and N. Figures ((d)–(f)) show 1D concentrations corresponding to a cylinder (cf. Figure 4(b)) with a diameter of 5 nm of the same interfaces as in ((a)–(c)).

B. Simulation results

Figures 6(a) and 6(b) show the simulated decomposed microstructure of the $Ti_{0.34}Al_{0.66}N$/TiN multilayer resulting from small and large initial elemental fluctuations, respectively. The starting state with small initial fluctuations results in a layered structure with a dominant wave vector perpendicular to the interfaces, while larger initial fluctuations generate a more randomly oriented decomposed structure. At the interface there is, however, an uninterrupted AlN-rich layer followed by elongated Ti-rich domains. Similar simulated structures were obtained for the $Ti_{0.50}Al_{0.50}N$/TiN case.

The total energies of the system versus simulation time of the $Ti_{0.34}Al_{0.66}N$/TiN multilayer and $Ti_{0.34}Al_{0.66}N$ monolith, with large and small fluctuations, are given in Figure 7. The observed decrease of the energies, starting from 2280 s, is due to the decomposition. It is seen that the multilayer system, regardless of initial elemental fluctuation size, decompose earlier than the monolith. The differences are however larger for the small fluctuation case. In addition, the decomposition transpires over a longer period of time in multilayers. Similar graphs were obtained for $Ti_{0.50}Al_{0.50}N$ and the extracted data are given in Table I for a direct comparison.

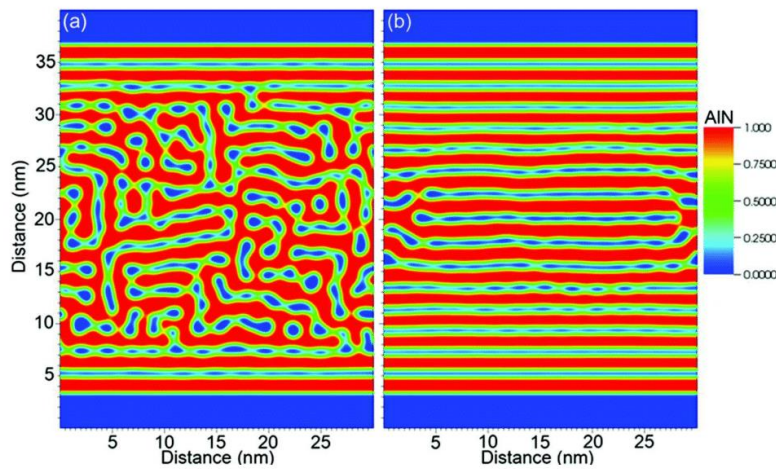FIG. 6. Simulated decomposed microstructure of $Ti_{0.34}Al_{0.66}N$/TiN multilayer with (a) small and (b) large initial elemental fluctuations, where red and blue represent Al and Ti, respectively.
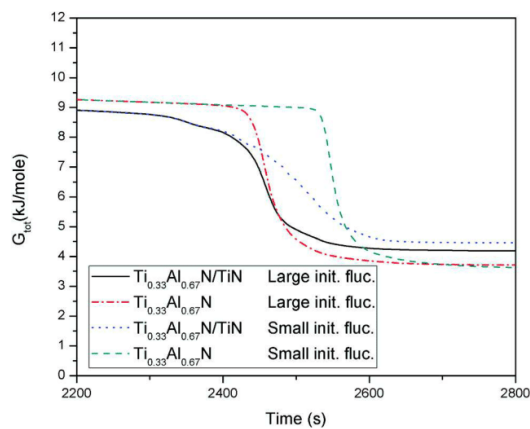
FIG. 7. Total energy versus simulation time of multilayer and monolithic $Ti_{0.34}Al_{0.66}N$ for large and small elemental fluctuations. The decreases in energy correspond to the spinodal decomposition.

Table I gives the onset times of the spinodal decomposition in the simulations of the monolithic and multilayer coatings for large and small initial elemental fluctuations for both compositions. The onset time of the multilayer coatings is always lower in comparison to the monolithic coatings. Furthermore, the onset time of the multilayers is the same regardless of the initial elemental fluctuations. The used time and temperatures in the simulations are not sufficient for decomposition onset of the $Ti_{0.50}Al_{0.50}N$ monolith with low initial fluctuations.

V. DISCUSSION

Based on the experimental XRD and TEM findings, we conclude that the $Ti_{1-x}Al_xN$ layers in the multilayer and the monolithic coatings are initially in equivalent cubic states, which makes comparisons useful. Furthermore, the multilayer coatings characterized in this work reconstruct exceptionally well due to the insignificant difference of the evaporation field between the layers during APT data collection. Thus, the APT characterization provides trustworthy information of the compositional variations seen at the interfaces. The discussion is separated into two parts, the first part describes how the multilayer interfaces affect the decomposed structure and the second part how they influence the thermal stability.

A. The influence of interfaces on the decomposed microstructure

The simulations of the $Ti_{0.34}Al_{0.66}N/TiN$ and $Ti_{0.50}Al_{0.50}N/TiN$ multilayers with small elemental fluctuations

TABLE I. Onset times of the simulated decomposition of the two compositions.

Coating	Onset time (s)			
	$Ti_{0.50}Al_{0.50}N$	$Ti_{0.34}Al_{0.66}N$	$Ti_{0.50}Al_{0.50}N/TiN$	$Ti_{0.34}Al_{0.66}N/TiN$
Small initial fluc.	No decomp.	2520	2340	2280
Large initial fluc.	2460	2400	2340	2280

show that, regardless of composition, a clear SDSD with a compositional wave proceeds throughout the entire $Ti_{1-x}Al_xN$ layer (cf. Figure 6(a)). The obtained compositional wave closely resembles simulations of SDSD in other material systems.[32–35] Based on the simulations and the confirmed power of the model to predict the microstructural evolution,[21] one could also expect a layered microstructure in the experimental observations of the annealed multilayer coatings, which is not the case here. Instead, the STEM micrographs reveal an isotropically decomposed structure in the $Ti_{0.34}Al_{0.66}N/TiN$ multilayers annealed at 800, 850, and 900 °C. This structure resembles earlier observations of the typical spinodal decomposition in monolithic $Ti_{1-x}Al_xN$ coatings.[14,48,52] However, a dark layer that is AlN-rich, is visible along the interfaces in all the annealed $Ti_{0.34}Al_{0.66}N/TiN$ coatings. This microstructural feature is confirmed by the APT measurements where the proxigrams, Figures 5(b) and 5(c), show a clear increase of the Al concentration at the multilayer interfaces of the annealed coatings. The lack of periodicity of the concentration further into the decomposed $Ti_{0.34}Al_{0.66}N$ layers indicates that there is no dominant wave vector directed normal to the surface after the first layer on a larger scale ($\sim$80 nm), which is again in accordance with the STEM images. The decomposed state revealed by the STEM imaging inside the $Ti_{0.34}Al_{0.66}N$ layer is confirmed by the 1D concentration profiles. Figures 5(e) and 5(f) show inverse relationships between the Al and Ti concentrations after the first Al-enrichments. The APT results, thus imply that there is an elemental periodic fluctuation of the decomposed structure on a short scale (5 nm), as is expected from spinodal decomposition,[1] but it is not aligned parallel to the interface on a larger scale. To explain this decomposition behavior one has to consider the initial elemental fluctuations. The formed microstructure with an AlN-rich layer parallel to the interface followed by a weak increase of TiN and an isotropic decomposition inside the layer instead resembles well the simulations in Figure 6(b). Here the simulations represent a situation, where the compositional fluctuations have been increased to ±0.035 at. %. Elemental fluctuations in the as-deposited state are expected, considering both earlier published data[11,48] and our 1D-concentration profile of the $Ti_{0.34}Al_{0.66}N$ layer in its as-deposited state. With these starting conditions, the simulated decomposition is initiated at the multilayer interface as SDSD, but before the periodic structure propagates throughout the $Ti_{1-x}Al_xN$ layer, the isostructural spinodal decomposition initiates inside the layer. The outcome is a competitive decomposition behavior that results in a less developed SDSD microstructure, cf. Figures 2 and 6(b). This is also confirmed in Figure 7, where two different slopes are seen in the energy decrease of the multilayers, an earlier slope due to the SDSD and a later one connected to the internal decomposition. The hindrance of the propagation of the compositional wave into the layer is similar to what was observed in the simulations by Lee *et al.*[38] They reported that the layering from SDSD may disappear when the thermal noise level in the simulations is increased.

The compositional wavelengths, extracted from the STEM images, of the isostructural decomposition inside the $Ti_{0.34}Al_{0.66}N$ layer is in good agreement with our measurements by *in-situ* small angle x-ray on similar monolithic

$Ti_{0.34}Al_{0.66}N$ coatings.[53] The observed compositional wavelength increase, extracted from $\lambda = 2.3$ nm to $\lambda = 3.2$ nm between 800 and 900 °C annealing, indicates that the $Ti_{0.34}Al_{0.66}N$ is in a coarsening stage already after the relatively short thermal spike used in this work. This is again in accordance with our earlier publications showing very short times for the spinodal decomposition of $Ti_{0.34}Al_{0.66}N$.[53] The evidence that a coarsening process is active strengthens our hypothesis that the typical SDSD structure, further into the layer, has been dissolved in the experimental case. Based on the agreement between experimental and simulated results, we conclude that SDSD occurs in $Ti_{0.34}Al_{0.66}N/TiN$ multilayers.

The observed AlN-rich layer seen in this work may explain the more pronounced age hardening at elevated temperature of the $Ti_{0.34}Al_{0.66}N/TiN$ multilayer relative to the monolithic $Ti_{0.34}Al_{0.66}N$, seen in Ref. 12, due to an evolving Koehler hardening effect.[42] The hardness increase might also be attributed to the mechanism explained by Sonderegger and Kozeschnik in Ref. 43 where an enhanced strengthening is observed for elongated domains compared to spherical ones. Thus, SDSD offers a new possibility to tailor the decomposed structure and resulting mechanical properties of hard coatings.

B. The influence of interfaces on the thermal stability

The thermal response corresponding to spinodal decomposition of the monoliths is located $\sim$60 °C lower for $Ti_{0.34}Al_{0.66}N$ compared to $Ti_{0.50}Al_{0.50}N$. This is expected from the calculated asymmetric free energy curve of the system with a maximum at approximately x = 0.66 (Ref. 54) and has previously been observed.[21] On the other hand, the two multilayer compositions have thermal onsets corresponding to the spinodal decomposition only 16 °C apart (751–767 °C). The onsets of spinodal decomposition are shifted by 66 and 108 °C to lower temperatures when compared to the corresponding monoliths. The earlier onset in the multilayers must hence be attributed to the presence of interfaces. The simulations confirm this behavior and show that the SDSD occurs earlier compared to the monoliths, as illustrated in Figure 7. A broader DSC peak of the spinodal decomposition in the multilayer coatings can thus be an effect of the competitive decomposition behavior, with decomposition starting initially at the interfaces (SDSD) followed by internal decomposition, as discussed in Sec. V A. This is also seen in the energy graphs where the decrease of energy occurs over a longer period of time for the multilayers compared to the monolith. It should be noted that as the initial fluctuations are increased in the simulations, the differences in onset time between the monolithic and multilayer coatings are decreased. The trends with an earlier decomposition in the multilayers compared to the monolithic coatings due to the SDSD is, however, still present.

The main reason for the narrow time and temperature differences (16 °C) for decomposition in the multilayers is the strong driving force for decomposition attributed to the multilayer interfaces. However, the coherency strains generated by the lattice mismatch between TiN and $Ti_{1-x}Al_xN$ have also to be considered. The coherency strains will increase the elastic energy. An increased elastic energy is observed to delay the decomposition in our simulations because of a resulting decrease of the driving force. The delay will therefore be more pronounced in the $Ti_{0.34}Al_{0.66}N/TiN$ multilayer coating with its smaller lattice parameter giving a larger misfit to TiN and a resulting increased elastic energy. The strains in the coatings were calculated to be 47% larger in IP and 60% in GD for the $Ti_{0.34}Al_{0.66}N/TiN$ compared to the $Ti_{0.50}Al_{0.50}N/TiN$. The cumulative effect of the SDSD and the elastic energy of the $Ti_{1-x}Al_xN$ layer are then the reason for the small difference in onsets for the two multilayer compositions observed in the thermograms. However, it should be noted, that the effects of strains are small compared to the effect from the interfaces. Moreover, in the simulations the interface and the Al-rich layer are parallel to IP, but in fact, the formation of the wave is independent of crystallographic orientation and whether the $Ti_{1-x}Al_xN$ layer is in tension or compression.

VI. CONCLUSIONS

In this work, we report on the spinodal decomposition in isostructural c-$Ti_{0.50}Al_{0.50}N/TiN$ and c-$Ti_{0.34}Al_{0.66}N/TiN$ multilayers. The presence of internal interfaces shifts the onset of spinodal decomposition to lower temperatures. The main reason for this is surface directed spinodal decomposition that occurs earlier than internal spinodal decomposition. The evolving SDSD microstructure inside the $Ti_{1-x}Al_xN$ layers is confirmed by STEM and APT and is likely to contribute to the improved hardness seen in these multilayers. Furthermore, the lattice mismatch between the layers generates elastic energy, which decreases the driving force for decomposition. However, this effect is small in comparison to surface directed spinodal decomposition.

[1] J. W. Cahn, Acta Metall. **9**, 795 (1961).
[2] J. W. Cahn, Acta Metall. **14**, 1685 (1966).
[3] J. W. Cahn and J. E. Hilliard, J. Chem. Phys. **28**, 258 (1958).
[4] W. Guo and J. S. Higgins, Polymer **32**, 2115 (1991).
[5] J. Gao, C. Huang, N. Wang, W. Yu, and C. Zhou, Polymer **53**, 1772 (2012).
[6] S. M. Allen and J. W. Cahn, Acta Metall. **24**, 425 (1976).
[7] G. Rogl, A. Grytsiv, M. Falmbigl, E. Bauer, C. Mangler, C. Rentenberger, M. Zehetbauer, and P. Rogl, Acta Mater. **60**, 4487 (2012).
[8] P. Hedström, S.Baghsheikhi, P. Liub, and J. Odqvist, Mater. Sci. Eng., A **534**, 552 (2012).
[9] P. H. Mayrhofer, A. Hörling, L. Karlsson, J. Sjölén, C. Mitterer, and L. Hultman, Appl. Phys. Lett. **83**, 2049 (2003).

[10]A. Hörling, L. Hultman, M. Odén, J. Sjölen, and L. Karlsson, J. Vac. Technol. A **20**, 1815 (2002).
[11]R. Rachbauer, S. Massi, E. Stergar, D. Holec, D. Kiener, J. Keckes, J. Patscheider, M. Stiefel, H. Leitner, and P. H. Mayrhofer, J. Appl. Phys. **110**, 023515 (2011).
[12]A. Knutsson, M. P. Johansson, L. Karlsson, and M. Odén, J. Appl. Phys. **108**, 044312 (2010).
[13]A. Hörling, L. Hultman, M. Odén, J. Sjölen, and L. Karlsson, Surf. Coat. Technol. **191**, 384 (2005).
[14]N. Norrby, M. P. Johansson, R. M'Saoubi, and M. Odén, Surf. Coat. Technol. **209**, 203 (2012).
[15]A. Knutsson, M. P. Johansson, P. O. A. Persson, L. Hultman, and M. Odén, Appl. Phys. Lett. **93**, 143110 (2008).
[16]A. E. Santana, A. Karimi, V. H. Derflinger, and A. Schutze, Tribol. Lett. **17**, 689 (2004).
[17]B. Alling, A. V. Ruban, A. Karimi, O. E. Peil, S. I. Simak, L. Hultman, and I. A. Abrikosov, Phys. Rev. B **75**, 045123 (2007).
[18]R. F. Zhang and S. Veprek, Mater. Sci. Eng., A **448**, 111 (2007).
[19]R. Rachbauer, J. J. Genglerc, A. A. Voevodin, K. Resch, and P. H. Mayrhofer, Acta Mater. **60**, 2091 (2012).
[20]D. Rafaja, A. Poklad, V. Klemm, G. Schreiber, D. Heger, M. Sìma, and M. Dopita, Thin Solid Films **514**, 240 (2006).
[21]L. Rogström, J. Ullbrand, J. Almer, L. Hultman, B. Jansson, and M. Odén, Thin Solid Films **520**, 5542 (2012).
[22]R. Forsen, M. P. Johansson, N. Gahfoor, and M. Odén, J. Vac. Sci. Technol. A **30**, 061506 (2012).
[23]R. Rachbauer, A. Blutmager, D. Holec, and P. H. Mayrhofer, Surf. Coat. Technol. **206**, 2667 (2012).
[24]R. Rachbauer, D. Holec, and P. H. Mayrhofer, Surf. Coat. Technol. **211**, 98 (2012).
[25]L. Chen, D. Holec, Y. Du, and P. H. Mayrhofer, Thin Solid Films **519**, 5503 (2011).
[26]L. A. Donohue, I. J. Smith, W. D. Munz, I. Petrov, and J. E. Greene, Surf. Coat. Technol. **94–95**, 226 (1997).
[27]N. Norrby, H. Lind, G. Parakhonskiy, M. P. Johansson, F. Tasnádi, L. S. Dubrovinsky, N. Dubrovinskaia, I. A. Abrikosov, and M. Odén, J. Appl. Phys. **113**, 053515 (2013).
[28]D. Holec, F. Rovere, P. H. Mayrhofer, and P. B. Barna, Scr. Mater. **62**, 349 (2010).
[29]B. Alling, M. Odén, L. Hultman, and I. A. Abrikosov, Appl. Phys. Lett. **95**, 181906 (2009).
[30]A. Knutsson, M. P. Johansson, L. Karlsson, and M. Odén, Surf. Coat. Technol. **205**, 4005 (2011).
[31]M. Nordin, R. Sundström, T. I. Selinder, and S. Hogmark, Surf. Coat. Technol. **133–144**, 240 (2000).
[32]R. C. Ball and R. L. H. Essery, J. Phys. Condens. Matter **2**, 10303 (1990).
[33]G. Brown and A. Chakrabarti, Phys. Rev. A **46**, 4829 (1992).
[34]S. M. Wise, J. S. Kim, and W. C. Johnson, Thin Solid Films **473**, 151 (2005).
[35]B. Zhou and A. C. Powell, J. Membr. Sci. **268**, 150–164 (2006).
[36]R. A. L. Jones, L. J. Norton, E. J. Kramer, F. S. Bates, and P. Wiltzius, Phys. Rev. Lett. **66**, 1326 (1991).
[37]F. Bruder and R. Brenn, Phys. Rev. Lett. **69**, 624 (1992).
[38]B. P. Lee, J. F. Douglas, and S. C. Glotzer, Phys. Rev. E **60**, 5812 (1999).
[39]G. Krausch, C.-A. Dai, E. J. Kramer, and F. S. Bates, Phys. Rev. Lett. **71**, 3669 (1993).
[40]B. Aichmayer, P. Fratzl, S. Puri, and G. Saller, Phys. Rev. Lett. **91**, 015701 (2003).
[41]F. Adibi, I. Petrov, L. Hultman, U. Wahlström, T. Shimizu, D. McIntyre, and J. E. Greene, J. Appl. Phys. **69**, 6437 (1991).
[42]J. S. Koehler, Phys. Rev. B **2**, 547 (1970).
[43]B. Sonderegger and E. Kozeschnik, Scr. Mater. **66**, 52 (2012).
[44]L. Karlsson, A. Horling, M. P. Johansson, L. Hultman, and G. Ramanath, Acta Mater. **50**, 5103 (2002).
[45]M. K. Miller and K. F. Russell, Ultramicroscopy **107**, 761 (2007).
[46]Flex PDE 6, V 6.16. PDE Solutions Inc. (2011).
[47]F. Tasnádi, I. A. Abrikosov, L. Rogström, J. Almer, M. P. Johansson, and M. Odén, Appl. Phys. Lett. **97**, 231902 (2010).
[48]L. J. S. Johnson, M. Thuvander, K. Stiller, M. Odén, and L. Hultman, Thin Solid Films **520**, 4362 (2012).
[49]U. Wahlström, L. Hultman, J. E. Sundgren, F. Adib, and I. Petrov, Thin Solid Films **235**, 62 (1993).
[50]R. Rachbauer, S. Massl, E. Stergar, P. Felfer, and P. H. Mayrhofer, Surf. Coat. Technol. **204**, 1811 (2010).
[51]B. Alling, A. Karimi, L. Hultman, and I. A. Abrikosov, Appl. Phys. Lett. **92**, 071903 (2008).
[52]R. Rachbauer, E. Stergar, S. Massl, M. Moser, and P. H. Mayrhofer, Scr. Mater. **61**, 725 (2009).
[53]M. Odén, L. Rogström, A. Knutsson, M. R. Terner, P. Hedström, J. Almer, and J. Ilavsky, Appl. Phys. Lett. **94**, 053114 (2009).
[54]B. Alling, A. V. Ruban, A. Karimi, L. Hultman, and I. A. Abrikosov, Phys. Rev. B **83**, 104203 (2011).